The dynamics of microplates and application in biosensing

Zhangming Wu

Mechanical Engineering Design

ASTON UNIVERSITY

Doctor of Philosophy

October 2009

Abstract

The thesis presents the work of dynamics study of fluid-loaded microplate and its application in a novel biosensing system, which is designed to be able to detect the properties of biological cells in a liquid (fluid) environment. Knowledge and understanding the dynamic characteristics of microplates in fluid is critical to its application in biosensing. The thesis presents the theoretical models and first analytical solution of the vibration of microplates involving two loading conditions, distributed mass and fluid loading. Various microplates with different dimensions and boundary conditions are manufactured using microfabrication techniques and their dynamics are experimentally tested. A novel biosensing system is developed utilising the dynamical characteristics of microplates. A new system identification methodology based on artificial neural network and distributive sensing approach for biosensing is also developed and tested using bio-experimental data. This work of the thesis paves the way of a real time continuous cell monitoring biosensing system.

The thesis first proposes two mathematical models developed for the dynamics analysis of fluid-loaded microplate. The first model based on Rayleigh-Ritz energy method is to estimate the resonant frequencies and mode shapes, while damping mechanisms of this coupling system is analyzed by using the second model built upon Guz's formulations of hydroelasticity for compressible viscous fluid. Either the first model or the second model can be widely applied to dynamics analysis of fluid-loaded of rectangular plates with various boundary

conditions. The equations derived for the damping mechanism analysis in second model is the first analytical solution to this problem. Moreover, these theoretical models and corresponding analytical solutions also give fundamental contributions to the general engineering problem of fluid-structure interactions. The dynamic properties of fluid-loaded micro-scale plates are examined and discussed through the numerical simulations based on these models.

A testing system is then designed and employed to experimentally determine the dynamics of fluid-loaded microplates. In this experimental system, the base excitation technique combined with pseudo-random test signals and cross-correlation analysis is applied to test microplates. The dynamic experiments cover a series of testing of various microplates with different boundary conditions and dimensions, both in air and immersed in water. It firstly demonstrates the ability and performances of base excitation in the application of dynamic testing of microstructures that involves a natural fluid environment. Additionally, this experimental system and analytical methodologies presented in this part contribute a convenient and fast way in the field of dynamics testing of microstructures. The obtained experimental data provide important information to further understand the dynamic characteristics of fluid-loaded microplates, and also verified the proposed theoretical models.

Next an integrated biosensing system, which is using the microplate as sensing platform and is capable to be self-sensing and self-excitation, is proposed and manufactured. In this microsystem, a scheme of distributed piezoresistive sensors is used to measure the deflection of the sensing surface that is actuated by the PZT thin films. This is the first design to apply a distributive sensing strategy into a microsystem. In addition, this novel configuration of actuators and sensors allows the microsystem is able to work both under static mode and dynamic mode.

Finally biological cells are planted onto the sensing surface of microplates to test their performance in the application of biosensing. A series of bio-experiments are implemented on several different types of microplates. The bio-experiments involve planting different certain amount of cells onto the sensing surface of microplates, and measuring the corresponding dynamics information in the forms of a series of frequency response functions (FRFs). All of those experiments are carried in a truly cells culture medium to simulate a practical working environment and a large number of such bio-experiments are implemented, which are seldom achieved in other researches of biosensors. The shifts of resonant frequencies of microplates are firstly used to give a preliminary analysis on the coated cells. Afterwards, the distributed sensing scheme with artificial neural network algorithm is then used to process the measured data and perform a more accurate identification on the features of cells. The latter methodology has been widely used in many researches, but it is of a brand new concept in the area of biosensing. The analytical results in this work demonstrate great potential advantages of applying this methodology into the area of biosensing.

I would like to dedicate this thesis to my family

Acknowledgements

First of all, I would like to express my thanks to my supervisor Dr. Xianghong Ma for her continual support, encouragement, and invaluable guidance for my PhD studies. I would also like to convey my gratitude to Prof. Peter Brett for leading me into the biomedical research area with his frontier research ideas. I owe special acknowledgments to Prof. Helen Griffths and Prof. Mike Wright who provided me very useful support and suggestions in the biology and dynamics fields respectively. I should also thank my previous supervisor, Prof. Jinwu Xu. who suggested that I came to UK and get involved in this interesting research.

Many thanks should also go to some of my colleagues and friends. Without their support, assistance and help, it would have been almost impossible to finish this research project. I need to thank firstly to Dr. Mark Prince, who patiently taught me how to use the laboratory facilities and helped me on the design of dynamical experiments. Secondly, I want to give thanks to Dr. Dan Gao and Dr. Khjesta, for teaching me a basic knowledge of biology and biotechnology, and providing me with considerable support on the celluar culture experiments. Thirdly, I would also like to thank Yunfei Liu for his microfabrication support and Dr. Garma from Cambridge University for his suggestions on numerical simulation. I am also grateful to all the colleagues in the Biomedical Engineering Research Group at Aston, for creating a relaxed and enjoyable research environment.

I wish to thank all the people who ever helped me or gave me precious suggestions during the past three years of my PhD, in particular Dr.

Paul Slack and Dr. Mark Elliott. I also would like to express thanks to my friends, with whom I really spent a lot of happy time at Aston and in the UK, especially Songjie Chen, Songxiao Song, Jiawei Wang, Iskandar Petra, Huiwen Dong, Xinli Du, Xianfeng Cheng, and Xiaomei Hu etc.

In addition, I would like to acknowledge the staff in the department and workshop of Engineering Systems and Management at Aston, especially Prof. Toby Norris, Prof. John Penny, Mr. David Hall and Ms. Danan etc. I would also like to thank the the Scottish Microelectronics Centre for providing rapid and high-quality microfabrication services, and in particularly to thank Dr. Peter Lomax. Moreover, I wish to acknowledge funding support for this research project from EPSRC.

Finally, I must express my deepest thank to my parents and my elder sister for their love and support.

Contents

List of Figures

Nomenclature

Roman Symbols

$[C]$	Damping matrix of vibration
$[K]$	Stiffness matrix of vibration
$[M]$	Mass matrix of vibration
β_{mn}	Added mass factor
γ_x, γ_y	Double Fourier transform parameters
$\mathbf{I_{mnqr}}$	Fluid-loading impedance
$\mathbf{u}^p$	Displacement vector of plate
$\mathbf{v}$	Velocity vector of fluid
$\mathbf{v}^f$	Velocity vector of fluid
μ	Dynamic viscosity coefficient of fluid
μ^v	Second viscosity coefficient of fluid
∇	Laplacian operator
ν	Poisson's ratio
ω	Vibration frequency

$\omega_{f,mn}$ Natural frequencies of plate in fluid

$\omega_{v,mn}$ Natural frequencies of plate in vacuo

$\overline{m}_c$ The mass per unit area of cell

Φ Scalar potential of fluid

Ψ Vector potential of fluid

ρ_{f0} Quiescent fluid density

ρ_f Density of fluid

ρ_p Volume density of plate

$\vec{\sigma}^f$ Stress tensor of fluid

$\vec{\sigma}^p$ Stress tensor of plate

ζ Damping ratio

c Sound velocity

c_s Shear wave speed

D The flexural rigidity

E Young's modulus

F External force function applied on the plate

F_{hydro} Hydrodynamic force function

h Thickness of plate

$H(\omega)$ Frequency response function

k Acoustic wave number

kx, ky Double Fourier transform parameters

L_a Plate's length

L_b Plate's width

m, n Modal number

p Acoustic pressure

Q Quality factor

R Radius of the simulated cell domain

S Integral domain of the whole rectangular plate

T_f Kinetic energy of fluid

T_m Kinetic energy of cell

T_p Kinetic energy of plate

U_p Potential energy of plate

w The transverse deflection function of the plate

$X_m(x), Y_m(y)$ Mode shape functions of plate

Chapter 1

Introduction

1.1 Dynamics of Microstructures In Fluid

Micro electromechanical systems (MEMS) can be applied in a variety of practical sensing or actuating functions. Systems utilizing micromachined structures ranging in size from a few hundred nanometers to a few millimeters have attracted more and more interest over the past decades, especially in the field of biosensing. The performance and reliability of most MEMS devices are largely determined by the dynamic behavior of those core microstructures[1]. Moreover for biosensing applications, a natural liquid environment is usually required for the biological organism growth. Consequently an understanding the dynamical properties of these microstructures when vibrating in a fluid environment is critical for the preliminary design of MEMS-based biosensors.

The dynamical study of fluid-structure interaction is one of the most significant problems in many engineering fields, and indeed, the simulation of MEMS devices in a fluid environment has received extensive attention. Although there are many numerical methods (such as FEM, BEM etc) that can be used to approximately

predict dynamical responses of the fluid-interacting structures, the discovery of theoretical models and accurate analytical solutions remains a challenge.

The specific problem of the vibration of a thin microplate immersed in fluid is studied in this thesis. In the design of a microplate based biosensing system, a model can be set up to infer the loading conditions from the sensory data of the vibrating plate through the dynamic simulation of a submerged microplate.

1.2 Cell Detection

Cell detection is one of most important topics involved in the study of such varied areas as cell culture, clinical pathologic diagnosis and pharmacology analysis. Currently, the measurement of physical properties and the behaviour of biological cells is mainly performed using microscopy imaging systems. However, the process of cell growth is difficult to visualise continuously in real time. The tasks of cell culture, monitoring and manipulation can therefore be tedious and time consuming. Cell responses to external stimuli are also frequently difficult to visualise in real time. More advanced tools are required to improve these measurements.

Driven by the rapid development of MEMS(Microelectromechanical Systems) technology, the design and creation of rapid, ultrasensitive, and economical biosensors for the detection of cell growth becomes possible. In the past decade, many researchers and practitioners have used bending and oscillating cantilevers as the sensing element to detect cell growth as well as other femtogram-level($10^{-18}kg$) mass entities. Moreover, the concept of measuring mass changes by tracking corresponding resonant frequency shifts in micro-cantilevers has become a well-established technology in chemical and biological sensing applications.

Limitations On reviewing the results of the research works of micro-cantilevers, it is clear that some limitations exist when using cantilever as the sensing elements in micro-mass sensors.

a) The detection resolution of the microcantilever mass sensors is sharply decreased in a fluid medium(even in air ambient) due to the reduction of the resonator quality factor caused by increased viscous damping by the liquid. However in many cases, majority cells can only live in liquid ambient.

b) The position of the mass(cell) along the cantilever also affects the frequency shift. If this condition cannot be identified, it could give wrong measurement results.

c) Micro-cantilever mass sensors based on the principle of frequency shifts can only be used to measure mass changes. Due to the one-dimensional space of microcantivlever, it is difficult to provide more information such as the shape and position of the masses. This may also be important under some situations of cell culturing detection.

1.3 A Novel Biosensing Microplate Transducer

The research discussed in this thesis utilises silicon-based microplates with distributed sensors and actuators to replace the conventional cantilever-type sensing element for cell detection.

In macroscale devices, it is common to use plates as sensing surfaces. One example of these is the force plate, which can provide very accurate measures of the force and moment components generated as a person walks over a surface and can hence be used as a tool for gait analysis[2]. In addition, distributed sensors and actuators embedded in plates have found wide application in dynamic measurements and vibration control of structures[3], especially in plate damage detection[4, 5]. Through correlating and analysing input signals from actuators and output signals from sensors, changes in plate modal parameters can be estimated. The variation of modal parameters can usually be used as effective indicators of the measurement subjects. Similarly, in microscale systems it is also possible to use microplates to identify cells.

Some researchers have already made attempts to apply silicon-based micromachined plates(membranes) as the basic sensing element in bio-sensors for real-time biological measurements. Cedric Ayela and Liviu Nicu[6] developed High-Q-factors(up to 150) circular micromachined piezoelectric membranes as a potential alternative to cantilevers for biological applications in liquid environments. They also experimentally proved that Lamb's theoretical model for a plate vibrating in a fluid is valid for microscale structures and that the variation of liquid viscosity has no effect on the dynamic behaviour of the membranes as long as the viscosity is lower than 10cP. Edwin et al[7] have also devised a micromachined surface stress sensor based on a thin suspended crystalline silicon circular plate. They successfully utilised differential surface stress changes in the sensing plate to detect the bending behaviour caused by vapor phase chemisorption of the alkanethiol monolayers.

Advantages The aforementioned technologies and papers suggest that micro-fabricated plates possess attractive advantages comparing with cantilever beams as the basic sensing element in the application of micro-mass detection.

a) High Q-factor micro-plates can be achieved in liquid environment[6], this will enhance the measurement resolutions of femtogram/attogram mass sensors.

b) The microplate with distributive sensors could potentially provide more information, rather than just the weight of cells, and could help to enhance the mass sensitivity too.

1.4 Objectives

The main Objectives of the research involved in this thesis may be summarised as follows:

1. Build mathematical models for the evaluation of dynamical characteristics of submerged microscale plates, the numerical results to be used as reference data for the design of microplate-based microsystems.
2. Manufacture a series of silicon micromachined rectangular plates and experimentally investigate their dynamic charactersitics.
3. The modelling, simulation and manufacture of integrated biosensing systems based on microplates.
4. Apply the microplate biosensor to detect various biological particles in a liquid environment and test their biosensing performance.

1.5 Thesis Organization

This thesis comprises six chapters, including four sections of original researches together with a chapter of literature review and a chapter of conclusions. Figure 1.1 shows the organization structure and work relationships of these chapters.

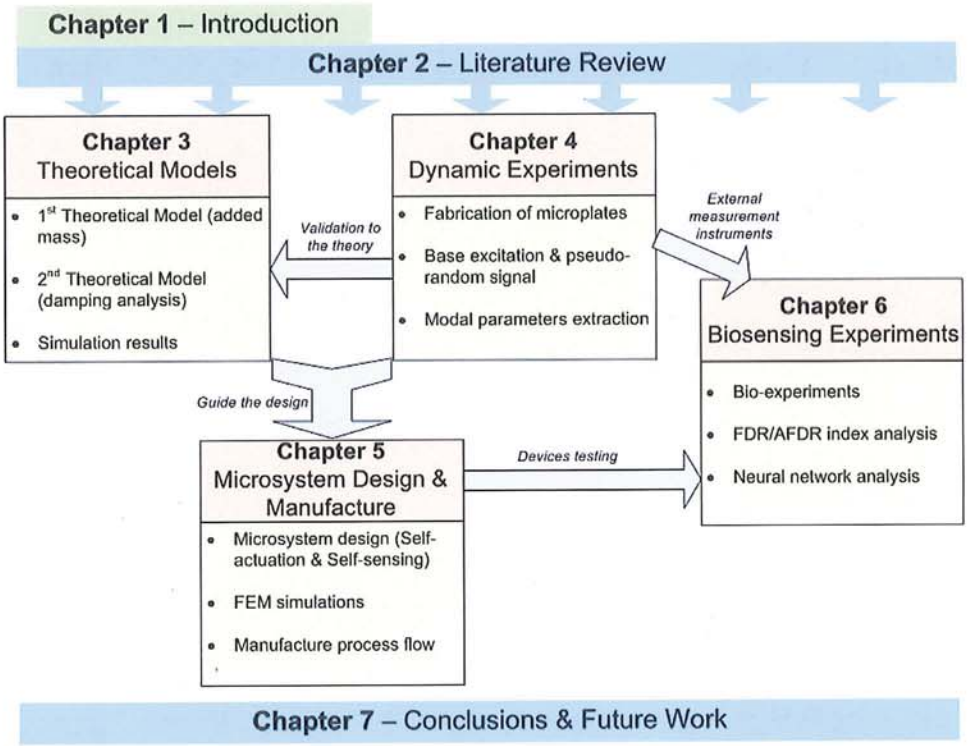

Figure 1.1: Thesis organization

In chapter 2, the published work related to the research of this thesis are reviewed. The work in the field of vibration analysis of rectangular plates with different loading cases (fluid, distributive mass attachment) is extensively examined in the first section. The next section presents various experimental approaches for the excitation and measurement of microstructures, in which the based-excitation method is mainly discussed. The design and manufacture of some existing integrated microsystems is then introduced in the following section. The last part in this chapter reviews different types of mechnical biosensors. In the meanwhile

the advantages and disadvantages of these biosensors with different biological applications are commented upon.

Chapter 3 describes the first task completed in this research, ie building theoretical models for the analysis of the vibration of submerged microplates. General formulations and equations of a vibrating isotropic rectangular plate are presented. The effects of fluid loading on submerged plates is discussed, for neglecting viscous damping. The balance of this chapter concerns two alternative mathematical models. The first model is based on Rayleigh-Ritz energy method. Numerical results for natural frequencies and mode shapes of three different types of microplates, involving both fluid-loading and external distributed mass loading are obtained. Based on the first model, the scaling of fluid loading effect on a microplate is analyzed. Another, more complex, mathematical model is developed for the analysis of the damping mechanism in submerged microplates, including *acoustic radiation damping* and *viscous damping*. Damping ratios as well as the Q-factors of microplates then can be evaluated from this second model.

In chapter 4, a base-excitation experimental system is developed for testing the dynamics of submerged microplates. The theory, testing apparatus and PRBS excitation signals for this experimental system are then described in detail. Several modal analysis methods are introduced and employed to extract modal parameters from the measured data. Finally, the experimental results for a series of submerged microplates are presented and compared with the numerical results obtained from the two theoretical models.

Chapter 5 presents the biosensing systems based on microplates that have been designed and fabricated in this thesis. Simulations on PZT thin films and piezoresistive gauges are implemented and discussed for the optimal designs of microsystems. The fabrication processes for these microsystems are also introduced at the end of this chapter.

The details of bio-experiments involving the planting cells on the sensing surface of microplates and examination of the dynamic differences are firstly described in chapter 6. Afterwards a large number of bio-experimental results of a series

of microplates, using the resonant frequency based indices, are presented which verify the biosensing ability of microplates working under liquid environment. A further analysis using neural network method on these experimental results is demonstrated lastly.

Chapter 7 presents the conclusions as well as the limitations that have been drawn or found during the works in this research. Potential applications utilizing the achivements of this research are discussed next in this chapter. Some suggestions for further research on topics of this thesis are also presented.

Chapter 2

Literature Review

2.1 Introduction: Scope of the literature survey

The research presented in this thesis mainly consists of three parts: the dynamical investigation of fluid-loaded microplates, the study of the biosensing ability of a microplate and an integrated biosensing system design. The work thus, inevitably, covers a wide range of topics, including the vibration of microplates, acoustic radiation, microfabrication techniques, biosensors and system identification. The literatures related to these areaes of research is reviewed in this chapter.

Traditional vibration analysis for macro-scale plates provides critical theoretical basis and background to understand the dynamic characteristics of micro-scale plates. Various theories, models and approaches for the vibration analysis of plates *in vacuo, in fluid or with mass loading* are extensively reviewed in Section 2.2. Furthermore, some published researches on the effects of fluid viscosity on the motion of microstructures are also reviewed, with the purpose of building an accurate damping analysis model for submerged microplates. As a consequence, the literature review in this section leads to the development of theoretical models

of submerged micro-scale rectangular plates carrying distributed masses (Chapter 3).

Experimental work is essential to further understand the vibration behaviours of microplates and to validate the theoretical predictions. In Section 2.3, various experimental approaches for the excitation and vibration detection of microstructures are reviewed. Based on this previous experience, a base-excitation experimental system for the dynamical measurement of microplate behaviour is designed and demonstrated, in Chapter 4. Methods of modal analysis for base excitation and the modal parameters estimation in the frequency domain from FRF (frequency response function) data are also reviewed in this chapter. These methods are useful in extracting dynamic models of microplates from the experimental data.

Much previous work has been carried out on microcantilever-based biosensing systems. and developed lots of microsystem fabrication techniques, experimental approaches on coating bio-materials and corresponding identification methods, which are instructive to design the experiments of testing the performance of microplates as a biosensing element. In section 2.5 some examples of the application of microcantilevers in biosensing are discussed. Some attempts to apply micromachined plates(membranes) in biosensing, are also reviewed at the end of that section.

The literature that discusses the physical parameters and characteristics of PZT thin films and piezoresistors for MEMS applications are reviewed in section 2.4. Knowledge of PZT thin films and piezoresistive gauges is required in the design of integrated microplate-based biosensing systems, in which the PZT thin films are used to excite the microplate, while the distributive piezoresistive gauges are used to track the vibrational response of the microplate. Some of the critical microfabrication techniques in PZT films deposition and piezoresistive gauge manufacture are reviewed in relavent to optimal design practice.

In summary, all the research areas that covered in the literature review of this chapter is listed in Figure 2.1.

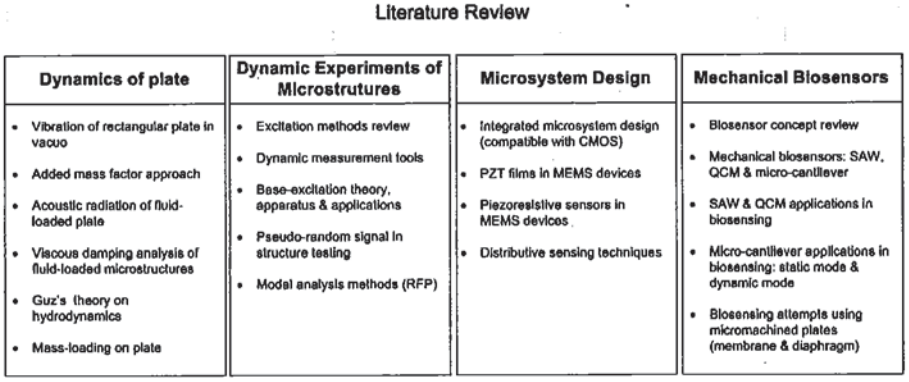

Figure 2.1: Literature review structure

2.2 Vibration of Submerged Rectangular Plates

The vibration analysis of isotropic rectangular plates in vacuo has been fully investigated by many researchers. Detailed formulation and description of the free vibrations of rectangular plates can be found in Leissa's paper[8] and book[9]. A summary of formulas and principles on the vibration of various types of plates also provided in Blevins's book[10]. These analytical methods always required to select the approximate mode shape functions in each of two axes. Warburton[11] first proposed the use of same mode shape functions for beams, which have the same boundary condition as plate. In addition, Bassily and Dickinson[12] stated that the beam functions used in the analysis of plates with one or more free edges need to be modified. Throughout these analytical solutions, the superposition method[13, 14] gradually was used as an analytical procedure to solve the plate vibration problem, especially for the plates with ordinary boundary conditions(simple supported, clamped and free). The Rayleigh-Ritz energy method is also widely used to extract the natural frequencies and mode shapes of free vibration in plate systems[15, 16, 17]. Both the superposition method and Rayleigh-Ritz energy method are adopted in this thesis as a basis and origin to develop advanced theoretical models for submerged microplates.

The study of the vibration of thin plates in contact with fluids started with

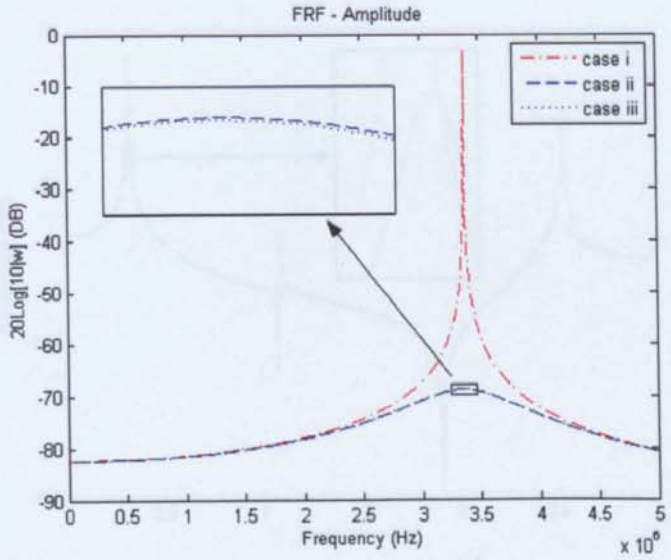

(a)

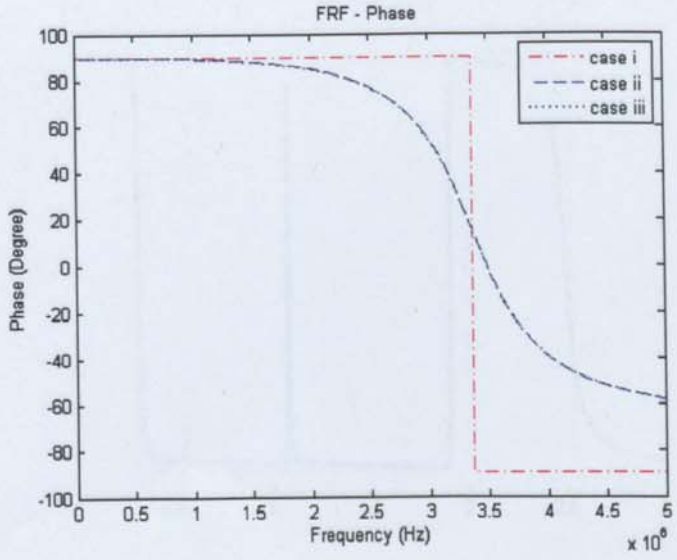

(b)

Figure 3.8: FRF at point $(L_a/2, L_b/2)$ of forced vibration of a fluid-loaded $100\mu m \times 100\mu m \times 5\mu m$ C-C-C-C microplate (frequencies scanning from 1kHz to 5MHz)

the work of Lamb[18], who presented a simple model and calculated resonant frequencies of a thin circular plate in contact with water. In Lamb's model, fluid is assumed to be inviscid, incompressible and have no effect on the vibration mode shapes of the plate. The concept of added mass was proposed to calculate the resonant frequencies with fluid loading on the plate. Subsequently a large number of researchers had worked out the vibration modelings of submerged or floating plates with varied geometries and boundary conditions based on Lamb's method and the added mass assumption. More recently Kwak and Kim[19, 20, 21] presented the non-dimensional added virtual mass incremental (NAVMI) factors computation method for circular or rectangular plates. They pointed out that NAVMI factor can be predicted by the ratio between the kinetic energies of the fluid and the plate. Liang et al.[22] used an empirical added mass formulation and the Rayleigh-Ritz method to analyse the vibration frequencies and mode shapes of submerged cantilever plates. The added mass method was then widely employed to approximately evaluate the natural frequencies of fluid-loaded plates and other structures.

Apart from the added mass(mass-loaded) effect the surrounding fluid medium generates additional damping. This is referred to as *acoustic radiation damping.* The radiation of acoustic energy from the plate causes cross-modal couping between the surrounding fluid and the vibrating plate. It induces two different types of external forces on the motion of the plate, acoustic reactance force(inertial forces) and resistive force.

The reactance force will decrease the resonant frequencies of plate. This effect is indicated by the well-known *added mass factor.* Whereas the resistive term appears as a damping and reflects the energy dissipation from the plate to the fluid, as acoustic radiation[23]. Lax[24] was the first to explain the acoustic damping phenomenon in terms of the plate cross-modal couping, and in his paper the self and mutual radiation modal impedances for a clamped circular plates were computed.

Junger and Feit[25] presented detailed theoretical foundations for the problem

of acoustic structural coupling on vibrations. They showed how the acoustic impedance can be a useful parameter in evaluation of acoustic radiation damping. Many approximate analytical and numerical approaches were proposed to obtain the solution for acoustic modal impedances for fluid-loaded simply supported plates. These have the simplest mode shape functions and are ideal for analysis. There are two different forms of the acoustic radiation pressure[25, 26], both of which can be used to deduce the acoustic impedance of plate. One is the Rayleigh formula with finite integral domain[27], from which close-form analytical expressions for the acoustic impedance in a restricted frequency domain can be derived. The other form is yielded from the Helmholtz equation and double Fourier transform[25]. The latter form of acoustic pressure involves an infinite integral domain, but is useful in the analysis of high-frequency behaviour and for asymptotic solutions[26]. Based on the Rayleigh formula, Wallace[28] approximately evaluated the cross-modal acoustic radiation resistance of a simply supported plate in an infinite rigid baffle for under the critical frequencies.

A detailed derivative process of the theoretical formulations of the cross-modal coupling acoustic impedance for the simply supported rectangular plate in an infinite rigid baffle was derived by Davies[23]. In his paper, an asymptotic solution was also presented for low frequencies and the fluid-loading effect on plate was studied by direct comparison with the unloaded case.

Subsequently this approach has been widely used to analysis the acoustic radiation effect on the vibration of rectangular plates. Pope and Leibowit[29] presented a more complete calculation procedure than Davies's asymptotic solution for the acoustic coefficient by employing contour integration. A numerical algorithm for calculating this acoustic modal impedance was also developed and proposed by Chang[30]. By decomposing the integrand into a series sum expansion, Li and Yam[31] also proposed a new simple analytical solution for the self- and mutual radiation impedance of a rectangular plate. Graham[32, 33] in 1995 presented a detailed process of asymptotic analytical solution of this acoustic modal impedance by using contour integration to replace the double Fourier transform.

Sandman[34] proposed an analytical expression for the non-dimensional acoustic impedance by using Rayleigh's formula and a neat integral transformation.

All of these analysis however are based on the simply supported plate. The investigation of acoustic impedance for other boundary conditions is very limited. In Chapter 3 general analytic solution, which is appropriate for all of the ordinary boundary conditions, relevant to the acoustic impedance of a baffled rectangular plate is proposed. Additionally an effective numerical Monte Carlo algorithms is adopted to the compute t'he complicated acoustic-related integration .

Unfortunately, the added mass factor and the acoustic impedance are difficult to evaluate for rectangular plates, especially for plates without simply supported edges. Therefore some researchers resort to approximate numerical methods, such as finite element method[35, 36], boundary element method[37] and doubly asymptotic approximations[38] etc. These numerical methods have been extensively used for solving fluid-structure interaction problems within commercial codes. The difficulty of obtaining the analytical solution of added mass or fluid loading effect is mainly due to the integral singularity of acoustic impedance[30]. In recent years some useful explicit integration methods have been developed for evaluating the acoustic impedance of special cases. Pierce et al.[26] eliminated the integral singularity by reducing each double integral into single integral and transforming from the Cartesianism coordinates to a polar coordinates. Although Pierce only analysed the situation where each integrand of impedance is of finite sum of exponential function, it is clear that this integration technique is applicable to more general cases.

In this thesis Pierce's method is used to evaluate the kinetic energy of the fluid, which can be represented as the effect of incompressible fluid loading and that has an analogous form with acoustic impedance.

The hydrodynamic force of a viscous fluid acting on a solid boundary is mainly composed of the inertial force and viscous force. The ratio of inertial force to viscous force can be indicated by *Reynolds number* ($Re = \rho\omega L^2/\mu$) [39, 40], which is a dimensionless quantity. For most macro-scale cases, the *Reynolds number* is

always very large and this implies that the viscous force is small enough to be neglected, comparing with the inertial force and the fluid can be assumed to be inviscid. For a microstructure the resonant frequencies are typically in the range from kHz to MHz and the characteristic length, is at most few hundreds of microns. In such case the *Reynolds number* for fluid over a microstructure decreases to $Re \sim O(1)$ [41]. Consequently, the inertial force and viscous force of a fluid acting on the microstructures are of the same order of magnitude and the inertial force can no longer dominate the motion of fluid.

The analysis of the effects of fluid viscosity on the motion of microstructures is a challenge, due to the difficulties of solving the Navier-Stokes equations. Nevertheless some asymptotic approaches have been developed to predict the frequency response of the widely-used microcantilever, immersed in a viscous fluid. The earliest attempts on the viscosity damping analysis are based on the idea that the microcantilever can be considered as a moving sphere in the fluid[42, 43]. Obviously this approach makes a strong approximation to the actual geometries and is unable to obtain satisfied simulation results. For more accurate analysis, theoretical model was proposed by Sader[41] in 1998, in which analytical solutions of the microcantilever frequency response in a viscous incompressible fluid were obtained with the help of a series of approximate hydrodynamic functions. Further experimental results demonstrated that Sader's analytical model can accurately predict the resonant frequencies of a micro-cantilever in viscous fluid for many cases[44, 45]. However the limitations of Sader's model are that the aspect ratio of the cantilever beam must be very large and fluid is assumed to be incompressible.

Some alternative approaches had been proposed to overcome the limitations of Sader's model or design to be suitable for specific cases. Decuzzi *et al*[46] analysed the dynamic response of a beam immersed in a viscous liquid in close proximity to a rigid substrate by using the Euler-Bernoulli model coupled with the Reynolds equation. Basak *et al*[47] proposed a three-dimensional, finite element fluid-structure interaction model. It was shown that their model can yield excellent predictions of the submerged microcantilever vibration. As most assumptions in

the damping analysis of microcantilevers are not valid for microplates, none of these microcantilever models can be directly applied to the microplates. However the simulation results from these models provided substantive information for the understanding of the viscous damping mechanism of a microstructure vibrating in fluid.

More recently, some investigators have made efforts on the viscosity analysis of plate-like structures, and their models have become good references in the design of microplate based microsystems[40, 48, 49]. Both Dohner and Sorokin proposed a two-dimensional closed form analytical model for a viscous fluid loaded flexural plate. Using this model, Dohner analysed the damping mechanism of an air loaded SiN plate, and found the viscous dissipation is the dominant damping rather than the sound radiation. Sorokin proposed a standard algebraic solution for that model and analysed in detail the attenuation of the propagating waves induced by the fluid viscosity. Atkinson *et al* also built an theoretical model for a wide rectangular cantilever plate vibrating in a viscous incompressible fluid through obtaining an analytic expression of the fluid reaction force. However in Dohner's plate analysis a simply supported boundary condition was used for simplification, whereas the second viscosity was neglected in Sorokin's solution and the acoustic radiation was not considered in Atkinson's model. Moreover, all of these models are of the two-dimensional, which means that one dimension of the plate (length) is always assumed to be infinite. Obviously it is far fetched to make such an assumption on a microfabricated plate or membrane, and may lead to inaccurate predictions for the plate frequency response.

Regarding the problems of the dynamics of rigid and elastic solid bodies in a quiescent or moving compressible viscous fluid, Guz has extensively investigated and presented a series of formulations in this field[50, 51]. By using the linearized Navier-Stokes equations, general solutions for each component of fluid velocities potential and stress tensors have been developed in Guz's model, which has shown to be appropriate for the analysis of small oscillations of solid bodies in fluid at low Reynolds numbers[52]. A three-dimensional theoretical model has been proposed

in this thesis for the vibration analysis of rectangular micro-plates submerged in a quiescent compressible viscous fluid.

In terms of predicting the dynamics of biosensing microplate carrying cells or particles, the presence of the biologcial molecules can be considered or simulated as distributive mass loading. Most of the published research on the vibration of mass loaded plate considers concentrated mass. Very few papers were found that study the effects of distributed mass in vacuo. Kopmaz and Telli[53] presented a mathematical model of a rectangular plate carrying a uniformly distributed mass, using the Galerkin method to discretize the plate partial differential equation. Wong[54] proposed a formulation to the eigenvalue problem of plates with distributed mass loading based on the Rayleigh-Ritz energy variational principle. Regarding the problem of the vibration of mass loading plate in fluid, the only published work found on this topic was that of Sandman[34].

2.3 Experimental Dynamics of Microstructures

The experimental investigation of the dynamic behaviour of microstructures plays a fundamental role in the study of MEMS, and is especially useful in providing guidance in the design of microsystems. The experimental evaluation of dynamics data is also in determining the natural vibration response of microstructures and validation of theoretical models [55]. However the dynamic testing of a micro scale structure always involves great challenges, as the direct approach of input excitation and output measurement is not possible[56]. The mechanical resonant frequencies of microstructures are typically in the range from kHz to MHz, and even GHz[55], and the dynamic and vibration analysis equipments are difficult to excite and measure at such high frequencies. Moreover, due to the miniature dimensions, it is difficult to directly apply physical external loads or attach extra sensing element on the test microstructures. Consequently conventional excitation tools (such as electric shaker and hammer) and mechanical sensors (like accelerometer), which are commonly used in the modal testing of

macro-structures, are not appropriate for microstructures. Nevertheless some alternative excitation and measurement techniques and tools have been developed for the dynamic testing of microstructures over recent decades.

These various excitation methods including: electrostatic actuation techniques, have been extensively applied to drive MEMS devices by integrating electrodes on the surface of the microstructures. Comb-drive actuators have designed to utilise electrostatic forces to excite microstructures. Examples can be found in IJntema *et al*[57], Burns *et al*[58] and Smith *et al*[59]. However the non-linearity of electrostatic force with input voltage and potential squeezed-film damping make the electrostatic actuation method unsatisfactory for the experimental study of microstructures.

Piezoelectric materials such as aluminum nitride, zinc oxide and PZT, have been extensively used to make MEMS actuators utilizing their inherent advantage of large actuation force and low power consumption. Tilmans *et al*[60] proposed an experimental system in which one piezoelectric element acts both as an actuator and a sensor for the resonance detection of micro-beams. Swei *et al*[61] also demonstrated the excitation ability of piezofilms in their experimental modal analysis of a suspension structure in a hard disk.

In the case where large force and large displacement is required for actuation[62], an electromagnetic method can be adopted to excite microstructures, through the use of implanted magnetic materials. Wilson *et al*[63] investigated the electromagnetic force as a source of excitation in an experimental modal analysis system for small structures. Although the electromagnetic method can provide non-contact excitation and its excitation force can be accurately measured and controlled, low frequency bandwidth limits its applications to dynamics of microstructures[55].

Other techniques such as electrothermal excitation[64, 65] and acoustic excitation[66] have also applied to drive microstructures for dynamic testing. However most of these techniques require complex experimental facilities and only suited to specific applications.

A major disadvantage of all of the above excitation methods is that an extra shaker element (additional materials or electrodes etc) is always attached to the test structure, which can significantly change the physical properties of the original test microstructures. The base excitation method was chosen for the work described i.e. the experimental investigation of isotropic thin microplates in fluid. The base excitation method for structural modal analysis is not particularly designed for MEMS devices but has been applied to applications in space vehicle and nuclear industries[67]. Chou and Wang[68] introduced the base excitation principle into experiments for testing MEMS structures and derived a mathematic model in terms of velocity frequency response functions. Lai and Fang[69] later applied a ultrasonic transducer as the base-shaker to excite the microstructures and to obtain a wide frequency range response. Hu *et al* [70] used a PZT ceramic plate as base-excitation source to execute dynamic testing on microcantilevers. They also found that the performance of base excitation was more powerful than self excitation in the stimulation in mode shapes of micro devices. Epp *et al*[56] presented an improved experimental facility for base excitation, in which the external noises from the facility and environment were reduced.

Although base excitation can be more easily affected by ambient noise and unexpected resonant frequencies of the system, it does not require any extra elements on the test structures. With the help of well-designed base excitation facilities[56] and modal analysis methods[67], the base excitation can be an ideal tool for the dynamic testing of microstructures.

To avoid extraneous disturbances and interference, non-contact, high frequency techniques are always desired for the measurement of the frequency response of microstructures. The Laser Doppler Vibrometer (LDV) is one of the most popular non-contact devices and has been extensively used in the experimental dynamic analysis of microsystems[71]. LDV measures the perpendicular velocity of the test subject surface through the Doppler effect in laser beams. When LDV is applied to a microsystem, the laser beam is usually ejected through a microscope and the size of the focused laser spot can be reduced to circa $1\mu m$. LDVs are thus capable of providing highly accurate point position measurement during the

motion of microstructures. In the experiments presented in this thesis the Polytec MSV-400 is used to record the vibration of the test microplates. MSV-400 is a scanning laser vibrometer, which can automatically measure multiple points in a predefined domain for a single test[1]. The MSV-400 can achieve picometer vibration resolution and up to 20 MHz frequency bandwidth.

Some other optical based non-contact instruments have also been developed and applied in the measurement of microsystems. Interferometry devices can capture the motion of the whole surface rather than a single point[1] and perform high frequency measurements (GHz) [55]. Video-imaging and stroboscopy instruments are suitable for the analysis of in-plane motions of microstructures[1].

The correct choice of input excitation signal to achieve experimental accuracy and efficiency in the structural modal analysis, depends mainly on the dynamic characteristics of the test subject. Nowadays, the most commonly used excitation signals for modal analysis are *random, pseudo random, burst random, sine chirp and stepped sine* [72]. As the fluid-loaded isotropic microplate is a fairly linear system pseudo-random excitation was employed in the dynamic tests. Pseudo-random signals have constant spectral amplitude over a wide frequency band of interest[72] and have almost the same properties as white noise, in terms of covariance function. Lowrey has demonstrated the advantages of employing pseudo-random excitation signals in a cross-correlation identification method for the dynamic analysis of plate systems: noise immunity, small amplitude disturbances and the avoidance of resonance excitation[73]. Rufer *et al* [74] also presented a "Built-In-Self-Test" implementation for the mechanical and thermal characteristic evaluation of cantilever MEMS structures, using pseudo-random sequence to simulate the impulse excitation. Due to the ergodic, repetitious and deterministic nature of the pseudo-random signal testing systems, it can achieve a steady state over a broadband frequency response, which is ideal for the scanning measurement of microstructures.

The aim of the experimental investigation of a structure is usually to obtain a sequence of vibrational modes, which are always characterized by natural frequency,

damping ratio and mode shape. The process of extracting modal parameters from a set of measured dynamic data is usually called *curve fitting*[75]. The measurements can be either in the frequency domain or the time domain. In this thesis frequency response function (FRF) (frequency domain) is measured and collected for modal analysis. For a conventional impact test or shaker test, the FRFs can be simply calculated as the ratio of Fourier transformation of input and output signals. However the modal parameter estimation method for a base-excitation system is slightly different. A detailed dynamic theory and modal parameter estimation methods for base excitation system is developed and presented by Beliveau *et al*[67]. Lee *et al* [76] presented a mathematical model on a general driven-base dynamic testing system, which gave the theoretical basis for the development methods of modal parameter estimation. Ozdoganlar *et al* [1] derived the specific formulations of vibrational microcantilevers under base-excitation testing. Once the analytic model for the testing system is built, modal parameters can be estimated by curve fitting on a set of measured FRF data. Richardson and Formenti [75] 's RFP (rational fraction polynomials) method was employed in this work to calculate modal parameters from dynamic experimental data. The RFP method can accurately and speedily perform both local and global curve fittings directly on the FRF data containing noise.

2.4 Integrated Microsystems Design

Integrated microsystems (active biosensors) which are capable of performing sensing and measurement without external hardware (self-sensing) and easily embedded into typical CMOS circuits, are gradually used in the real biosensing applications, especially for the lab-on-a-chip solutions. Wee *et al* [77] demonstrated a type of static-mode microcantilever with self-sensing piezoresistive gauges (ploysilicon) for protein detection. However, in the microbalance-mode or dynamic-mode biosensors, a self-actuation and self-sensing capability is required to complete the integrated microsystem. Jin *et al* [78] implanted a piezoresistive bridge

and a metal coil into the cantilever for dynamic sensing and magnetic force resonance excitation, respectively. With optimized electromagnetic excitation, high sensitivity and tens-picogram resolution for in-air mass sensing was achieved.

Piezoelectric materials, such as aluminum nitride (AlN), zinc oxide (ZnO) or lead zirconate titanate (PZT), based MEMS resonators have, in recent years, attracted more interest than other ways of actuation (e.g. electrostatic, thermal and electromagnetic resonator), due to the unique advantages of self-actuation and self-sensing capability, high driving force, ultra-low driving voltage and low power consumption[79]. Several types of microcantilever biosensors that embed with piezoelectric films for the function of both actuation and sensing have been presented[80, 81]. Furthermore very thick piezoelectric films, especially PZT films, with large actuation forces are believed to be able to overcome the viscous damping of microcantilevers in a fluid environment[81, 82]. On the other hand, Lu *et al* pointed out few disadvantages when using PZT films as an actuator or sensor in cantilevers:

a) The sensing signals from PZT films are weak and required additional high precision pre-amplification for the detection;

b) Placing PZT-film into a microcantilever results in a multi-layered structure for the transducer, which may include a silicon-based structure layer, PZT layer, electrode layer and bio-selective layer. Mechanical property differences between each layer results in dynamic responses which are more complex and more nonlinear than a single-layer structure. Moreover, it may contribute significant energy dissipation in the transducer due to the electro-mechanical energy conversion in the PZT film[83];

c) Residual stress and initial strain in PZT electrode layers also leads to difficulties in system integration[79].

Consequently, Lu *et al* developed a series of novel integrated mass sensing microsystems[79, 84], in which the PZT actuator is isolated from the resonant structure. The embedded piezoresistive gauges are employed to replace PZT sensors for dynamic

response detection. A similar integrated biosensing microsystem based on microplate is presented in chapter 5.

In practice the piezoelectric actuator is usually fabricated by depositing a layer of piezoelectric material (like PZT film) on the silicon membrane substrate, using sputter and sol-gel techniques[85]. A piezoelectric actuator is capable of converting the electric energy into mechanical energy (vibration); the ratio between the two converted energies mainly determinates the performance of piezoelectric actuator. Cho *et al* presented a one-dimensional mathematical model[86] and experimental results[87] for the effects of design parameters: such as the thickness ratio of the PZT film to the silicon substrate, size aspect ratio, residual stress. A finite element model of the micro/nano piezoelectric film is proposed by Southin *et al* [88], in which the electromechanical coupling factor is the target coefficient to be considered in the geometrically optimal design of the piezoelectric based structure. Lu *et al* [89] experimentally examined the influence of film-thickness on the mechanical/electric properties of PZT cantilever films. They discovered that the Q-factor of microcantilever films can be enhanced and the residual stress in the PZT film is decreased with increasing the film thickness. Jae Hong Park*et al* [90] believe that thick PZT films can provide lager excitation force, higher electromechanical coupling factor and low dissipation loss, which would be suitable to use in liquid environments. In their paper, a microcantilever with $22\mu m$ thick PZT layer on a $12.3\mu m$ thick silicon membrane substrate was fabricated and the characteristics of thick PZT film was experimentally demonstrated.

Micro-piezoresistive gauges acting as embedded sensors in a microsystem, are commonly fabricated through Boron diffusion[83] to form a doped poly-silicon or Boron ion implantation[77, 78, 91]. Wheatstone bridge circuit is required to amplify the output signals of the micro-piezoresistor. Kon *et al* [92] provided a theoretical model that governs the characteristics of piezoresistive strain sensors in the application of vibration measurement. They also revealed the relationships between the sensitivity (gauge factor) of piezoresistive gauges and their geometries and parameters, which can be used to guide the optimal design of

piezoresistive guages. Duval *et al*[91] employed piezoresistor sensors to measure the displacement and force of a PZT cantilever actuator.

Distributive sensing techniques have been widely used to monitor and reconstruct the static deformation or dynamic responses of conventional structures: in the fields of vibration control, damage detection and biomedical analysis etc. One notable instance is a beam-like or plate-like smart sensing surface with few distributive tactile sensors, which are placing at well-selected locations and used to collect the data of surface deformation. Any change upon the sensing surface can result in corresponding change of measurements in each sensor. The features or properties of contacted object are related to the sensory data. Advanced nonlinear feature analysis methods, for example neural network, can be applied to infer the properties of a contacted subject. These kinds of tactile sensing surfaces have been successfully applied to determine a description of force loading[93], localize a contacting subject[94] or even human gait analysis[95]. Apparently the design of integrated microsystems for biosensing can also borrow the concept of the smart sensing surface, in which multi-dimensional signals rather than single output from the sensing surface, can be collected and used for pro-processing and analysis. This system has potential to extract more information than previous mass microsystems, such as distribution or pattern, of analyses for biosensors. In chapter 5, a novel microplate biosensing surface equipped with distributive tactile sensors is designed and studied.

2.5 Microsystems in Biosensing

The development of biosensors can be traced back to 1962, with Leland C. Clark's first demonstration of an oxygen electrode based "biosensor" for enzyme detection. Since then, the research and development of biosensing devices has continued to the present. The applications of various biosensors have been extended into many fields such as clinical detection, health diagnosis, drug delivery, pathogen

detection of food and environment control etc. Nevertheless, seeking more precise, reliable and rapid biosensing materials, approaches and methodologies is an important topic and still posses many challenges in the field of bio-detection. The core components of a biosensor usually consists of a bioreceptor and a sensing transducer[96]. The bioreceptor is the interface where biosensors interact with the biological environment. The transducer is used to convert the physical/chemical information of the biological particles (such as cells, proteins or DNA) into a measurable signal.

Over the last two decades the fast development of MEMS/NEMS(Micro/Nano-Electro-Mechanical Systems) technologies provides great opportunities to design and create rapid, accurate, ultrasensitive and economical biosensors. Moreover as the MEMS/NEMS based biosensing devices can be easily embedded into standard microelectronic circuits like CMOS (complementary metal oxide semiconductors), some lab-on-chip solutions for automated biological testing have also been proposed and developed to replace the traditional expensive, labor intensive, and time consuming biological experiments[97].

The physics of MEMS/NEMS biosensing transducer usually involve mechanical, thermal, optical and magnetic phenomena etc. These different sensing elements can perform several types of combinations, suitable for various applications of biosensing[96]. A micromachined electro-mechanical transducer that detects surface-attached biological particles through the changes in mechanical energies or properties is the most common biosensing element used.

There are three popular types of electro-mechanical biosensing transducer that have been widely studied: surface acoustic wave (SAW), quartz crystal microbalances (QCM) and various micromachined cantilevers. SAW based biosensors implement the biosensing function through detecting the changes in surface acoustic waves induced by the absorption of biomolecules on the sensing surface[98]. The SAW devices are usually operated at very high frequencies, and thus high mass sensitivity can be potentially obtained[98].

The quartz crystal microbalancs measure the additional surface mass loading via

the decrease of resonance frequency and have been widely applied in gas sensors. More recently some experiments have also demonstrated that QCM systems can be used in sensing DNA and proteins[99]. Nevertheless, both SAW and QCM devices experiences difficulties when applied to stand MEMS fabrication[98] or integrating with MEMS devices[99]. Microcantilevers have attracted significant interest in the field of biosensing and are believed to be a promising platform for future biosensors. Microcantilever possesses several unique advantages such as high sensitivity and high throughput. They are suitable for batch fabrication and are easy to integrate etc[100].

A large number of inverstigators that have demonstrated the unparalleled sensing ability of microcantilevers in the detection of ultral small masses or mechanical stress[77]. With cantilever surface functionalization[100] that is selective coating/depositing with different biological receptors (such as antibodies and phages), microcantilever-based biosensors can achieve various specific applications of biodetection. In general, the microcantilever can perform in two different sensing modes: static deformation and resonance response variation[77, 101]. With adsorption of the target analytes into the receptor layer, additional surface stresses are accumulated that will inevitably result in the increase of static deformation of microcantilever. Several researchers have shown that the the steady-state deformation of the biosensing microcantilever is a function of detected analytes concentration[102, 103], or even a good linear relationship[104].

The second method mentioned above is a microbalance approach, which detects surface-attached mass using resonant frequency shift. Its principle is based on the fact that the added mass to the cantilever is proportional with the change of its fundamental resonance frequency, if the stiffness of cantilever is assuming to be a constant. The resonance sensing mode of microcantilevers is capable of measuring femtogram ($10^{-15}g$)[105] or even attogram ($10^{-18}g$)[106] mass entities. Furthermore, this resonant frequency-based mass detection approach has become a well-established technology in various biological sensing applications[107], such as bimolecular interactions[108, 109], specific cells/virus/bacteria detection[105, 110, 111] and DNA hybridization[112] etc. However, the sensitivity of microcantilever-

based biosensor depends heavily on the value of the quality factor (Q) of the microcantilever, which is largely decreased when the microcantilever is suffering with high damping. Consequently, several techniques have been proposed and developed to improve the low quality factor when the microcantilever is in a liquid biosensing environment. The Q-factor can be enhanced by an active feed-back circuit with a variable amplifier and phase shifter. Mehta *et al* [113] employed the cantilever as part of a passive feedback oscillator, and improved the Q-factor of the microcantilever up to two orders of magnitude. Vidic *et al* [114] later induced internal magnetic or electrostatic stimulation to microcantilevers and employed a closed feed-back loop to drive the cantilever into oscillation. More than two orders of magnitude of Q-factor of a microcantilever in liquid was achieved in their experiments[114].

In terms of actuation and sensing technologies, microcantilever-based biosensors can be operated in two ways: passive and active[115]. For the passive type, external actuation and measurement devices are usually required to stimulate microcantilever and monitor the dynamic behavior response. The microcantilevers of active biosensors can operate in the self-actuating and self-sensing modes. As the active operation mode is usually the ultimate form of biosensor for practical applications, several driving and readout techniques and approaches for self-actuating and self-sensing cantilevers have been developed, such as optical, piezoresistive, piezoelectric and magnetostrictive[115] cantilevers.

Micromachined plates (membrane and diaphragm) have become increasing interests as mass/stress sensing structure in last few years, and some researchers have already made attempts to apply micromachined plates (membranes) in biological detections. Li *et al* [116] introduced a piezoelectric micro-diaphragm (microplate) to replace the traditional microcantilever as the platform of mass detection for biosensing applications, and they theoretically found that the mass sensitivity of the micro-diaphragm is higher than the microcantilever for the same material and size. Carlen *et al* [7] also designed a micromachined surface stress sensor based on a thin suspended crystalline silicon circular plate. They successfully utilized differential surface stress changes of the sensing plate to detect

the bending behaviour caused by vapor phase chemisorption of the alkanethiol monolayers. Furthermore, Nicu *et al* [99] employed micromachined piezoelectric membranes in a flow injection analysis (FIA) system for DNA hybridization detection, and Xu *et al* [117] developed piezoelectric membrane-based biosensor array for immunoassay applications. Most of these proposed investigations and applications on micro-membrane based biosensors are using the same sensing modes with microcantilevers: static deformation[7] and resonance response variation[99, 116, 117]. In Chapter 6, the biosensing sensitivity and performance of silicon-based microplates (membranes) has been studied in detecting two different types of bio-particles.

2.6 Summary

This chapter has reviewed the literature of four areas related to the research in this thesis. These pertinent researches offer a strong background in the theories, methodologies, experimental instruments and design principles for the various analysis and designs of microplates.

A brief history of the dynamics of isotropic rectangular plates was reviewed initially, in which the superposition method and Rayleigh-Ritz energy method for solving plate-related dynamic problems were introduced. Both of these two methods have relative advantages and disadvantages: Rayleigh-Ritz method is more effective but it is normally used in the analysis of conservative systems. The superposition method is capable in principle of applying to all situations but it can be very difficult to get direct solutions in some cases. Previous researches with various methods in the fields of dynamic characteristics of submerged plates, adhesive mass loading effects and dampings of microstructures were presented. The shortcomings of these methods and some unreached research issues, such as the issue of a vibration plate involving fluid loading and distributive mass loading simultaneously, were also discussed.

The base excitation method is believed to be the best choice for testing microplates based on a review of a series of excitation approaches in dynamic experiments of microstructures. Several published papers that contain the theories, experimental devices or analysis methods surrounding base-excitation method were discussed.

A type of integrated system that is capable of self-excitation and self-sensing was then introduced in section 2.4. The characteristics and design principles of PZT films and piezoresistive guages were discussed. These are the key components in the microsystem that was designed and manufactured for the research discussed in this thesis.

Various investigations on mechanical biosensors were reviewed and presented. A range of biological experiments and corresponding applications of microcantilever-based biosensors which are of the most popular type over last decade were discussed. Finally, some pioneer works on microplate-based biosensors were also presented, in which the promising biosensing ability of microplates such as high sensitivity and large sensing area were demonstrated[99, 117].

Chapter 3

Theoretical model of submerged microplates with distributed mass

3.1 Introduction

Micromachined plate(membrane and diaphragm) gradually become a promising sensing structure in the field of chem/biosensors[6, 117, 118]. In general most microplates-based biosensors are sensing the biomolecules through detecting the resonant frequency variations due to the extra mass loading. These biosensors usually need to interact with biological particles in a fluid environment. Consequently an accurate theoretical model for the frequency response analysis of microplate in fluids is always desired to design a high sensitivity microplates based sensing system. The motivation of the research presented in this chapter is to build a mathematical model for the microplate sensing element in cell detection biosensors. This kind of biosensor is designed to be able to work in fluid

and the variation of microplate dynamic characteristics induced by the surface attached cells will be sensed for the measurement.

Two theoretical models have been built in this chapter to analyse vibration characteristics of the submerged microplates. In the situation that the fluid can be considered inviscous and incompressible, resonant frequencies and mode shapes of submerged plates can be roughly calculated by using the Rayleigh-Ritz energy method[119]. Rayleigh-Ritz method is very effective to evaluate the undamped modal parameters; thus it is useful in a large number of cases analysis. Vibration characteristics of the coupling system that fluid-loaded rectangular isotropic plate attached with a uniformly distributed mass are also investigated in this chapter. A lot of papers in literature have respectively presented the changes on the plate vibration behaviour induced by the acoustic field or the attached mass loading. This chapter investigated the issue of involving these two types of loading simultaneously. With Lamb''s assumption on the fluid-loaded structure motion and Rayleigh-Ritz energy method, an analytical solution is proposed to estimate vibration frequencies and mode shapes of the coupling system. Numerical results for the plates with different types of boundary conditions have also been obtained and compared with experimental or numerical results from previous pertinent research. Furthermore this theoretical model has been used in the design of novel biosensing devices.

Nevertheless the model based on Rayleigh-Ritz method is unable to be applied to analysis of the dampings of microplates, which is related to the biosensing sensitivity. At the micron scale significant discrepancies could occur when using the Rayleigh-Ritz approach to predict the dynamic responses[41], especially for the high modes. This is mainly due to the fact that energy dissipation becomes non-negligible when the submerged structure sizes reduce to micron levels. The dissipation of the vibration energy of a microplate in a viscous compressible fluid is caused by acoustic radiation, internal structure damping and viscous losses[120]. The energy losses in the structure is usually small[121], whereas the energy losses in fluid contribute the dominant damping to the vibration. A detailed damping analysis of the submerged microplates is presented, for which are due to the

acoustic radiation and viscous losses. Based on Guz's model and formulations, a three-dimensional theoretical model has been proposed in the analysis of vibration characteristics of a microplate immersed in viscous compressible fluid. This microplate-fluid interaction model is built based on the linearized Navier-Stokes equations and non-slip interface condition. The analytical solution of this specific problem of micro-plates has been obtained by applying the double Fourier transform in the Helmholtz equations of the scalar and vector velocity potentials. A complicated damping matrix is derived and used to study the effects of acoustic radiation and viscous loss. With the help of Quasi-Monte Carlo integration approach, numerical results are also provided to investigate the damping effects on the resonant frequencies and the corresponding Q-factors. Using this model, the effects of acoustic radiation and viscous loss on the fluid induced damping of vibrating microplate have been investigated. The results will show that acoustic radiation contributes the dominant damping of the microplate, however in some particular cases the viscous losses are enhanced and become unneglectable. This chapter also comments on the sensitivity of the microplate-based biosensors with the consideration of viscous fluid dampings.

3.2 Microplate Model with Distributed Mass

The schematic diagram of the sensing system(simplified model) is shown in Figure 3.1, the sensing microplate is assumed to be thin, elastic, isotropic and surrounding by the infinite rigid baffles. A small circular distributed mass resting on the plate sensing surface is used to simulate the cells attachment. In most theoretical vibration analyses of the plate contact with fluid, a simplified model that the plate is placed in an infinite plane baffle is usually considered. This case conforms with the microplate which is always surrounding by a thick wafer, and the size of the wafer could be 1000 times larger than the thin plate.

PAGE

NUMBERING

AS ORIGINAL

the cell covers on plate, it can be expressed in the following form.

$$\begin{aligned}\mathcal{H}(x,y) = &\{H[x-(x_c-R)] - H[x-(x_c+R)]\}\times \\ &\{H[y-(y_c-\sqrt{R^2-x^2})] - H[y-(y_c+\sqrt{R^2-x^2})]\}\end{aligned} \tag{3.2}$$

Heaviside function $H(x)$ is a discontinuous function whose value is zero for negative argument and one for positive argument. Consequently, it can be used to mathematically define a geometric domain. The first half of Eq. 3.2 described the region along x direction. The left part of Eq. 3.2 restricts the region of y and also gives the circular relation between x and y.

The linear solution of Eq.(3.1) can be obtained by summing a series of eigenfunctions in each separated mode[122].

$$w(x,y,t) = \sum_{m=1}^{\infty}\sum_{n=1}^{\infty} W_{mn}X_m(x)Y_n(y)\cdot\theta(t) \tag{3.3}$$

Where $\theta(t)$ is the time dependency of the transverse displacements, in a harmonic vibration $\theta(t) = sin(\omega t + \vartheta)$, ϑ is the initial phase difference. For the linear vibration without acoustic pressure ($p(x,y,0) = 0$) and mass attachment ($\overline{m}_c = 0$), $X_m(x)$ and $Y_n(y)$ are the orthogonal mode shape functions, which exactly satisfy the boundary conditions in the x and y direction, respectively. From Leissa's analysis([9], page 41), $X_m(x)$ and $Y_n(y)$ can be chosen as the same mode shape functions of beams that have the same boundary conditions. Four types of plate boundary conditions have been investigated in this thesis: simple supported(S-S-S-S), all clamped(C-C-C-C), cantilever(C-F-F-F) and two opposite edges free and the other two clamped(C-F-C-F). Thus the following four types of beam function are required:

(a)For simple supported at each end(S-S), the beam function is

$$X_m(x) = \sin\frac{m\pi}{L_a}x \quad (m = 1,2,3,\cdots) \tag{3.4}$$

where L_a and L_b are plate's length and width respectively, m represents the modal number.

(b)For clamped-clamped(C-C) boundary conditions,

$$X_m(x) = \cosh\left(\frac{\epsilon_m x}{L_a}\right) - \cos\left(\frac{\epsilon_m x}{L_a}\right) - \alpha_m\left[\sinh\left(\frac{\epsilon_m x}{L_a}\right) - \sin\left(\frac{\epsilon_m x}{L_a}\right)\right] \tag{3.5}$$

$$\cos(\epsilon_m)\cosh(\epsilon_m) - 1 = 0, \quad \alpha_m = \frac{\cosh(\epsilon_m) - \cos(\epsilon_m)}{\sinh(\epsilon_m) - \sin(\epsilon_m)} \tag{3.6}$$

(c)The beam function of clamped-free(C-F) boundary conditions has same form as clamped-clamped, but has different constants of ϵ_m and α_m,

$$\cos(\epsilon_m)\cosh(\epsilon_m) + 1 = 0, \quad \alpha_m = \frac{\sinh(\epsilon_m) - \sin(\epsilon_m)}{\cosh(\epsilon_m) - \cos(\epsilon_m)} \tag{3.7}$$

(d)For free-free(F-F) boundary conditions,

$$X_1(x) = 1 \qquad X_2(x) = \sqrt{3}(2x - 1) \tag{3.8}$$

$$X_m(x) = \mu_m\left[\cosh\left(\frac{\epsilon_m x}{L_a}\right) + \cos\left(\frac{\epsilon_m x}{L_a}\right)\right] - \alpha_m\left[\sinh\left(\frac{\epsilon_m x}{L_a}\right) + \sin\left(\frac{\epsilon_m x}{L_a}\right)\right] \quad (m = 3, 4, \cdots) \tag{3.9}$$

$$\mu_m = \frac{\cosh(\epsilon_m) - \cos(\epsilon_m)}{\sinh(\epsilon_m)\sin(\epsilon_m)}, \quad \alpha_m = \frac{\sinh(\epsilon_m) + \sin(\epsilon_m)}{\sinh(\epsilon_m)\sin(\epsilon_m)} \tag{3.10}$$

where the constant of ϵ_m for free-free boundary conditions is same as the one of clamped-clamped. $Y_n(y)$ is in the same form that replace x to y and L_a to L_b in each beam shape function, respectively.

3.4 The Effects of Acoustic Loading on Plate

It had been shown in a large number of published papers that heavy fluid (like water) loading has significant influences on the plate vibration characteristics. As seen from Eq. (3.3), a vibrating plate in vacuo has infinite discrete orthogonal modes. In the presence of fluid, each mode of the plate motion can generate an acoustic pressure. Therefore the total external force applied on the plate is the sum of excitation force and the resultant acoustic pressure field. Nevertheless in general the resultant acoustic pressure induced by a single *in vacuo* mode is not orthogonal to the other modes[25]. Therefore in the presence of fluid excitation of the plate for a single mode can bring out other modes. That means that one *in vacuo* mode can "indirectly apply" forces and transfer energy to another mode via the coupling medium, fluid[24]. This cross-modal coupling phenomenon will mainly result in two effects on the vibration of plate: (a)The fluid loading generates an additional inertia to the plate, and it will lower the plate resonant frequencies. (b)The vibrating plate radiates acoustic energy into the fluid, this dissipation of the vibration energy of plate adds a resistive term of the impedances of plate[24], as a result the quality factor of the vibrating plate will decrease.

The acoustic velocity field induced by the plate motion is governed by a three-dimensional Helmholtz wave equation[25],

$$\nabla^2\Phi(x,y,z,t) = \frac{1}{c^2}\frac{\partial^2\Phi(x,y,z,t)}{\partial t^2} \tag{3.11}$$

where ∇^2 is the three-dimensional Laplacian operator, c is the sound velocity of fluid and $\Phi(x,y,z,t)$ is the velocity potential of fluid. Boundary conditions(continuity of normal velocity) at the interface between the fluid and the baffled plate($z=0$) can be expressed as,

$$\left.\frac{\partial\Phi}{\partial z}\right|_{z=0} = \frac{\partial w}{\partial t} \quad on\ the\ plate, \qquad \left.\frac{\partial\Phi}{\partial z}\right|_{z=0} = 0 \quad on\ the\ baffle\ plate \tag{3.12}$$

For a steady-state response of a harmonic motion, the acoustic velocity potential becomes $\Phi(x,y,z,t) = \phi(x,y,z)e^{-i\omega t}$. Then by using double Fourier integral

transforms to Helmholtz wave Eq.(3.11), the solution of acoustic velocity potential can be obtained[25]

$$\phi(x,y,z) = \frac{i\omega}{4\pi^2}\int_{-\infty}^{\infty}\int \frac{\widetilde{w}(\gamma_x,\gamma_y)\exp\left[i\gamma_x x + i\gamma_y y + i(k^2-\gamma_x^2-\gamma_y^2)^{1/2}z\right]}{\sqrt{k^2-\gamma_x^2-\gamma_y^2}} d\gamma_x d\gamma_x \tag{3.13}$$

where $\phi(x,y,z)$ is the spatial velocity potential function, $k = \omega/c$ is acoustic wave number and $\widetilde{w}(\gamma_x,\gamma_y)$ is the double Fourier transforms of plate deflection function. This above form of velocity potential solution is useful in obtaining asymptotic solutions for the purpose of the high modes analysis[26, 33]. However as a result of its integral singularity it will encounter great difficulty to acquire accurate numerical results for the most cases of boundary conditions. An alternative solution(Eq.3.14) given by Rayleigh's formula[25] is used in the following analysis.

$$\phi(x,y,z) = \frac{i\omega}{2\pi}\int\int_{S} \frac{w(\xi,\eta)\exp\left(ik\sqrt{(x-\xi)^2+(y-\eta)^2+z^2}\right)}{\sqrt{(x-\xi)^2+(y-\eta)^2+z^2}} d\xi d\eta \tag{3.14}$$

where S is the integral domain for the whole rectangular plate.

When we deal with the vibration analysis for first few modes of the plate, we can make the following assumptions and simplification on the fluid[19]: (a)The fluid is incompressible and inviscid. In general, water is ideally satisfying the "incompressible" assumption. Therefore the Helmholtz wave equation reduces to a single Laplace transform($c \to \infty, k \to 0$). The influence of fluid viscosity on the vibration of plate is very small, and it has been verified by Atkinsona et al.[40] and Ayela[6]. Ayela also experimentally proved that for a microplate as long as the viscosity of fluid is lower than 10cP (water is 0.894). (b)The fluid is infinite, irrotational and has no wall effects. Thus the primary effect of the surrounding fluid on the vibrating plate is the additional inertia. Thus the natural frequency

of fluid-loaded plate can be approximately determined by the added mass factor

$$\omega_{f,mn} = \frac{\omega_{v,mn}}{\sqrt{1+(M_a/M_p)}} = \frac{\omega_{v,mn}}{\sqrt{1+\beta_{mn}}} \tag{3.15}$$

where $\omega_{v,mn}$ and $\omega_{f,mn}$ are respectively the natural frequencies of plate in vacuo and in fluid. β_{mn} is the added mass factor. From the view of energy, the added mass can be evaluated as proportional to the kinetic energy of the fluid (T_f)[19], which is defined as

$$T_f = -\frac{1}{2}\rho_f \int_{-\infty}^{\infty}\int_{-\infty}^{\infty} \frac{\partial\phi(x,y,0)}{\partial z}\phi(x,y,0)dxdy \tag{3.16}$$

Substituting Eq.(3.14) into Eq.(3.16) with the case $k = 0$ and combining the fluid-structure interface boundary conditions of Eq.(3.12), we can rewrite T_f in the form

$$T_f = \frac{\rho_f\omega^2}{4\pi}\iint_S\iint_S \frac{w(x,y)w(\xi,\eta)}{\sqrt{(x-\xi)^2+(y-\eta)^2}}dxdyd\xi d\eta \tag{3.17}$$

3.5 Rayleigh-Ritz Solution

3.5.1 Using Rayleigh-Ritz Energy Method

Using Rayleigh's quotient[123], the natural frequencies of plate in vacuo can be approximately determined by the ratio between the maximum potential energy(U_p) and the reference kinetic energy(T_p^*) of the plate. When dealing with the coupling problem of fluid-loaded plate with mass attachment, the reference kinetic energy should be replaced by summing that of the plate, the fluid(T_f^*) and the mass(T_m^*). These relations can be written as[19]

$$\omega_v^2 = \frac{U_p}{T_p^*}, \qquad \omega_c^2 = \frac{U_p}{T_p^* + T_f^* + T_m^*} \tag{3.18}$$

where ω_c represent natural frequency of the coupling plate. The potential energy and reference kinetic energy of the plate are defined in the forms

$$U_p = \frac{D}{2}\iint_S \left\{ (\frac{\partial^2 w}{\partial x^2} + \frac{\partial^2 w}{\partial y^2})^2 - 2(1-\nu)\left[\frac{\partial^2 w}{\partial x^2}\frac{\partial^2 w}{\partial y^2} - \left(\frac{\partial^2 w}{\partial x \partial y} \right)^2 \right] \right\} dxdy \quad (3.19)$$

$$T_p^* = \frac{1}{2}\rho_p h \iint_S w^2(x,y)dxdy \quad (3.20)$$

The reference kinetic energy of fluid $T_f^* = T_f/\omega^2$.

The reference kinetic energy of distributed mass can be obtained by employing the aforementioned Heaviside function.

$$T_m^* = \frac{1}{2}\iint_S \overline{m}_c \mathcal{H}(x,y) w^2(x,y)dxdy \quad (3.21)$$

With the assumption that mode shapes of the plate remain almost the same in the fluid, all the above energy formulations can be approximately evaluated by using the plate "dry" mode shapes(Eq. (3.4)-Eq.(3.10)). The total energy of the coupling system then can be expressed as

$$V = U_p - \omega^2(T_p^* + T_f^* + T_m^*) \quad (3.22)$$

Substituting Eq. (3.3) into Eqs. (3.19), (3.17), (3.20), (3.21) we can obtain the expansion formula of these energy equations in terms of the plate orthogonal shape functions. By minimizing the Eq. (3.22) with respect to the unknown deflection coefficient W_{qr}

$$\frac{\partial V}{\partial W_{qr}} = 0 \quad (3.23)$$

we can obtain a series of eigenfunctions

$$\sum_{m=1}^{\infty}\sum_{n=1}^{\infty} \left\{ U_{p,mnqr} - \omega^2(T_{p,mnqr}^* + T_{f,mnqr}^* + T_{m,mnqr}^*) \right\} W_{mn} = 0 \quad (3.24)$$

where

$$U_{p,mnqr} = \frac{D}{2}\iint_S \Big\{ \ddot{X}_m(x)\ddot{X}_q(x)Y_n(y)Y_r(y) + X_m(x)X_q(x)\ddot{Y}_n(y)\ddot{Y}_r(y) + 2\nu\ddot{X}_m(x)X_q(x)Y_n(y)\ddot{Y}_r(y) + 2(1-\nu)\dot{X}_m(x)\dot{X}_q(x)\dot{Y}_n(y)\dot{Y}_r(y) \Big\} dxdy \tag{3.25}$$

$$T^*_{p,mnqr} = \frac{1}{2}\rho_p h \iint_S X_m(x)X_q(x)Y_n(y)Y_r(y)dxdy \tag{3.26}$$

$$T^*_{f,mnqr} = \frac{\rho_f}{4\pi}\iint_S \iint_S \frac{X_m(x)Y_n(y)X_q(\xi)Y_r(\eta)}{\sqrt{(x-\xi)^2+(y-\eta)^2}} dxdyd\xi d\eta \tag{3.27}$$

$$T^*_{m,mnqr} = \frac{1}{2}\overline{m}_c \iint_S X_m(x)X_q(x)Y_n(y)Y_r(y)\mathcal{H}(x,y)dxdy \tag{3.28}$$

Alternatively, we can rewrite Eq. (3.24) in the matrix form

$$\{[\mathbf{K}] - \omega^2[\mathbf{M}]\}\{x\} = 0 \tag{3.29}$$

where $\mathbf{K}$ and $\mathbf{M}$ are the stiffness matrix and inertial matrix of the vibration system respectively, and there elements are

$$K_{ij} = U_{p,mnqr}$$

$$M_{ij} = T^*_{p,mnqr} + T^*_{f,mnqr} + T^*_{m,mnqr}$$

$$i = l(q-1)+r, \quad j = l(m-1)+n, \quad l \in \mathbb{N}^+$$

Premultiplying the Eq. (3.29) by $\mathbf{M}^{-1}$, we can arrive another form of the former matrix equation[71]

$$\{[\mathbf{A}] - \lambda[\mathbf{I}]\}\{x\} = 0 \tag{3.30}$$

where $\mathbf{A} = \mathbf{M}^{-1}\mathbf{K}$ and $\mathbf{I}$ is the unit matrix. λ is equal to the square of circular frequency. Hence, the natural frequencies and corresponding mode shapes of the

coupled plate are liable to obtain by extracting the eigenvalues and eigenvectors of matrix **A** respectively[15].

As mentioned before, reference kinetic energy of fluid $T^*_{f,mnqr}$ has a integral singularity of square root and cannot be straightforward to numerical evaluation. Following Pierce's integral methodology[26], the fourfold integral of $T^*_{f,mnqr}$ can be reduced into a double integral form

$$T^*_{f,mnqr} = \frac{\rho_f}{4\pi} L_a^2 L_b^2 \int_0^1 \int_0^1 \frac{1}{\mathcal{R}} FX(u,m,q) FY(v,n,r) du dv \tag{3.31}$$

where $\mathcal{R} = \sqrt{L_a^2 u^2 + L_b^2 v^2}$ and inner integrand function $FX(u,m,q)$, $FY(v,n,r)$ are defined as

$$FX(u,m,q) = \int_u^1 X_m(x') X_q(x'-u) dx' + \int_0^{1-u} X_m(x') X_q(x'+u) dx' \tag{3.32}$$

$$FY(v,n,r) = \int_v^1 Y_n(y') Y_r(y'-u) dy' + \int_0^{1-v} Y_n(y') Y_r(y'+u) dy' \tag{3.33}$$

where $x' = x/L_a$, $y' = y/L_b$, $\xi' = \xi/L_a$, $\eta' = \eta/L_b$, and $u = x' - \xi'$, $v = y' - \eta'$. Substituting the beam shape functions(Eq. (3.4)-Eq.(3.10)) into Eq.(3.32), Eq.(3.33) and decomposing them into a series of single integrals, functions $FX(u,m,q)$ and $FY(v,n,r)$ can be evaluated in closed forms[1].

In order to eliminate the square root singularity, the whole integral of Eq.(3.31) can be transformed into a polar coordinate system. Then dividing the square

[1]Each of these separated integrals can be solved in closed forms, in Appendix B the solutions for the clamped boundary conditions are demonstrated. All the cases of three different boundary conditions (C-C-C-C, C-F-F-F, C-F-C-F) have also been worked out in this work, which were turned into the MATLAB codes (provided in the source code disk).

integral domain of (u, v) plane into two right triangles[26], we can define $u = \mathcal{R}\cos\theta/L_a$, $v = \mathcal{R}\sin\theta/L_b$ with the new integral domain $0 < \mathcal{R} < L_a/\cos(\theta)$, $0 < \theta < \tan^{-1}(L_b/L_a)$ for lower triangle and analogous relations for upper triangle. The integral of Eq.(3.31) becomes

$$T^*_{f,mnqr} = \frac{\rho_f}{4\pi} L_a L_b \Bigg(\int_0^{\theta_1} \int_0^{\frac{L_a}{\cos(\theta)}} FX(\frac{\mathcal{R}\cos(\theta), m, q}{L_a}) FY(\frac{\mathcal{R}\sin(\theta)}{L_b}, n, r) d\theta d\mathcal{R} + \int_0^{\theta_2} \int_0^{\frac{L_b}{\cos(\theta)}} FX(\frac{\mathcal{R}\sin(\theta)}{L_a}, m, q) FY(\frac{\mathcal{R}\cos(\theta)}{L_b}, n, r) d\theta d\mathcal{R} \Bigg) \tag{3.34}$$

where $\theta_1 = \tan^{-1}(L_b/L_a)$ *and* $\theta_2 = \tan^{-1}(L_a/L_b)$

Normalizing the integral domain of $\mathcal{R}$ into $[0, 1]$, we can rewrite Eq.(3.34) in the form

$$T^*_{f,mnqr} = \frac{\rho_f}{4\pi} L_a L_b \Bigg(\int_0^{1} \int_0^{\theta_1} FX(\mathcal{R}, m, q) FY(\frac{\mathcal{R}L_a\sin(\theta)}{L_b\cos(\theta)}, n, r) \frac{L_a}{\cos(\theta)} d\mathcal{R} d\theta + \int_0^{1} \int_0^{\theta_2} FX(\frac{\mathcal{R}L_b\sin(\theta)}{L_a\cos(\theta)}, m, q) FY(\mathcal{R}, n, r) \frac{L_b}{\cos(\theta)} d\mathcal{R} d\theta \Bigg) \tag{3.35}$$

Consequently, with the close-form solution of functions FX and FY we can accurately evaluate Eq.(3.35) by using normal numerical quadrature routines.

3.5.2 Numerical Results of Natural Frequencies and Mode Shapes

The resonant frequencies and mode shapes of the submerged microplate carrying a distributed mass are obtained by numerically solving a truncated subset of the

infinite series of Eq. (3.24) in MATLAB codes. All of the simulation results presented in this part are generated by using (25×25) terms of Matrix **A**, and the reference kinetic energy of fluid(T_f^*) is doubled for the case of submerged microplate. It can be proved that (25×25) terms are able to result in sufficient convergence. The material properties of the plate, fluid (water) and attached mass used in numerical computation are as follows:

- Plate Length: $L_a = 100\mu m$
- Plate Width: $L_b = 100\mu m$
- Plate Thickness: $h = 5\mu m$
- Plate Young's Modulus: $E = 150GPa$
- Plate Poisson's Ratio: $\nu = 0.17$
- Plate Density: $\rho_p = 2330kg/m^3$
- Fluid Density: $\rho_f = 1000kg/m^3$
- Radius of Attached Mass: $R = 20\mu m$
- Surface Mass Density of Attached Mass: $\overline{m}_c = 0.02kg/m^2$

From Eq.(3.24), it can be seen that when $T_f^* = 0$ and $T_m^* = 0$, the coupled system reduces to the case of unloaded plate motion *in vacuo*, and if $T_m^* = 0$, the problem becomes the one of an unloaded plate vibrating in a fluid. Figure. 3.2-3.4 respectively shows the plate resonant frequencies and mode shapes for three types of boundary conditions in four different loading cases: (A)plate in vacuo without carrying the mass, (B)plate only under fluid loading, (C)involved both fluid-loading and a center mass attachment($x_c = L_a/2$, $y_c = L_b/2$), (D)is the case with a corner mass attachment(In Figure 2 and 4, the corner mass is at $x_c = L_a/4$, $y_c = L_b/4$. In Figure 3, the corner mass is at $x_c = 3L_a/4$, $y_c = 3L_b/4$).

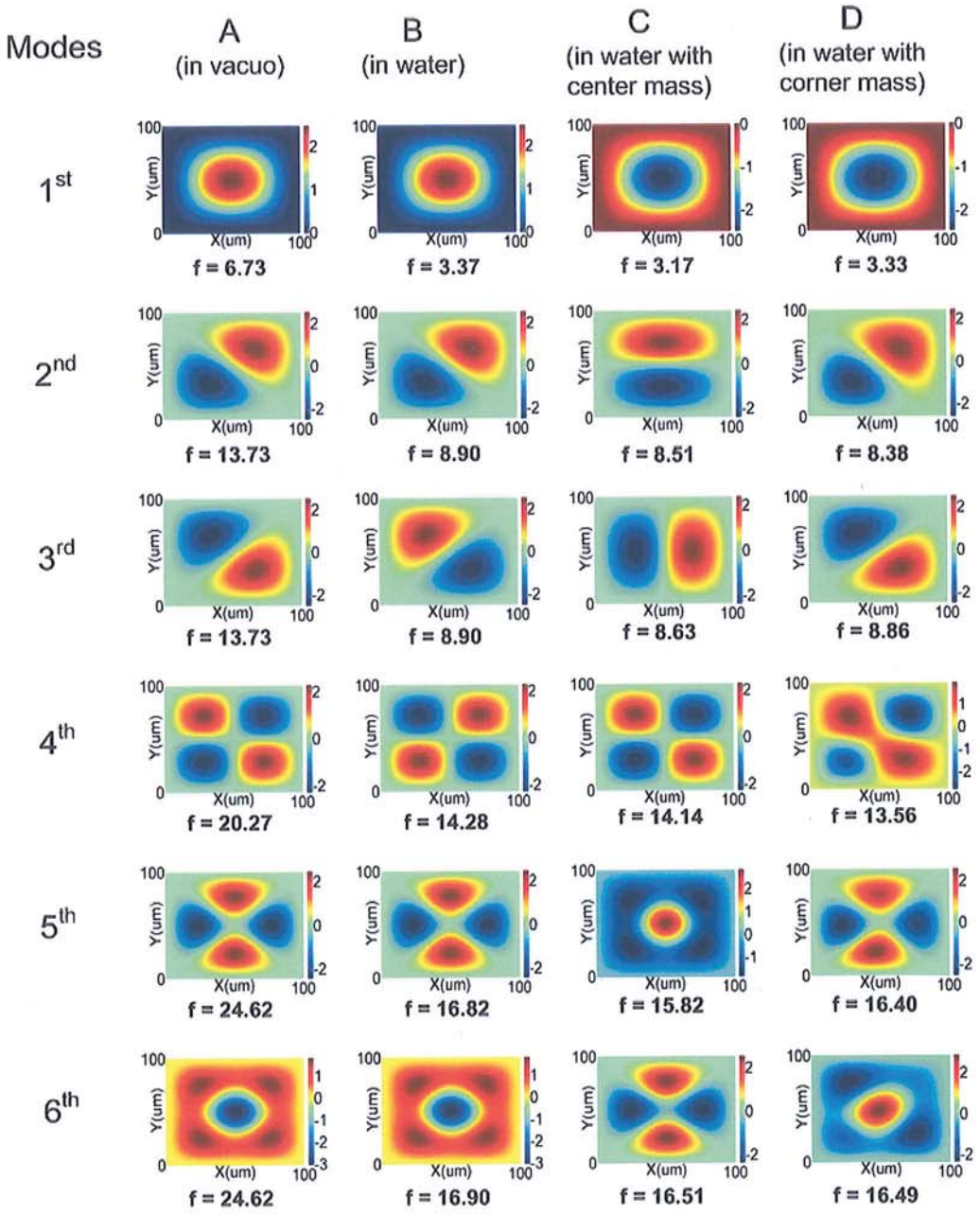

Figure 3.2: C-C-C-C plate resonant frequencies(MHz) and mode shapes

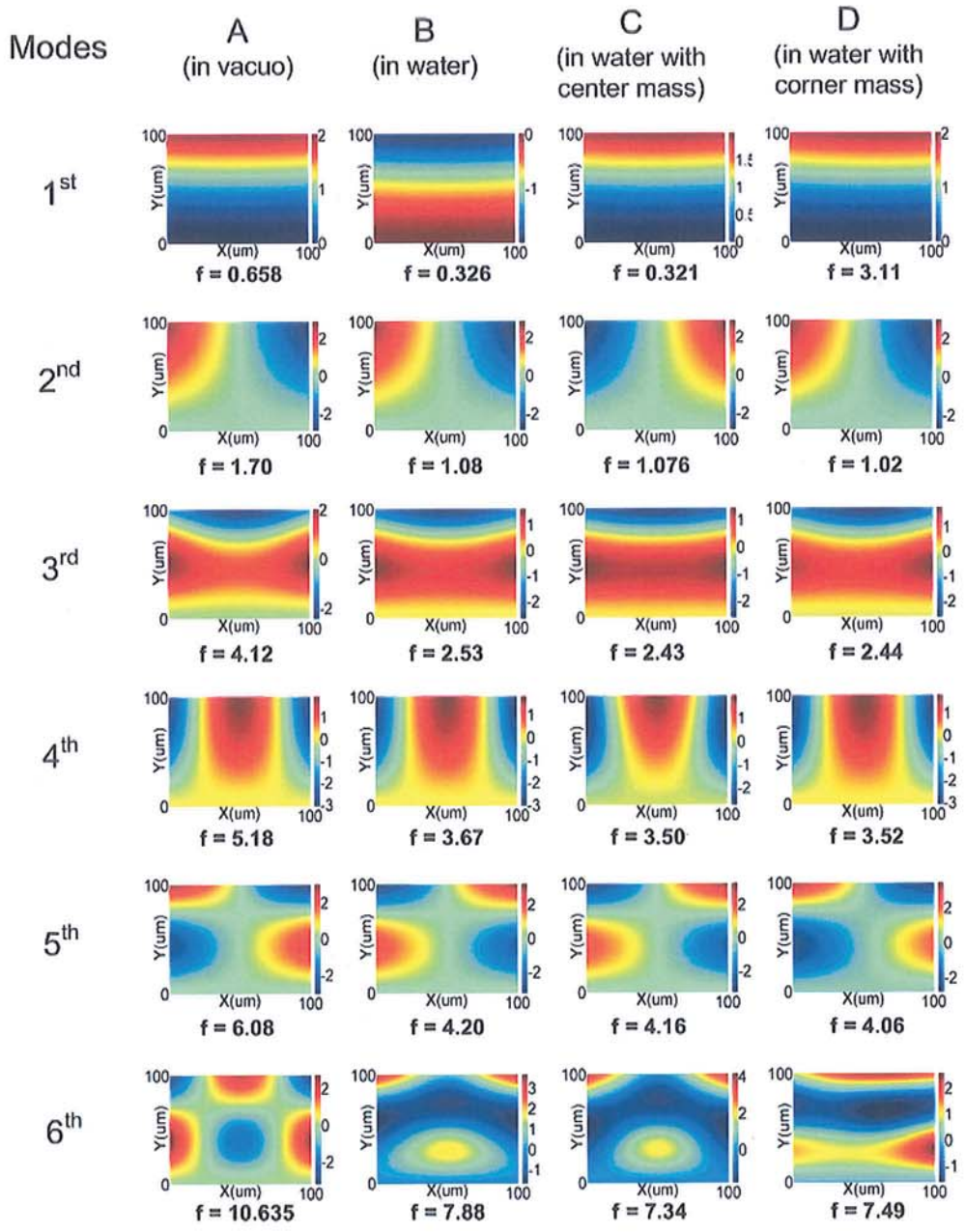

Figure 3.3: C-F-F-F plate resonant frequencies(MHz) and mode shapes

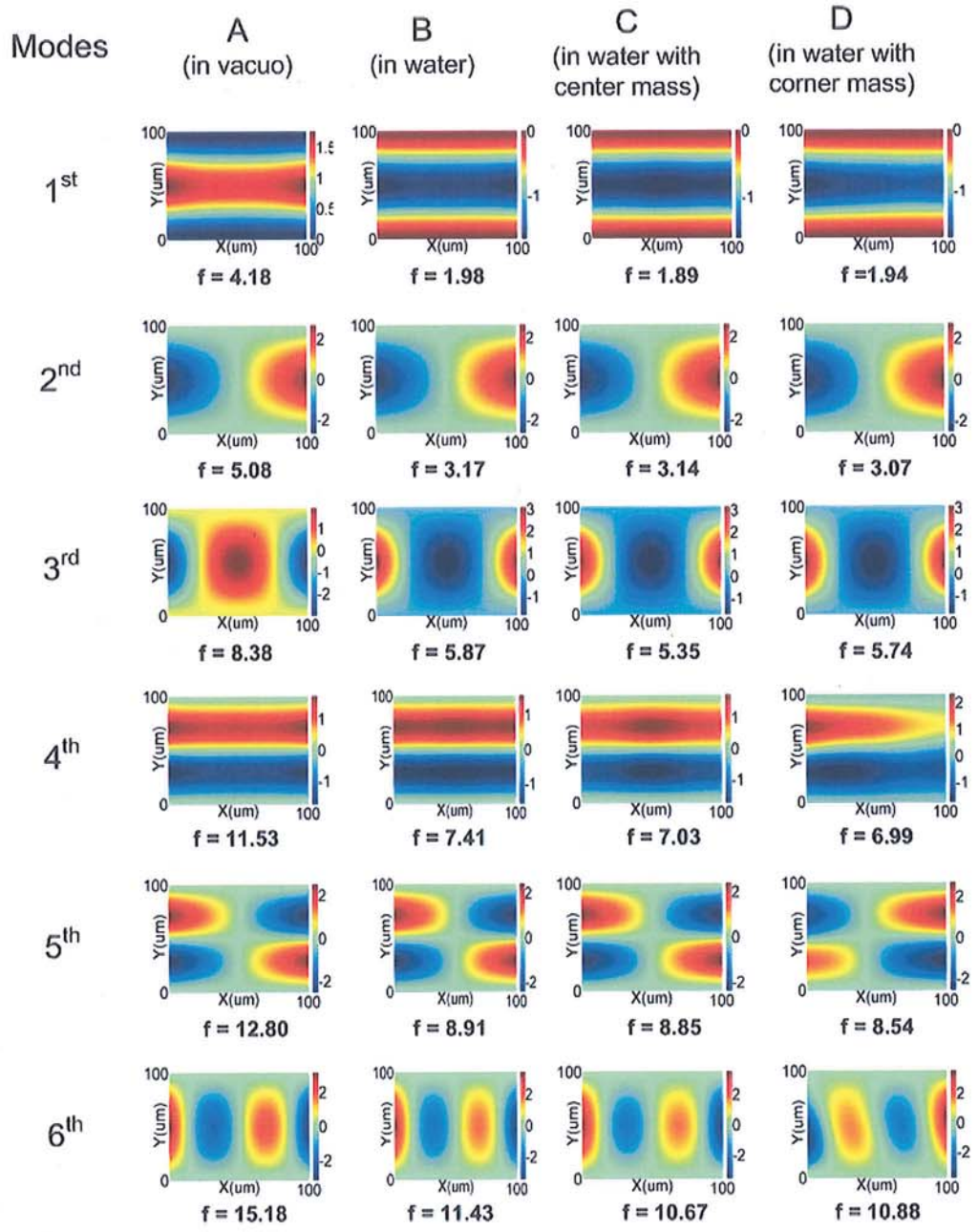

Figure 3.4: C-F-C-F plate resonant frequencies(MHz) and mode shapes

From the above three data plots, we can see that both the fluid loading and the attached distributive biological particles have significant impact on the resonant frequencies and mode shapes of micro plates. The inertial forces of fluid sharply reduce resonant frequencies, especially in the fundamental modes (by more than 50%). Fluid has a reduced effect on most of mode shapes, some phase changes can be found in a few cases. On the other hand, due to the low density ratio(density of attached mass vs density of micro plate) the distributed mass caused very small changes on the resonant frequencies. However it induced distinct changes to the most mode shapes, especially in high modes.

3.5.3 Validation of the Rayleigh-Ritz Solution

There are very few papers that discuss the dynamics of a distributive mass-loaded plate in a fluid. In order to verify the present method, the numerical results for plates without mass attachment vibrating in fluid are obtained to compare with the published results. An experimental dataset suitable for this comparison is the one published by Lindholm (1965) for the submerged cantilever plates[124]. The dimensions and properties of the cantilever plate used here for comparison are: $L_a = L_b = 8inch$, $\rho_p = 7.324 \times 10^{-4} lb/in^3$, $E = 30 \times 10^6 psi$, $\nu = 0.3$. Table 3.1 compares the first five natural frequencies for this plate *in vacuo* and in water respectively.

The results of Table 3.1 show close agreement between the method of this paper and Lindholm's measurements. However quite large differences exist in the first two wet mode frequencies, as the plate used in our model is surrounded by an infinite baffle plane, while the plate of Lindholm's approach is resting on a free surface.

The comparison of NAVMI (Non-dimensional Added Virtual Mass Incremental) factors for simple-supported and clamped plates between the present method and Kwak's results(read from his data plot)[21] are listed in Table 3.2. The aspect

Table 3.1: Comparison of natural frequencies(Hz) of a cantilever plate submerged in fluid with Lindholm's experimental results

	In Vacuo		In Water	
Modes	Lindholm	Present	Lindholm	Present
1	99.5	99.3	51.4	45.0
2	243.0	243.5	154.0	144.8
3	610.0	622.5	355.0	358.7
4	782.0	769.2	534.0	511.4
5	887.0	898.2	585.0	590.9

ratio ε here is equal to 1. It can be seen that this method can accurately calculate the NAVMI factors and therefore the natural frequencies of the submerged plates.

Table 3.2: Comparison of NAVMI factors of simple-supported and clamped plates with Kwak's BEM results

	S-S-S-S		C-C-C-C	
Modes	Kwak	Present	Kwak	Present
1,1	0.41	0.41	0.35	0.3484
1,2(2,1)	0.18	0.1823	0.16	0.1609
2,2	0.13	0.128	0.12	0.1182

3.5.4 The Effect of Distributed Mass Loading

All of the numerical results in Figure 3.2,3.3,3.4 have demonstrated the effect of a small distributed mass loading. Additional mass attachment on a microplate decreases natural frequency and distorts mode shape of each resonant mode. Comparing with center mass. the corner mass has less influence on natural frequencies, but could cause much more mode shape distortion in some cases. In

general the level of these changes of dynamic parameters are mainly determinated by the size and position of attached mass, assuming that surface mass density is uniform and constant. In other words, physical properties and behaviour of the attached distributed mass have very close relationships with the dynamic information of the sensing microplate. This is the principle of using a microplate as the biosensing transducer to detect cells.

A simple simulation demonstrates that the plate dynamics change with different cases of cells adhesion herein. Larger radius and higher thickness of a circular distributed mass is used to simulate more quantity of attached cells, natural frequencies and mode shapes of 6 different loading cases on a $300\mu m \times 300\mu m \times 5\mu m$ cantilever microplate are evaluated by using the Rayleigh-Ritz theoretical model in the simulation. The first 5 natural frequency shifts of these 6 cases are shown in Table. Figure 3.5 illustrates the differences of the first 5 mode shapes between case 1 and case 6.

Table 3.3: Simple Simulation Results of the First 5 Natural Frequencies (KHz) of a Microplate With Cells are Growing on Its Surface

No. of Cells	1 mode	2 mode	3 mode	4 mode	5 mode
0	22.850	82.163	190.088	291.117	336.667
1	22.847	82.163	189.968	290.818	336.666
5	22.759	82.096	187.584	285.389	336.113
10	21.476	76.530	168.644	261.207	307.755
50	17.727	61.847	123.832	201.674	240.354
100	14.988	51.638	99.066	165.749	197.678

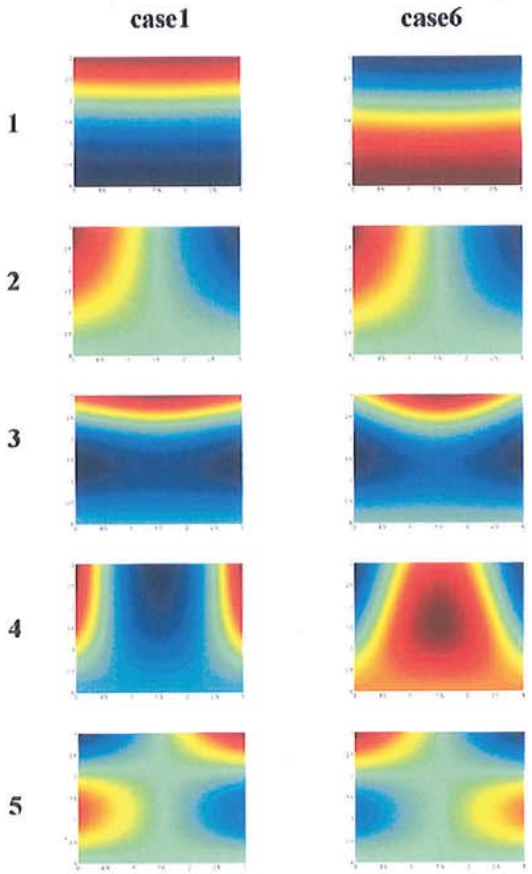

Figure 3.5: Mode shapes comparison between case 1 (no cells) and case 6 (100 cells) adhesion

3.6 Damping Analysis of Fluid-loaded Microplates

3.6.1 Equations for Quiescent Compressible Viscous Fluid

When a solid structure is excited in a fluid by prescribed external forces, the resultant inertial and friction forces of fluid react against the motion of structure and represents the dissipation of energy. In order to analyse these reaction forces and the dissipating mechanism, the fluid has to be modeled as viscous and compressible. Both the solid and fluid media are assumed to be homogeneous herein, and the fluid medium is considered to be at rest initially. The motion of a viscous compressible fluid is governed by the linearized Navier-Stokes equations, in which the non-linear convective inertial term is ignored[39]:

$$\rho_{f0}\frac{\partial \mathbf{v}}{\partial t} - \mu\nabla^2\mathbf{v} - (\mu + \mu^v)\nabla(\nabla \cdot \mathbf{v}) + \nabla p = 0 \tag{3.36}$$

where $\mathbf{v}$ is the velocity vector of fluid, p is the fluid pressure, ρ_{f0} is the quiescent fluid density, μ is the dynamic viscosity coefficient of fluid, and μ^v is the second viscosity coefficient of fluid and can be considered to equal $-2/3\mu$. The motion of fluid also satisfies the continuity equation:

$$\frac{\partial \rho_f}{\partial t} + \rho_{f0}\nabla \cdot \mathbf{v} = 0 \tag{3.37}$$

and momentum equation:

$$\frac{\partial p}{\partial \rho_f} = c^2 \tag{3.38}$$

The solution of the fluid velocity field can be expressed as a sum of a scalar and a vector potentials[51]:

$$\mathbf{v} = \nabla\Phi + \nabla \times \Psi \tag{3.39}$$

with an additional condition:

$$\nabla \cdot \Psi = 0 \tag{3.40}$$

Substituting this solution back into Eq.(3.36,3.37,3.38), we can obtain the following equations[50]:

$$p = \frac{4}{3}\mu\nabla^2\Phi - \rho_{f0}\dot{\Phi} \tag{3.41}$$

$$\nabla^2\Phi + \frac{4\mu}{3\rho_{f0}c^2}\nabla^2\dot{\Phi} - \frac{1}{c^2}\ddot{\Phi} = 0 \tag{3.42}$$

$$\nabla^2\Psi - \frac{\rho_{f0}}{\mu}\dot{\Psi} = 0 \tag{3.43}$$

If only the situation of harmonic motion is considered $\Phi(x,y,z,t) = \phi(x,y,z)e^{-i\omega t}$ and $\Psi(x,y,z,t) = \psi(x,y,z)e^{-i\omega t}$, the above two equations can be rewritten as the following forms:

$$\nabla^2\phi + k_l^2\phi = 0 \tag{3.44}$$

$$\nabla^2\psi + k_s^2\psi = 0 \tag{3.45}$$

where

$$k_l^2 = \frac{\omega^2/c^2}{1 - 4i\mu\omega/3\rho_{f0}c^2} \tag{3.46}$$

$$k_s^2 = \frac{i\rho_{f0}\omega}{\mu} \tag{3.47}$$

where k_l and k_s can be considered to be virtual wave number, which are complex numbers.

3.6.2 Vibration of Rectangular Plate

The governing equation of the forced vibration of a rectangular isotropic plate is defined as

$$D(\frac{\partial^4 w}{\partial x^4} + 2\frac{\partial^4 w}{\partial x^2 y^2} + \frac{\partial^4 w}{\partial y^4}) + \rho_p h\frac{\partial^2 w}{\partial t^2} = F(x,y,t) \tag{3.48}$$

$F(x, y, t)$ is the external force function applied on the plate, which includes the hydrodynamic loading and excitation force. However this classical thin plate theory is only valid in the frequency range[25]:

$$\frac{\omega h}{\pi c_s} < 0.1 \tag{3.49}$$

where $c_s = \sqrt{E/(2\rho_p(1+\upsilon))}$ is the shear wave speed of the material. Take a $5\mu m$ thick $200\mu m$ square silicon micro-plate as an example, the above condition can be satisfied within the frequency band of 20MHz (critical frequency), which is adequate for the frequency analysis of microplates in this thesis.

3.6.3 Boundary Conditions at the Fluid-Plate Interface

In such a situation of small oscillations, it is generally believed that at the fluid-plate interface the fluid will have no velocity relative to the plate[125]. This condition is known as the *no-slip condition*, which can be stated by the following equality constraints:

$$\frac{\partial \mathbf{u}^p}{\partial t} = \mathbf{v}^f, \quad \vec{\sigma}^p = \vec{\sigma}^f \tag{3.50}$$

where $\mathbf{u}^p$ is the displacement vector of plate. It means at the contact interface the velocity of fluid is equal to the velocity of plate, and the stress tensor along the fluid boundary ($\vec{\sigma}^f$) is identical to the stress vector of plate surface($\vec{\sigma}^p$). Expanding the above boundary conditions in the Cartesian coordinates($\vec{x}, \vec{y}, \vec{z}$), then the vector potential ψ is written as:

$$\psi = \psi_x \vec{x} + \psi_y \vec{y} + \psi_z \vec{z} \tag{3.51}$$

The velocity field Eq.(3.39) is expanded as the following form(the superscript " f

" is indicated for the fluid):

$$v_x^f = \frac{\partial \phi}{\partial x} + \frac{\partial \psi_z}{\partial y} - \frac{\partial \psi_y}{\partial z}$$
$$v_y^f = \frac{\partial \phi}{\partial y} + \frac{\partial \psi_x}{\partial z} - \frac{\partial \psi_z}{\partial x}$$
$$v_z^f = \frac{\partial \phi}{\partial z} + \frac{\partial \psi_y}{\partial x} - \frac{\partial \psi_x}{\partial y}$$

The velocity field of a vibrating plate in the form of flexural waves(bending waves) can be represented as[126]:

$$\begin{aligned} v_x^p &= -\frac{h}{2}\frac{\partial^2 w}{\partial x \partial t} \\ v_y^p &= -\frac{h}{2}\frac{\partial^2 w}{\partial y \partial t} \\ v_z^p &= \frac{\partial w}{\partial t} \end{aligned}$$

Supposing the fluid-plate contact interface is located at $z = 0$, the no-slip boundary condition for the velocity field is then expressed as:

$$v_x^f = v_x^p|_{z=0}, \quad v_y^f = v_y^p|_{z=0}, \quad v_z^f = v_z^p|_{z=0} \tag{3.52}$$

The continuity of the stress tensor along the boundary implies the hydrodynamic forces loading on the plate are determinated by the motion of fluid. The six components of the fluid stress are obtained in the following forms(Stokes's hypothesis)[125]:

$$\begin{aligned} \sigma_x &= -p + 2\mu\frac{\partial v_x^f}{\partial x} - \frac{2}{3}\mu(\frac{\partial v_x^f}{\partial x} + \frac{\partial v_y^f}{\partial y} + \frac{\partial v_z^f}{\partial z}) \\ \sigma_y &= -p + 2\mu\frac{\partial v_y^f}{\partial y} - \frac{2}{3}\mu(\frac{\partial v_x^f}{\partial x} + \frac{\partial v_y^f}{\partial y} + \frac{\partial v_z^f}{\partial z}) \\ \sigma_z &= -p + 2\mu\frac{\partial v_z^f}{\partial z} - \frac{2}{3}\mu(\frac{\partial v_x^f}{\partial x} + \frac{\partial v_y^f}{\partial y} + \frac{\partial v_z^f}{\partial z}) \\ \tau_{xy} &= \tau_{yx} = \mu(\frac{\partial v_y^f}{\partial x} + \frac{\partial v_x^f}{\partial y}) \\ \tau_{yz} &= \tau_{zy} = \mu(\frac{\partial v_z^f}{\partial y} + \frac{\partial v_y^f}{\partial z}) \\ \tau_{zx} &= \tau_{xz} = \mu(\frac{\partial v_x^f}{\partial z} + \frac{\partial v_z^f}{\partial x}) \end{aligned}$$

3.6.4 Hydrodynamic Force Function on A Rectangular Plate

In this part we present an analytical expression of hydrodynamic force loading on a rectangular plate. When the plate is immersed in the fluid and is excited into motion, the motion of plate generates a new stress field of the fluid on both sides of the plate. The hydrodynamic loading $F_{hydro}(x, y, 0, t)$ on the transverse motion of the plate is the difference of the surface hydrodynamic force between plate top-surface and bottom-surface:

$$F_{hydro}(x, y, 0, t) = F_{hydro}(x, y, 0-, t) - F_{hydro}(x, y, 0+, t) \tag{3.53}$$

where $F_{hydro}(x, y, 0-, t)$ and $F_{hydro}(x, y, 0+, t)$ are the surface hydrodynamic force on the bottom side and top side of the plate respectively. As the thickness of plate is small, we can assume:

$$F_{hydro}(x, y, 0-, t) = -F_{hydro}(x, y, 0+, t) \tag{3.54}$$

According to the no-slip condition, each component of the surface hydrodynamic force are all depend on the fluid stress tensor, thus it is expressed in the following form:

$$F_{hydro}(x, y, 0+) = \sigma_z - \frac{h}{2}\left(\frac{\partial \tau_{zx}}{\partial x} + \frac{\partial \tau_{zy}}{\partial y}\right) \tag{3.55}$$

Substituting the expressions of velocity field into the fluid stress tensors, the $\sigma_z, \tau_{zx}, \tau_{zy}$ can be rewritten as followings:

$$\sigma_z = -2\mu\nabla^2\phi + \rho_{f0}\dot{\phi} + 2\mu\left(\frac{\partial^2\phi}{\partial z^2} + \frac{\partial^2\psi_y}{\partial x \partial z} + \frac{\partial^2\psi_x}{\partial y \partial z}\right) \tag{3.56}$$

$$\tau_{zx} = \mu\left(2\frac{\partial^2\phi}{\partial x \partial z} + \frac{\partial^2\psi_z}{\partial y \partial z} - \frac{\partial^2\psi_x}{\partial y \partial x} - \frac{\partial^2\psi_y}{\partial z^2} + \frac{\partial^2\psi_y}{\partial x^2}\right) \tag{3.57}$$

$$\tau_{zy} = \mu\left(2\frac{\partial^2\phi}{\partial y \partial z} + \frac{\partial^2\psi_y}{\partial x \partial y} - \frac{\partial^2\psi_z}{\partial x \partial z} - \frac{\partial^2\psi_x}{\partial y^2} + \frac{\partial^2\psi_x}{\partial z^2}\right) \tag{3.58}$$

The scalar and vector potential fields ϕ, ψ can be obtained through applying double Fourier transforms on the Eqs.(3.44,3.45). The solution for the ϕ, ψ of the transformed Helmholtz equations have the following forms:

$$\hat{\phi}(k_x, k_y; z) = A \cdot \exp\left(i\sqrt{k_l^2 - k_x^2 - k_y^2} \cdot z\right) \tag{3.59}$$

$$\hat{\psi}(k_x, k_y; z) = B \cdot \exp\left(i\sqrt{k_l^2 - k_x^2 - k_y^2} \cdot z\right) \tag{3.60}$$

where $\hat{\phi}$ and $\hat{\psi}$ are the Fourier transform of scalar and vector fields.

Then the potential fields have the following solutions by applying inverse Fourier transformation:

$$\phi(x, y, z) = \frac{1}{4\pi^2} \iint_{-\infty}^{\infty} A \cdot \exp\left(ik_x x + ik_y y + i\sqrt{k_l^2 - k_x^2 - k_y^2} \cdot z\right) dk_x dk_y \tag{3.61}$$

$$\psi(x, y, z) = \frac{1}{4\pi^2} \iint_{-\infty}^{\infty} B \cdot \exp\left(ik_x x + ik_y y + i\sqrt{k_s^2 - k_x^2 - k_y^2} \cdot z\right) dk_x dk_y \tag{3.62}$$

where A and $B(B_x, B_y, B_z)$ are the coefficients need to be determinated. B_x, B_y, B_z are the coefficients for the each component of vector field ψ_x, ψ_y, ψ_z respectively. Substituting the solutions of potential fields into the double transformed continuity condition Eq.(3.52) of the velocity field at the fluid-plate interface($z = 0$) and Eq.(3.40), we can list four linear equations for these four undeterminated coefficients:

$$
\begin{aligned}
i\sqrt{k_l^2-k_x^2-k_y^2}\cdot A - ik_yB_x + ik_xB_y &= \tilde{w} \\
k_xA - \sqrt{k_s^2-k_x^2-k_y^2}\cdot B_y + k_yB_z &= -\frac{h}{2}k_x\tilde{w} \\
k_yA + \sqrt{k_s^2-k_x^2-k_y^2}\cdot B_x - k_xB_z &= -\frac{h}{2}k_y\tilde{w} \\
k_xB_x + k_yB_y + \sqrt{k_s^2-k_x^2-k_y^2}\cdot B_z &= 0
\end{aligned}
$$

Thus the coefficients A, B_x, B_y, B_z can be obtained,

$$
\begin{aligned}
A = \Bigg[& \frac{-h(k_x^2+k_y^2)+2i(k_x^2+k_y^2)/\sqrt{k_l^2-k_x^2-k_y^2}}{2(k_x^2+k_y^2+\sqrt{k_l^2-k_x^2-k_y^2}\sqrt{k_s^2-k_x^2-k_y^2})} \\
& - \frac{i}{\sqrt{k_l^2-k_x^2-k_y^2}}\Bigg]\tilde{w}
\end{aligned} \tag{3.63}
$$

$$
B_x = -\frac{hk_y\sqrt{k_l^2-k_x^2-k_y^2}-2ik_y}{2(k_x^2+k_y^2+\sqrt{k_l^2-k_x^2-k_y^2}\sqrt{k_s^2-k_x^2-k_y^2})}\tilde{w} \tag{3.64}
$$

$$
B_y = \frac{-hk_x\sqrt{k_l^2-k_x^2-k_y^2}+2ik_x}{2(k_x^2+k_y^2+\sqrt{k_l^2-k_x^2-k_y^2}\sqrt{k_s^2-k_x^2-k_y^2})}\tilde{w} \tag{3.65}
$$

$$
B_z = 0 \tag{3.66}
$$

Now we can present the analytical expression of the hydrodynamic force by substituting the solutions of potential fields Eqs.(3.61,3.62)into Eq.(3.55), and it can

be written in a concise form,

$$F_{hydro}(x,y,0+) = \frac{1}{4\pi^2}\iint_{-\infty}^{\infty} T(k_x,k_y)\tilde{w}\exp(ik_x x + ik_y y)dk_x dk_x \tag{3.67}$$

where the inner function $T(k_x,k_y) = T_1(k_x,k_y) - \frac{h}{2}T_2(k_x,k_y)$. $T_1(k_x,k_y)$ and $T_2(k_x,k_y)$ are the coefficient functions from the solutions of normal stress and shear stresses respectively.

$$\begin{aligned} T_1 = {} & [2\mu(k_x^2+k_y^2) - i\rho_{f0}\omega]A' - \\ & 2\mu(k_x\sqrt{k_l^2-k_x^2-k_y^2}B_y' - k_y\sqrt{k_l^2-k_x^2-k_y^2}B_x') \end{aligned} \tag{3.68}$$

$$\begin{aligned} T_2 = {} & -i\mu[2\sqrt{k_l^2-k_x^2-k_y^2}(k_x^2+k_x^2)A' + \\ & k_y(k_l^2-2k_x^2-2k_y^2)B_x' + k_x(-k_l^2+2k_x^2+2k_y^2)B_y'] \end{aligned} \tag{3.69}$$

where $A' = A/\tilde{w}, B_x' = B_x/\tilde{w}, B_y' = B_y/\tilde{w}$.

Concerning the specific case of inviscid compressible fluid ($\mu = 0$), the virtual wave numbers in Eqs.(3.44,3.45) becomes $k_l = \omega/c, k_s \to \infty$ and the hydrodynamic force function of Eq.(3.67) reduces to the form of acoustic pressure.

$$F_{hydro}(x,y,0+) = -p(x,y,0+) = \frac{1}{4\pi^2}\iint_{-\infty}^{\infty} \frac{\rho_{f0}\omega\tilde{w}\exp(ik_x x + ik_y y)}{\sqrt{k_l^2-k_x^2-k_y^2}}dk_x dk_x \tag{3.70}$$

The form of Eq.(3.70) has been found widely used in the study of plate-borne acoustic radiation[25, 30, 32, 127]. It implies that Eq.(3.67) can also be applied in the situation of very low viscosity, in which case the *no-slip condition* is violated.

3.6.5 Analytical Solution - I (Directly Using Governing Equations)

If the excitation force is assumed to be a concentrated force(F_{ex}), which is applying at the point (x_0, y_0), then the whole external force $F(x, y, t)$ in Eq.(3.48) loading on a submerged plate can be expressed,

$$F(x,y) = F_{ex}\delta(x-x_0)\delta(y-y_0) + F_{hydro}(x,y,0) \tag{3.71}$$

Substituting the Eqs.(3.3,3.71,3.67) into Eq.(3.48) and multiplying W_{qr} and integrating over the whole region of the plate, we can obtain the solutions of the submerged plate vibration in the following matrix form,

$$\sum_{m}^{\infty}\sum_{n}^{\infty}\left(\mathbf{\Gamma} + i\omega\mathbf{I_{mnqr}}\right)\{W_{mn}\} = F_{qr} \quad q,r = 1,2,\cdots,\infty \tag{3.72}$$

Where F_{qr} is the generalized external force and can be represented in the form,

$$F_{qr} = \iint_S F_{ex}\delta(x-x_0)\delta(y-y_0)X_q(x)Y_r(y)\,dx\,dy \tag{3.73}$$

and $[\mathbf{\Gamma}]$ is the modal coefficients of plate stiffness and its elements are,

$$\mathbf{\Gamma} = M\left[\omega_{mn}^2 - \omega^2\right]\mathbf{E} \tag{3.74}$$

where $\mathbf{E}$ is an identity matrix, M is the mass of plate and ω_{mn} is the plate natural frequency *in vacuo* of (m, n) mode. For an all clamped rectangular plate,

the natural frequencies can be evaluated from the following formulation:

$$\omega_{mn}^2 = \frac{D}{\rho_p h}\left(k_m^4 + 2\frac{\iint_S X_m \ddot{X}_m Y_n \ddot{Y}_n dxdy}{\iint_S X_m^2 Y_n^2 dxdy} + k_n^4\right) \tag{3.75}$$

$\mathbf{I_{mnqr}}$ is the direct and mutual mode fluid-loading impedance including the effects of acoustic radiation and viscosity. It can be seen that $\mathbf{I_{mnqr}}$ is the coupling coefficient linked two discrete vibrating modes of plate, namely (m, n) and (q, r). $\mathbf{I_{mnqr}}$ is expressed in the following form,

$$I_{mnqr} = \frac{1}{4\pi^2}\iint_{-\infty}^{\infty} T(k_x, k_y)\chi_{mn}(k_x, k_y)\chi_{qr}^*(k_x, k_y)dk_x dk_y \tag{3.76}$$

where $\chi_{mn}(k_x, k_y)$ and $\chi_{qr}^*(k_x, k_y)$ are double Fourier transform of the plate modal shape functions,

$$\chi_{mn}(k_x, k_y) = \iint_S X_m(x)Y_n(y)\exp(-i(k_x x + k_y y))dxdy \tag{3.77}$$

The fluid-loaded impedance function $\mathbf{I_{mnqr}}$ involves a 6-folder integration and tedious to be numerically evaluated. Fortunately, the inner function χ_{mn} and χ_{qr}^* can be solved in closed forms for the ordinary boundary conditions (all clamped, cantilever and etc). The solution of χ_{mn} for an all clamped rectangular plate is shown in the following formulations 3.78. Solutions for other boundary conditions are similar and have also been worked out in this thesis.[1].

$$\chi_{mn}(k_x, k_y) = [I_{Xcos}(m, k_x) - iI_{Xsin}(m, k_x)]\,[I_{Ycos}(n, k_y) - iI_{Ysin}(n, k_y)] \tag{3.78}$$

[1]Refer to the Matlab Source Codes in Appendix D

where

$$I_{Xcos}(m,k_x) = \Bigg[\frac{1}{2(k_m^2+k_x^2)}(e^{k_m L_a}(k_x \sin(L_a k_x) + k_m \cos(k_x L_a)) + e^{-k_m L_a}(k_x \sin(L_a k_x) - k_m \cos(k_x L_a))) - \frac{1}{2}(\frac{\sin(L_a(k_m+k_x))}{k_m+k_x} + \frac{\sin(L_a(k_m+k_x))}{k_m-k_x})\Bigg] - \alpha_m \Bigg[\frac{1}{2(k_m^2+k_x^2)}(e^{k_m L_a}(k_x \sin(L_a k_x) + k_m \cos(k_x L_a)) + e^{-k_m L_a}(k_x \sin(L_a k_x) - k_m \cos(k_x L_a)) - 2k_m) + \frac{1}{2}(\frac{\cos(L_a(k_m+k_x))-1}{k_m+k_x} + \frac{\cos(L_a(k_m-k_x))-1}{k_m-k_x})\Bigg] \tag{3.79}$$

$$I_{Xsin}(m,k_x) = \Bigg[\frac{1}{2(k_m^2+k_x^2)}(e^{k_m L_a}(k_m \sin(L_a k_x) - k_x \cos(k_x L_a)) - e^{-k_m L_a}(k_m \sin(L_a k_x) - k_x \cos(k_x L_a)) + 2k_x) + \frac{1}{2}(\frac{\cos(L_a(k_m+k_x))-1}{k_m+k_x} - \frac{\cos(L_a(k_m-k_x))-1}{k_m-k_x})\Bigg] - \alpha_m \Bigg[\frac{1}{2(k_m^2+k_x^2)}(e^{k_m L_a}(k_m \sin(L_a k_x) - k_x \cos(k_x L_a)) + e^{-k_m L_a}(k_m \sin(L_a k_x) + k_x \cos(k_x L_a))) + \frac{1}{2}(\frac{\sin(L_a(k_m+k_x))}{k_m+k_x} - \frac{\sin(L_a(k_m-k_x))}{k_m-k_x})\Bigg] \tag{3.80}$$

The forms of $I_{Ycos}(n,k_y)$ and $I_{Ysin}(n,k_y)$ are the same with $I_{Xcos}(n,k_y)$ and $I_{Xsin}(n,k_y)$ by replacing k_m to k_n and L_a to L_b, respectively. Consequently, the integration in function $\mathbf{I_{mnqr}}$ reduces into a two-fold form and is easier to solve numerically.

3.6.6 Analytical Solution - II (Principle of Virtual Work)

In the previous section 3.6.5, the solution is explicitly obtained from the governing equation of plate vibration along with the superposition method. It leads to the

concept of fluid impedance, which is useful to analyse various fluid-loading effects on the motion of microplates. However this solution is only appropriate for the plates with orthogonal mode shape functions, for example the all clamped plates. It would result in significant errors when applied to the plates involving two opposite free edges, such as C-F-F-F or C-F-C-F plates. This is due to that the first two mode functions of a F-F boundary condition are not orthogonal. For example the first mode function is usually selected to be equal 1, which is not orthogonal to the other mode functions as shown in Eq. 3.81.

$$I_{1n} = \int_L X_1(x)Y_n(y) = \int_L Y_n(y) \neq 0, \quad n > 2 \tag{3.81}$$

A more general solution is derived in this section from the following equations giving by the principle of virtual work[128].

$$\delta \cdot U_p + \iint_S \rho_s h \frac{\partial^2 w}{\partial t^2} \delta w dx dy - \iint_S \left(F_{ex} + F_{hydro}\right) \delta w dx dy = 0 \tag{3.82}$$

where U_p is the potential energy of plate defined in Eq. 3.19, δw is the virtual displacement of plate and assumed to be very small and constant over the plate domain. Substituting the solutions or expressions of U_p, w (Eq. 3.3), F_{hydro} (Eq. 3.70) into Eq. 3.82, an analytical solution based on the principle of virtual work is obtained.

$$\sum_m^\infty \sum_n^\infty \left(U_{p,mnqr} - \omega^2 T^*_{p,mnqr} + i\omega \cdot \frac{\mathbf{I_{mnqr}}}{2}\right) \{W_{mn}\} = F_{qr} \quad q, r = 1, 2, \cdots, \infty \tag{3.83}$$

where $U_{p,mnqr}$ and $T^*_{p,mnqr}$ have the same forms with Eq. 3.25 and 3.26 respectively. It can be seen that the form of Eq. 3.83 is similar to the solution (Eq. 3.24) of Rayleigh-Ritz method. Both methods don't require the mode shape functions

to be orthogonal. Therefore the solutions on C-F-F-F or C-F-C-F plates can be obtained by using Eq. 3.83.

3.6.7 Numerical Simulations

As the simulations of microplates are at micron level (10^{-6}), direct evaluation of integrations of impedance and dry natural frequencies could result in arithmetic overflow or significant errors due to the precision limitations of computer. Before one performs numerical evaluation of the vibration of fluid-loaded microplates, it is necessary to normalize these mathematical expressions. The inner integrations in Eq. 3.75 can be transferred into the following form, which is independent of plate dimensions.

$$\omega_{mn}^2 = \frac{D}{\rho_p h}\left(k_m^4 + 2\frac{\int_0^1\int_0^1 X_m' \ddot{X}_m' Y_n' \ddot{Y}_n' dxdy}{\int_0^1\int_0^1 X_m'^2 Y_n'^2 dxdy} + k_n^4\right) \tag{3.84}$$

where $X_m'(x)$ and $Y_n'(y)$ are the non-dimensional mode shape functions.

$$X_m'(x) = \cosh(\epsilon_m x) - \cos(\epsilon_m x) - \alpha_m\left[\sinh(\epsilon_m x) - \sin(\epsilon_m x)\right] \tag{3.85}$$

The fluid-loaded impedance integral is naturally scaled with acoustic wave-number ($k = \omega/c$), and then all the other wave-numbers (k_l, k_s, k_x, k_y) can be normalized to be non-dimensional[32]. If defining $k_x = kK_x$ and $k_y = kK_y$, the fluid-loaded impedance becomes:

$$I_{mnqr} = \frac{k^2}{4\pi^2}\iint_{-\infty}^{\infty} T(K_x, K_y)\chi_{mn}(K_x, K_y)\chi_{qr}^*(K_x, K_y)dK_x dK_y \tag{3.86}$$

The modal coefficients (W_{mn}) at a specific frequency of the forced vibration of a fluid-loaded microplate thus are determinated from a truncated subset of Eq.

3.72. As the analysis presented in this part is mainly concentrated at the first few modes, only 9×9 terms of Eq. 3.72 or Eq. 3.83 are taken and calculated in every simulation, which can be proved to have sufficient accuracies. The deformation of the vibrating microplate at each point then can be evaluated from Eq. 3.3. If performing this kind of simulation at a series of linearly spaced frequency-sequence, the frequency response function (FRF) of the fluid-loaded microplate over a specified frequency range is then produced. Using the FRFs, theoretical results of the modal parameters, natural frequencies, damping ratios and mode shapes of fluid-loaded microplates can be obtained.

The material properties of microplate and water selected are the same as the values used in Rayleigh-Ritz model in this simulation. The sound velocity and viscosity of water are chosen as $c = 1482m/s$, $\mu = 1.003cP$. Although this theoretical model is derived to involve both the acoustic radiation damping and viscous damping, it is also appropriated to the extreme cases. If assuming no viscous damping $\mu = 0$, the motion of microplate only suffers acoustic radiation damping and the simulation results can be used to analyze acoustic damping effects. If assuming no damping that $\mu = 0$ and $c \to \infty$, this vibration of microplate therefore reduces to be a conservative system and the corresponding simulation results should match the results obtained from Rayleigh-Ritz model.

However most difficult part in numerical simulation of the forced vibration of fluid-loaded microplates (Eq. 3.72) is the evaluation of fluid-loaded impedance $\mathbf{I_{mnqr}}$. The integration of impedance involves double infinite ranges and exists square root singularities. As the inner integrands $T(k_x, k_y)$ and $\chi_{mn}(k_x, k_y)$ are of very complicated forms, acquiring accurate solutions like the aforementioned Rayleigh-Ritz method becomes unachievable. Quasi-Monte Carlo integral algorithm (see Appendix A) is then employed to obtain an approximate numerical solution of the impedance. The infinite integral ranges $([-\infty, \infty], [-\infty, \infty])$ have also to be truncated into finite ranges $([-l, l], [-l, l])$ in the process of numerical evaluation. Figures 3.6 and 3.7 demonstrate the convergence and acceptable associated errors with the selected number of Monte Carlo integration samples and truncated integration ranges respectively, in the process of evaluation of the

impedance $\mathbf{I_{mnqr}}$ for a $100\mu m \times 100\mu m \times 5\mu m$ C-C-C-C rectangular microplate at frequency $3.37MHz$ (around its first wet resonance mode). The values of $\mathbf{I_{1111}}$, $\mathbf{I_{1212}}$, $\mathbf{I_{2222}}$ and $\mathbf{I_{3333}}$ with a series of different sampling number and integral ranges are tested. The results prove that good convergent results can be obtained when the number of sample points and truncated integral ranges are sufficient large. Eventually the sample number for each Monte Carlo integration is chosen as 5×10^5 and the double infinite integral ranges are truncated into $[-10, 10], [-10, 10]$ in all subsequent simulations of C-C-C-C microplates. The selected parameters for C-C-C-C micrplates are indicated with the perpendicular red lines in these Figures. Similar convergence testing is also preformed on C-F-C-F and C-F-F-F microplates, for which integral ranges have to be extended into $[-100, 100], [-100, 100]$ and the number of Monte Carlo sampling is set to 5×10^6 correspondingly.

3.6.8 Numerical Results of Fluid Damping

Numerical results of the vibration of microplates with three different cases of fluid loading are estimated from this theoretical model: (i)Assuming no damping, $\mu = 0$ and $c \to \infty$; (ii)Only acoustic radiation damping is considered, $\mu = 0$ and $c = 1482m/s$; (iii)Consider both acoustic damping and viscous damping, $\mu = 1.003cP$ and $c = 1482m/s$. The FRF for each case of the three different boundary conditions (C-C-C-C, C-F-F-F, C-F-C-F) microplates are presented in Figures 3.8, 3.9 and 3.10 respectively, and all of which have dimensions at $100\mu m \times 100\mu m \times 5\mu m$.

The predicted resonance frequencies in these three cases are well matched and have a good agreement with the results of Rayleigh-Ritz model. Additionally in all these three figures the FRF curves of case (ii) and case (iii) are almost coincidence. It demonstrates that the dominant damping of fluid loading is caused by acoustic radiation rather than viscous relaxation. It can conclude that viscous damping is negligible when the fluid viscosity is very low (like water) for the dynamic analysis of fluid-loaded microplates. This conclusion is very different than the viscous

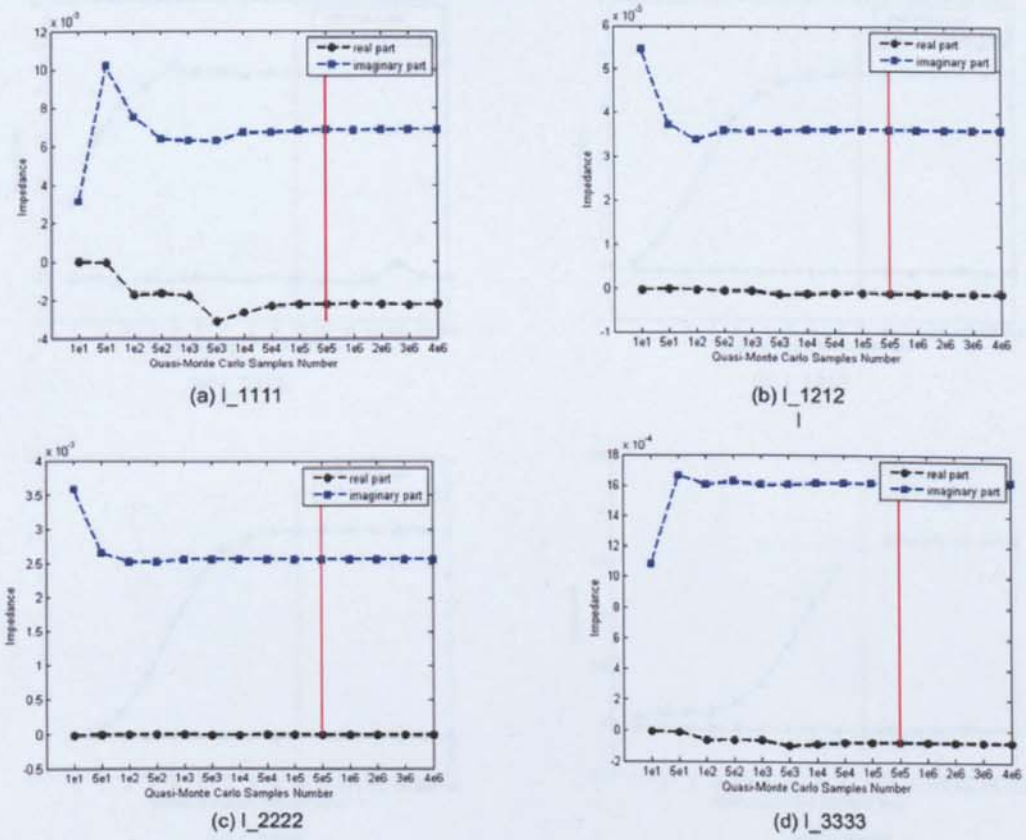

Figure 3.6: Convergence demonstration of Monte-Carlo integration algorithms in evaluation of fluid-loaded impedance (integral ranges are all truncated into [-10,10], [-10,10])

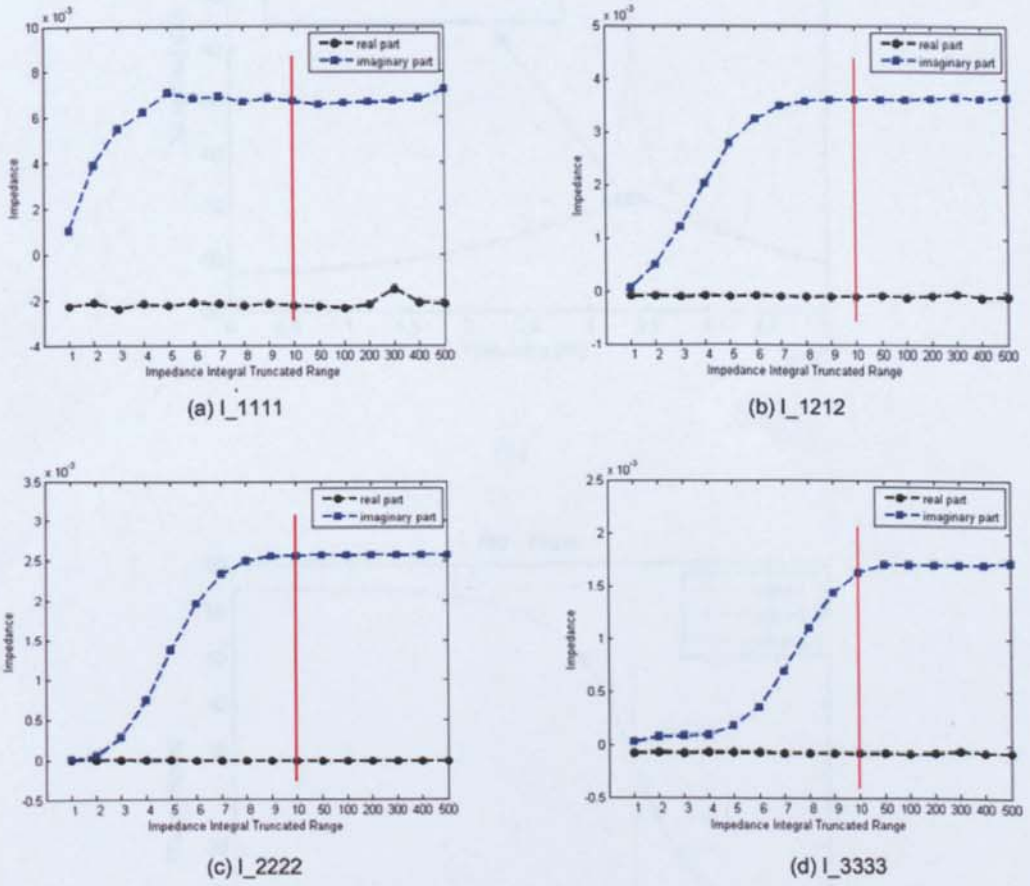

Figure 3.7: Convergence demonstration of truncated infinite integral ranges ($[-l, l], [-l, l]$) of fluid-loaded impedance (number of samples in each monte carlo integration is $5000 \times l$)

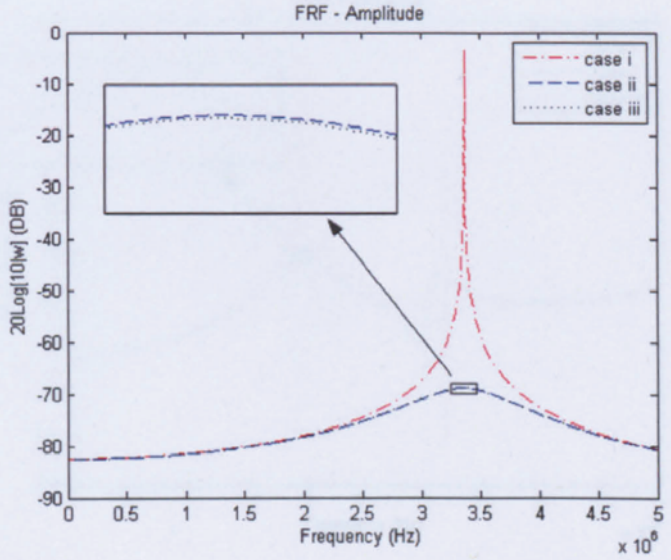

(a)

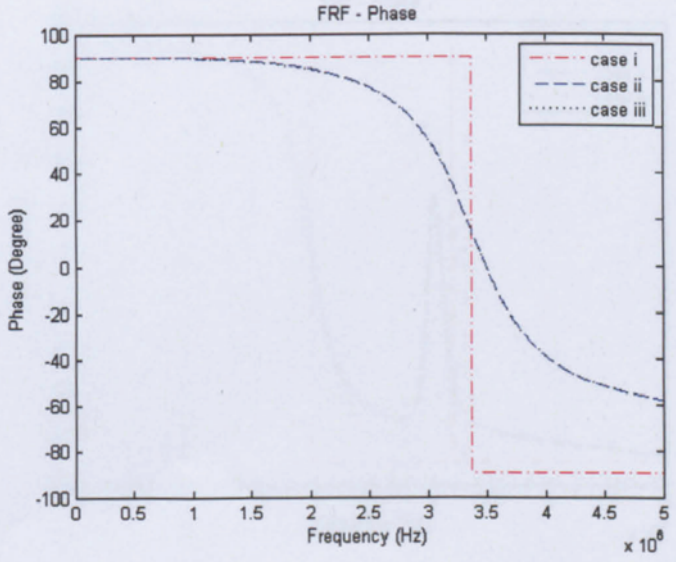

(b)

Figure 3.8: FRF at point $(L_a/2, L_b/2)$ of forced vibration of a fluid-loaded $100\mu m \times 100\mu m \times 5\mu m$ C-C-C-C microplate (frequencies scanning from 1kHz to 5MHz)

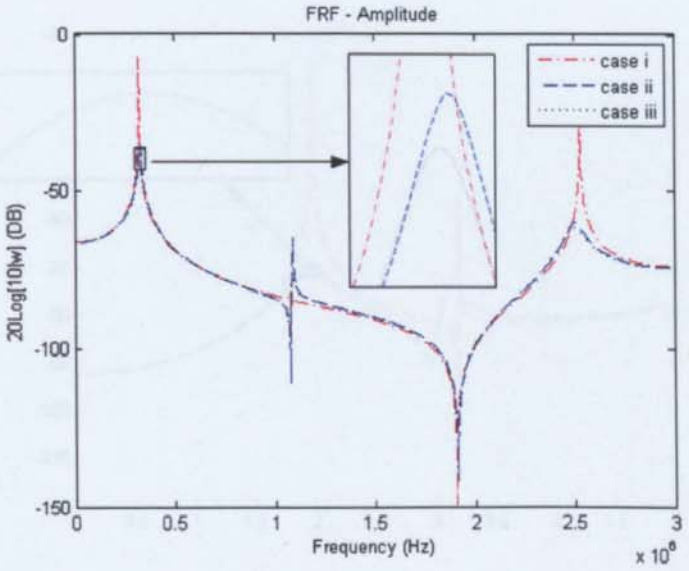

(a)

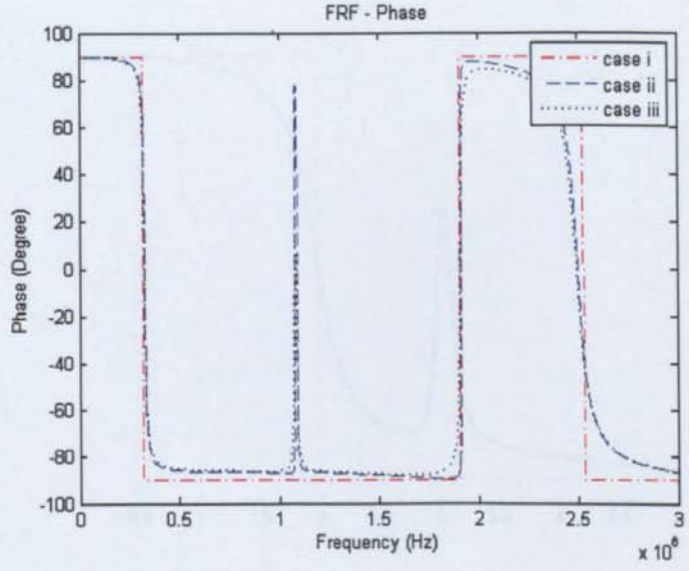

(b)

Figure 3.9: FRF at point $(L_a/2, 0)$ of forced vibration of a fluid-loaded $100\mu m \times 100\mu m \times 5\mu m$ C-F-F-F microplate (frequencies scanning from 1kHz to 3MHz)

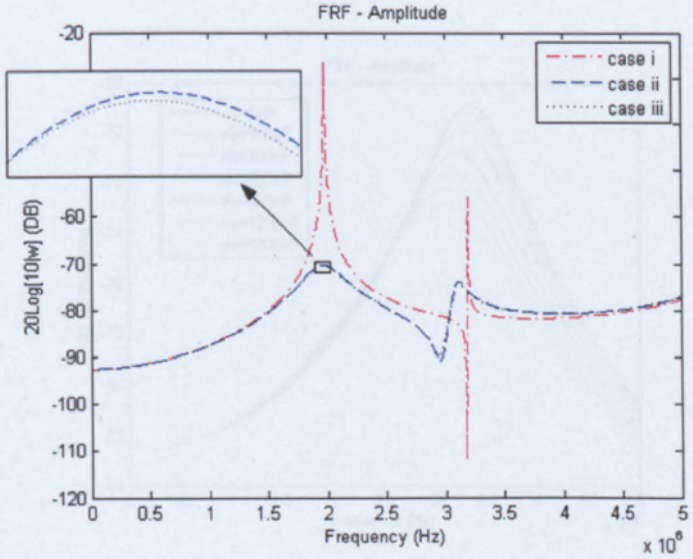

(a)

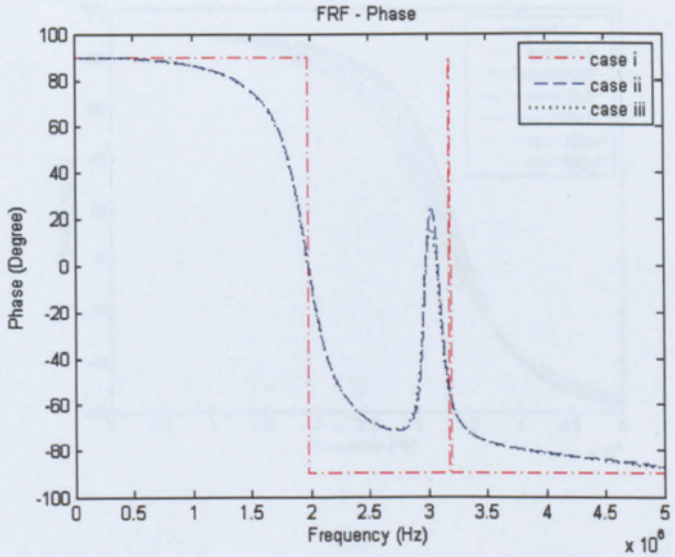

(b)

Figure 3.10: FRF at point $(L_a/2, L_b/4)$ of forced vibration of a fluid-loaded $100\mu m \times 100\mu m \times 5\mu m$ C-F-C-F microplate (frequencies scanning from 1kHz to 3MHz)

analysis of fluid-loaded micro-cantilevers[41, 47], where viscous damping is more dominant. This is primarily due to that microplates have much higher Reynolds number than microcantilevers. In the applications of mass sensing, it proves that microplates are more robust in resistivity of fluid viscosity than micro-cantilevers. A normalized Reynolds number that reflects the ratio between inertial forces and viscous forces of fluid is proposed by Sader[41] with the following form

$$\overline{Re} = \frac{\rho_f \omega_{wet,0} b^2}{4\mu} \tag{3.87}$$

Where $\omega_{wet,0}$ is the damped resonant frequency of micro-structures and b is the width. Take a $100\mu m \times 100\mu m \times 5\mu m$ cantilever type (C-F-F-F) microplate and a $100\mu m \times 5\mu m \times 5\mu m$ micro-cantilever with same material properties as examples, Reynolds number of this cantilever microplate is estimated to be 5118, whereas the value of micro-cantilever is only 12.29, which is more than 400 times less than that of the microplate. It also can be calculated that microplates with other boundary conditions (C-C-C-C or C-F-C-F) have much higher Reynolds numbers. It implies that viscous forces are extremely small comparing with inertial forces of fluid that load on the submerged microplates. Therefore only considering acoustic radiation damping is accurate enough for the damping analysis of fluid-loaded microplates in the case of low viscosity. Fluid-loaded impedance $\mathbf{I_{mnqr}}$ of Eq. 3.76 is then reduced into the following form of acoustic radiation impedance $\mathbf{I^a_{mnqr}}$. Most damping analysis of fluid-loaded microplates presented in this thesis directly employs this Eq. 3.88, which is more computationally efficient comparing with Eq. 3.76. The corresponding Q-factor at each mode can be evaluated by using the damping ratio (Eq. 3.89).

$$I^a_{mnqr} = \frac{\rho_f \omega}{4\pi^2} \iint_{-\infty}^{\infty} \frac{\chi_{mn}(k_x, k_y)\chi^*_{qr}(k_x, k_y)}{\sqrt{k^2 - k_x^2 - k_y^2}} dk_x dk_y \tag{3.88}$$

$$Q = \frac{1}{2\zeta} \tag{3.89}$$

Due to the term $\sqrt{k^2 - k_x^2 - k_y^2}$, we can separate the impedance I^a_{mnqr} into the acoustic resistance r_{mnqr} and reactance m_{mnqr} in the following way[25, 127],

$$r_{mnqr} = Re(I^a_{mnqr}), \quad when \;\; k_x^2 + k_y^2 < k^2; \tag{3.90}$$

$$m_{mnqr} = -\frac{1}{\omega_F} Img(I^a_{mnqr}), \quad when \;\; k_x^2 + k_y^2 > k^2; \tag{3.91}$$

As seen from these equations, the acoustic resistance term r_{mnqr} stems from the supersonic ($k_x^2 + k_y^2 < k^2$) sound radiation induced by the plate motion and represents an energy loss of the plate; the reactance term m_{mnqr} comes from the subsonic($k_x^2 + k_y^2 > k^2$) pressure field and appears as an additional inertial term to the plate[127], which results in the *added mass factor.*

3.6.9 Numerical Simulation of High Viscosity Effects

In this section, the dynamics of fluid-loaded microplates suffered high viscous damping are discussed with the numerical results from the theoretical model. Cedric Ayela and Liviu Nicu [6] have experimentally investigated the relations between fluid viscosity and the dynamic behaviours of fluid-loaded circular microplates. Their experimental results demonstrate lower fundamental frequencies and lower Q-factors when increasing liquid viscosity. They also proved that liquid viscosity has no effect on the dynamic characteristics of the microplates when it is lower than $10cP$.

Numerical results of 7 different fluid viscosity[1] on the three different types of microplates (C-C-C-C, C-F-C-F and C-F-F-F) are generated and compared for

[1]($0.001cP$, $100cP$, $300cP$, $600cP$, $900cP$, $1200cP$, $1500cP$), $1500cP$ is the viscosity of 100% glycerol at $25°C$, all the other simulated viscosity are also reasonable in practice if considering the liquid mixture of water/glycerol. However in fact the density of water/glycerol solution varies at different proportion of glycerol[6], for example 100% glycerol is $1258.02kg/m^3$ while

the analysis of high viscosity effects. Figures 3.11, 3.13 and 3.16 illustrate the amplitudes and phases of FRFs at each different viscosity of these three types of microplates respectively. These FRF plots prove that microplates suffer more dampings and resonant frequencies are slightly decreased when increasing the fluid viscosity. Quantities of resonant frequencies shifts and Q-factor (damping) changes due to the high viscous damping are also plotted against the viscosity, as show in Figures 3.12, 3.15 and 3.17. Approximate linear relationships are existed in both of the two curves. Cedric Ayela and Liviu Nicu also reached similar conclusions from their experimental analysis[6].

3.7 Scaling of Fluid Loading Effect on A Microplate

3.7.1 Scaling on Added Mass Factor

The above equations and analysis are based on the general dynamic problem of a fluid-loaded rectangular plate, by no means specific to micro scale. However the issue of physical and mechanical changes due to the size reduction are always concerned in the design and analyse of MEMS devices. In this section the scaling of fluid loading effect on a microplate is investigated. *added mass factor* is employed for the scaling analysis of fluid inertial effect on a microplate. The *added mass factor* at each mode can be approximately evaluated as the ratio between the reference kinetic energies of the fluid (T_f) and plate (T_p), which is defined

50% is $1123.75 kg/m^3$. In order to clearly and only demonstrate the fluid viscosity effects on the behaviours of microplates, the fluid density in all theoretical simulations herein is assumed to be the same of $1000 kg/m^3$.

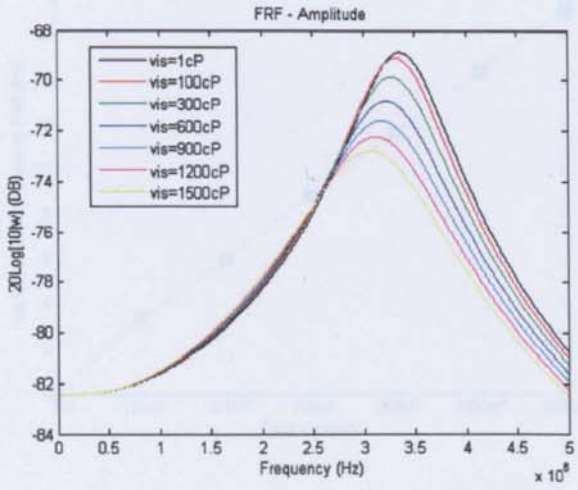

(a)

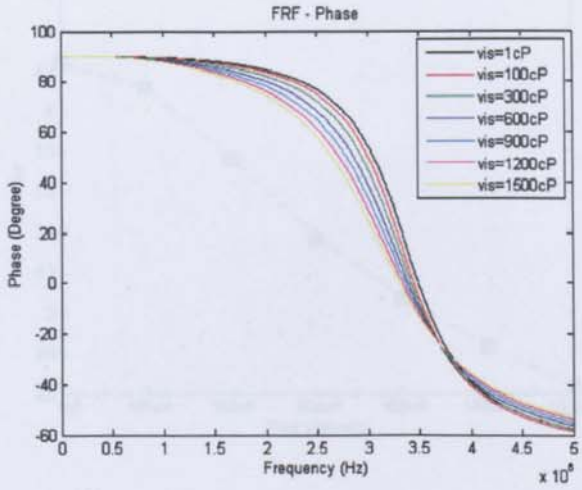

(b)

Figure 3.11: FRFs of a C-C-C-C $100\mu m \times 100\mu m \times 5\mu m$ microplate under different high viscous dampings

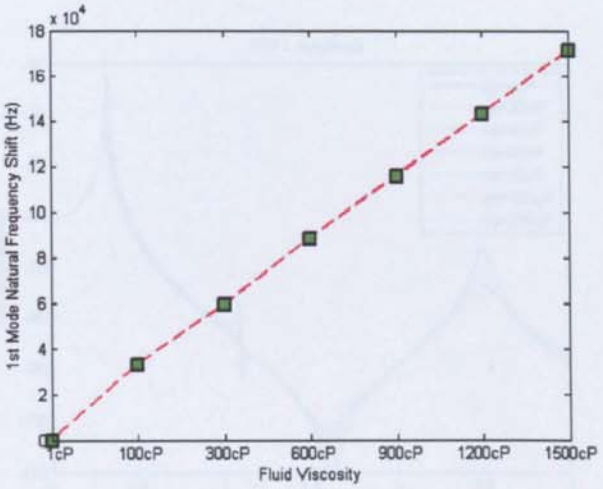

(a)

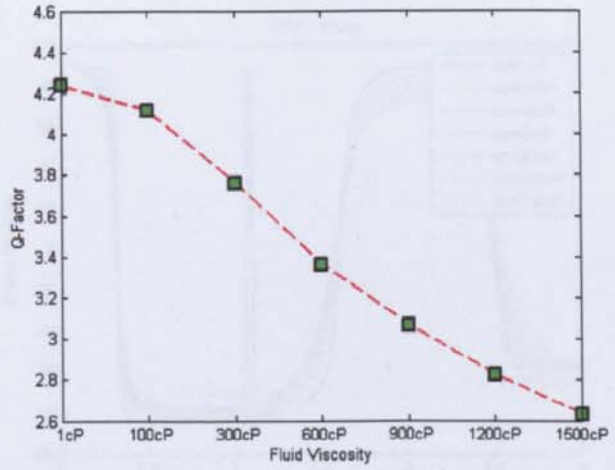

(b)

Figure 3.12: Shifts trend of first mode resonant frequency (a) and corresponding Q-Factor (b) of a C-C-C-C $100\mu m \times 100\mu m \times 5\mu m$ microplate under different high viscous dampings

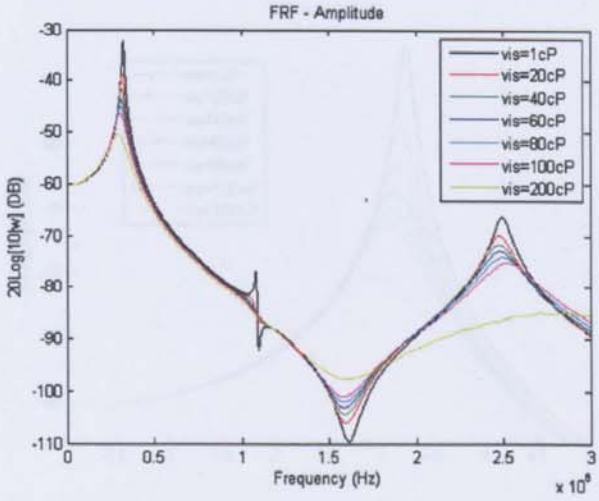

(a)

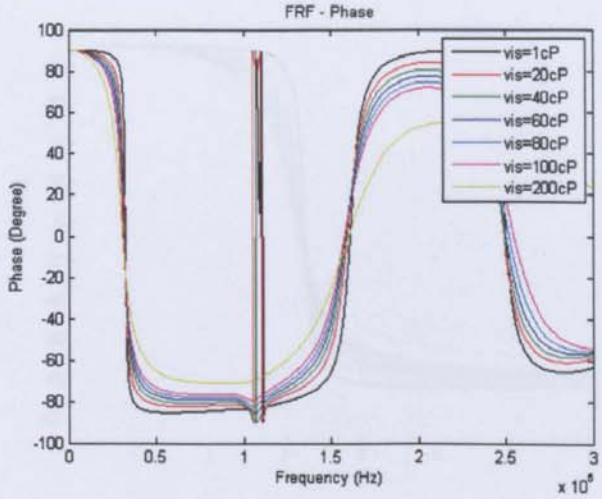

(b)

Figure 3.13: FRFs of a C-F-F-F $100\mu m \times 100\mu m \times 5\mu m$ microplate under different high viscous dampings

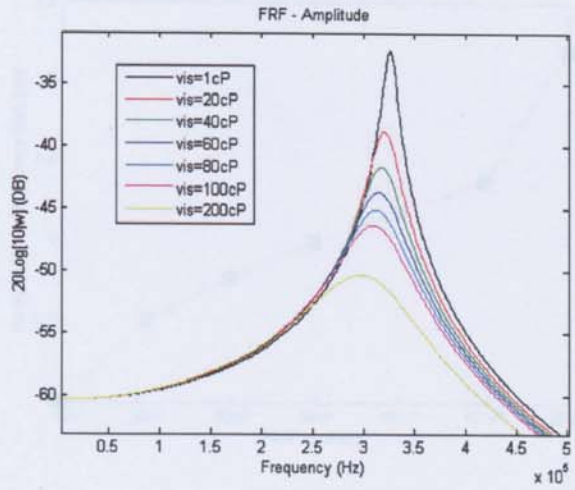

(a)

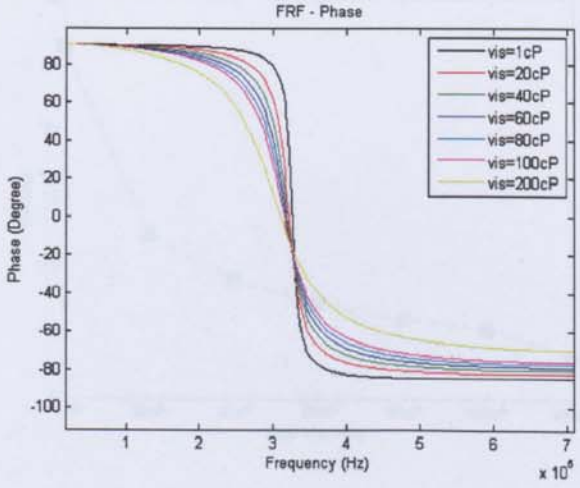

(b)

Figure 3.14: FRFs of a C-F-F-F $100\mu m \times 100\mu m \times 5\mu m$ microplate under different high viscous dampings: partial enlarged view for the first mode

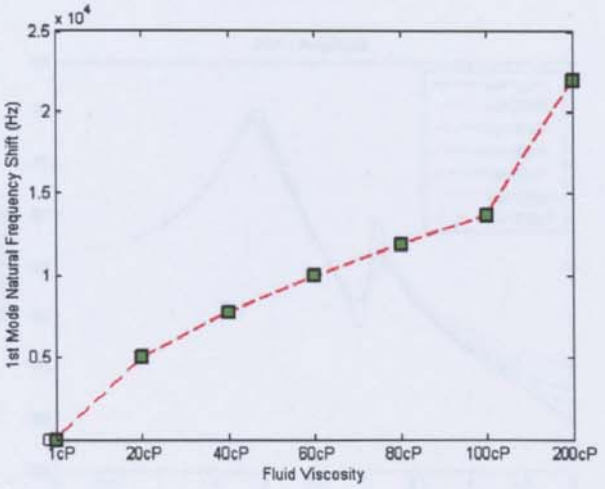

(a)

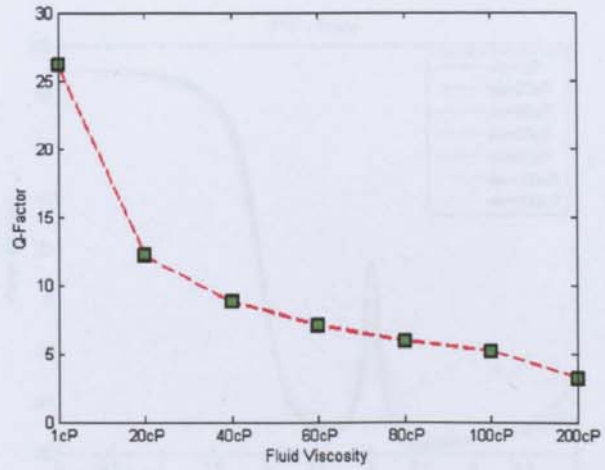

(b)

Figure 3.15: Shifts trend of first mode resonant frequency (a) and corresponding Q-Factor (b) of a C-F-F-F $100\mu m \times 100\mu m \times 5\mu m$ microplate under different high viscous dampings

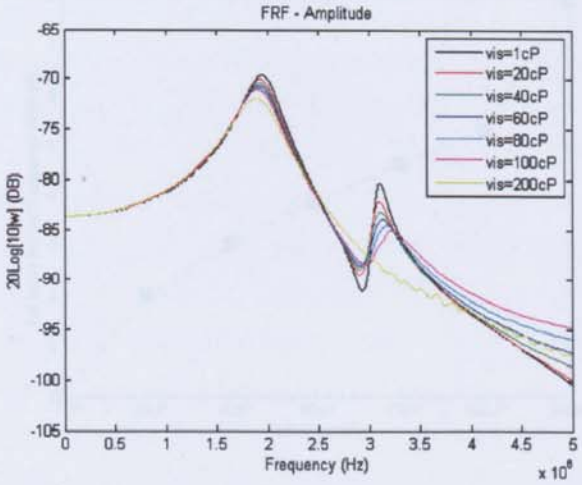

(a)

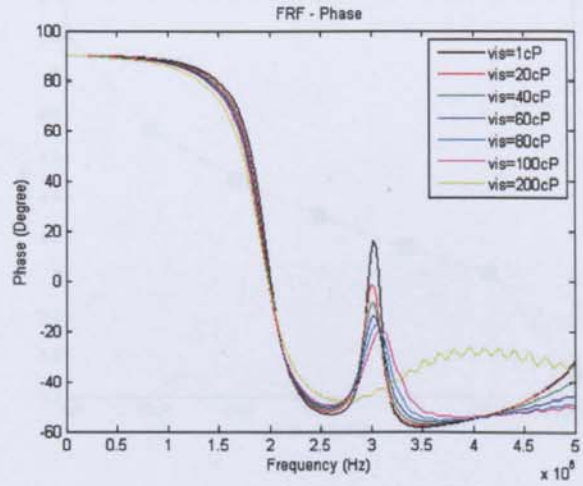

(b)

Figure 3.16: FRFs of a C-F-C-F $100\mu m \times 100\mu m \times 5\mu m$ microplate under different high viscous dampings

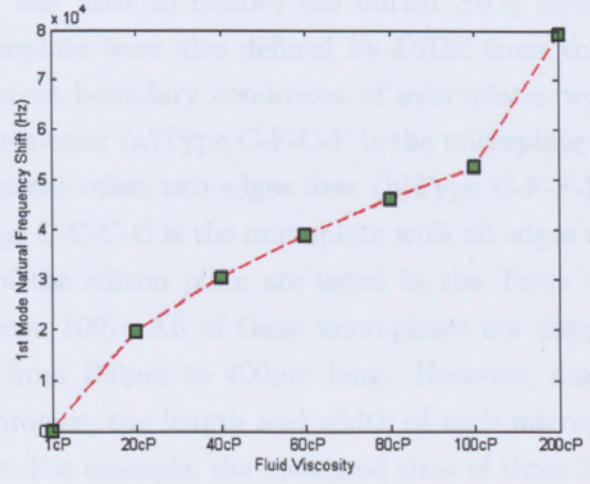

(a)

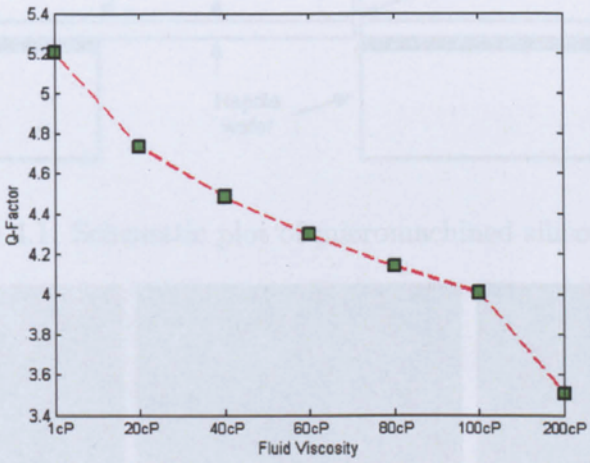

(b)

Figure 3.17: Shifts trend of first mode resonant frequency (a) and corresponding Q-Factor (b) of a C-F-C-F $100\mu m \times 100\mu m \times 5\mu m$ microplate under different high viscous dampings

as[19]

$$\beta_{mn} = \left(\frac{w_{v,mn}}{w_{f,mn}}\right)^2 - 1 = \frac{T^*_{f,mnmn}}{T^*_{p,mnmn}} \tag{3.92}$$

The inner integral part in each formulation of these two energies can be written as the following non-dimensional form,

$$T^*_{f,mnmn} = 2 \cdot \frac{\rho_f}{4\pi}\varepsilon^2 L_b^3 \int_0^1 \int_0^1 \frac{1}{\mathcal{R}'} FX(u,m,m)FY(v,n,n)dudv \tag{3.93}$$

$$T^*_{p,mnmn} = \frac{1}{2}\rho_p h\varepsilon L_b^2 \int_0^1 \int_0^1 X_m^2(L_a x)Y_n^2(L_b y)dxdy \tag{3.94}$$

where ε is the plate aspect ration L_b/L_a, $\mathcal{R}' = \sqrt{(\varepsilon u)^2 + v^2}$. The functions FX and FY are naturally non-dimensional and mode shape functions $X_m(L_a x)$ and $Y_n(L_b y)$ are non-dimensional. Therefore in terms of geometrical dimensions,

$$\beta_{mn} \propto \frac{\varepsilon L_b}{h} \tag{3.95}$$

From Eq.(3.95) it can be seen that the *added mass factor* scales by L_b/h for a uniform rectangular thin plate with fixed aspect ratio. However the size reduction of width (L_b) and thickness (h) of plate are usually of the same order. Consequently there is no scaling difference of the inertial effect of fluid loading between on a macro plate or on a micro plate. In other words the decrease of natural frequencies of plate due to the fluid loading will also happen for a micro plate and the proportion of frequency shift are the same as that of a macro plate.

3.8 Conclusion

This chapter first proposed an analytical model for the dynamic system of fluid-loaded plates with distributed mass attachment based on Lambs model and the RayleighRitz energy method. Pierces integral technique is used to overcome the difficulty of evaluating the effects of fluid loading. The numerical results calculated using this novel methodology are compared with Lindholms experimental results and Kwaks NAVMI-based results and show close agreement. It is concluded that the methodology based on RayleighRitz energy principle proposed in this chapter can be widely applied to most boundary conditions of rectangular plates, provided that the mode shape functions are known. It is the first analytical solution to this problem, taking into consideration both fluid loading and distributive mass loading effects. Both of these factors are important in microbiosensor design using microstructures. Numerical results of the plate-resonant frequencies and mode shapes under different loading cases are presented. This novel methodology and the dynamical characteristics of microplates derived can be applied in the design of microplate-based biosensing systems. A simple simulation of cell attachment derived from this theoretical model was used to examine the effect of mass loading on micrplates, in which both of the changes of natural frequencies and mode shapes are demonstrated.

In order to analyse the damping mechanisms of fluid-loading on the microplate, a more precise model considering both of acoustic damping and viscous damping is derived. In the process of derivation the linearized Navier-Stokes equations for the fluid dynamics is solved based on the non-slip boundary conditions of the fluid-structure interface. Due to the complicated forms of this second model, the Monte Carlo simulation method is used to obtain an approximate solution. From the numerical results of second mode under different assumptions of fluid, it reveals that acoustic damping dominant the dampings of the dynamics of fluid-loaded plates when the viscosity of fluid is low. From the simulation results obtained under different high fluid-viscosity, it reaches a conclusion that fluid viscosity has smaller effects on the dynamics of microplates than micro-cantilevers. The scaling of fluid loading effects based on these two theoretical models are then

investigated. It is theoretically proved that the added mass factor is independent the scaling of plate.

In summary, we developed two different mathematical methods for the dynamic analysis of fluid-loaded plate in this chapter. These two models have different features and are appropriate to use in different situations.

For the first model, which is based on RayleighRitz energy method:

(a) The solution of this model is obtained through the evaluation of eigenvalues and eigenvectors of a matrix. Therefore the natural frequencies and mode shapes can be fast to estimate by using this method.

(b) It provides an alternative way that can more accurately evaluate the *added mass factor* of the fluid-loading on rectangular plate, comparing with the approximate formulation in [10].

(c) As it ignores the damping effect of fluid, this method is not appropriate to perform damping analysis or sensitivity (Q-factor) analysis for fluid-loaded plates.

For the second model, which is using the non-slip boundary conditions:

(a) Comparing with the first model, this theoretical model is more precise with considering both the acoustic damping and viscous damping. This model is suitable to analyse the damping mechanism of the fluid-loaded plate.

(b) This model is capable to trace out the frequency response graph of a fluid-loaded plate. The frequency response trends are very helpful for fully understanding the dynamic characteristics of fluid-loaded plate.

(c) However, it usually requires to sweep over a certain frequency range to obtain the frequency response function. In each single simulation at a sepecific frequency it has to calculate the corresponding hydrodynamic force, which is

a very complex mathematical form. Consequently, this is a time-consuming process to use this method to analyse the dynamics of fluid-loaded plate.

Although these two methods is designed for the dynamics of rectangular plate, their concept can also be extanded to apply to other fluid-structure interaction problems.

Chapter 4

Experimental dynamics analysis of submerged microplates

4.1 Introduction

An experimental testing system for the study of dynamics behavior of fluid-loaded rectangular micromachined silicon plates is designed and presented in this chapter. In this experimental system, the base excitation technique combined with pseudo-random signal excitation and cross-correlation analysis is applied to test fluid-loaded microstructures. The dynamic experiments cover a series of testings of various microplates with different boundary conditions and dimensions, both in air and immersed in water. This is the first work that demonstrates the ability and performances of base excitation in the application of dynamic testing of microstructures that involves a natural fluid environment. Traditional modal analysis approaches are used to evaluate natural frequencies, modal damping and mode shapes from the experimental data. The obtained experimental results are discussed and compared with theoretical predictions. This research experimentally determines the dynamic characteristics of the fluid-loaded silicon microplates,

which can contribute to the design of microplate based microsystems.

In this dynamic testing system designed for the fluid-loaded micro-plates, an ultrasonic transducer with 1.65MHz bandwidth of frequency response is used for base-excitation and the micro scanning laser vibrometer (Polytec MSV-400) is used to record the vibration signal of the micro-plate. MSV-400 Vibrometer is developed specially for the vibrational analysis of MEMS devices, and its fast, accurate and non-contacting properties makes it an ideal tool for studying micro structure dynamics. MSV-400 can achieve picometer vibration resolution and up to 20 MHz bandwidth. Pseudo-random signal is used in the experiments for excitation. Pseudo-random signal is of deterministic signal and has almost the same properties as white noise in terms of covariance function.

The fabrication process and mechanical properties of measured silicon microplates are introduced first in this chapter. A detailed description of base-excitation based experimental system has been presented. It is followed by the mathematical model of the testing system, and analysis of pseudo-random excitation signal and cross-correlation techniques in modal testing of microplates. Lastly, RFP curve fitting approaches were applied to extract modal parameters that include resonant frequencies, modal damping ratios and modal constants from the measured FRF spectrums. The experimental results of vibration characteristics of submerged microplates are compared with the simulation results predicted by theoretical models in Chapter 3.

4.2 Manufacture of Rectangular Microplates

The microplates were fabricated from silicon on insulator (SOI) wafers with $5\mu m$ or $3\mu m$ thickness active silicon layer. The material of the active silicon layer is silicon(100). As illustrated in Figure 4.1, the membrane structure for each microplate was etched out by inductively coupled plasma (ICP) using the Deep

Reactive Ion Etching (DRIE) process from the back side of SOI wafer. Afterwards Nitric acid was used to remove the buried SiO_2 layer. The boundary conditions of microplate were also defined by DRIE from the top side of SOI wafer. Three different boundary conditions of microplates were fabricated and tested in our experiments: (a)Type C-F-C-F is the microplate with two opposite edges clamped and the other two edges free; (b)Type C-F-F-F is the cantilever microplate, (c)Type C-C-C-C is the microplate with all edges clamped. The material properties of the silicon plate are listed in the Table 4.1, which is refer to the data of silicon(100). All of these microplates are designed to be square and with lengths from $100\mu m$ to $400\mu m$ long. However, due to nature of the microfabrication process, the length and width of each microplates is not quite the designed value. For example, the measured sizes of three $300\mu m$ microplates are measured and listed in Table 4.2.

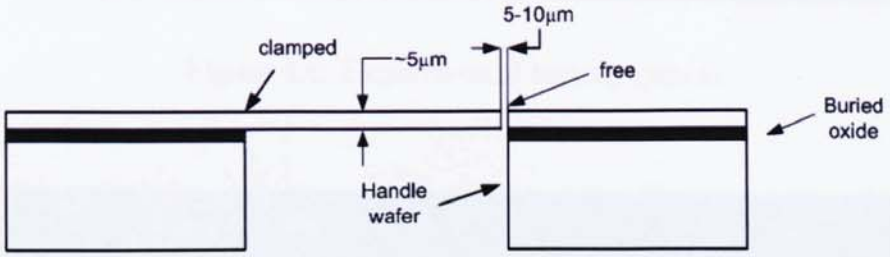

Figure 4.1: Schematic plot of micromachined silicon plate

Figure 4.2: LSM images of $300\mu m$ microplates (Type C-F-C-F, Type C-F-F-F, Type C-C-C-C)

Table 4.1: Material parameters of the silicon plate

	Thickness $h(\mu m)$	Young's E(GPa)	Poisson's (ν)	Density $\rho_p(kg/m^3)$
Plate	5	150	0.17	2330

Table 4.2: Measured sizes of each type plate($L_a \times L_b$, $\mu m \times \mu m$)

C-F-C-F	C-F-F-F	C-C-C-C
296.9×309.5	294.3×295.3	358.1×359.9

4.3 Experimental Testing System

4.3.1 Theory of Base Excitation On Microplate

Mathematical modelling of this testing base excitation system designed for microplates is similar to previous pertinent work[1, 67, 68, 76]. Formulation derivation of the vibration of fluid-loaded microplates stimulated by base excitation are specially discussed in this section. Figure 4.3 illustrates the motion of a microplate under the testing of a base excitation system. The vibration of an isotropic thin-film rectangular microplate can be expressed in Eq. 3.48. Here $w(x, y, t)$ indicates the function of plate absolute deflection. The boundary conditions of clamped edges of microplate that continuously linked with the rigid base are changed to (as example the clamped edge is along $x = L_a$),

$$(w)\Big|_{x=L_a} = v(t), \quad \left(\frac{\partial w}{\partial x}\right)\Big|_{x=L_a} = 0 \tag{4.1}$$

On the other hand, the boundary conditions of free edges in base excitation system remain the same,

$$\left(\frac{\partial^2 w}{\partial x^2} + \nu\frac{\partial^2 w}{\partial y^2}\right)\Big|_{x=L_a} = 0, \quad \left[\frac{\partial^3 w}{\partial x^3} + (2-\nu)\frac{\partial^3 w}{\partial x \partial y^2}\right]\Big|_{x=L_a} = 0 \tag{4.2}$$

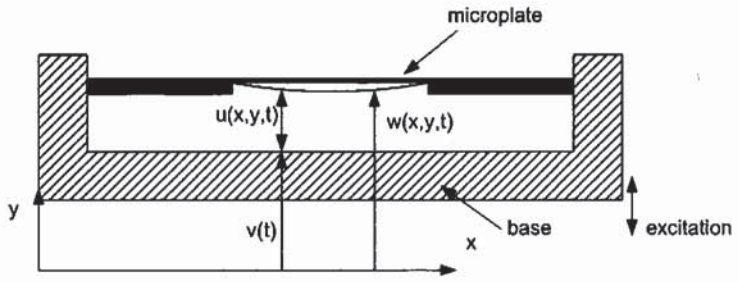

Figure 4.3: Schematic plot of micromachined silicon plate

Applying the new boundary conditions of Eqs. 4.1 and 4.2, the deflection of microplate under base excitation can be solved from the plate governing equation. However it would be an intractable process due to the non-homogeneous nature of the new boundary conditions[1]. In order to change the boundary conditions to be homogeneous, relative motion of the microplate to the excited base is employed to obtain the solution. The absolute velocity of microplate $\dot{w}(x,y,t)$ and the velocity of base $\dot{v}(t)$ can be directly measured and recorded by the vibrometer respectively. All system motions are assumed to be mainly along the vertical direction of the base excitation apparatus, therefore the relative motion of microplate $u(x,y,t)$ to the excited base can be expressed as,

$$u(x,y,t) = w(x,y,t) - v(t), \quad \dot{u}(x,y,t) = \dot{w}(x,y,t) - \dot{v}(t) \tag{4.3}$$

Notice that the base motion of $v(t)$ is assumed to be an independent form with respect to the plane coordinate (x,y), therefore the governing function of microplate vibration and the boundary conditions in terms of relative motion $v(t)$ can be expressed in the following forms. The boundary conditions of free edge remain the same forms and are naturally homogeneous.

$$D\nabla^4 u(x,y,t) + \rho_p h \frac{\partial^2 u(x,y,t)}{\partial t^2} = f(x,y,t) - \rho_p h \frac{\partial^2 v(t)}{\partial t^2} \tag{4.4}$$

$$(u)\Big|_{x=L_a} = 0, \quad \left(\frac{\partial u}{\partial x}\right)\Big|_{x=L_a} = 0 \tag{4.5}$$

Therefore the relative motion of microplate can be solved in Eq. 4.4 by using the same routines presented in chapter 3. That is substituting mode shape functions $X_q(x), Y_r(y)$ (Eqs. 3.5 $\sim$ 3.8) into Eq.4.4, multiplying both sides with cross-modal functions $X_m(x), Y_n(y)$, and integrating over the whole plate domain. Then the following characteristic equation for the relative motion of based-driven microplate is obtained considering a simple harmonic motion at frequency ω,

$$MW_{mn}(\omega_{mn}^2 - \omega^2) = F_{mn} + \omega^2 \rho_p h C_{mn} v(t) \tag{4.6}$$

where M is the mass of plate and ω_{mn} is the plate natural frequency *in vacuo* of (m, n) mode. F_{mn} is the generalized force and can be represented in the form,

$$F_{mn} = \int_0^{L_a} \int_0^{L_b} F\delta(x - x_0)\delta(y - y_0) X_m(x) Y_n(y)\, dx\, dy \tag{4.7}$$

C_{mn} is a scaling constant,

$$C_{mn} = \int_0^{L_a} \int_0^{L_b} X_m(x) Y_n(y) dx dy \tag{4.8}$$

The last term of Eq.4.6 represents the base excitation force acting on the microplate. It can be seen that base excitation force is an inertial force of base motion scaled by the integral of normalized mode shapes[1]. The external force F_{mn} equates zero when the experiment is executing in vacuo. In the case that the whole base excitation system immerses in fluid (water), the external force F_{mn} is the fluid loading force on the testing microplate. According to the analysis presented in Chapter 3, the effect of fluid can be described with adding an added mass term and an additional damping term into Eq.4.6,

$$\left[(M + M_a)(\omega_{mn}^2 - \omega^2) + 2j\zeta_{mn}\omega_{mn}\omega\right] W_{mn} = \omega^2 \rho_p h C_{mn} v(t) \tag{4.9}$$

If substituting the solution of the coefficient for each mode shape function in Eq.4.9 into Eq. 3.48, the relative motion $u(x, y, t)$ can be evaluated. Consequently the theoretical model for the vibration of base-driven microplate is set up.

Due to the importance and convenience of using the frequency response function (FRF) in the practical experimental modal analysis, a mathematical model on FRFs of the base-excited microplate is derived in following section. For the vibration of the microplate in the relative coordinates, the mechanical force and damping force are functions of relative displacement and relative velocity respectively, while the virtual external force depends on the absolute acceleration of the microplate[67]. Therefore the relative vibration of the microplate in the base excitation in Eq.4.9 can also be written in the following matrix form,

$$[M]\{\ddot{u} - \ddot{v}\} + [C]\{\dot{u}\} + [K]\{u\} = [F] \tag{4.10}$$

where the matrices $[M]$, $[C]$ and $[K]$ are the mass, viscous damping and stiffness of microplate respectively.

If Eq.(4.10) is transfered into the frequency domain, we can obtain the following equation,

$$\begin{aligned} U(\omega) &= H(\omega)V(\omega) \\ H(\omega) &= \frac{\omega^2}{-\omega^2[M] + i\omega[C] + [K]} \end{aligned} \tag{4.11}$$

where $H(\omega)$ is called the frequency response function, it can be directly applied to perform the modal analysis of microplate. However both relative displacement $U(\omega)$ of microplate and displacement of base $V(\omega)$ are not the direct measurements in the experiment. Therefore the velocity based frequency response

function is adopted, which is determined in the following form[56],

$$H_v(\omega) = \frac{\dot{U}(\omega)}{\dot{V}(\omega)} = \frac{\dot{W}(\omega)}{\dot{V}(\omega)} - 1 \tag{4.12}$$

As $\dot{W}(\omega)$ and $\dot{V}(\omega)$ are the direct output of vibrometer, the modal parameters of microplate can be extracted from the velocity based frequency response function.

4.3.2 Experimental Setup of Base Excitation

An experimental system has been designed for the dynamic characteristics measurement of micro-plates *in air* or *immersed in water*. Figure 4.4 shows this testing system. The petri dish containing the base excitation facility is situated on the stage of a microscope, which is used to visualize the microplates and accurately localize the laser spot for the velocity measurement. The laser vibrometer (MSV-400) is connected to the microscope through mounting its adapter on the camera port of the microscope. The embedded signal generator in MSV-400 is used to provide excitation signals, the signal output port on the junction box of MSV-400 connects the electrode wires of an actuator in the petri dish. Figure 4.5 shows the details of base excitation apparatus. At the lowest layer there is a glass slide, which is used to support the actuator for the base excitation. The actuator is an ultrasonic piezo-transducer with 1.65MHz bandwidth of frequency response. A plastic jig with a trapezoid slot is tightly bonded on this actuator. A $10mm$ long and $10mm$ wide silicon die, in which the microplate is embedded at the center, is inserted into the trapezoid slot and can be tightly clamped. Figure 4.6 illustrates the signal flow in each of this modal testing experiment. The excitation signal returns back to pro-analyzer (embedded in MSV-400) as a reference signal, and then it is cross-correlated with the original measured response from the laser vibrometer. Ultimately the frequency response functions of the testing microplate are obtained from the cross-correlation result by performing FFT.

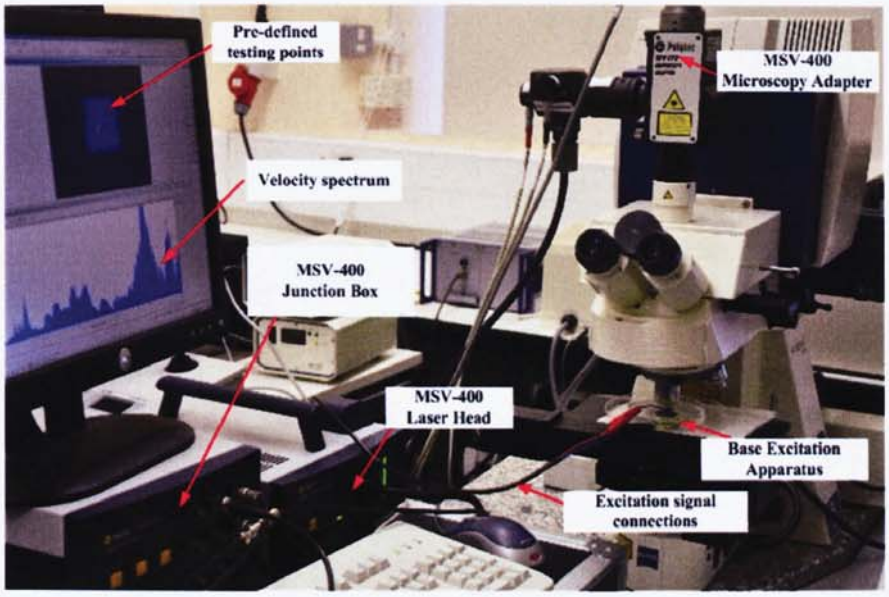

Figure 4.4: Experimental testing system

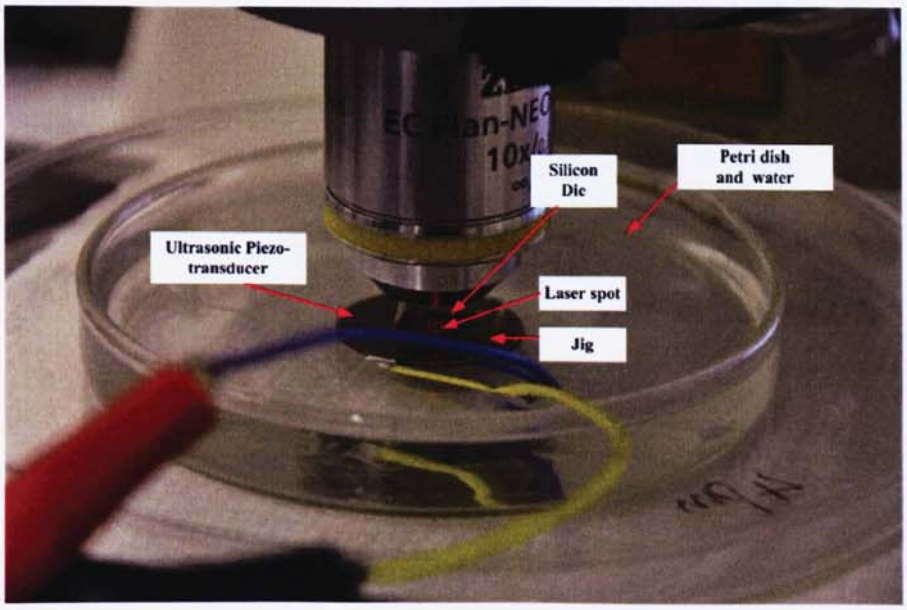

Figure 4.5: Base excitation apparatus

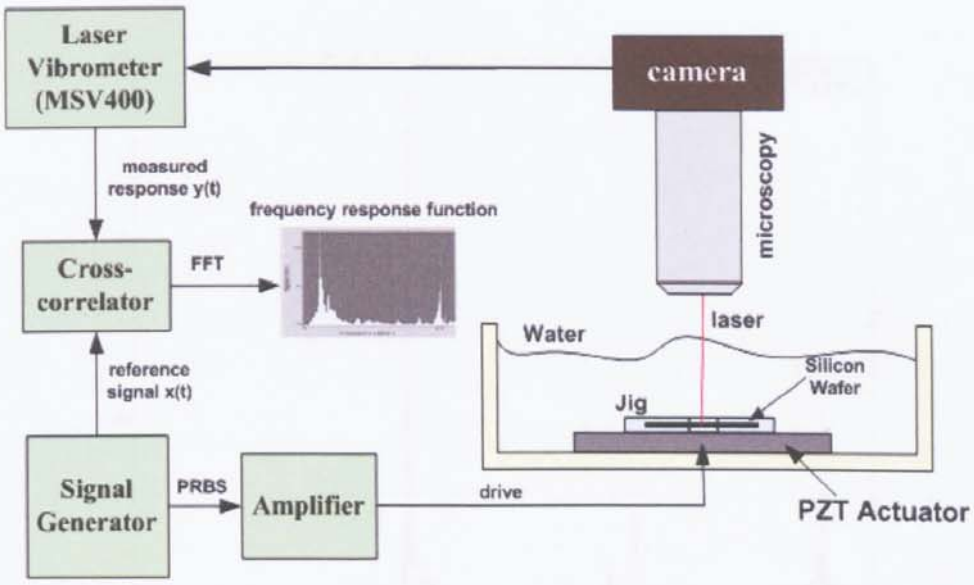

Figure 4.6: Schematic diagram of experimental signal flow

Before the vibration testing of microplates, multiple uniformly distributed testing points that can cover the whole domain of the microplate are defined. Afterwards pseudo-random signal from the embedded generator is amplified to 10 volts and applied to the actuator to excite the whole apparatus. As the mass of petri dish and glass slide is much lager than the mass of exciter (ultrasonic transducer), the excited motion from the actuator is mainly transfered towards the silicon die along the perpendicular direction[56]. Simultaneously the laser beam projects on the surface of microplate and measures the velocity of vibration. The output signal of vibrometer is then correlated to the input excitation signal to determine the frequency response function(FRF), which can be used directly to extract modal parameters. The FRFs at each of these predefined points are recorded, therefore the vibration shape of microplate at any frequency within the testing band (2MHz) can be reconstructed.

4.3.3 Pseudo-random Excitation Signal and Correlation Techniques

As stated previously pseudo-random signal was chosen to excite the microplates for the dynamic modal testing. The binary maximum length sequences (m-sequences) are the normally used type of pseudo-random signal. The pseudo-random signal is a periodic signal with the period of $T = N\Delta t$, where N is the sequence length and must be an odd integer and Δt is the clock period. The characteristics of pseudo-random signal in both time and frequency domain are deterministic, as a result the system response of a linear structure under pseudo-random signal excitation is also deterministic and it makes the measurements in the dynamic testing experiments become reproducible.

The usage of pseudo-random signal in structural modal testing is close to its application in system identification[129], that correlation functions have to be induced to process the measurement of system response. The left part of Figure 4.6 shows the signal conversion in the dynamic testing system, in which $y(t)$ is the direct measurement (system response), $x(t)$ is the excitation signal and also the reference signal used for post-processing. The testing system is fairly linear, deterministic and also follows superposition principle [129]. Therefore the system response (vibration of microplate) can be modeled by an impulse response function $h(t)$. Once the model of impulse response function $h(t)$ is built up, the complete dynamic responses caused from any excitation input can be determined by using a convolution integral[73].

The following gives a brief derivation on how to determinate a system natural model $h(t)$ from the direct system measurement $y(t)$ in a pseudo-random stimulated testing system. The cross-correlation function $R_{xy}(\tau)$ of system output $y(t)$ and input $x(t)$ is defined in the following form[129],

$$R_{xy}(\tau) = \int_0^\infty R_{xx}(\tau - \lambda)h(\lambda)d\lambda \tag{4.13}$$

where τ is the time delay in cross-correlation and R_{xx} is the autocorrelation function of pseudo-random signal $x(t)$. The pseudo-random signal can be designed to approximate white noise, then the auto-correlation function of $x(t)$ approaches a impulse function,

$$R_{xx}(\tau - \lambda) = S_0\delta(\tau) \tag{4.14}$$

where S_0 is the power spectral density of pseudo-random signal. Then Eq. 4.13 becomes a simple linear form and the system model function $h(\tau)$ can be expressed in the form,

$$h(\tau) = \frac{R_{xy}(\tau)}{S_0} \tag{4.15}$$

As a result the system model function $h(\tau)$ can be directly evaluated as a proportion of the cross-correlation function of system input $x(t)$ and output $y(t)$. Applying Fourier transform to the above functions, the frequency system response $H(f)$ can also be obtained as to be proportional of $R_{xy}(f)$.

Figure 4.7 demonstrates the pseudo-random signal employed to excite the microplates in this work, including three plots that are one period of pseudo-random sequence, its autocorrelation function and its power spectrum respectively. It can be seen that autocorrelation function is ideally an impulse and the distribution of power spectrum is fairly uniform over the frequency range less than clock frequency $f_c = 1/\Delta t$. The pseudo-random signal here has the following parameters: sequence length is $N = 16384$ and clock period is $\Delta t = 58e - 6s$.

Figure 4.8 shows an example of processing experimental result of a C-C-C-C microplate using correlation techniques. The first plot is the original time series data collected from Laser Vibrometer. The following plot is the frequency response function, which is‘ obtained from the Fourier transformation of the correlation result between original time series and pseudo-random signal. Resonant peaks of the testing microplate are distinctly appeared in this FRF plot.

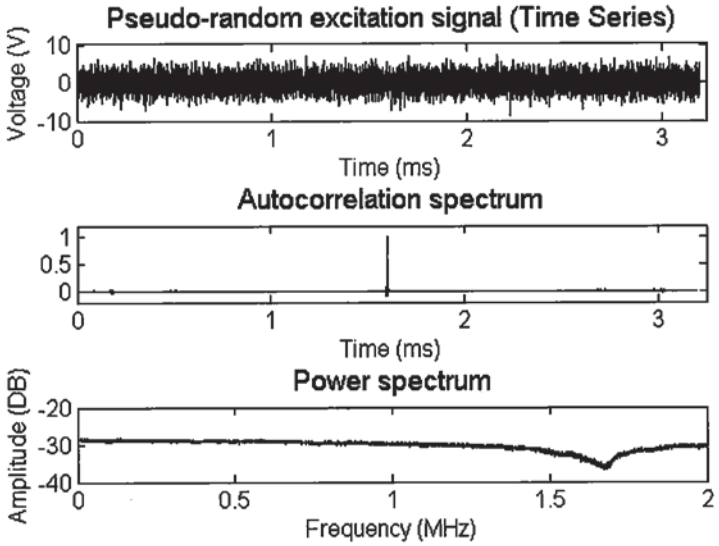

Figure 4.7: A sample of pseudo-random signal used in testing

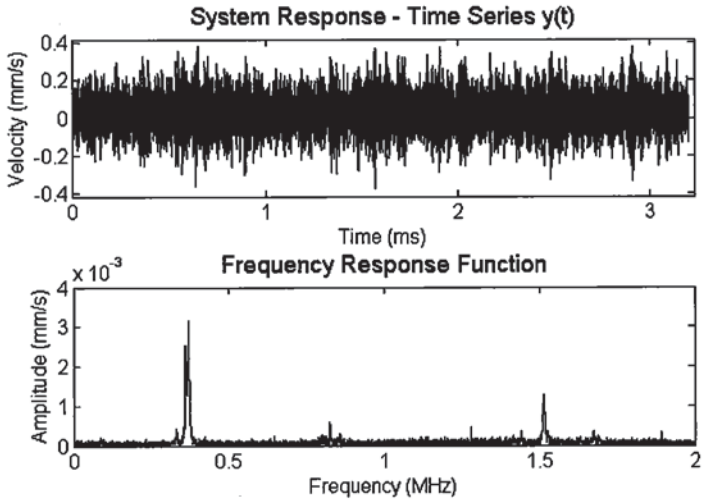

Figure 4.8: An example of microplate experimental data

4.4 Experimental Modal Analysis

4.4.1 Modal Analysis Procedures

The aim of experimental modal analysis is to determine the modal parameters (natural frequencies, modal damping ratios and mode shapes) from experimental data. As the vibration of a microplate either *in air* or *in water* is a fairly linear, time-invariant system, the modal parameters at each resonant mode are essential to describe the dynamic characteristics of microplate. The FRFs the resonant modes of a testing microplate become evident and the corresponding resonant frequencies can be directly obtained. On the other hand, modal damping ratios and modal constants (mode shapes) are more difficult to obtain[130], because the results can be easily affected by local perturbations of the original signal. Therefore further process and calculation are required to obtain more accurate modal parameters. The FRF spectrum in Figure 4.8 as an example is based on the absolute motion of a microplate, however it is not appropriate for implementing conventional modal analysis methods.

Figure 4.9 illustrates the significant errors of modal parameters, especially on the damping ratios, when directly applied modal evaluation on the absolute motion based FFT spectrum. According to the theoretical analysis presented in section 4.3.1, the direct output of FFT has to be transformed into the form of relative motion (Eq. 4.12) in order to obtain an ordinary vibration model (Eq. 4.10) of the base-excited microplate. The denominator in the frequency response function of Eq. 4.11 is the *complex characteristic equation* of vibration system[71]. The *complex roots (complex poles)* of this equation are highly related to each modal frequencies and modal dampings. A particular element in the matrix function of $[H(\omega)]$ can also be rewritten in terms of the complex poles[67].

$$H_{mn}(\omega) = \sum_{r=1}^{k} \frac{A_{mn}^{r}}{i\omega - p_r} + \frac{A_{mn}^{r*}}{i\omega - p_r^*} \tag{4.16}$$

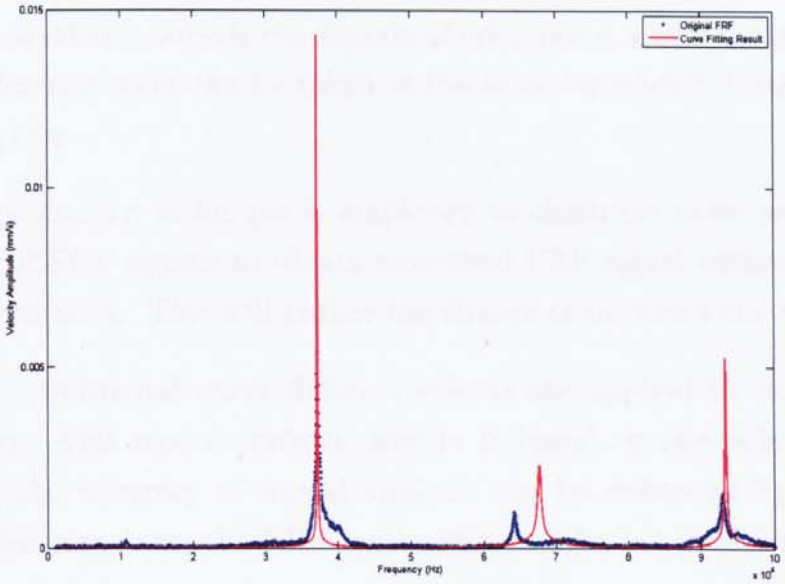

Figure 4.9: An incorrect curve fitting result with using the FRF spectrum of absolute motion

where A_{mn}^{r} is modal residue (modal constant) and p_r is the modal pole.

The work of modal analysis (modal parameters extraction) is to match the mathematical model of Eq. 4.16 with the experimental data and determine the unknown coefficients using *curve fitting* techniques. A schematic diagram in Figure 4.10 shows the signal process procedures for modal parameter extraction in this base-excitation dynamical experiments of microplates. The whole process of modal analysis is divided into four phases:

a) The measured system outputs are entered in a cross-correlator to obtain the FFT of the absolute motion. This work can be automatically finished in the laser vibrometer MSV-400.

b) Both magnitude and phase components of the complex FFT of a particular testing point, are then transfered into a form of relative motion refer to the Eq. 4.12. A FFT spectrum of excited base is required as the reference of base

motion in this transformation. The base-reference point is usually defined on the silicon die that is outside the domain of microplate, where the measurement of base-reference point can be taken at the same time when testing scanning the microplate.

c) A signal processing technique is employed to eliminate noise and local disturbances of FRF signals to obtain smoothed FRF signal without losing the modal information. This will reduce the chance of incorrect curve fitting.

d) Eventually traditional curve fitting methods are applied to extract modal parameters. This modal analysis process is based on one-point FRF measurement, the accuracy of modal analysis can be enhanced by performing modal estimation from the FRF measurements of a set points or the whole microplate-domain.

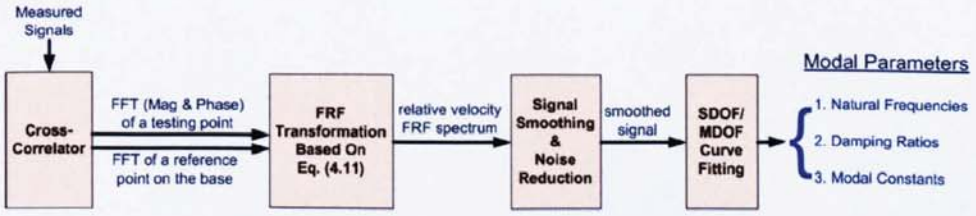

Figure 4.10: Experimental modal analysis procedures

4.4.2 Signal Smoothing and Noise Reduction

An order 3 polynomial SavitzkyGolay smoothing filter is chosen to execute an initial curve matching and reduce noise of the transformed FRF signals. The FRF signals of dynamic microplate usually contains very high frequency components (up to MHz) and has a very large frequency span. The Savitzky-Golay filtering method is believed to be better to process frequency-based signals than standard averaging FIR filters, which would suppress some modal information of the FRF signals. The main advantage of SavitzkyGolay filter is that it is able to preserve the high-frequency components of the signal. The frame size of this filter is set at

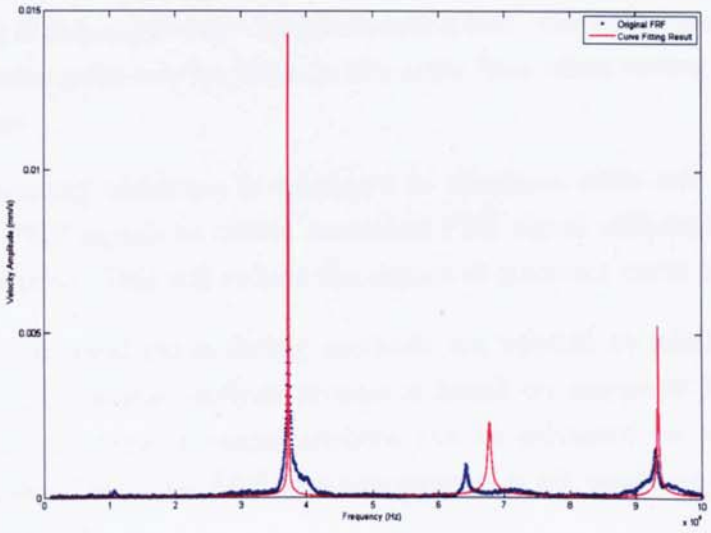

Figure 4.9: An incorrect curve fitting result with using the FRF spectrum of absolute motion

where A_{mn}^{r} is modal residue (modal constant) and p_r is the modal pole.

The work of modal analysis (modal parameters extraction) is to match the mathematical model of Eq. 4.16 with the experimental data and determine the unknown coefficients using *curve fitting* techniques. A schematic diagram in Figure 4.10 shows the signal process procedures for modal parameter extraction in this base-excitation dynamical experiments of microplates. The whole process of modal analysis is divided into four phases:

a) The measured system outputs are entered in a cross-correlator to obtain the FFT of the absolute motion. This work can be automatically finished in the laser vibrometer MSV-400.

b) Both magnitude and phase components of the complex FFT of a particular testing point, are then transfered into a form of relative motion refer to the Eq. 4.12. A FFT spectrum of excited base is required as the reference of base

motion in this transformation. The base-reference point is usually defined on the silicon die that is outside the domain of microplate, where the measurement of base-reference point can be taken at the same time when testing scanning the microplate.

c) A signal processing technique is employed to eliminate noise and local disturbances of FRF signals to obtain smoothed FRF signal without losing the modal information. This will reduce the chance of incorrect curve fitting.

d) Eventually traditional curve fitting methods are applied to extract modal parameters. This modal analysis process is based on one-point FRF measurement, the accuracy of modal analysis can be enhanced by performing modal estimation from the FRF measurements of a set points or the whole microplate-domain.

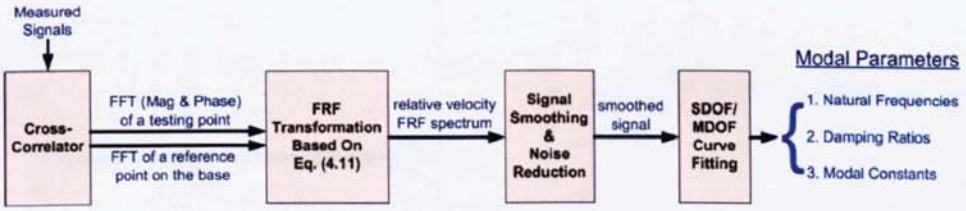

Figure 4.10: Experimental modal analysis procedures

4.4.2 Signal Smoothing and Noise Reduction

An order 3 polynomial SavitzkyGolay smoothing filter is chosen to execute an initial curve matching and reduce noise of the transformed FRF signals. The FRF signals of dynamic microplate usually contains very high frequency components (up to MHz) and has a very large frequency span. The Savitzky-Golay filtering method is believed to be better to process frequency-based signals than standard averaging FIR filters, which would suppress some modal information of the FRF signals. The main advantage of SavitzkyGolay filter is that it is able to preserve the high-frequency components of the signal. The frame size of this filter is set at

7. Few measured FRF samples are used to experimentally test the performance of these parameters of this filter, which are shown in Figure 4.11. Plots (a-i) and (a-ii) are real and imaginary parts of the relative FRF spectrum of a $300\mu m$ C-C-C-C microplate *in air*, respectively. (b-i) and (b-ii) are the same plots but for the microplate immersed *in water*. It can be seen that a smooth curve is produced and noise is also suppressed in each of these fitting results. In the meanwhile some of noise components and fake resonant peaks are still remaining after the SavitzkyGolay filtering. Smoothed signal with less noise can be obtained by setting a higher frame size, but more modal information around the resonant peak would be lost. In the next step, modal analysis method with noise immunization capability is required.

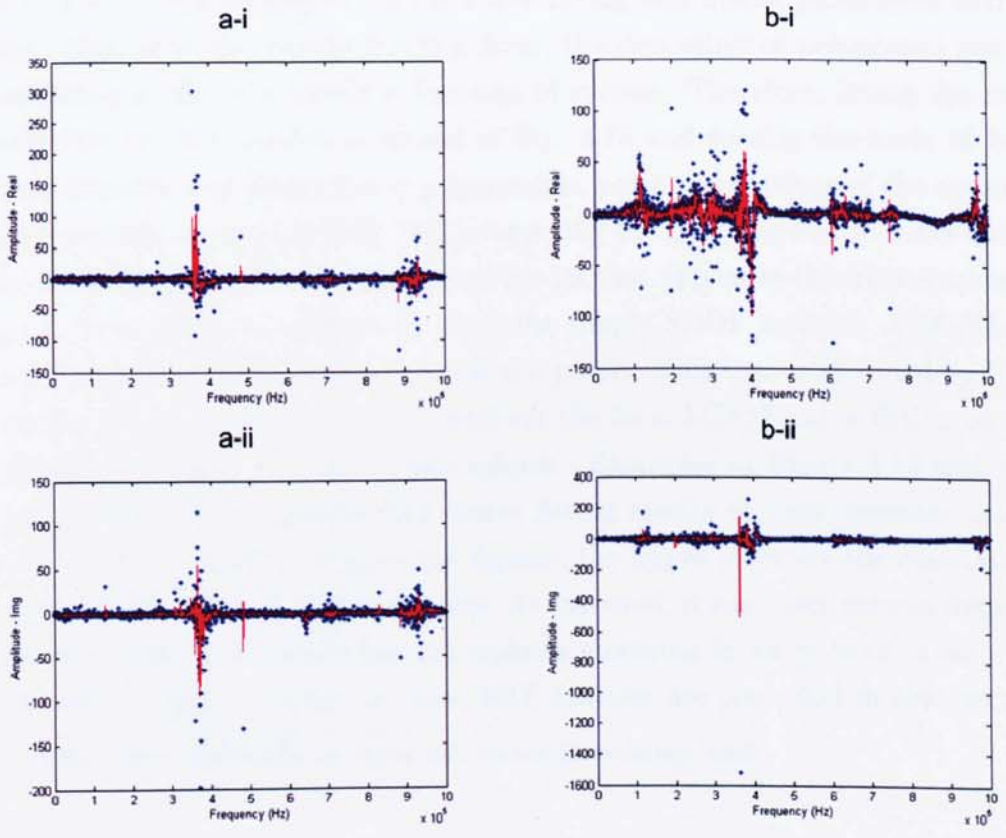

Figure 4.11: Example samples of signal smoothing

4.4.3 Modal Parameters Estimation

Numerous curve fitting methods have been developed to estimate structural modal parameters in the frequency domain using FRF measurements, and they can be categorized as four types: Local SDOF, Local MDOF, Global and PolyReference[131]. In this section SDOF or MDOF methods are introduced to evaluate modal parameters.

The Local SDOF curve fitting method is only applied on one FRF measurement of a selected testing point and individually analyses the parameters of each resonant mode that dominantly appears in the FRF plot[131]. A process of simply SDOF fitting employed in this work is illustrated in Figure 4.12, in which the modal frequency is approximately evaluated as the center frequency (f_n) at resonance peak of imaginary FRF spectrum and the modal damping ratio is estimated by using the following formulation Eq. 4.17. The signal sample in Figure 4.12 is taken from the segment of around the first mode of a $300\mu m$ C-F-F-F microplate FRF spectrum. Both the real and imaginary trends in this sample are clear and easy to identify, as they are close to the theoretical forms.

As mentioned previously, vibration shapes of the testing microplate at each frequency can be automatically reconstructed in the software provided by MSV-400. The vibration shape at each frequency peak can be used to identify and eliminate the fake resonance modes, as well as to more accurately localize the resonance frequencies. Approximate resonant frequencies and damping ratios can be determined in the simply process of SDOF modal analysis.

$$\zeta = \frac{f_r - f_l}{2f_n} \tag{4.17}$$

The MDOF curve fitting method used in this thesis is called Rational Fraction Polynomials (RFP), which is developed by M. H. Richardson and D. L. Formenti[75]. Rather than using the partial fraction form of Eq. 4.16 to present the mathematical model of FRF, a rational fraction form of two polynomials

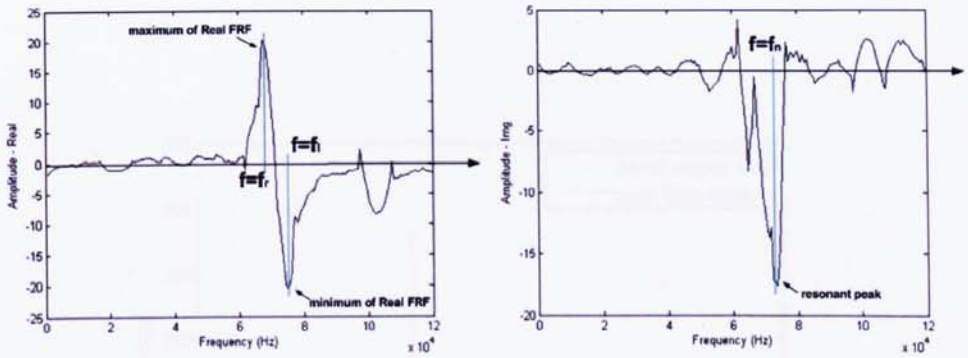

Figure 4.12: Simply SDOF modal analysis

as in Eq. 4.18 is developed for the curve fitting and modal parameters extraction. Similar to the partial fraction form, the denominator polynomial can be considered as the characteristic function of system. Therefore, fitting the measured data to this analytical model of Eq. 4.18 and solving the roots of both the numerator and denominator polynomials, poles and residues of the dynamic system can be determined[75]. Before applying the RFP method to curve fitting the experimental FRFs, the number of modes that appear in the frequency band has to be specified in advance by using the simply SDOF method. A MATLAB program of RFP method using orthogonal polynomials that is provided by Cristian Gutierrez Acuna[1], is used to perform the local MDOF curve fitting on the dynamic experimental data of microplates. Examples in Figure 4.13 and 4.14 demonstrate that acceptable RFP curve fitting results at most resonant modes were achieved. In both of these two figures, the upper plots are the case testing *in air* and the lower plots are *in water*. As expected, it has lower natural frequencies and higher dampings when microplates vibrating in water than in air. The obtained modal parameters of these FRF samples are presented in next section

[1]http://www.mathworks.co.uk/matlabcentral/fileexchange/3805

and used to validate the theoretical model.

$$H(\omega) = \frac{\sum_{k=0}^{m} a_k (j\omega)^k}{\sum_{k=0}^{n} b_k (j\omega)^k} \tag{4.18}$$

4.5 Validation of Theoretical Model

The resonant frequencies and mode shapes of the fluid-loaded microplate are obtained by numerically solving. The densities of air and water are assumed to be constant, and equal to $\rho_a = 1.225 kg/m^3$ and $\rho_w = 1000 kg/m^3$ respectively. The material properties of the silicon plate are listed in the Table 4.1.

The numerical results and The experimental results of three different types of micro scale plates are presented and compared in Tables 4.3, 4.4, 4.5 and 4.6. Although these three microplates were all designed to be $300 \mu m$, the length and width of each microplates are not the designed value due to the nature of microfabrication process. Most data set of natural frequencies shows a good agreement between the numerical and experimental results. However there are few cases of large derivations in the data of natural frequencies of Type C-F-C-F and Type C-C-C-C plates. One main reason is that the rectangular corners of microplates along the clamped edges can not exactly satisfy design requirements due to limitations of the microfabrication processes. On the other hand, the experimental results and corresponding theoretical predictions on damping ratios in Table 4.6 are only at the same order of quantities, which hard to be accurately matched. It is mainly due to that the damping ratios measurement are easily effected by ambient noise and system errors. Nevertheless both numerical results and experimental results reveal that high resonant modes of microplate suffer less damping, which is related to the high Q-factors.

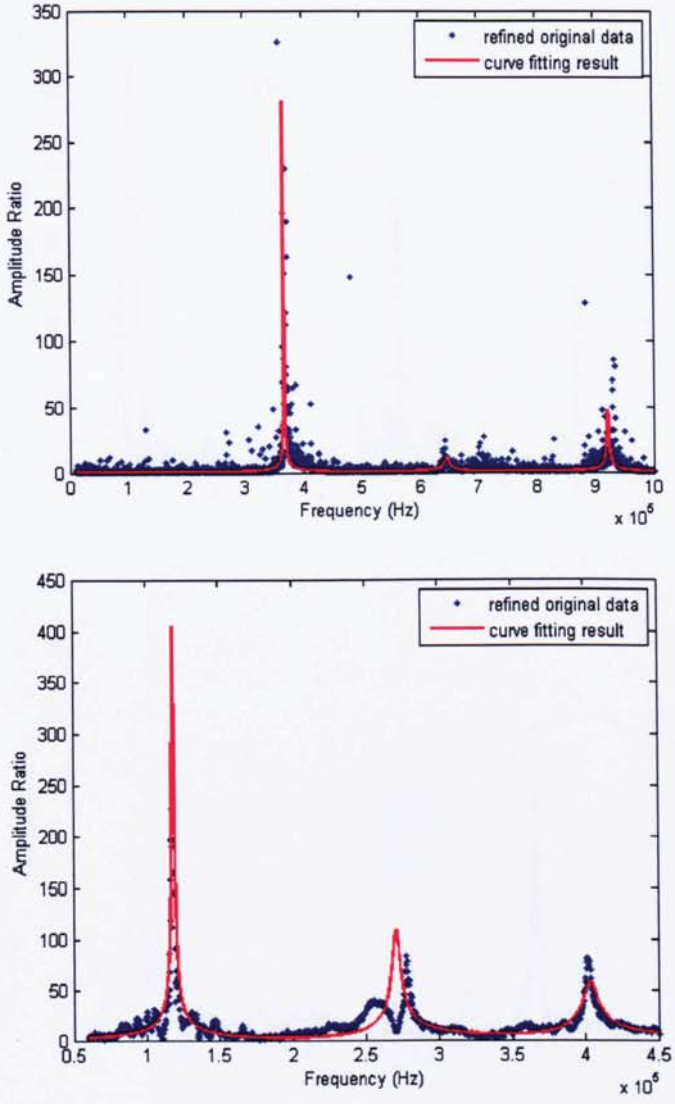

Figure 4.13: Curve fitting results of microplates (C-F-C-F) experimental data by using RFP methods (the upper plot is *in air* and the lower plot is *in water*)

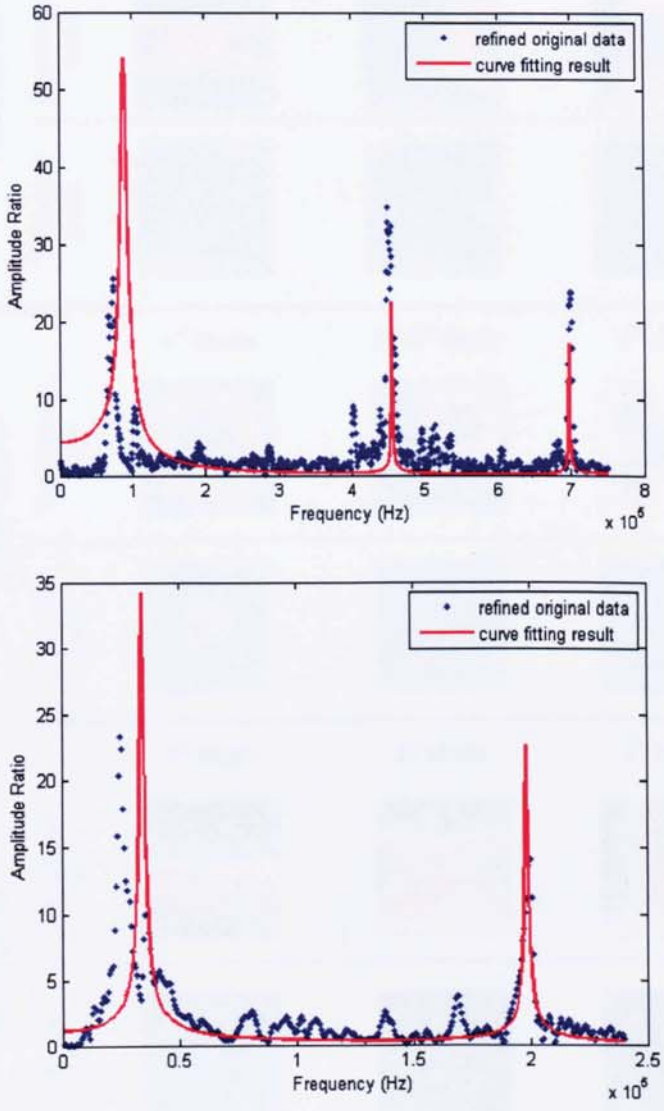

Figure 4.14: Curve fitting results of microplates (C-F-F-F) experimental data by using RFP methods (the upper plot is *in air* and the lower plot is *in water*)

Table 4.3: Theoretical and experimental results on natural frequencies of a C-F-C-F microplate(kHz)

	In Vacuo	In Air		In Water	
Modes		Theo.	Expe.	Theo.	Expe.
1st	436.80	433.3	371.87	130.40	117.2
2nd	537.59	534.5	542.19	227.98	278.1
3rd	911.98	909.6	929.06	453.65	405.0

Table 4.4: Theoretical and experimental results on natural frequencies of a C-F-F-F microplate(kHz)

	In Vacuo	In Air		In Water	
Modes		Theo.	Expe.	Theo.	Expe.
1st	75.9	75.4	73.1	23.9	25.0
2nd	195.3	194.8	191.9	84.5	-
3rd	475.7	474.1	464.4	199.9	200.0

Figures 4.15 $\sim$ 4.23 show the raw data of velocity based frequency response function of a series of microplates in air or in water (the three different types on $200\mu m, 300\mu m, 400\mu m$). The first few modes of in air or in water were labeled in these plots respectively.

As the whole domain of the microplates have been scanned in each experiment, the vibration mode shapes of microplates can be constructed. Figure 4.24 shows the comparison of wet mode shapes (in water) of each type of microplates from the theoretical analysis and experimental measurement respectively. It can be seen that the mode shapes derived from the theoretical analysis agree well with those from the experimental testing.

Table 4.5: Theoretical and experimental results on natural frequencies of a C-C-C-C microplate(kHz)

	In Vacuo	In Air		In Water	
Modes		Theo.	Expe.	Theo.	Expe.
1st	523.08	519.67	460.0	152.67	153.44
2nd	1065.8	1062.6	1018.1	436.44	445.3
4th	1581.3	1577.8	1542.8	733.78	793.75

Table 4.6: Theoretical and experimental results on damping ratios of the three types of microplates

	C-F-F-F		C-F-C-F		C-C-C-C	
Modes	Theo.	Expe.	Theo.	Expe.	Theo.	Expe.
1st	2.83%	2.13%	2.38%	1.47%	3.21%	1.81%
2nd	-	-	0.21%	0.27%	0.20%	0.32%
3rd(4th)	0.38%	0.26%	0.17%	0.18%	0.02%	0.08%

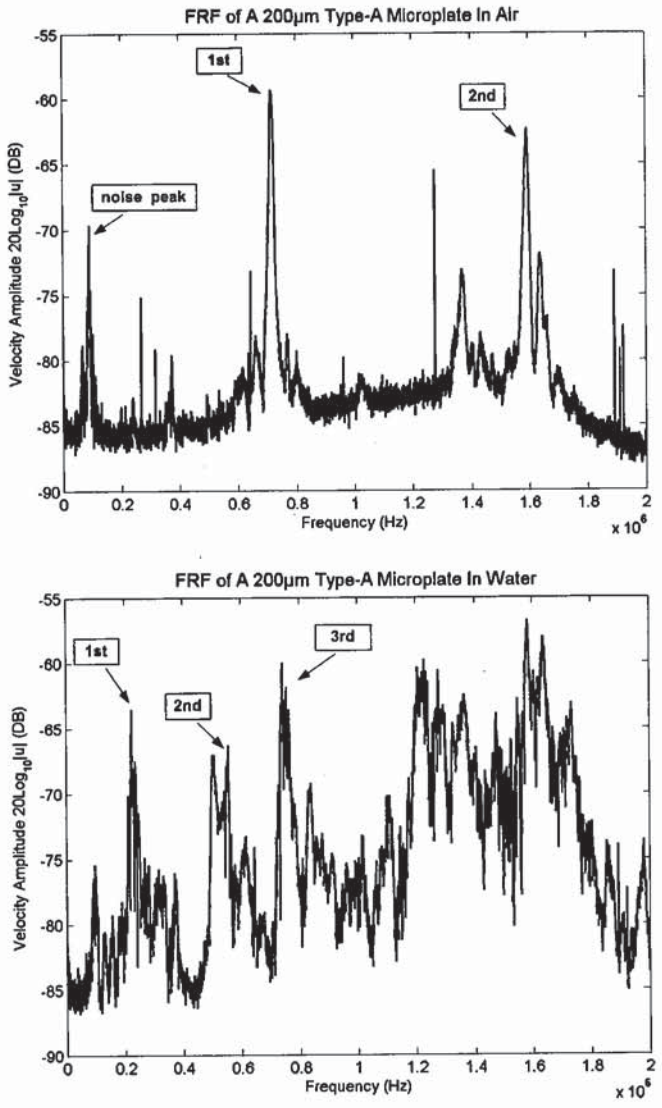

Figure 4.15: Original measured FRFs of a $200\mu m$ C-F-C-F microplate

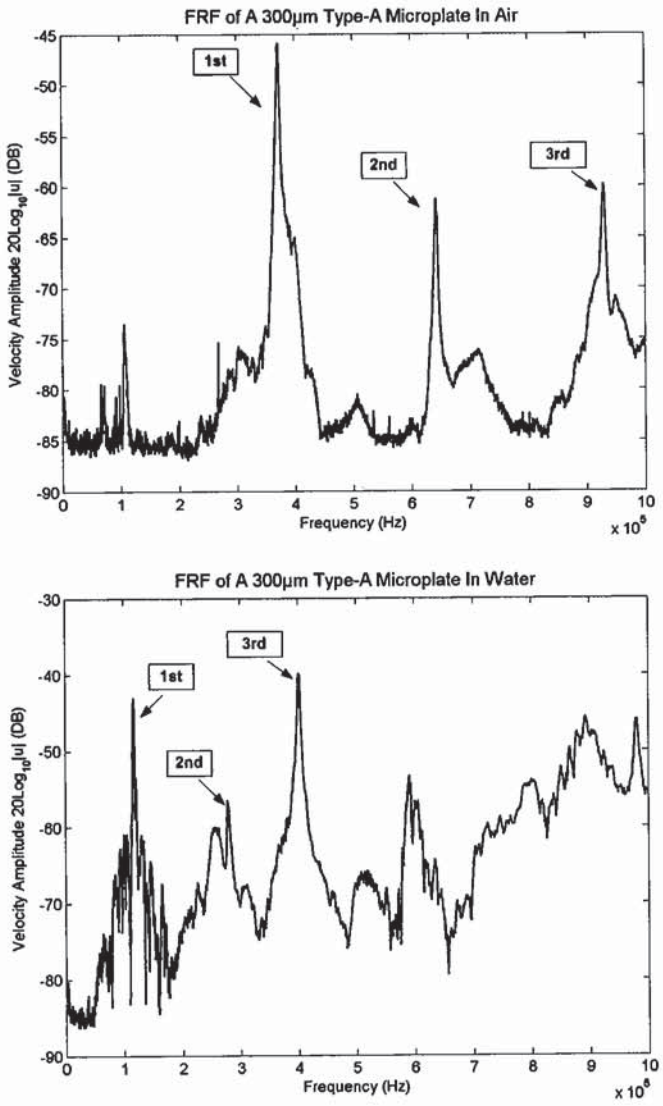

Figure 4.16: Original measured FRFs of a $300\mu m$ C-F-C-F microplate

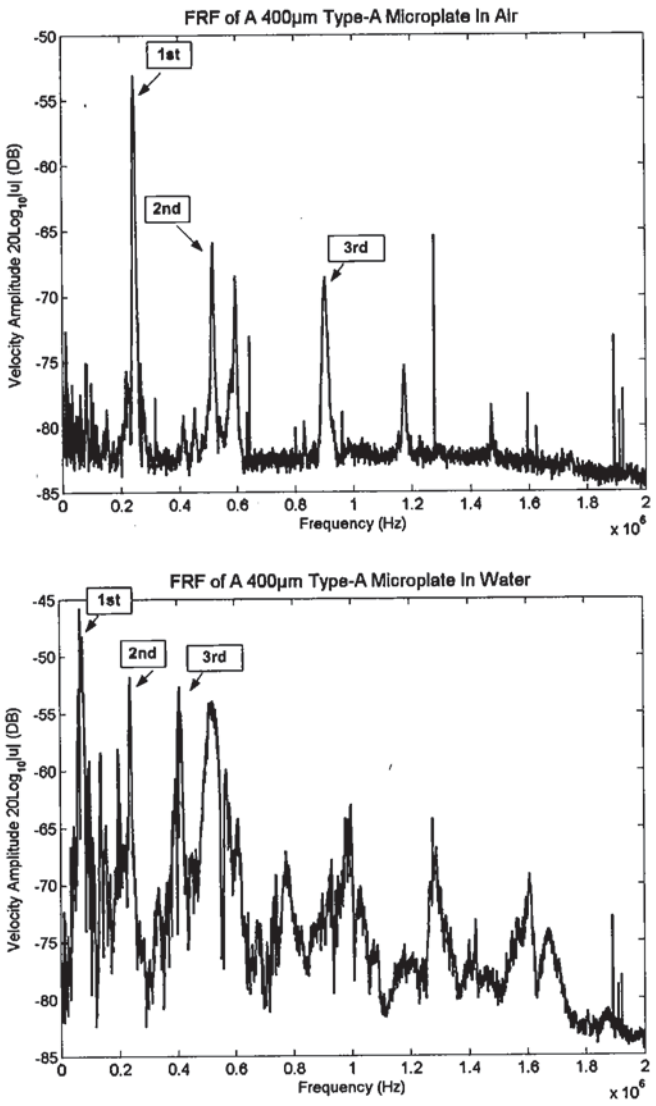

Figure 4.17: Original measured FRFs of a $400\mu m$ C-F-C-F microplate

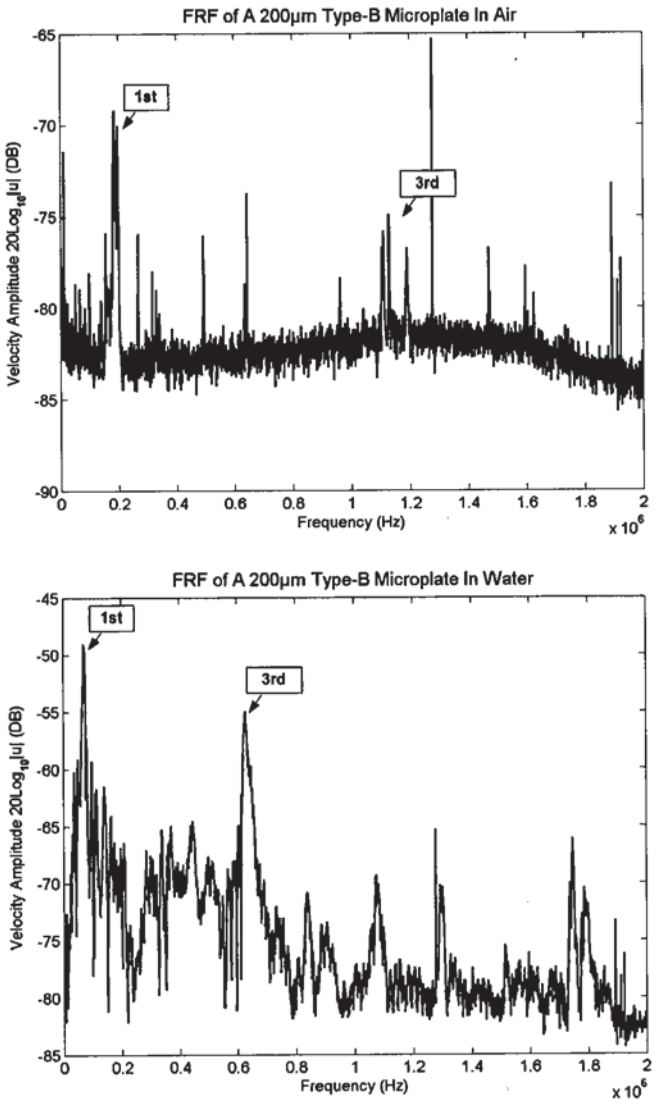

Figure 4.18: Original measured FRFs of a $200\mu m$ C-F-F-F microplate

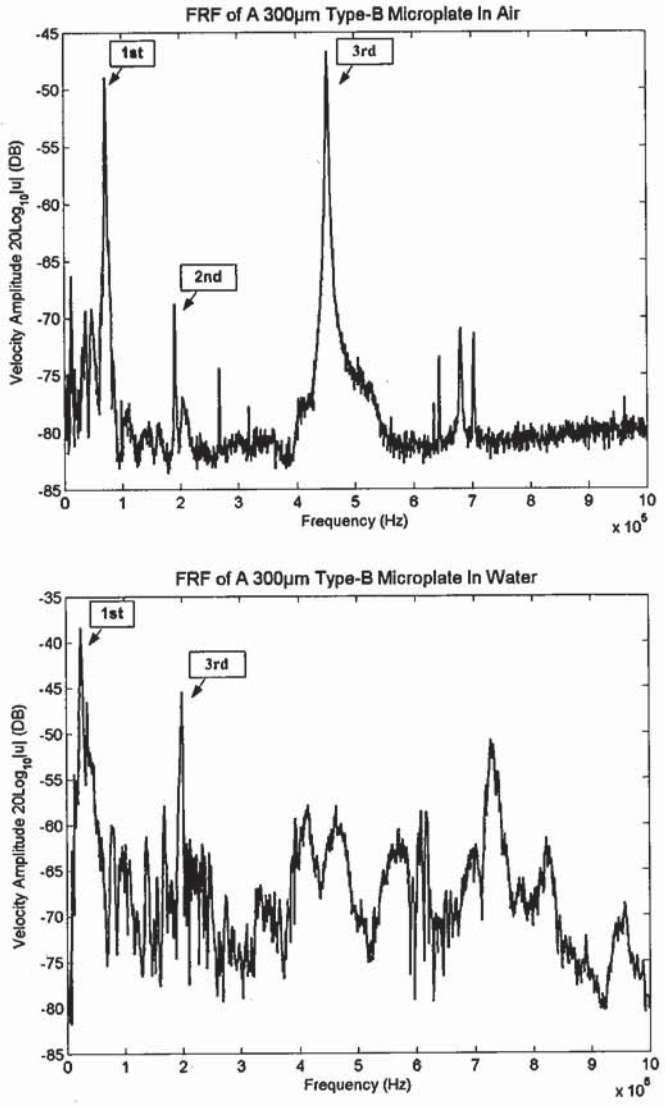

Figure 4.19: Original measured FRFs of a $300\mu m$ C-F-F-F microplate

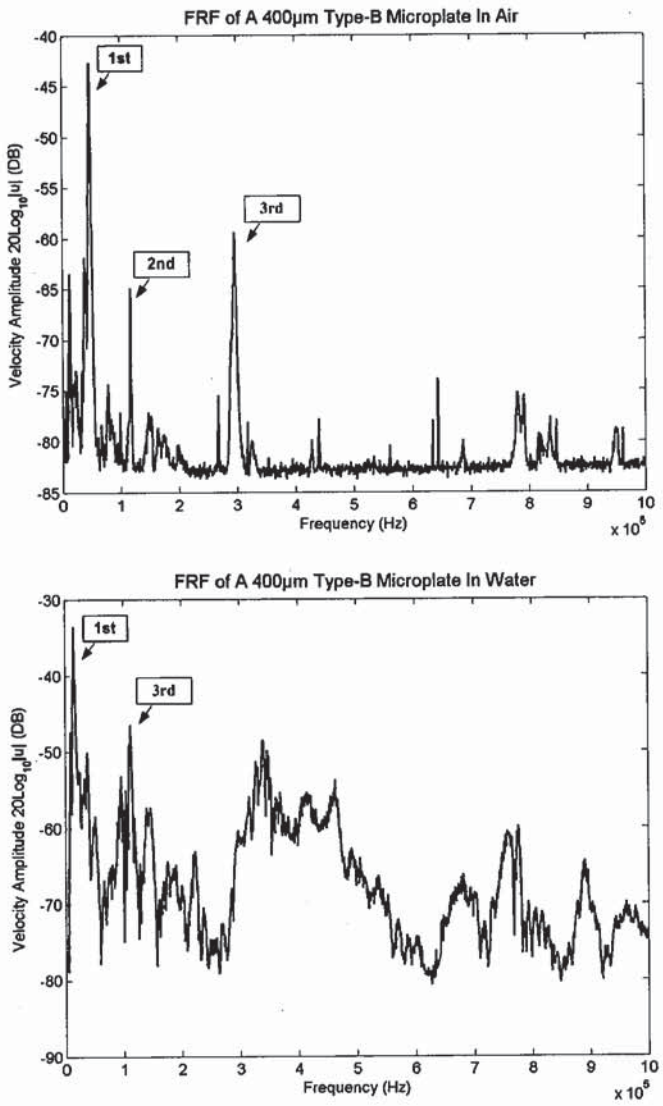

Figure 4.20: Original measured FRFs of a $400\mu m$ C-F-F-F microplate

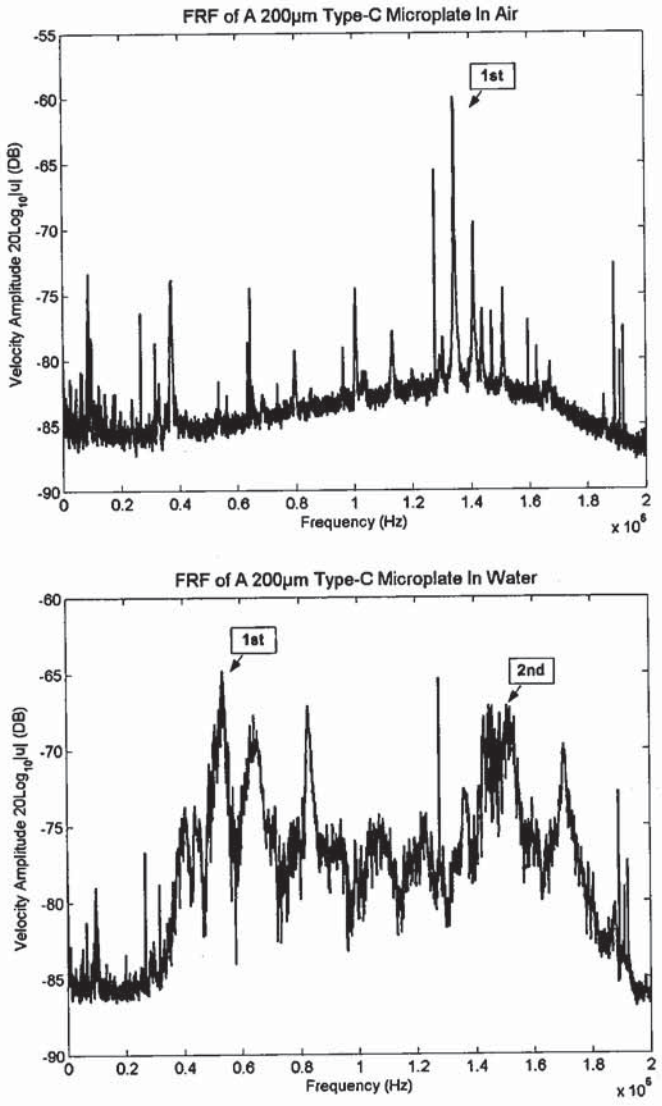

Figure 4.21: Original measured FRFs of a $200\mu m$ C-C-C-C microplate

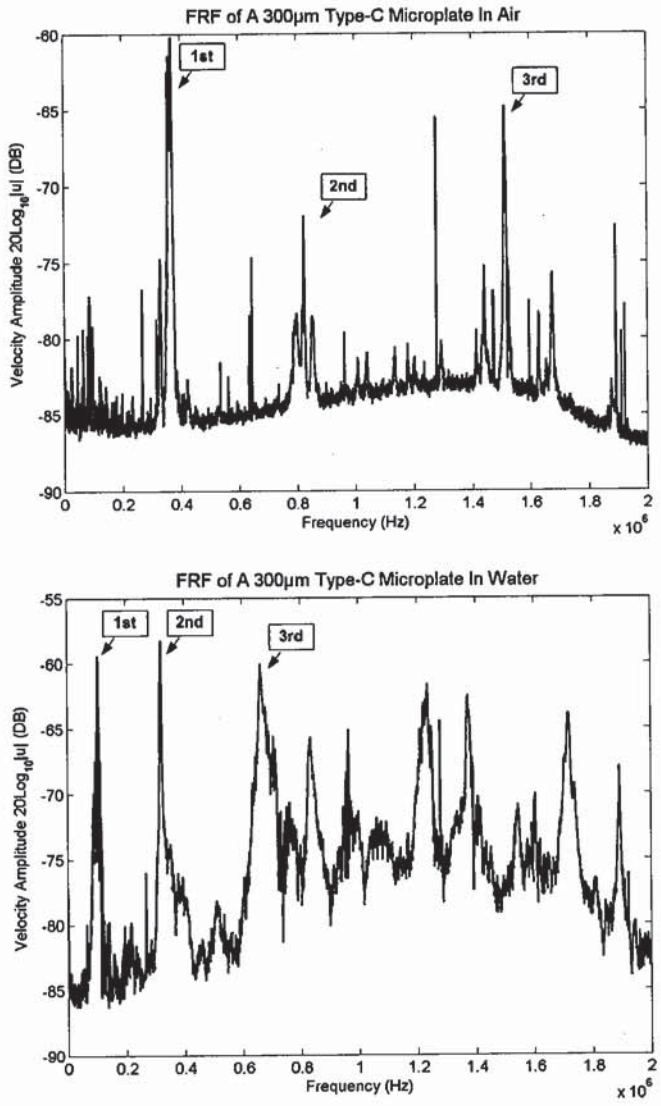

Figure 4.22: Original measured FRFs of a $300\mu m$ C-C-C-C microplate

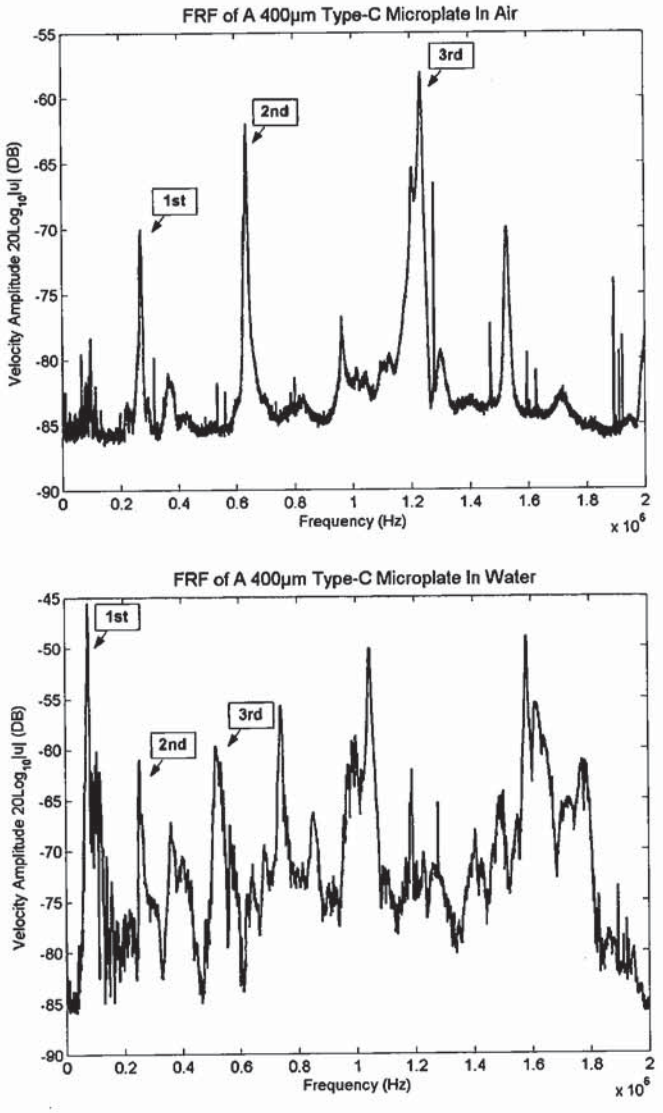

Figure 4.23: Original measured FRFs of a $400\mu m$ C-C-C-C microplate

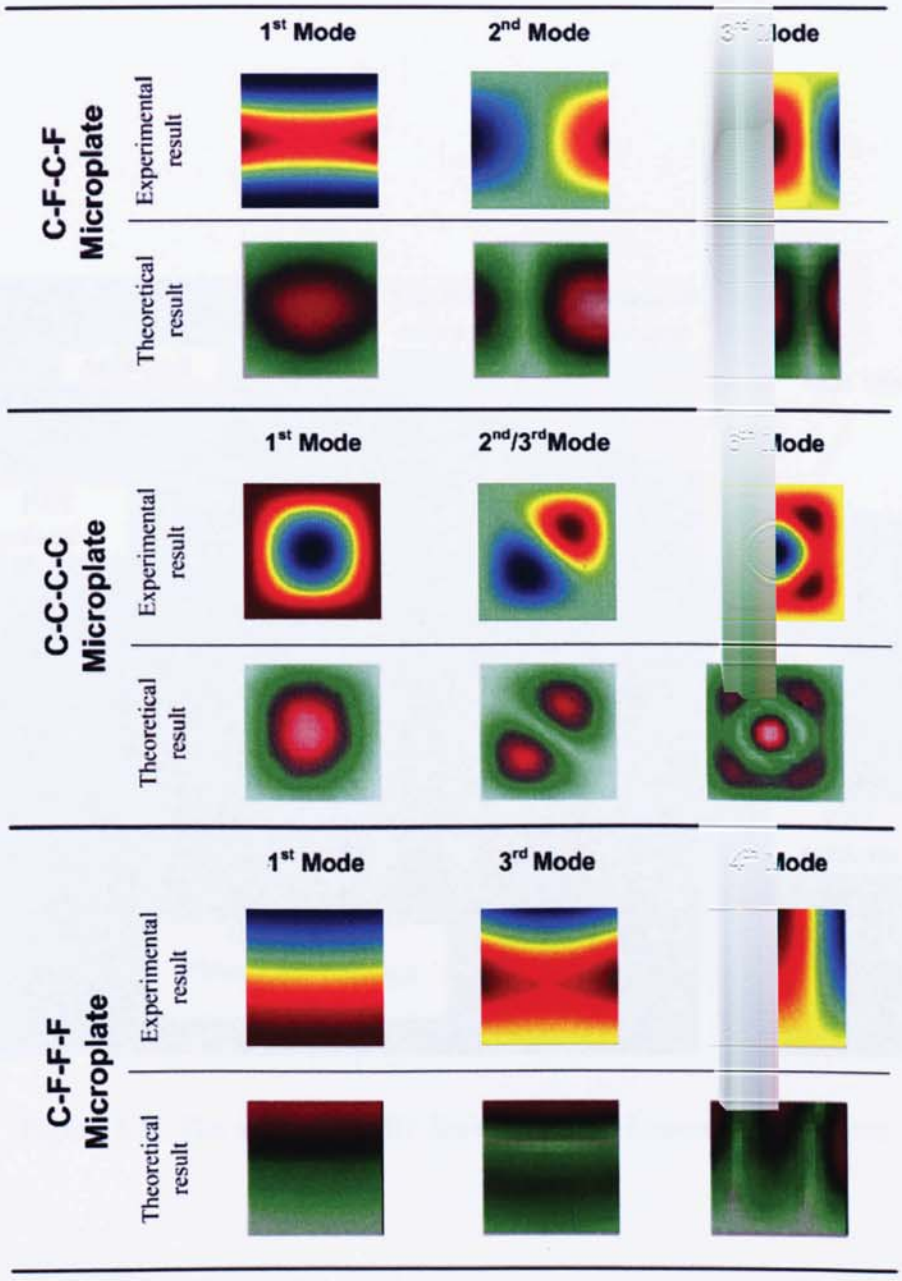

Figure 4.24: Theoretical and experimental mode shapes comparison of three $300\mu m \times 300\mu m \times 5\mu m$ immersed microplates

4.6 Conclusion

Both theory and apparatus design of the base-excitation experiments on the dynamics testing of microplates had been presented in this chapter. The function of pseudo-random excitation signal and cross-correlation techniques in the modal testing were studied in the application of microplate testing. Lastly, different curve fitting approaches were applied to extract modal parameters that include resonant frequencies, modal damping ratios and modal constants from the measured FRF spectrums.

Although there are many published works that have successfully used base-excitation system to study the dynamics of microstructures, most of those experiments were usually implemented in a very ideal environment - vacuo or very low air pressure. The work presented in this chapter is the first time to apply base-excitation technique together with a well-designed pseudo-random excitation signal in the dynamic testing of fluid-loaded micro-structures. It proves again that the base-excitation method is able to stimulate the dynamic information of microstructures in a normal damping ambient (in air), or even under a very high damping circumstance (in water). It also demonstrates the distinct advantages of using pseudo-random excitation signal in the process of experimental testing of microstructures.

A series of different types and sizes of microplates were tested, measured and analysed in this work, both *in air* and *in water*. The modal parameters (natural frequencies, mode shapes and damping ratios) of fluid-loaded microplates extracted from experimental FRF measurements are compared with the theoretical results, and they matched very well. Additionally, the obtained experimental data provide important information to fully understand the dynamic characteristics of fluid-load microplates, and are also very useful in the design of related microsystems. Finally it comes to the conclusion that the proposed experimental system and methodologies provide a convenient and fast way in the field of dynamics testing of microstructures.

Chapter 5

Design and manufacture of a microplate-based biosensing system

5.1 Introduction

This chapter is aimed to design a new integrated biosensing platform for discriminating biological cells' property or behaviour. The developed biosensing system is able to work independently and can be integrated into a CMOS circuit to form a lab-on-chip system. The sensing system employs a microplate (thin membrane) with different configurations as the transducer. There are five different types of platform that have been designed in this chapter, with varying boundary conditions (clamped, free or point supported), different excitation and sensing locations. The biosensing platform uses the variation of its dynamic characteristics as the information source to sense the properties of the surface-contact biological cells and particles. The sensing system is designed to be capable of self-excitation

(actuators) and self-sensing (sensors). The microplate (membrane) in this system could be excited by the sinusoidal function or a wide frequency band random signal (white noise, pseudo random and burst random, etc) due to different implementation purposes.

During design process, Finite-element analysis (FEA) of microsystems is performed to determine the dimensions of microplates, actuators and sensors. Further FEM simulations on the whole microsystems are also carried out to examine the performance of these microsystems before fabrication.

Advanced microfabrication tools and techniques are used for the manufacture of these microsystems. Most processes are implemented in the Scottish Microelectronics Center. Section 5.4 gives a brief description on these fabrication processes and the corresponding techniques used in each step.

5.2 The Microsystem Design

Figure 5.1 shows the 3-D schematic view of one of proposed microsystems. The microplate is a thin membrane which acts as a micro-scale sensing platform. The microplate is deformable and has dimensions in the range of hundreds of microns in the X- and Y-directions. The thickness of microplate in the Z-direction is about 3 μm. The microplate illustrated in Figure 5.1 is supported by four hinges, each hinge is located centrally along a respective one of the four sides of the microplate. This is one example of the microplate boundary conditions. The microplate may be supported by means of a variety of different boundary conditions to achieve different sensitivities and biosensing purposes (e.g. clamped, cantilever, free and point supported, etc.). Figures 5.2 and 5.3 list all the design sketches on 5 different types of microsystems fabricated in this work.

Actuators are required to excite the microplate into vibration in a cell culture medium. The actuators in the microsystem are two PZT (Lead Zirconate Ti-

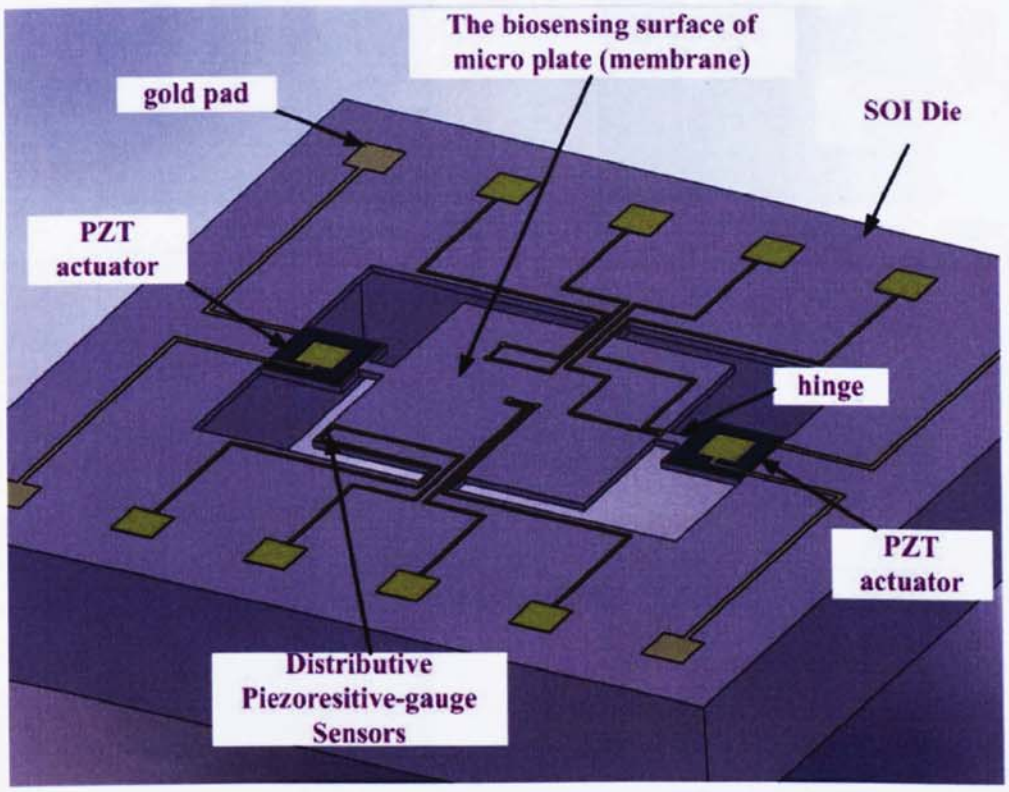

Figure 5.1: The schematic 3D drawing of the biosensing platform

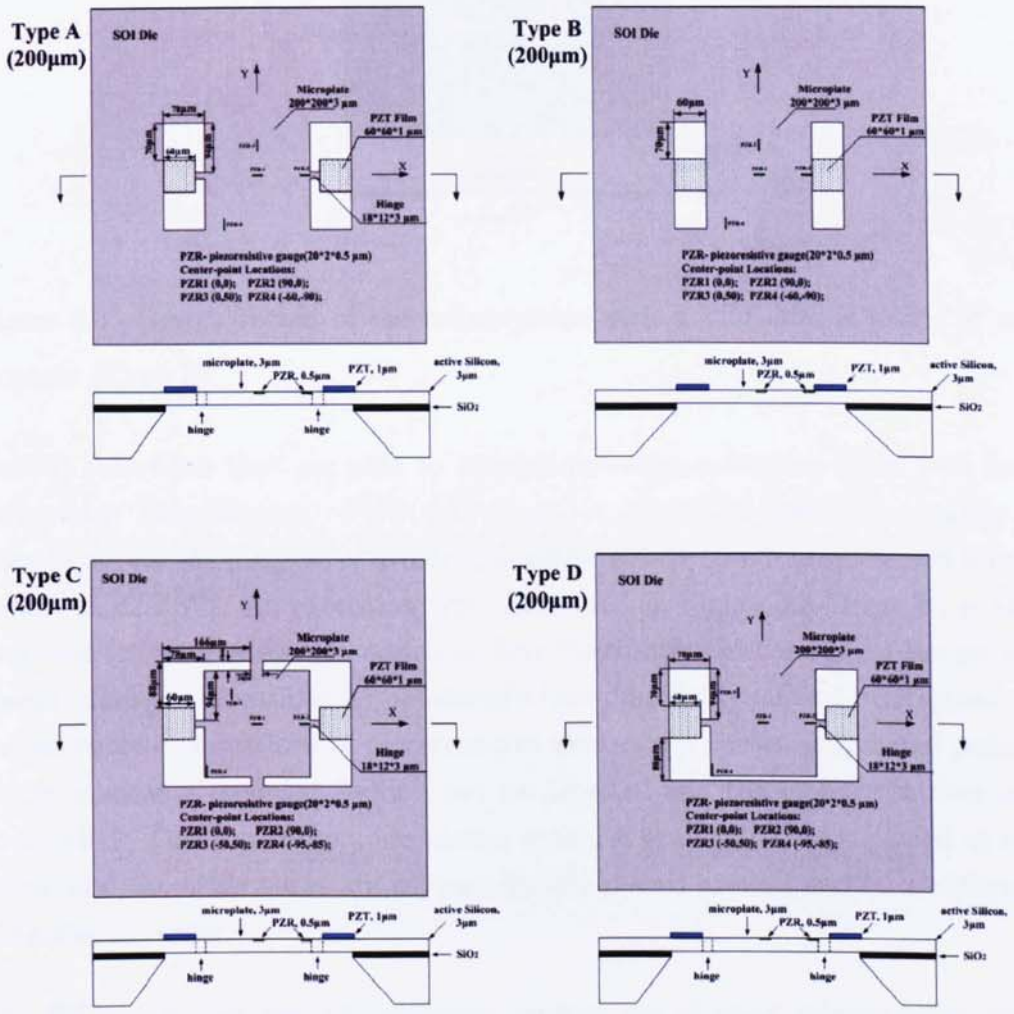

Figure 5.2: Design sketches of four different types of microsystems with PZT films beside microplate (Type A $\sim$ Type D)

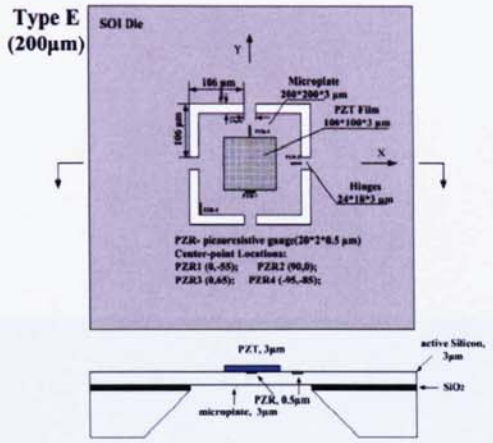

Figure 5.3: Design sketch of the microsystem with a PZT film is inside of microplate (Type E)

tanate) thin films that are able to provide powerful excitation force with limited energy consumption. PZT thin films are deposited beside the region of microplate, for the purpose of avoiding negative effects (residual stress and initial strain) of PZT[79]. An exception type illustrated in Figure 5.3 (Type E) is also proposed for comparison. In addition, four distributive piezoresistive gauges are placed at selected locations for obtaining whole-domain dynamical information of the microplate. Locations of piezoresistive sensors are chosen at optimal points, where maximum modal deflection can be detected and the modal contours can be avoided. The four sensors are always schemed such that one is placed at the center and the other three are asymmetrically placed around and have different distances to center.

The PZT actuators and piezoresistive sensors are of good compatibility with CMOS circuits and could be easily integrated with other electronic components. The electronic part of this system (electrode wires, gold pads, and connecting probes) are sealed with biocompatible material. The whole platform is packaged using standard DIL (Dual in-line) technique. The signal flow (input and output signals) would be processed either through external instruments or internal electronic chips.

The surface is in the form of a $100 \sim 300\mu m$ square microplate and its materials (silicon, gold wires and PZT etc) are biocompatible. The microsystem is designed to be able to work in fluid (water) with an acceptable bio-sensitivity under the high damping conditions. Therefore the platform could be either single-sidely or double-sidely immersed in cell culture media to maintain the natural cell living environment.

5.3 Actuators and Sensors

Key components in the integrated microsystem are PZT films and piezoresistive gauges, which provide the functions of vibration excitation (actuator) and detection (sensor) respectively and can determine the performance of microsystem. Simulations on PZT films and piezoresistive gauges are separately carried out using finite-element method and theoretical model. The electromechanical coupling factors and sensitivity obtained from the simulation results are then used to optimize the design parameters of the PZT films and piezoresistive gauges, respectively.

5.3.1 PZT thin film

PZT film is one of piezoelectric material that has been widely used for microactuators in MEMS. As PZT has a much larger piezoelectric coefficient (d_{33}) than other piezoelectric materials such as aluminum nitride (AlN) or zinc oxide (ZnO)[85], it is excellent for excitation in microsystems. Usually a PZT thin film actuator has multiple layers sandwiched between two electrode layers on the silicon membrane. During the process of PZT thin film actuation, the electrical energy applied is converted into mechanical energy. Therefore the work efficiency of PZT based actuator can be indicated by the ratio of energy conversion. This ratio is also called effective electromechanical coupling factor k. In a certain vibrational

mode, the resonance and anti-resonance frequencies of this multi-layer structure can be used to indicate the electromechanical coupling factor. The definition of k is given in the following form[88].

$$k^2 = \frac{f_a^2 - f_r^2}{f_a^2} \tag{5.1}$$

where f_r is resonant frequency and f_a is anti-resonant frequency.

Obviously, the electromechanical coupling factor k will be affected by the actuator geometry. The aspect ratio between PZT thin film and the silicon substrate needs to be studied in order to obtain a high electromechanical coupling factor.

The finite element models for the whole microsystem were built in ANSYS to optimize the design parameters of PZT thin films. To simplify the model and concentrate on the study of PZT thin films, the top and bottom metal electrode layers and piezoresistive gauges are ignored and only the microplate part is considered. The physical/mechanical parameters of silicon microplate in the simulation are the same as those in the theoretical model in chapter 3, while PZT-4 material with Z-polarization was selected for the PZT thin film in this ANSYS model and the corresponding piezoelectric matrix is formed (refer to VM231). ANSYS APDL source codes for the FEM model of one type microsystem are attached in appendix C, all other models were also built with a similar way in this work. In the codes, three different analyses (modal analysis, static deformation analysis and harmonic motion analysis) are respectively defined and executed.

Figure 5.4 shows an initial static deformation analysis of the microsystem when apply an $5V$ electric field to both of the PZT films. It proves that the side-placed PZT thin films can produce sufficient deformations on the microplate.

Figure 5.5 shows the frequency response function at the center of microplate obtained from harmonic analysis on the FEM model. The resonant frequencies can be clearly identified from this FRF plot, which verifies that the proposed

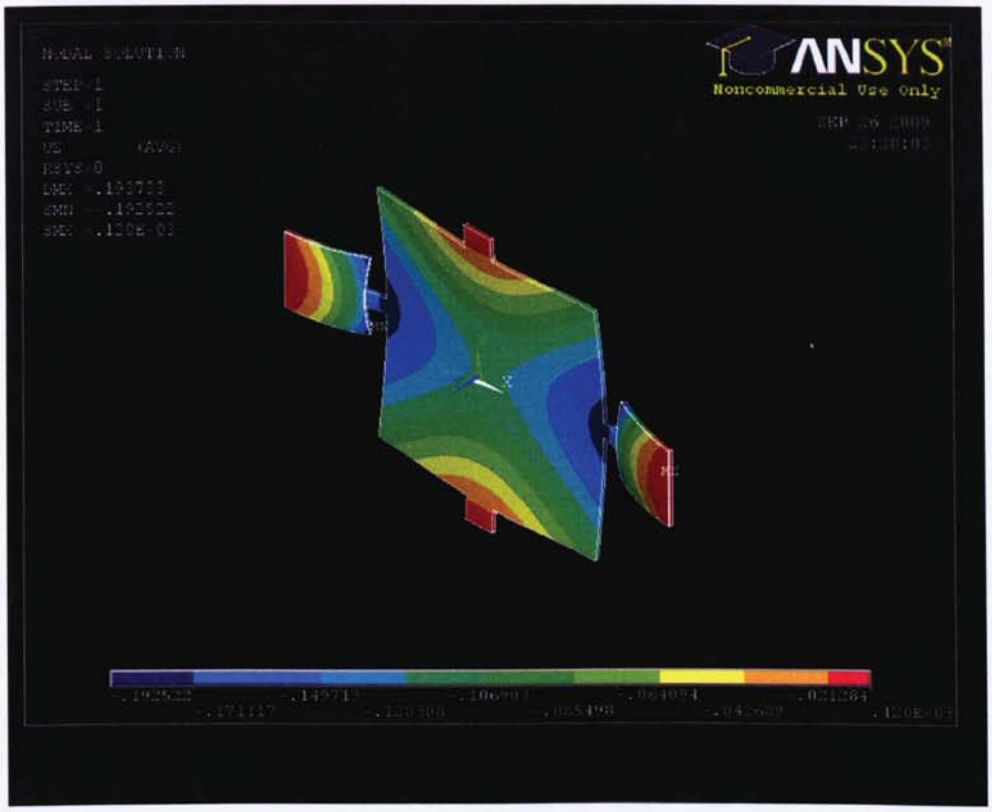

Figure 5.4: FEM simulation result of static deformation microsystem

configuration of excitation and sensing mechanism is capable of capturing the dynamics of the microsystem.

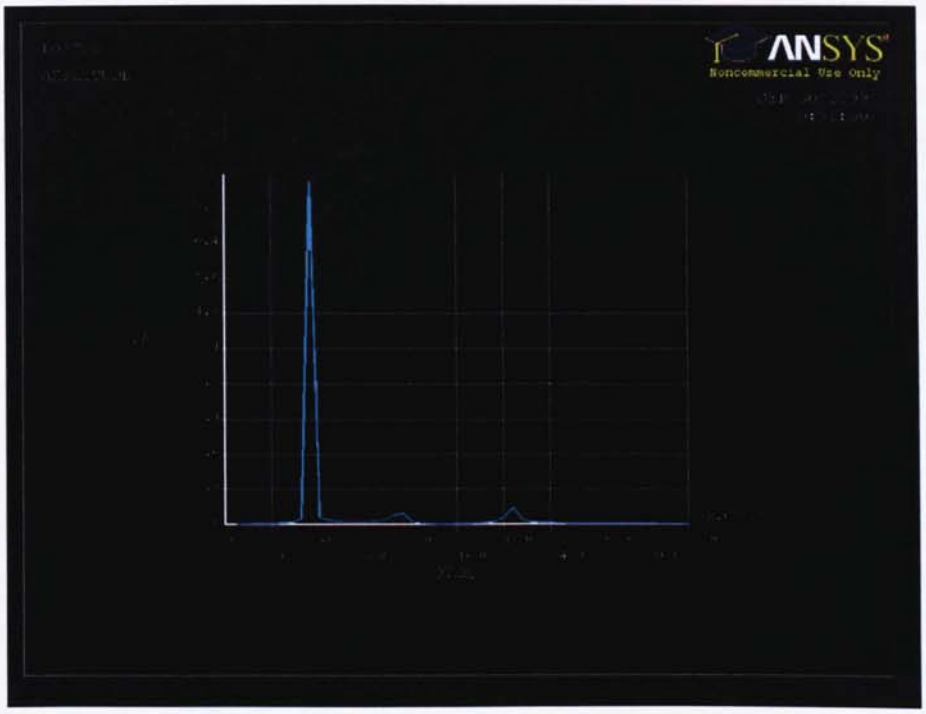

Figure 5.5: A FRF plot from harmonic analysis on the FEM model of a Type-C microsystem

The electromechanical coupling factor k can be evaluated from modal analysis in the FEM models. Resonance frequencies are obtained in the case of short circuit (all electrode elements are applied to voltage 0), while anti-resonance frequencies can be solved in open circuit (only ground electrode elements are applied with voltage 0)[88]. Figure 5.6 shows the electromechanical coupling factor square (k^2) varying with the thickness ratio of PZT thin film and silicon membrane. In most cases, when the ratio is in the range of $0.3 \sim 0.45$ the microsystem can achieve a maximum of energy conversion efficiency. Figure 5.7 demonstrates the coupling factor square k^2 and surface deflection varying with the aspect ratio of one PZT film and microplate (both are square). When the length of PZT is half of the silicon microplate, the coupling factor is a maximum. The surface

deflections at the selected two points (one is the microplate center and the other is the maximum deflection on the hinge) are continuously increasing with higher aspect ratio of PZT and microplate in plot (b) of Figure 5.7. For the eventual design with considering practical fabrication limitations, the thickness of silicon membrane is selected as $3\mu m$ and thickness of PZT film is $1\mu m$, the size of each PZT film is designed to be $60\mu m$ by $60\mu m$ for a $200\mu m$ square sensing microplate.

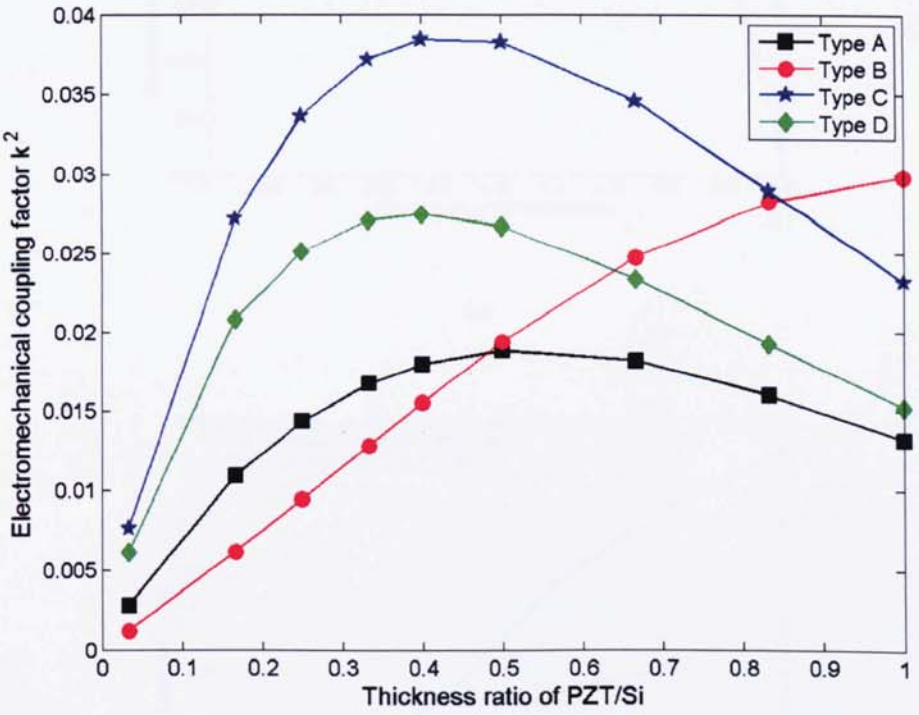

Figure 5.6: Electromechanical coupling factors square k^2 of first resonance mode for each microsystem varying with the thickness ratio of PZT/Si

5.3.2 Piezoresistive gauge

Four piezoresistive sensors are distributively placed on the microplate sensing surface, two of which are on the x axis and the other two are parallel to the y

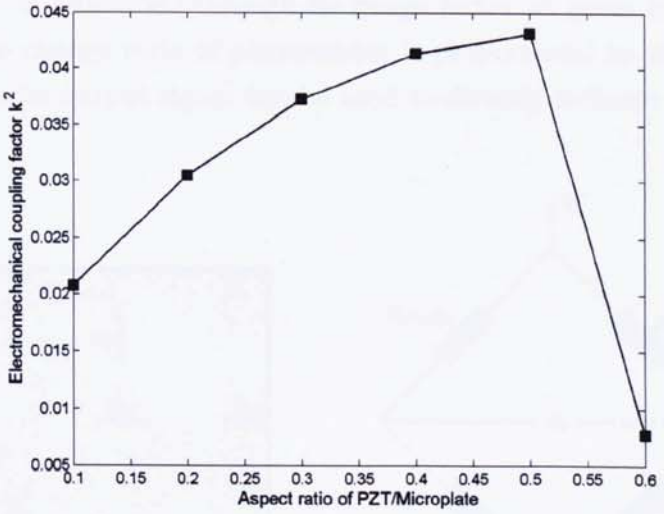

(a)

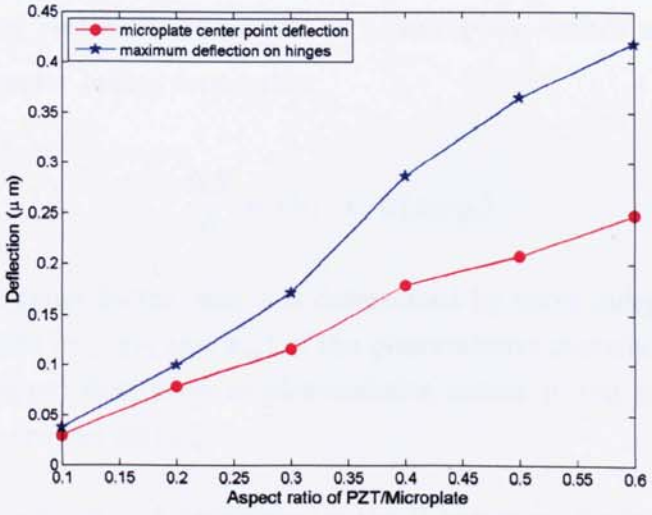

(b)

Figure 5.7: Electromechanical coupling factors square k^2 (a) and deflections (b) of a Type-C microsystem varying with the aspect ratio of PZT/Microplate

axis as shown in left plot of Figure 5.8. The sensitivity of a piezoresistive sensor (strain gauge) is quantified through its guage factor as given by Eq. 5.2 [132]. The resistance change ratio of piezoresistor is proportional to its local deformation, therefore its output signal can be used to directly indicate the vibration of microplate.

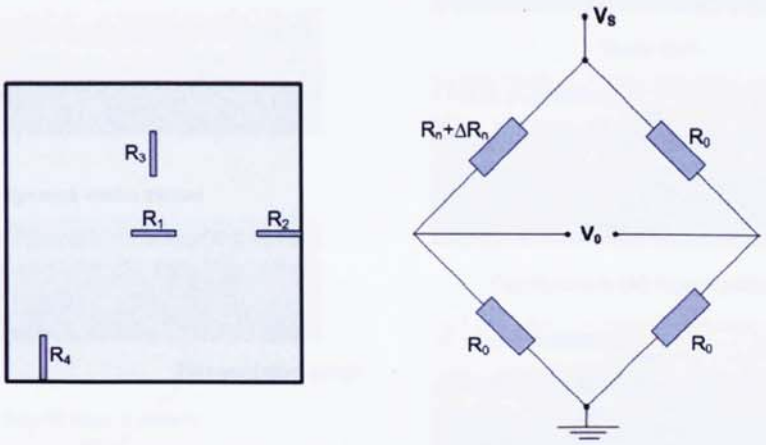

Figure 5.8: Four piezoresistive sensors on a microplate surface and Wheatstone-Bridge with quarter bridge connection

$$\frac{\Delta R}{R} = G\epsilon_l \propto w(x_0, y_0) \tag{5.2}$$

where G is the gauge factor, and it is determined by three independent piezoresistive coefficients (π_{11}, π_{12} and π_{44}) of the piezoresistive material. For the doped polysilicon (n-type) that used as piezoresistive sensor in our microsystem, the gauge factor is around 30[132].

The right plot in Figure 5.8 demonstrates the Wheatstone-Bridge circuit used for each piezoresistive sensor. The three reference resistors (R_0) are exactly same with the active sensor and just placed beside the microsystem. Wheatstone-Bridge is commonly used to improve accuracy of piezoresistive measurement and compensate the variations induced from environment (temperature). For the configuration with quarter bridge connection, the ratio between the applied voltage

V_S, and the output voltage V_0, can be roughly determined by in Eq. 5.3 in the case of $\Delta R \ll R$.

$$\frac{V_0}{V_S} = \frac{1}{4}\frac{\Delta R}{R} \tag{5.3}$$

In practical experiment the output signal V_0 is usually very small and need an amplifier. Assuming a maximum strain at the center of microplate is $100\mu\epsilon$ (refer to the analysis in above section), the piezoresistive gauge factor is 30 and applied voltage is $5V$, the calculated output voltage V_0 is then $3.75mV$. Therefore an $200 \sim 500$ amplifier is required to the measurement system.

Refer to the FEM analysis results presented in [133](plot a. of Figure 3), a rectangular piezoresistive gauge can achieve better sensitivity with smaller thickness and width. The eventual dimension in each piezoresistive sensor is chosen to be $20\mu m \times 2\mu m \times 0.5\mu m$.

5.4 Manufacture Processes

All the microsystems are fabricated using $3\mu m$-thick SOI wafers. Figure 5.9 illustrates the detailed microfabrication processes. The following paragraph presents a short description on each step.

1. **Oxide growth**
   The first step was to grow 100 nm-thick SiO_2 layer on the whole SOI wafer for the protection of active silicon.

2. **Alignment marks etched**
   Afterwards, some marks were dry etched on the SiO_2 layer for the purpose to align the masks used in following fabrication processes. As there are totally seven masks that will be used in this fabrication, it is necessary to use one or two cross marks to precisely localize the masks in operation.

3. **Piezoresistive sensors**
   A 500 nm-thick poly-silicon layer (piezoresistive sensor layer) was deposited onto the oxidised device layer of a SOI wafer by low pressure chemical vapour deposition (PCVD) . This layer was then doped by ion beam implantation using a 50Kev Boron source giving a doping denisty of 1e15 to enhance the piezoresistive deflection sensitivity. The sensor shapes were formed by photo-lithography and subsequent reactive ion etching (RIE).

4. **PZT films**
   In the PZT film fabrication, a sandwiched structure of a 100 nm-thick Pt/Ti bottom electrode, a 1 μm-thick PZT film and a 100 nm-thick Pt top electrode was deposited on the SOI. The top and bottom electrodes were deposited by evaporation using e-beam evaporator systems, the deposited PZT was deposited as a spin on sol-gel which was then annealed to produce the required PZT film. The top and bottom electrodes was patterned and etched by ion beam milling. The redundant PZT material was wet etched.

5. **Oxidation protection & etch**
   After that a SiO_2 layer was coated on the top surface of this processed SOI wafer for protecting the PZT-electrode stacks. Electric contact windows for both of the PZT-electrodes and piezoresistive sensors were also created by using the RIE to remove the coated SiO_2.

6. **Top electrode layer (Al) deposit & patterning**
   In this step, an additional 500nm-thick electrode (Aluminum) layer was deposited and patterned to form the electric pads and wires.

7. **Top SOI wafer etch**
   All the redundant SiO_2 and other materials were etched and removed from the top surface of SOI wafer, especially on the defined domain of membrane.

8. **Bottom silicon etch & oxide etch**
   Finally, back side silicon and buried SiO_2 layer were etched and removed to form the membrane structure of microplate.

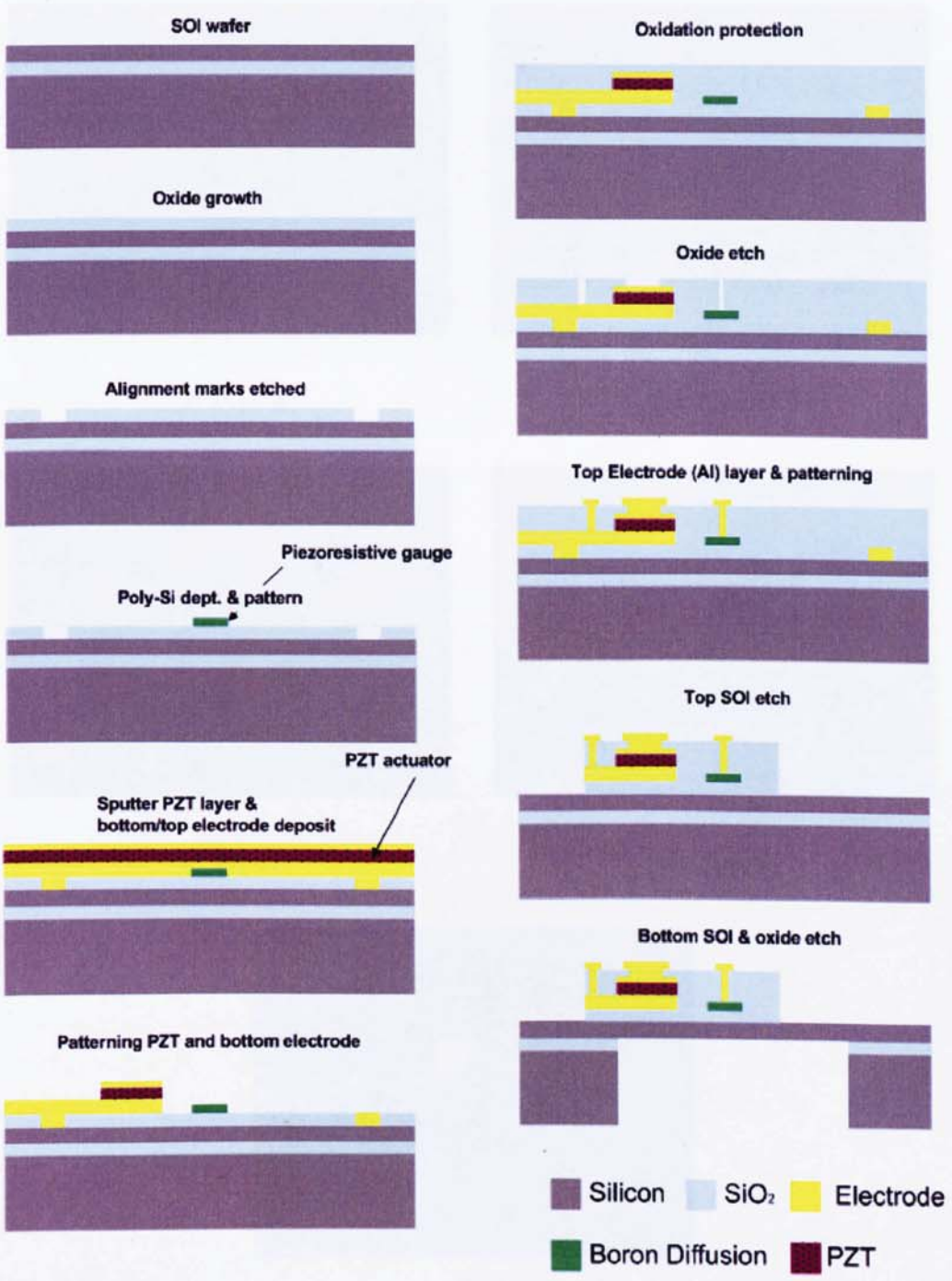

Figure 5.9: Microsystem fabrication process

Figure 5.10 shows the SEM images of the 5 types of fabricated microsystems, in which the microplates are roughly $100\mu m$ squares. Microsystems with other dimensions of microplates ($200\mu m$, 300μ and $400\mu m$) were also manufactured.

5.5 Discussion

A novel bio-sensing microsystem is proposed, designed and fabricated. In the design of such a microsystem, two key components that are PZT actuators and piezoresistive gauges are specifically investigated. The electromechanical coupling factor is used to guide the design of PZT actuators. Optimal thickness ratio between PZT film and silicon substrate for the microsystem is calculated. The design of piezoresistive gauges is mainly based on the published results of piezoresistor in the application of MEMS. The amplification requirement of the Wheatston-Bridge is calculated according to the microplate deflection in the FEM simulation. 5 types of microsystems with different boundary conditions of microplates are proposed and manufactured. Those various microsystems will provide the opportunity to find out an optimal structure (boundary condition) in the application of biosensing.

Comparing with the traditional microcantilever biosensors, this microplate-based bio-sensing platform have the following advantages:

a) The microplate is believed to have higher sensitivity (Q-factor) than microcantilever and be more suitable to work under heavy damping circumstance (natural cells culture media)[99, 117];

b) Distributive sensors are used to this sensing surface, which will then potentially be able to provide more information (such as spatial) of the target molecules/cells rather than only the mass measurement;

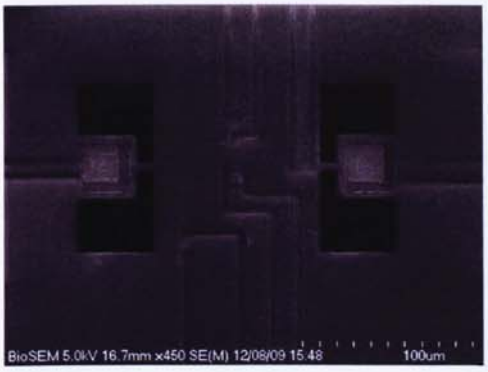

(a) Type A

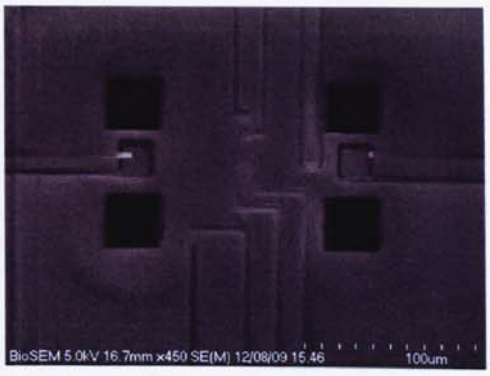

(b) Type B

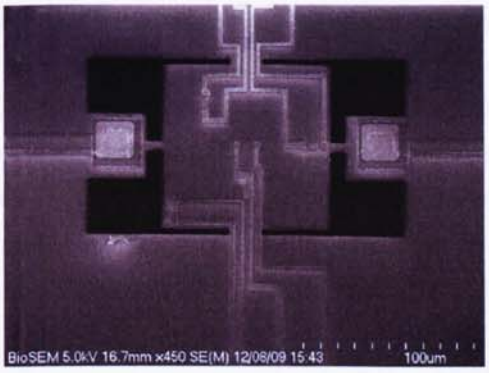

(c) Type C

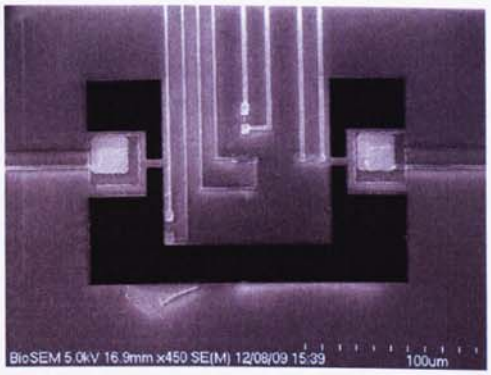

(d) Type D

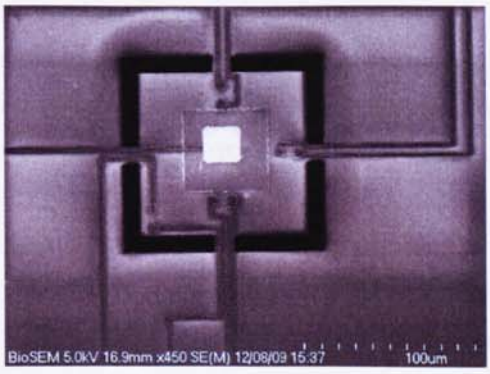

(e) Type E

Figure 5.10: SEM images of the fabricated microsystems (Type A $\sim$ Type E) with $100\mu m$ square microplate

c) This novel microsystem can also work both under dynamic mode and static mode. In a dynamic mode PZT and piezoresistors can work together as actuators and sensors for the dynamic/vibrational excitation and detection respectively. While for the static mode the piezoresistors can work independently to sense the static deflections of microplate due to the accumulation of target molecules.

Chapter 6

The investigation of microplates as biosensing platform

6.1 Introduction

In this chapter, biological experiments are implemented by culturing different types of cells on the microplates. Without specifying any particular bio-application, the investigation is mainly concentrated on the performance of microplates as a general biosensing platform. Therefore there is no layer of functionalized material such as antibody coated on the sensing surface of microplates beforehand, and testing cells are directly cultured to the microplates. From the engineering point of view, the ability to sense ultra-small mass change related to cell growth by a submerged microplate is the primary goal. Furthermore, all the bio-experiments discussed in this chapter are conducted in true cell culture environment.

Most of the previous experimental works of MEMS-based biosensors are usually taken very few experimental instances or samples. For the dynamic mode of mechanical biosensors, inference of cells or other biological particles from these

samples is commonly based on the natural frequency shifts. However, due to the individual difference of biological entities few bio-experimental samples are not capable to provide convincing evidence in biosensing application. Many batches of bio-experiments on microplates are carried out and repeated in the work of this chapter. A large number of experimental results, including various distribution of cells on microplates and the corresponding dynamic measurements for each set of experiment, are then measured and recorded. These experimental data provide a good opportunity to seek and derive the relationship between cell attachment and the dynamics variation of microplates.

The measured dynamics information of microplates with or without cell adhesion are recorded in the forms of a series of FRFs over the whole sensing domain. However, for instance two sets of FRF data, in which one belongs to the microplate coating with cells and the other is a reference data with empty coating, are difficult to directly make a comparative analysis. According to the analysis presented in chapter 4, modal parameters can be extracted from the measured FRF curves. It has been proved that changes of modal parameters, for example the natural frequency, are highly related to the information of cells.

Natural frequency shifts at each measured mode are firstly used to perform a preliminary analysis with cells culture density. In this analysis, some cases demonstrate a linear relationship between frequency change ratio and cells density, but it is not always the case in other experiments. The reasons behind these opposite results in the analysis of using the frequency-based method are then discussed. Even in the situations that linear relationships exist, this frequency method can only produce very approximate estimates of cells densities. Consequently, more robust and more accurate methods are desired to infer information on cells. The last section in this chapter introduces a Back-Propagation Neural Network based nonlinear system identification method to successfully evaluate cell population.

6.2 Biological Experiments on Microplates

6.2.1 Bio-Experiments Design

The work of bio-experiments on microplates are divided into two discrete phases. Initially, cells with selected density are coated onto the surface of the microplate and then incubated for a prescribed period. Afterwards the dynamics of microplates attached with a certain amount of cells will be measured by using the testing system presented in chapter 4.

Before making plans for the completed bio-experiments of microplates, some preliminary trials have to be implemented in advance. A very clean environment is always critical for cell culture, sterilisation effects on the silicon dies as well as the base-excitation testing devices as shown in Figure 6.2 are examined. The silicon dies can easily pass the sterilisation test with just an ethanol wash and a short period of UV light exposure. However, the testing devices are unable to maintain a sterilised state for cell culture in dynamic experiments. It means that cell culture and performing dynamics measurement simultaneously is impossible and they have to be separated, because cells can't grow in the environment involving testing devices. The next challenge is to coat cells onto the silicon-surface of a microplate. Fortunately many biological cells are inherently able to tightly attach to the bottom surfaces of culture containers, on which the attached cells will then be divided and propagated.

Two different schemes of bio-experiments as illustrated in Figure 6.2 are designed in this chapter. In both of them, four different times of cell culture in each batch of experiment are accomplished and every batch of these experiments is repeated two or three times for validation. In the first scheme, labeled as BioExperiment-I, identical microplates are repeatedly used four times for cell culture with progressively increased cell density and a fixed incubation period. The cells in these four experiments belong to four different generations, which are believed to be in a close physical properties but might be different in biological activities. On the

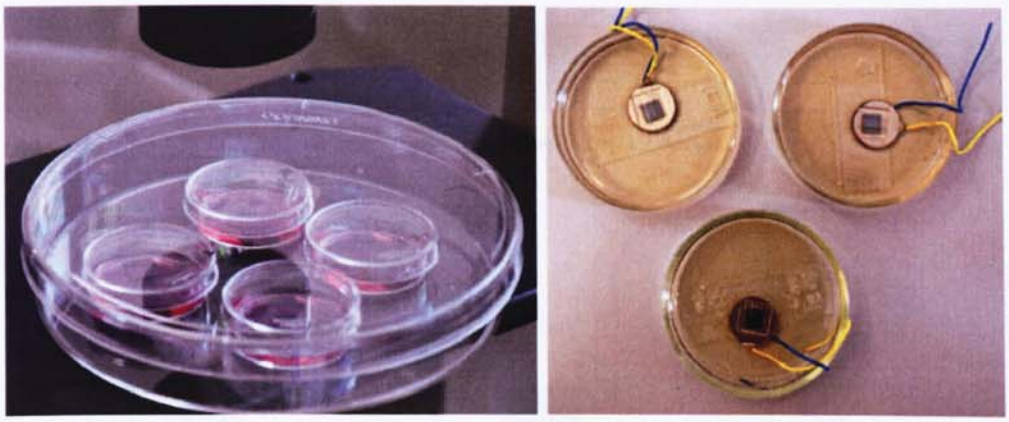

Figure 6.1: Cells attachment experiment: left image is only on microplates and right image is on base-excitation testing devices

other hand, the second type bio-experiment (BioExperiment-II) employs four different microplates but with same size and same boundary conditions to perform these four times cells culture simultaneously. The initial cells density are all the same in these four experiment, and multiple extended incubation time are prescribed to each of these microplates. The cells in BioExperiment-II are therefore of the same generation.

Consequently, both of BioExperiment-I and BioExperiment-II are able to provide four different situations of cell growth with the corresponding dynamic measurement for a perticular microplate in each batch experiment. For BioExperiment-I, the dynamic measurements in each experiment of a microplate with different cell adhesion will be referred to the dynamics of this microplate that has no cells. Because the microfabrication process results in different practical sizes of microplates even if they are of a same type (in section 4.2), four different dynamic references are then required for each of the testing microplate in the BioExperiment-II. In other words, the experimental factors of uncertainty in BioExperiment-I are supposed to be less than BioExperiment-II. Therefore, the measured data and results from BioExperiment-I are assigned to the primary analysis in cells discrimination.

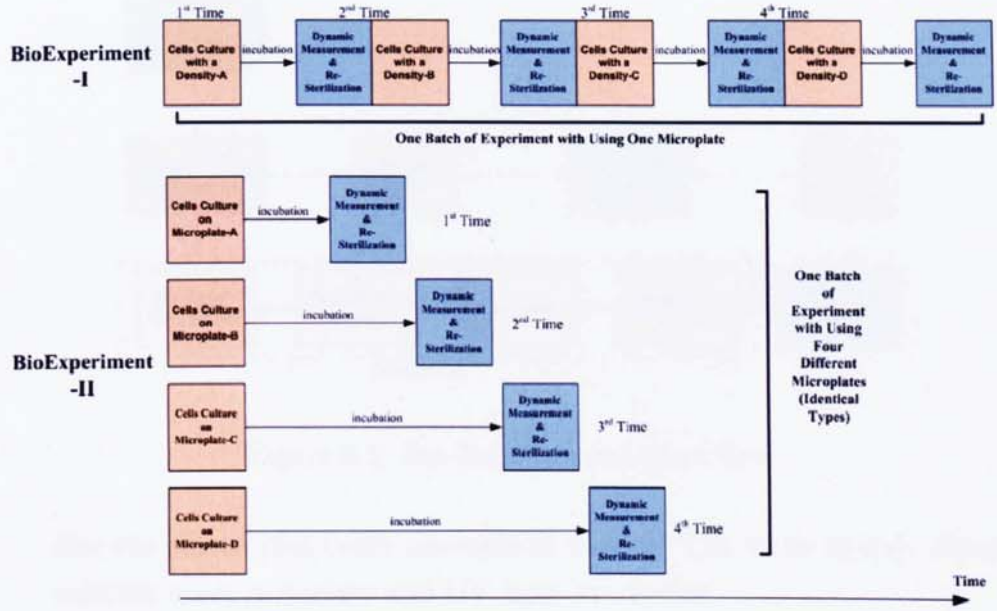

Figure 6.2: Two schemes of Bio-Experiments

6.2.2 Work Flow of Bio-Experiments

Cells are easily affected or contaminated in a natural environment and can only grow under very severe conditions, such as a sterilized container, specific temperature and humidity. Therefore all the experimental operations related to cell culture on microplates have to be under a sterile environment and follow certain regulations. However, the dynamics measurement of a microplate carrying cells is very difficult to execute in a sterilized environment, unless a clean room is provided. Sterilization of the microplates is then required before each cell culture. Figure 6.3 demonstrates the series of operational flows for each bio-experiment. The cycle of work flows means that each microplate can be repeatedly used in bio-experiments after Re-Sterilization. The following part gives a detailed description on some of the work phases.

1. **Cleaning and Sterilisation**

   Few steps were successively applied in order to thoroughly clean and ster-

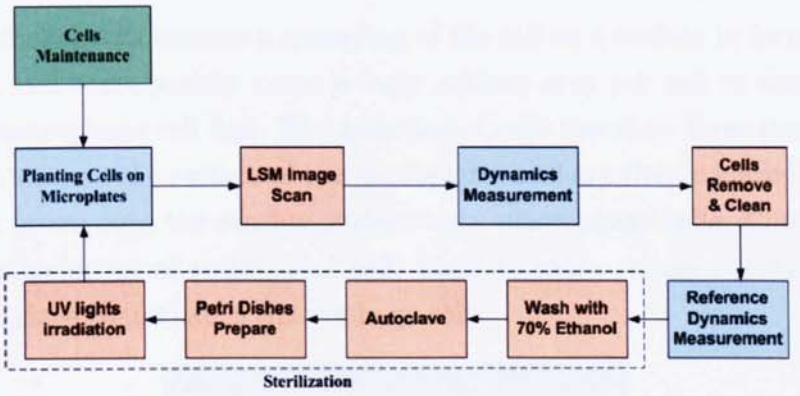

Figure 6.3: Bio-Experimental work flow

ilise the silicon dies (with microplates inside). The steps include chemical solution wash, autoclave and UV light irradiation.

The silicon dies were initially swilled in a flood of $70 \sim 80\%$ ethanol to remove dust as well as bacteria. Some tightly attached residuum can be wiped off by using a piece of soft pledget or lens tissue with the mixed solution of ethanol and acetone. Cleanliness of the top surface of silicon die, especially around the region of the microplate, is optically inspected.

Afterwards, autoclave was applied to provide a more severe sterilisation for the silicon dies. A program of heating the stem up to $121°C$ and lasting 15 minutes was selected, which is standard for glassware autoclave. However, early experiments reveals that the top surface of a silicon die could be easily oxidated under this high temperature, and some impurities of the chamber could be permanently deposited on the surface in the process of autoclave. In order to avoid this issue, a water bath environment was provided to these silicon dies and bottom surfaces were faced upward during the process of autoclave.

The silicon dies picked out from the autoclave machine have to be dried and examined again under a microscope. Those intact silicon dies were then going to be used in pre-sterilised petri dishes($35mm \times 10mm$), and washed by $70 \sim 80\%$ ethanol again in order to kill any microbial or bacterial organisms. This operation should be carried out in a fuming hood to ensure

a bacteria-free environment. Eventually, the petri dishes including the dies were dried and sterilised using the UV light irradiation for a period of $2 \sim 3$hours.

2. **Cells Maintenance**

   Two types of cells are chosen for the bio-experiments of the silicon microplates: an endothelial cell line (EA.hy 926) and a macrophage cell line (J774.2). The human hybrid EA.hy 926 cell is derived from the fusion of the human umbilical vein endothelial cells with A549/8 human lung carcinoma cell line. EA.hy 926 is a permanent human endothelial cell line that expresses highly differentiated functions characteristic of human vascular endothelium. The J774.2 cell is derived from a tumour in adult female BALB/c mouse. Macrophages are phagocytes, acting in both non-specific defense (and innate immunity) as well as to help initiate specific defense mechanisms (or adaptive immunity) of vertebrate animals. It is necessary to keep culturing a certain quantity of live and EA.hy 926 and J774.2 cells during the period of Bio-Experiments of microplates.

   J774.2 cells were maintained in $30ml$ Dulbecco's Modified Eagle's Medium (DMEM) supplemented with $2mM$ glutamine and streptomycin $100\mu g/ml$ and penicillin $100U/ml$ and 10% heat inactivated foetal bovine serum (FBS). Cells were cultured in an incubator at $37°C$ with an atmosphere of 5% CO2 and 95% air. Cells were grown in a $75cm^2$ flask and passaged when reaching $\sim$ 90% confluence. Once cells roughly reached 90% confluence the media was removed and the cells washed with $5ml$ phosphate buffered saline (PBS). Cells were detached from the bottom surface of the flask by using a cell scraper and the cell clusters were then separated with repeated pipetting. The PBS was then removed and $5ml$ fresh media was added to the cells in a new $75cm^2$ flask, in which the cells grow into next generation.

   Human EA.hy 926 endothelial cell lines are also maintained with DMEM, but supplemented with 10% FBS, streptomycin $100\mu g/ml$ and penicillin $100U/ml$, and $10ml$ HAT ($100\mu M$ hypoxanthine, $0.4\mu M$ aminopterin, $16\mu M$ thymidine). The environment for the EA.hy 926 cells growth is exactly the same as that of the above J774.2 cells. The process of passage of EA.hy 926

cells is also similar. Cell culture media was removed from the cells and the cells were then washed with $10ml$ sterile PBS until the media appears colorless. EA.hy 926 cells were then detached by the addition of $2.5ml$ Trypsin with a 3 minute standard incubation. Cell clusters were also dispersed for a fairly uniform distribution by repeated pipetting with $5ml$ new DEME media. Afterwards the cell suspension was centrifuged at $1500rpm$ for 5 minutes and the media was then removed and cells were re-suspended in $10ml$ fresh media. Finally a prescribed cell density of the mixed media was made by adding certain mount meida and then went into a brand new flask for the next generation growth.

3. **Planting Cells on Microplates**
   Before planting cells on the microplates, the cell density of suspension during the process of passage has to be established in advance. The numbers of viable cells were estimated by taking $20\mu l$ of the cell suspension and mixing it with a $20\mu l$ trypan blue. Cell count was then performed from this new mixture by using improved Neubauer haemocytometer. Once the cell density was established a $5ml$ cell suspension of EA.hy 926 or J774.2 cells at a certain density was made up using the media of these cell lines. Tables 6.1 and 6.2 list the EA.hy 926 and J774.2 cells density respectively used in each time during BioExperiment-I. However, in order to increase the chances of planting the cells to the $100\mu m \times 100\mu m$ microplates that have the smallest sensing area, double cell density was usually used rather than that shown in Tables 6.1 and 6.2.

   Eventually the above cells were poured into the fully sterilised Petri dishes with silicon dies (microplates) for culturing the cells on the microplates. The cells were then incubated in an incubator at $37°C$ with an atmosphere of 5% CO2 and 95% air for at least 24 hours to ensure cell attachment to the sensing surface.

   Preliminary experiments as shown in Figure 6.4 and 6.5 have proved that both of EA.hy 926 cells and Macrophages are able to tightly stick onto the surfaces of silicon dies as well as the domain of microplates after a period of incubation. Comparing with the attachment of cells, the physiology of

Table 6.1: EA.hy 926 Cell Suspension Density Used in Microplates at Different Time of Bio-Experiment

Times	Volume of Cell Suspension Added (μl) with Density of $5 \times 10^5/\mu l$	Volume of Media Added (μl) for EA.hy926 Cells	Final Cell Density used on Microplates (per μl)
1^{st}	100	1900	25×10^3
2^{nd}	200	1800	50×10^3
3^{rd}	400	1600	100×10^3
4^{th}	800	1200	200×10^3

Table 6.2: J774.2 Cell Suspension Density Used in Microplates at Different Time of Bio-Experiment

Times	Volume of Cell Suspension Added (μl) with Density of $1 \times 10^6/\mu l$	Volume of Media Added (μl) for J774.2 Cells	Final Cell Density used on Microplates (per μl)
1^{st}	100	1900	5×10^4
2^{nd}	200	1800	10×10^4
3^{rd}	400	1600	20×10^4
4^{th}	800	1200	40×10^4

endothelial cells ensures a spreading of the cell on a surface to form a monolayer and consequently cover a lager surface area per cell as compared to the macrophage cell line. The endothelial cells therefore form more attachment sites on the surface of the microplates and are then believed to induce more stress onto the sensing surface than macrophage cells. Consequently, the attachment of endothelial cells leads to more changes of dynamics of microplate than that of macrophage cells.

Figure 6.4: Endothelial cells coating on the surface of a microplate

Figure 6.5: Macrophage cells coating on the surface of a microplate

Table 6.3: Measured Density and Viscosity of the DEME media

Density	Viscosity
$\rho_f(kg/m^3)$	$\mu(cP)$
993.86	0.8247

4. **Cells Image Scan**
   In order to record the cell growth situation, images of the surfaces of microplates coated with cells are captured by using a confocal laser scan microscopy (LSM) - Zeiss Axioplane 210. From these LSM images, the information of cell number and distribution can be easily obtained. It is required to take silicon dies out of the cell culture media and perform the image scan in a dry environment for the purpose of obtainning clear images. The dynamic measurement must be implemented immediately after finishing the image scan, as the cells could start to perish after a period of $2 \sim 3$ hours in a dry environment.

5. **Dynamics Measurement**
   The dynamics of microplates with cells adhered can be measured through the base-excitation apparatus, in which the fluid of cells culture media (DMEM) is used instead. Afterwards, the cells are removed and the dynamics of microplate measured again. The FRF data for each specific microplate with cells and without cells are compared to infer the information of cells, which is recorded in the LSM scanned images.

   From the dynamic standpoint of view the fluid-structure interaction, density and viscosity of fluid are the primary factors that can affect the dynamic behaviours of the vibrating structure. The density and viscosity of DMEM media around $20°C$ is measured, which are listed in the following Table. It can be seen that the measured properties of DMEM media are very close to water.

6. **Cell Removal**
   The process of removing the attached cells on the surface of silicon die is similar to the normal procedures of cleaning.

6.3 Preliminary Identification on Cell Density

6.3.1 Changes of Dynamic Information Related to Cells Distribution

In chapter 3, it is theoretically demonstrated that additional mass loading on a submerged microplate can generate distinct changes of its dynamic characteristics, such as resonant frequencies or mode shapes. Therefore, it is concluded that the features of attached cells on a microplate can be inferred from the changes of dynamic information. The reconstruction of an exact image of cell distribution from dynamic information of the microplate is highly challenging. This work attempts to find the inherent links between variations of dynamic information and cell distribution on a microplate sensing surface. Different densities of cell distribution are identified by using various indices of microplate dynamics.

Figures 6.6 and 6.7 present the frequency response function of a microplate with cells attaching and without cells attaching on it, respectively. The FRF plots in Figure 6.6 are on a $100\mu m$ type C-F-F-F microplate with endothelial cells, and Figure 6.7 is for a $300\mu m$ type C-C-C-C microplate with macrophage cells. The first and forth measured mode shapes are compared between the cases of cells-loading and without cells. It can be seen that first mode shapes are almost identical, while the forth mode shapes have distinct changes. This shows that changes of mode shapes of microplates due to cell adhesion is more obvious at high resonant modes. It is in agreement with the theoretical results presented in Figures 3.2$\sim$3.4 in chapter 3.

Generally, additional mass loading of attached cells on the surface of microplates results in both resonant frequency shifts and resonance amplitude variations, which are indicated in the FRF plots. Resonant frequencies are the inherent property of the dynamic system and can be used for straightforward comparison. However, the amplitude of FRFs can be largely affected by the pre-tightening loads on the silicon die or external disturbances at each experiment. As the first

mode shapes remain almost constant, the amplitudes of each FRF can be self-normalized with respect to the amplitude of the first resonant mode. Then the changes of the resonant amplitudes of two self-normalized FRFs can be compared and evaluated on higher modes. Figure 6.6 shows much more FRF changes than the case presented in Figure 6.7. It implies that the first type microplate has higher sensitivity in detection of attached cells than the second type and endothelial cells induced more stresses to the bio-sensing surface than macrophage cells. It is also noticed that nonlinearity occurs on the dynamics of microplates due to the cell attachment in Figure 6.6. In fact most experimental results of FRFs microplates involved cell attachment are suffered with nonlinearities to a certain degree.

6.3.2 Resonant Frequency Based Indices

Most dominant change of the dynamics of microplates induced by cells loading is the resonant frequencies shift. The following two resonant frequency based indices (Eq. 6.2) are utilized to perform a preliminary analysis on the experimental results. The index of FDR_n (Frequency Difference Ratio) is evaluated as the normalized resonant frequency difference between the cell-loaded and barren (reference) microplate at each corresponding measured resonant mode. The index of $AFDR$ is the average of all measured FDR_n. Considering the submerged microplate as a general oscillation system, resonant frequency can be approximately determinated only by its stiffness and mass, the first equation in 6.1. If one assumes the system stiffness is a constant, the mass change ratio is proportional with frequency change ratio as shown in second equation of 6.1. It is therefore believed that indices FDR_n and $AFDR$ are able to roughly reflect the cells density. However in realistic situations cell attachment would also affect the stiffness of sensing microplate more or less, especially the endothelial cells. This leads to complication and makes FDR_n and $AFDR$ unable to indicate the cells density

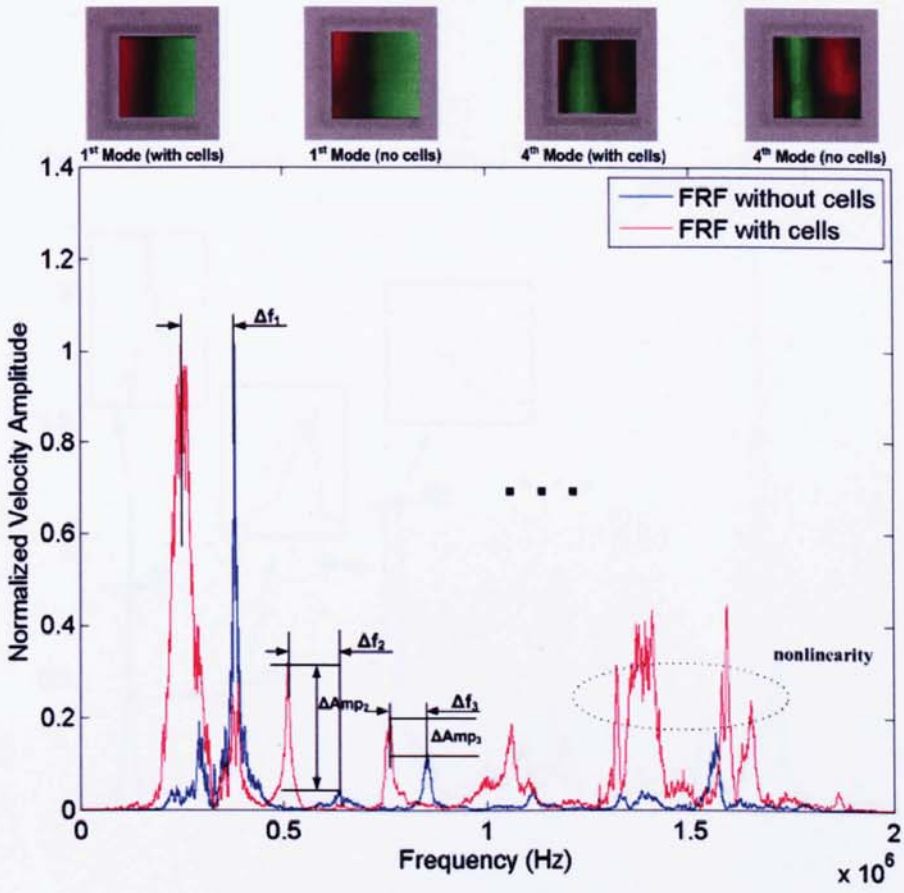

Figure 6.6: Frequency response functions comparison of a C-F-F-F Microplate with endothelial cells attaching and without cells attaching (Normalized to first resonant mode)

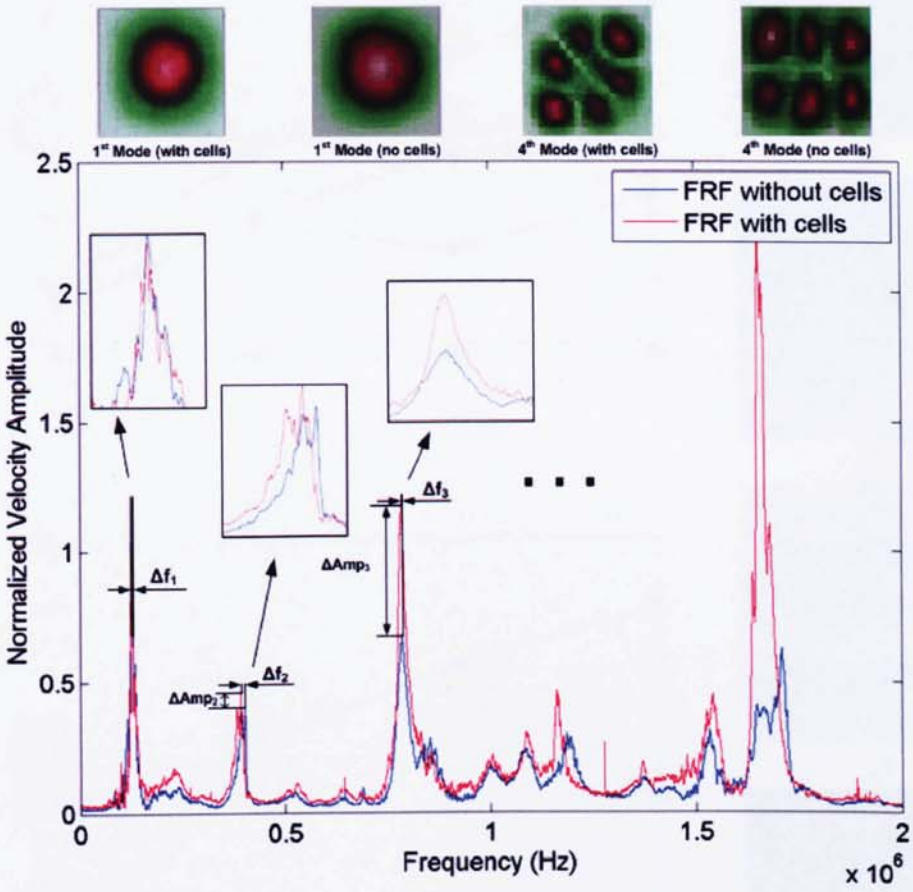

Figure 6.7: Frequency response functions comparison of a $300\mu m$ C-C-C-C Microplate with macrophage cells attaching and without cells attaching (Normalized to first resonant mode)

in some cases.

$$f = \frac{1}{2\pi}\sqrt{\frac{k}{m}}, \quad \frac{\Delta m}{m} = \frac{k}{4\pi^2}(\frac{1}{f_1^2} - \frac{1}{f^2}) \approx 2\frac{\Delta f}{f} \tag{6.1}$$

$$FDR_n = \left|\frac{\Delta f_n}{f_n}\right|, \quad AFDR = \frac{1}{N}\sum_{n}^{N} FDR_n \tag{6.2}$$

Figures 6.8∼6.18 are the analytic results of using FDR_n and $AFDR$ on twelve different batches of bio-experiments. Results in Figures 6.8∼6.14 are from the bio-experiments on endothelial cells and Figures 6.15∼6.16 are of macrophage cells experiments. In all of these figures the left two plots are the evaluated results of FDR_n and $AFDR$ respectively at each time experiment in one batch, while the right four or three images illustrate the corresponding different cell coating situations, in which cell densities are gradually increased. Four or three measured resonant modes are chosen to calculate the indices and these modes are usually the dominant resonances in the measured FRFs. The cells distribution images are all double enlarged and their contrast are also enhanced for clarity. The first ten figures of experimental results present fairly linear relationships between cell density and the indices of FDR_n and $AFDR$, particularly $AFDR$. On the other hand, the results in Figure 6.17 and Figure. 6.18 demonstrate cases when FDR_n and $AFDR$ failed to indicate cells density.

After detailed examination of these experimental results, we can conclude the following on the microplates when their resonant frequencies are used as indices in the detection of cells distribution.

1. First of all, some trends of the index FDR_n at one or two modes are not the same with the increase of cell quantity. This phenomenon is quite different from the bio-experimental results of microcantilevers, where the FDR at the fundamental mode always has a linearly relationship with cell number[105, 111]. The potential reasons for this phenomenon are:

(a)Microplates usually have much larger sensing area and carry much more cells than microcantilever in the bio-experiments. Apart from mass change, the accumulation of cells may also result in change of structural stiffness. In such cases, the linear relationship of the FDR will be violated. (b)The bio-experiments presented in this work for microplates are involved a very practical environment, for example the dynamics of microplates are all measured in a truly cell culture media. (c)Nonlinearity of the dynamics of submerged microplates with randomly distributed cells are also existed in most experimental measurements.

2. For most types of microplates index $AFDR$ is capable of giving an approximate prediction of cell density. However the values of $AFDR$ for different microplates don't always appear in a same range (same type in a close range). This is due to the fact that the sensitivities of index $AFDR$ are very different on different types of microplates, as shown in these figures the $200\mu m$ C-F-C-F and $100\mu m$ C-F-F-F microplates have much higher sensitivity than the $200\mu m$ and $300\mu m$ C-C-C-C microplates. Comparing the results in Figure 6.8 and Figure 6.15, it can be noticed that endothelial cells generate higher values of $AFDR$ than macrophage cells, that is corresponding to more changes of dynamic information. Consequently self-calibration for each distinct microplate and cells will be necessary when applying $AFDR$ index to indicate cells density in microplate-based biosensing systems.

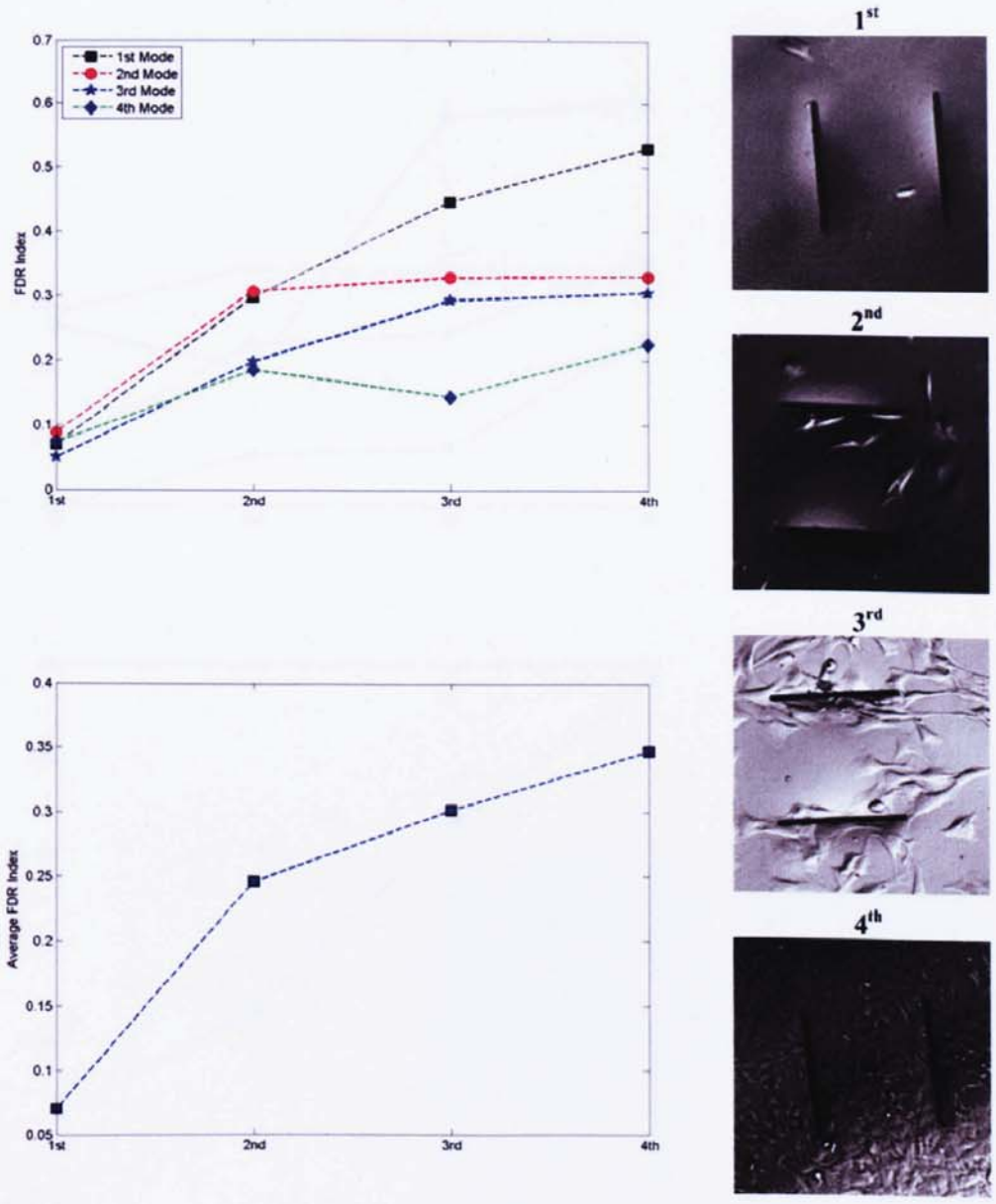

Figure 6.8: Results of a batch BioExperiment-I on a C-F-C-F 200μm square microplate with endothelial cells and corresponding trends of frequency based indices (experiment dates: Feb. 4th 2009 - Feb. 12th 2009)

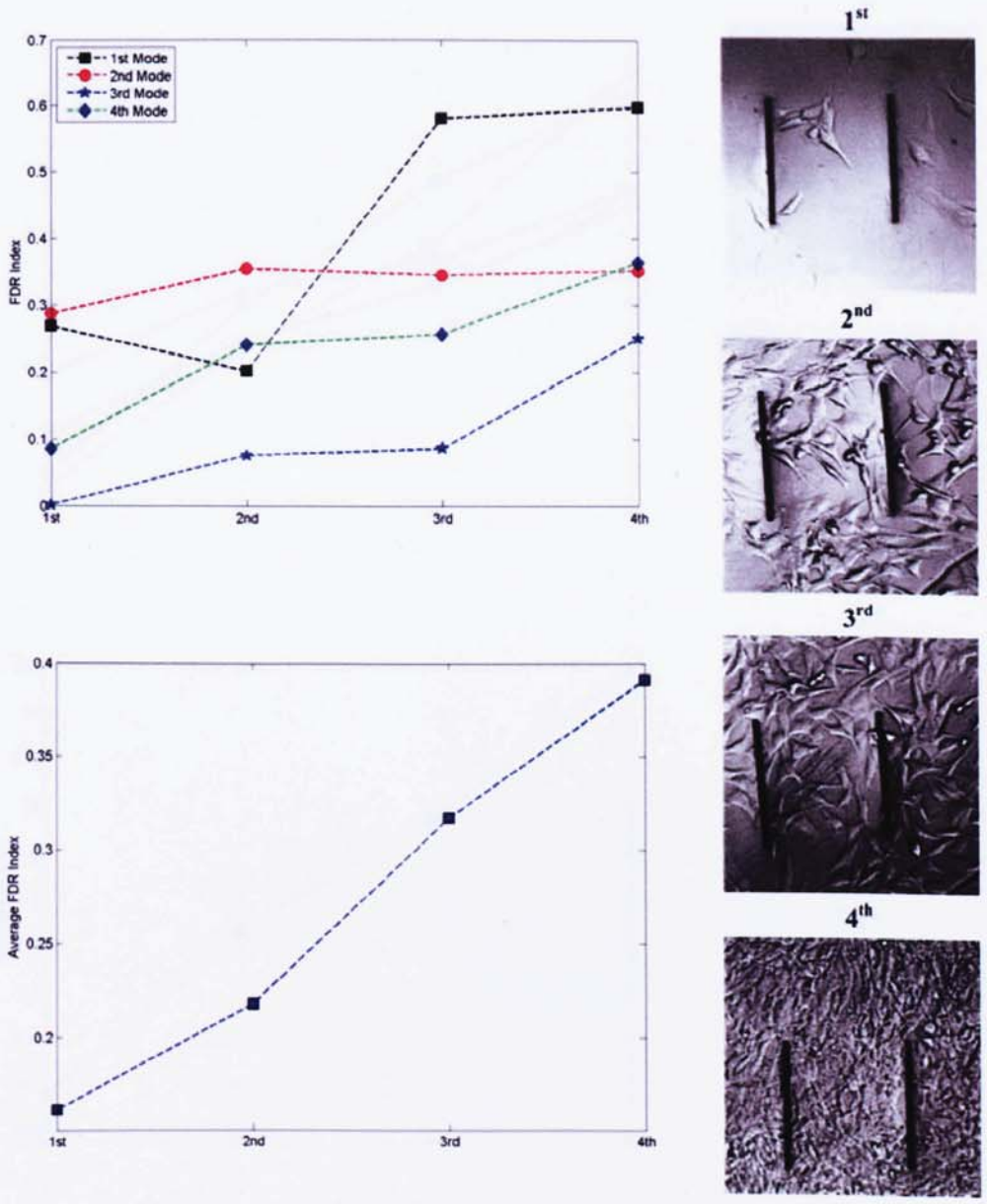

Figure 6.9: Results of a batch BioExperiment-I on a C-F-C-F 200μm square microplate with endothelial cells and corresponding trends of frequency based indices (experiment dates: Apr. 2nd 2009 - Apr. 10th 2009)

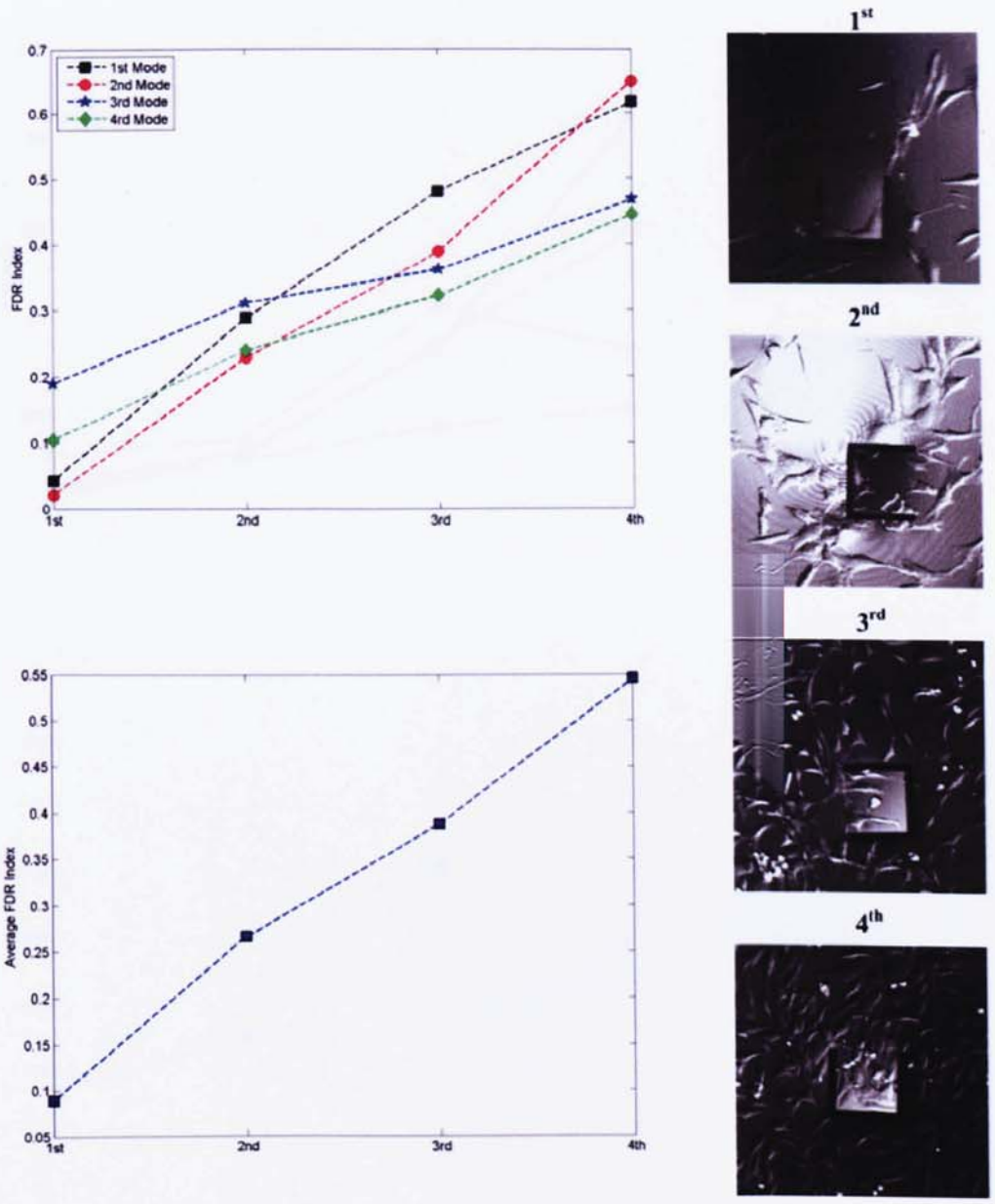

Figure 6.10: Results of a batch BioExperiment-I on a C-F-F-F 100μm square microplate with endothelial cells and corresponding trends of frequency based indices (experiment dates: Feb. 4th 2009 - Feb. 12th 2009)

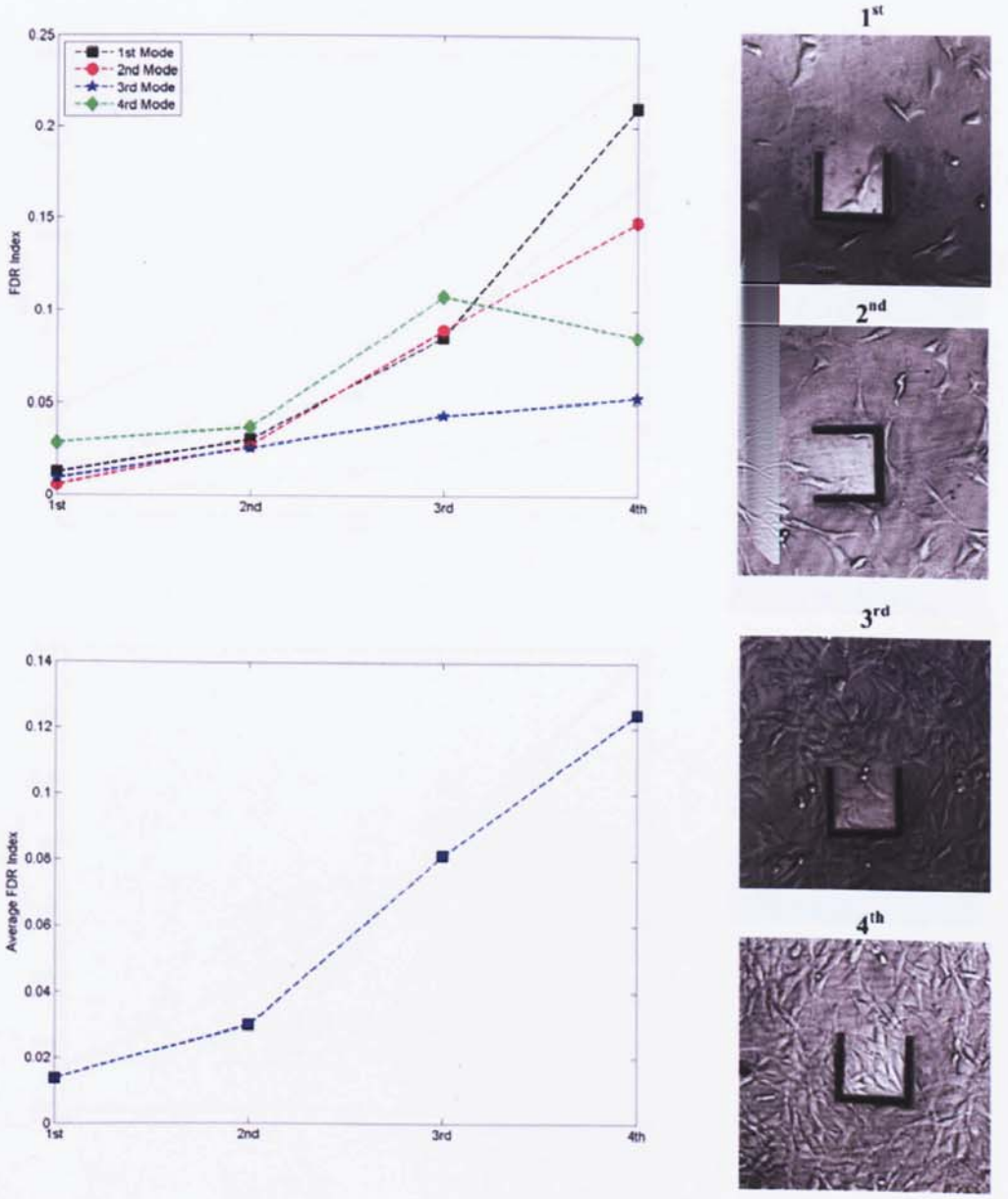

Figure 6.11: Results of a batch BioExperiment-I on a C-F-F-F $100\mu m$ square microplate with endothelial cells and corresponding trends of frequency based indices (experiment dates: Apr. 2nd 2009 - Apr. 10th 2009)

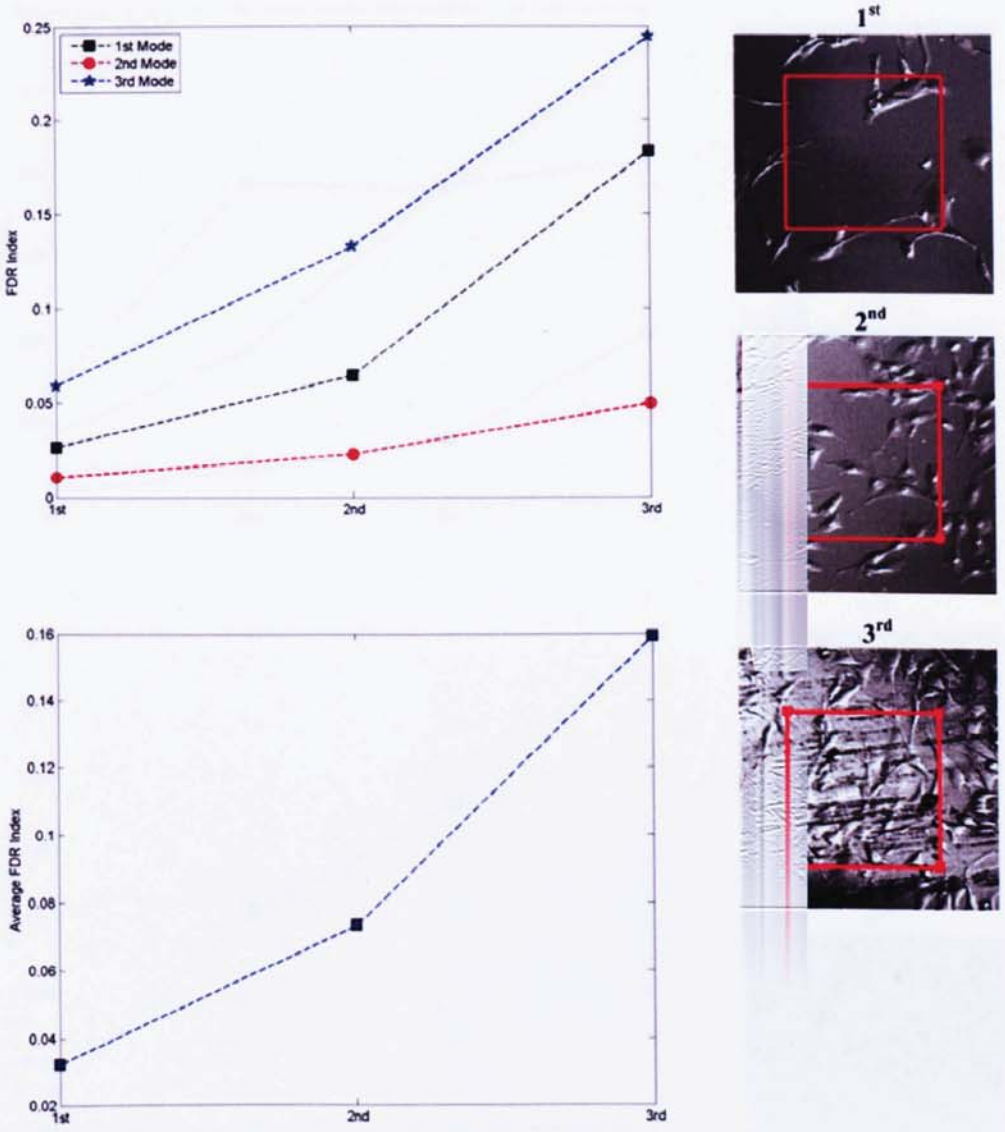

Figure 6.12: Results of a batch BioExperiment-I on a C-C-C-C 200μm square microplate with endothelial cells and corresponding trends of frequency based indices (experiment dates: Feb. 4th 2009 - Feb. 12th 2009)

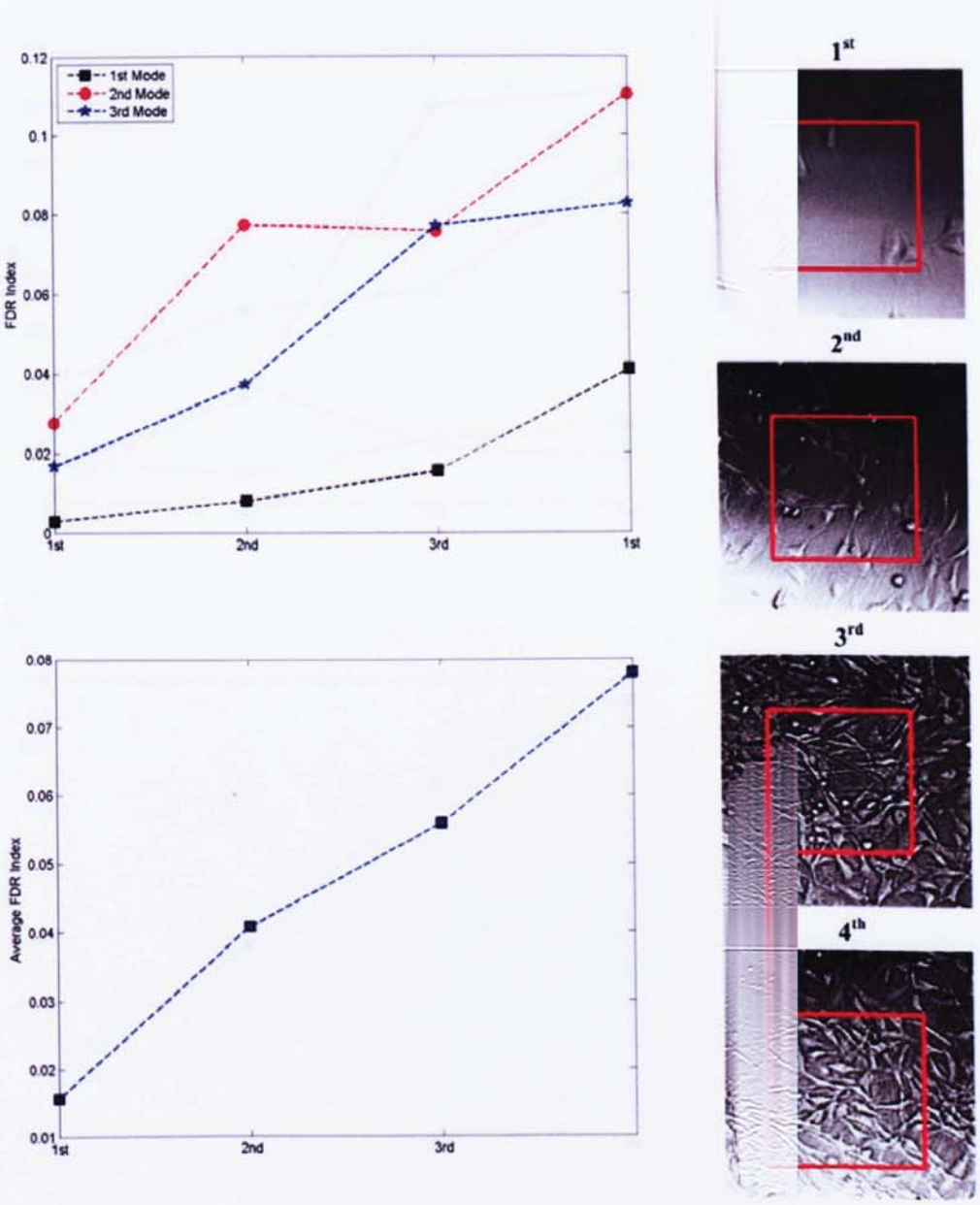

Figure 6.13: Results of a batch BioExperiment-I on a C-C-C-C 200μm square microplate with endothelial cells and corresponding trends of frequency based indices (experiment dates: Apr. 2nd 2009 - Apr. 10th 2009)

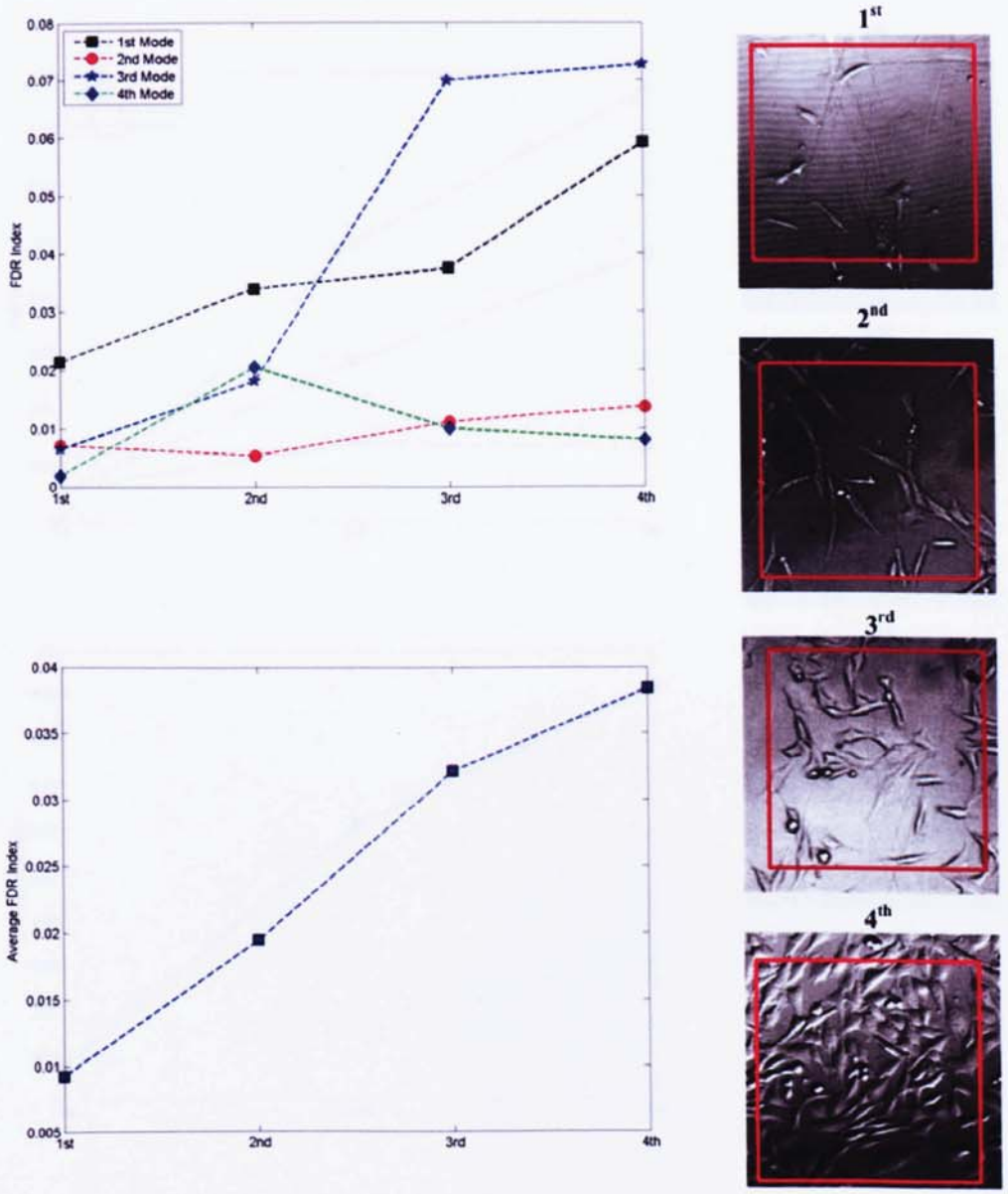

Figure 6.14: Results of a batch BioExperiment-I on a C-C-C-C 300μm square microplate with endothelial cells and corresponding trends of frequency based indices (experiment dates: May 20th 2009 - May 30th 2009)

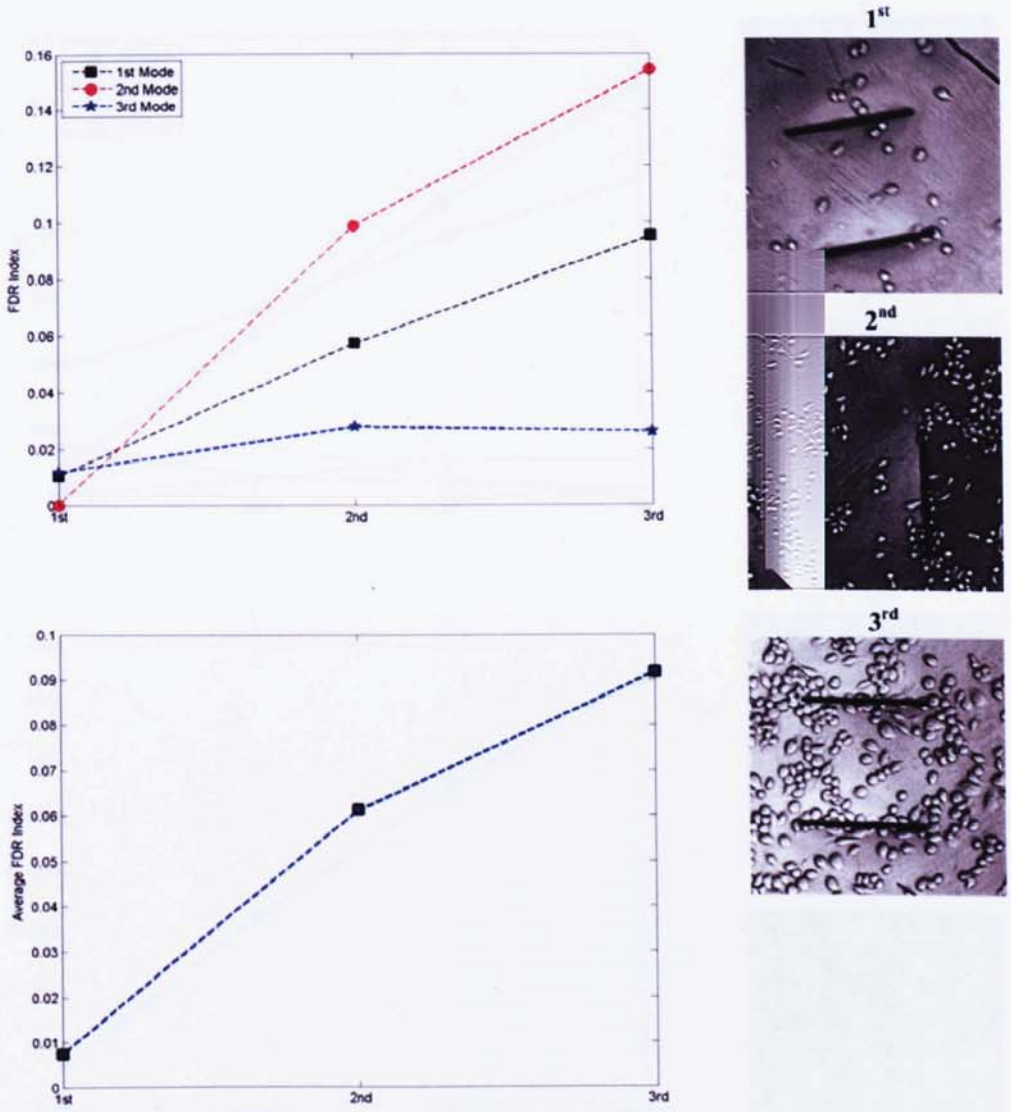

Figure 6.15: Results of a batch BioExperiment-I on a C-F-C-F 200μm square microplate with macrophage cells and corresponding trends of frequency based indices (experiment dates: May 20th 2009 - May 30th 2009)

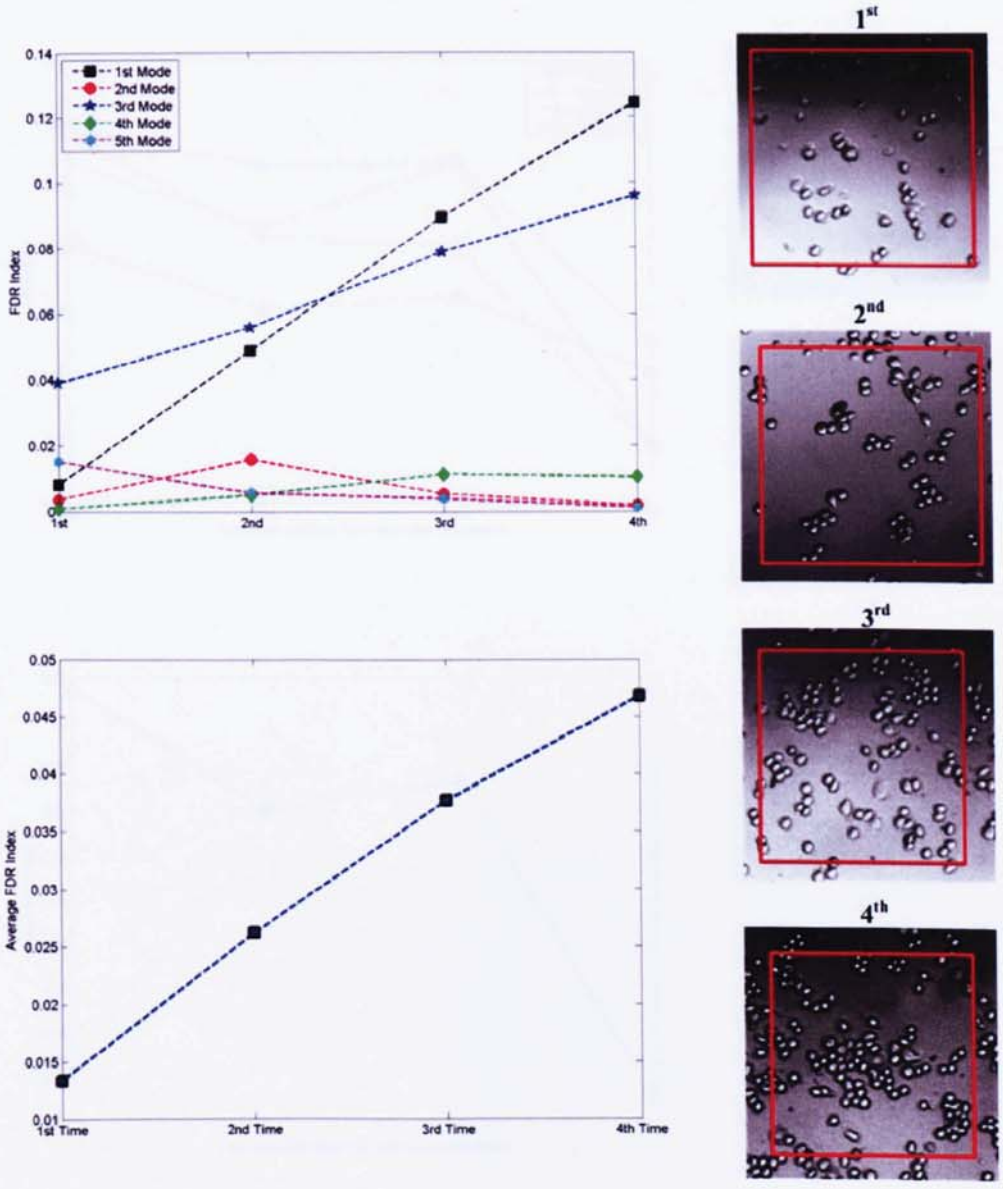

Figure 6.16: Results of a batch BioExperiment-I on a C-C-C-C $300\mu m$ square microplate with macrophage cells and corresponding trends of frequency based indices (experiment dates: June 11th 2009 - May 22th 2009)

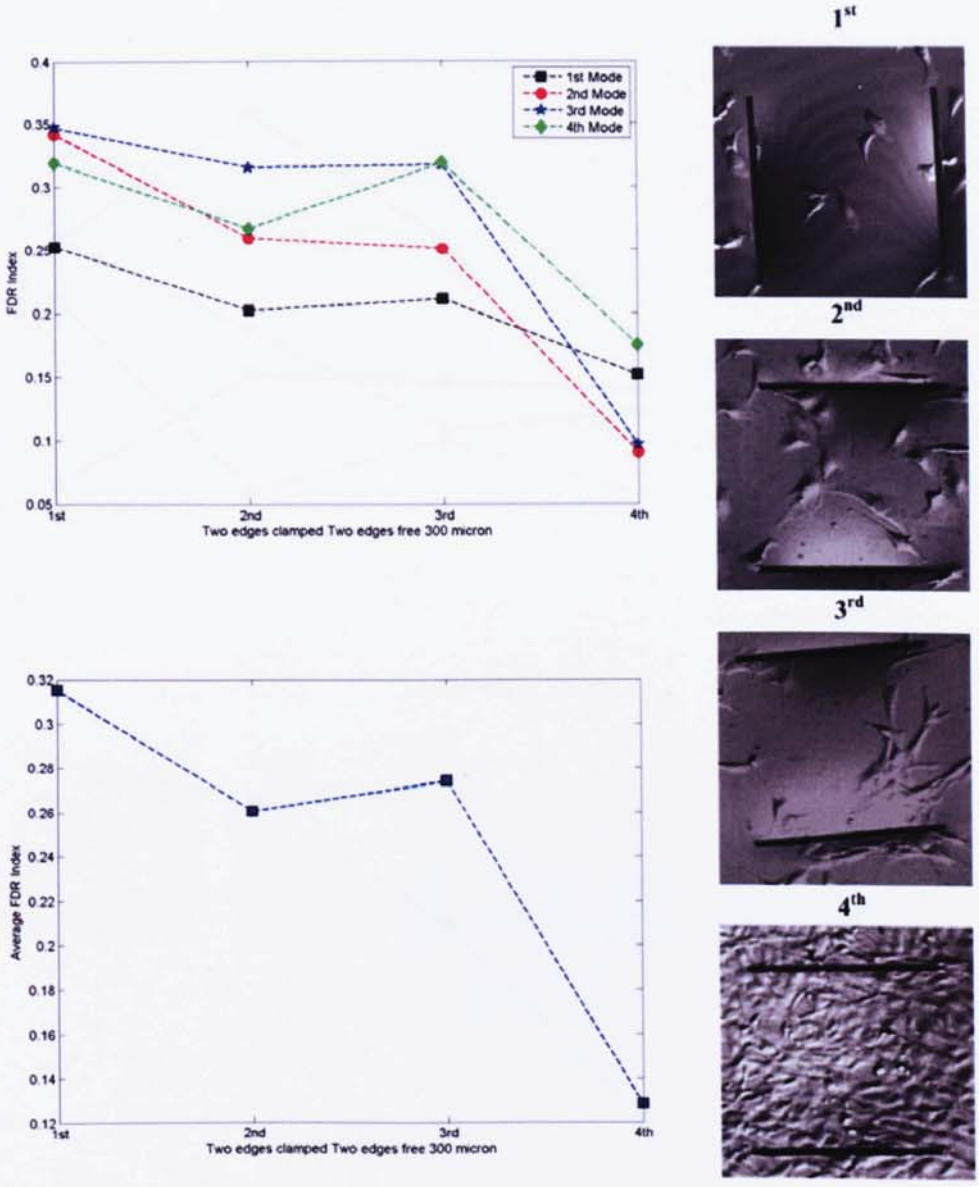

Figure 6.17: Results of a batch BioExperiment-II on four C-F-C-F 300μm square microplates with endothelial cells and corresponding trends of frequency based indices (experiment dates: Oct. 4th 2008 - Oct. 12th 2008)

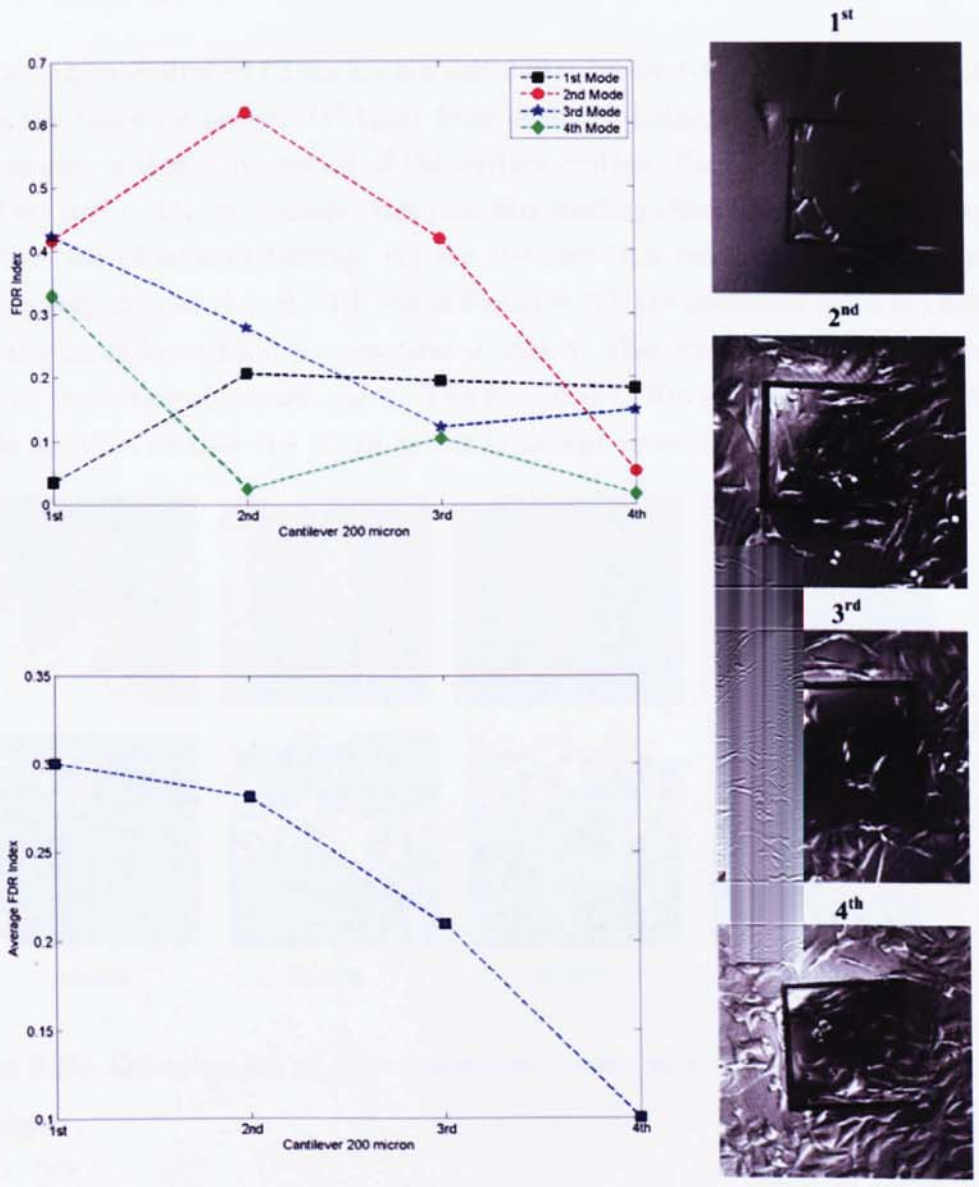

Figure 6.18: Results of a batch BioExperiment-I on a C-F-F-F 200μm square microplate with endothelial cells and corresponding trends of frequency based indices (experiment dates: Feb. 4th 2009 - Feb. 12th 2009)

6.4 Neural Network Method

On a whole, resonant frequency based indices either FDR_n or $AFDR$ are only able to predict the cell density with very limited accuracy. This is mainly due to the complication and nonlinearities of a microplate sensing system. Other algorithms are desired to perform more accurate and reliable identification on cell distribution from the measured dynamics data. In this section, a simple attempt that an artificial neural network technique to build the relationship between the sensory data and cell distribution is carried out.

6.4.1 Quantization of Cell Population

In the above experimental results, LSM images were used to intuitively presented the cell population in the microplate sensing domain. However a quantitative index is also necessary to indicate the number of cells for a more precise analysis. This is especially true for endothelial cells, the number of which are very hard to count. A simple image processing method was carried out on each LSM image to convert it into a binary image by using the MATLAB Image Processing Toolbox. Initially the LSM image is loaded and the most clear layer is selected for the following processes, as the LSM image taken under the reflection mode usually contains three layers. Then the background image of this LSM image is created by using morphological opening technique. Afterwards the background image is subtracted from the original image and the image contrast is enhanced, to highlight the domain of cells occupied. Finally the corresponding binary image is created, in which the background (microplate sensing area) is black and the parts of implanted cells are white. Therefore the cell population on the sensing domain can be approximately evaluated by the white area ratio in this binary image. This ratio is called cell density ratio (CDR) in this thesis. Figure 6.19 demonstrates the results of this evaluation processes on four different LSM images, which are obtained in a same batch of bio-experiments. It can be seen that the white region of each binary image can roughly indicate the shapes of endothelial cell

distribution, although some local errors exist in the binary images. The evaluated ratios of white region are also listed in the bottom of Figure 6.19.

However, these evaluated CDRs are not suitable to be used directly in the analysis due to the following points: (1)Apart from each cell bulge, the endothelial cells also generate a thin film over all of the culture surface. Each evaluated CDR is raised up $10\% \sim 15\%$ to consider this thin film loading effects, for distinguishing from the case of no cells loading; (2) For the case that cells covered nearly the whole sensing domain, i.e. the 4th one in Figure 6.19), the predicted value of CDR is usually much lower than the practical situation. Therefore the predicted value needs to be increased in such cases. The modified CDRs for each experimental sample are then used as the target values in neural network applications.

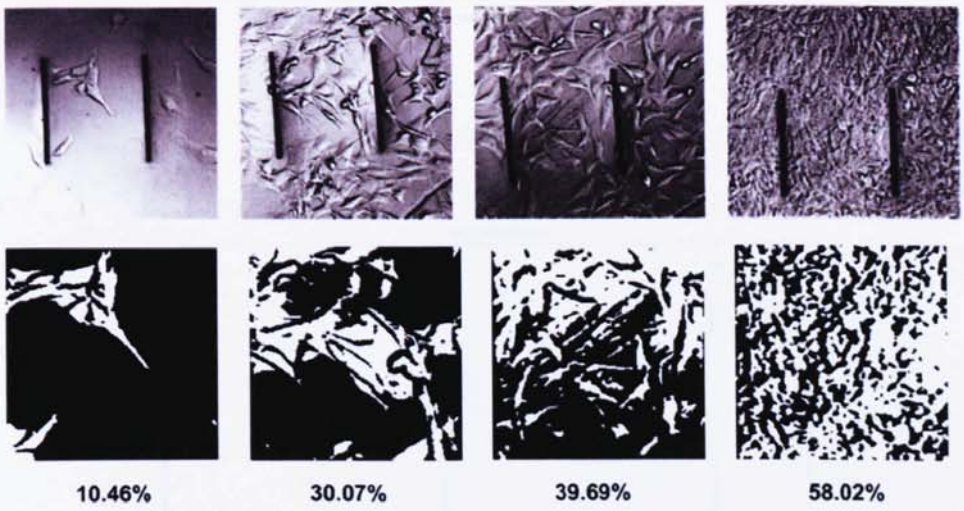

Figure 6.19: Quantization of cells population based on a simple image process technique

6.4.2 FRF Data Normalization and Order-Reduction

Although the experimental settings are the same for all the dynamic experiment, the amplitudes of every FRF measurements are varied due to different experimen-

tal environment and external disturbances. Consequently it is better to normalize the measured FRFs and scale them into a same level for comparison and analysis. On the other hand, there are multiple FRF datasets ($50 \sim 100$ for one microplate) in each dynamics measurement and each FRF dataset contains 6400 frequency spectral lines. Obviously such FRF datasets ($50 \sim 100 \times 6400$) are too large to directly apply into the neural network. Therefore the dimension of dataset has to be reduced before the application of neural network.

Only four FRF sets are chosen for each microplate to apply into the neural network. The Locations of selected sample points of FRF are in the same configuration as illustrated in Figure 5.8.

For the FRF normalization, it should be firstly converted into the relative motion according to Eq. 4.12. Then each FRF spectrum is normalized with respect to the amplitude of its own first resonant mode. The reason that choosing the first resonant mode as the reference is based on the theoretical analysis results in chapter 3, in which the mass loading has the slightest effects on the first resonant mode of a rectangular plate. Figure 6.20 illustrates the normalization results on a batch of FRFs. In plot (b) the amplitudes of all FRFs are roughly scaled into a very close range.

For the dimensionality reduction of FRF datasets, Karhunen-Loeve (K-L) decomposition method is used to extract the principal components on a multiple-FRF dataset. The Karhunen-Loeve (K-L) decomposition is a useful method to create low dimensional, reduced-order models of dynamical systems[134]. Assuming there are M FRFs with N frequency spectral lines in each dynamics measurement of a microplate, this dataset forms a $M \times N$ matrix $[H(\omega)]_{M\times N}$. The process of principal components extraction of the matrix $[H(\omega)]$ using Karhunen-Loeve (K-L) method has the following steps:

1. First, a correlation matrix $[C]_{M\times M}$ is defined based on the FRF matrix $[H(\omega)]_{M\times N}$.

$$[C]_{M\times M} = [H(\omega)]_{M\times N}[H(\omega)]^T_{N\times M} \tag{6.3}$$

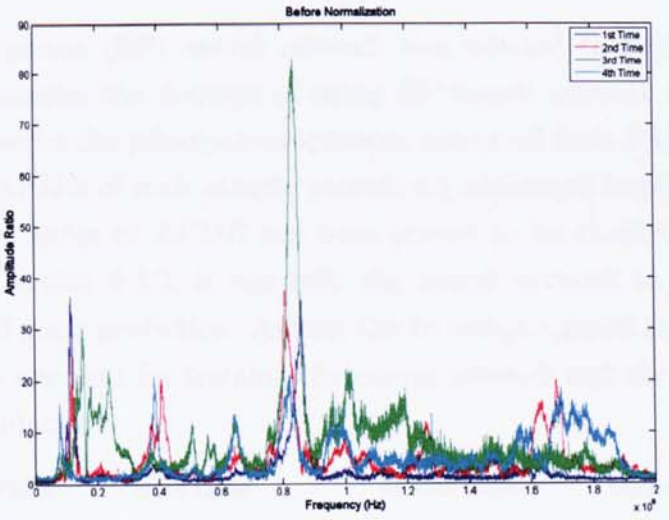

(a)

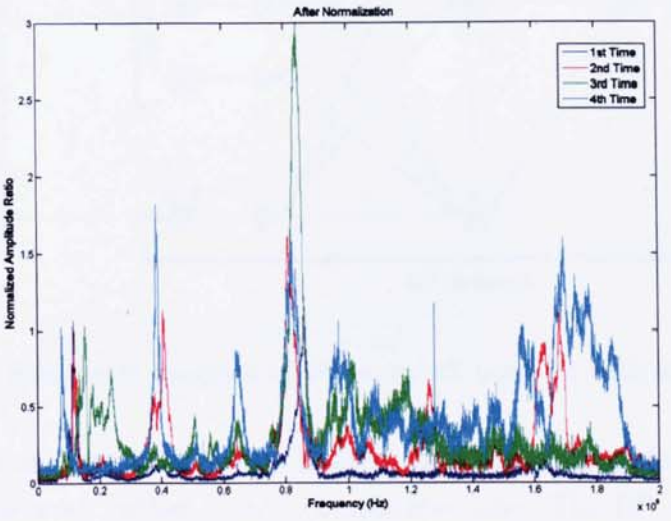

(b)

Figure 6.20: FRF normalization on a batch of experimental results

2. The principal components are then obtained from calculating the eigenvalues and corresponding eigenvectors of matrix $[C]$.

$$[C][X] = \lambda[X] \tag{6.4}$$

3. Finally, the M extracted eigenvalues are examined and the first few largest eigenvalues are selected. The eigenvectors associated with these largest eigenvalues are then considered to be the principal components and be able to represent the most significant information of the original FRF dataset.

6.4.3 Dataset of Samples Creation

The analytical results of resonant frequency based indices in section 6.3.2 illustrates that different types of microplates have very different sensitivities and behaviours in the detections of different cells. All the samples for the application of neural network herein are selected from the sensing results of $200\mu m$ C-F-C-F microplate on endothelial cell detection. Figures 6.8 and 6.9 have demonstrated 4 different samples of Bio-experiment I respectively. Another 4 different experimental samples obtained in one batch of Bio-experiment II are employed to extend the dataset. FRFs of 4 different microplates without any cell loading are provided in the dataset as the reference cases. Two extra samples are also selected, one is from the batch of Bio-experiment I and the other from Bio-experiment II. Consequently a total of 18 different samples are created for training and validation of the neural network. The eigenvectors related to the largest eigenvalue of FRF datasets of each sample are extracted as the neural network input and the CDR of every samples are calculated as the the neural network output. Table 6.4 lists the data of all the samples used in neural network.

Table 6.4: Extracted data of 18 samples used in neural network

No.	PCA1	PCA2	PCA3	PCA4	AFDR	CDR
1	0.6330	0.4871	0.5124	0.3153	0	0
2	0.5356	0.5047	0.5373	0.4118	0.0702	0.1784
3	0.6278	0.4798	0.5288	0.3099	0.2461	0.2514
4	0.6635	0.4472	0.4350	0.4130	0.3475	0.8066
5	0.5966	0.4022	0.5686	0.3987	0	0
6	0.4796	0.5804	0.5597	0.3461	0.1610	0.2546
7	0.5576	0.4222	0.5437	0.4640	0.2180	0.4527
8	0.4573	0.7273	0.3829	0.3396	0.3175	0.5469
9	0.5216	0.7969	0.2957	0.0737	0.4212	0.9879
10	0.6623	0.3719	0.5341	0.3712	0	0
11	0.5210	0.5194	0.6053	0.3040	0.1082	0.1752
12	0.3935	0.6100	0.5029	0.4692	0.1151	0.2535
13	0.6015	0.3586	0.4932	0.5161	0.1674	0.5583
14	0.6383	0.6356	0.2818	0.3304	0.1813	0.4531
15	0.6588	0.4494	0.5148	0.3147	0	0
16	0.6551	0.4584	0.4686	0.3757	0.0334	0.1093
17	0.5415	0.5578	0.5159	0.3597	0.2198	0.2726
18	0.6050	0.3408	0.6455	0.3182	0.3020	0.4185

6.4.4 Network Design and Training

The back-propagation (BP) neural network was selected to perform the task. Figure 6.21 illustrates the concept of using BP neural network to predict cell distribution. Besides the principal components extracted from FRF datasets, the value of index $AFDR$ of each sample provide an additional input to the neural network. As the index of $AFDR$ has been proved to be closely related to cell distribution in section 6.3.2, it can help the neural network to achieve a fast convergence and good prediction. Among the 18 samples listed in Table 6.4, the first 14 samples are used for training the neural network and the left 4 samples are used for validation.

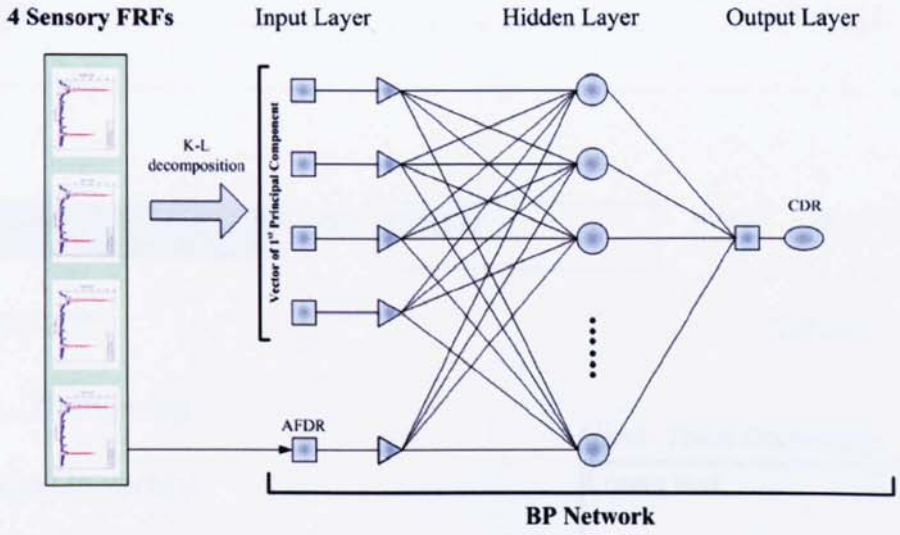

Figure 6.21: Schematic diagram of BP network used for cells identification

As the number of samples are very limited, it is sensible to design and use a simple neural network rather than a complicated one. The BP neural network used here is designed to have only one hidden layer with few neurons. Several trails with different number of hidden layer neurons were carried out to test the differences on the normalized system error. It is shown in Table 6.5 that the hidden layer with 5 neurons produces the best performance.

The training process of BP network is trying to setup an approximate function (nonlinear regression) between the inputs and output targets, through iteratively adjusting the weights and biases of the network to meet a setting goal (mean square error). The training parameters can affect the network convergence speed as well as the final predication accuracy. Bad parameters may lead to slow training process or over-fitting results. Several tests were carried out to determinate the suitable training parameters. The final training parameters used in this work are selected as: moment rate is 0.9, learning rate is 0.1, the max error is 0.001 and the max number of iteration is 3000.

Table 6.5: Normalized system error of the training process of BP network varies with the number of hidden layer neurons

No.	3	4	5	6	7	8
Err(%)	0.14	0.17	0.10	0.11	0.13	0.12

6.4.5 Prediction Results

Table 6.6 demonstrates the prediction results of CDR on samples No.15 $\sim$ No.18 obtained from the trained result of BP network using sample No.1 $\sim$ No.14. The prediction results are well matched to the CDR values calculated from corresponding LSM images.

Table 6.6: Prediction results on CDR

Sample No.	Calculated CDR (%)	Predicted CDR (%)	Error (%)
15	0	4.40	-
16	10.93	9.98	8.71
17	27.26	29.64	8.72
18	41.85	38.04	9.09

6.4.6 Discussion

This section demonstrates that a simple BP neural network can successfully predict the cell density from the extracted dynamic data of sensing microplate. The work presented in this section is a preliminary attempt, as the number of samples used in the neural network is limited and all the sensory data in dataset are of the same type microplate. Nevertheless it proves that the distributive sensing approach and artificial neural netwrok can be used to analyse the dynamics of the information output of the contacting biological cells.

6.5 Conclusion

The biosensing performances of microplates are examined in this chapter. A large number of bio-experiments using a series of different types of microplates have been implemented. First, the traditional method of evaluating the shifts of resonant frequencies due to the cell adhesion is employed to analyse experimental results. Although it is hard to achieve a fairly linear analytic conclusion using the resonant frequency based indices, it still demonstrates that microplates have attractive biosensing ability even under high-damping liquid conditions.

A novel methodology using the artificial neural network with a distributed sensing scheme on the microplate sensing surface is proposed to estimate the density of cell distribution. Karhunen-Loeve (K-L) decomposition method is successfully used to reduce the dimension of measured FRF datasets. Optimal parameters of a BP neural network are obtained based on a set of selected experimental samples. The final predicted results reveal that this methodology, using a neural-network based algorithm to perform the feature identification of biological particles from distributive sensory measurement, has great potential in the applications of biosensors.

Chapter 7

Conclusions and Future Work

7.1 Conclusions and Innovations of the Research

This thesis first investigated the dynamical characteristics of the fluid-loaded rectangular microplate, both theoretically and experimentally. The theoretical simulation results and experimental results on a series of microplates with different boundary conditions and dimensions are presented, compared and discussed. Then the impacts of fluid-loading on a microplate, such as *added mass, acoustic and viscous damping*, are fully studied. The dynamic investigation can be used to guide the design of biosensing systems. Then a series of novel biosensing integrated systems based on using the microplate as a sensing surface were designed, simulated and fabricated. A large number of bio-experiments were carried out to test the biosensing performances on different types of microplate. Several approaches including the neural network method are proposed and studied for the identification of cells coated on the microplates.

In chapter 3, two theoretical models were developed to study the dynamics of the fluid-loaded rectangular plates. The first one is based on Rayleigh-Ritz en-

ergy method. A very accurate solution for this model is achieved through using Pierce's integral technique and a series of closed-form solutions of the cross mode shape functions, which are demonstrated in appendix B. This first model is suitable to predict the natural frequencies and mode shapes of a series of rectangular plates, but it ignores all the system dampings. The second model is then designed to analyse the dampings of plates induced by the fluid-loading. The second theoretical model is built upon Guz's formulations for the problems of hydroelasticity for compressible viscous fluids. Both the acoustic damping and viscous damping are considered in this model. Numerical results for the second model are approximately solved using a Monte Carlo integration technique. It was proved by the numerical results that the acoustic damping of submerged microplates is much larger than the viscous damping, which can be ignored as long as the fluid viscosity is less than $10cP$.

Generally speaking, dynamic behaviour of fluid-structure interaction is a very fundamental and important engineering problem. However, most theories on this topic developed in previous research are limited to specific conditions. Therefore most engineering solutions for the question of fluid-structure interaction are obtained by using computation methods, such as FEM, BEM (Boundary Element Method) and SEA (Static Energy Analysis) etc. The two theoretical models developed in this thesis provide fairly complete analytical solutions for the linear dynamics analysis of fluid-loaded rectangular plates. The two models are able to be applied to most types of rectangular plates as long as their mode shape functions can be mathematically described. Furthermore the two theoretical models were applied to analyse the dynamics of microscale rectangular plates under fluid-loading. The numerical results on a series of different types of microplates form the fundamental knowledge on the research topic of this thesis, which is biosensing of cell properties.

Chapter 4 presents the work of experimental study of the dynamics of fluid-loaded microplates. The base-excitation method is the key technique used in this chapter. Theoretical analysis shows that relative motion of the microplates (or other testing structures) need to be evaluated for the modal analysis in the

base-excitation testing system. A dynamic testing system for the fluid-loaded microplates using a simple base-excitation apparatus was then realized. Pseudo-random signals also demonstrated their advantages in the modal testing of this work. A process of signal smoothing and modal parameter extraction using the RFP curve fitting method was applied to a series of microplates, with or without fluid-loading. The experimental results were then used to validate the theoretical models of chapter 3. The base-excitation approach is widely used to test the dynamics of microstructures; this work is the first investigation of this technique on dynamics testing in liquid environment.

The idea of the microsystems proposed in chapter 5 is novel compared with other biosensing systems. First of all the microplate is used as the biosensing platform in this microsystem. It has proved that microplates have attractive advantages for biosensing compared to microcantilevers. Furthermore, it would be able to work under high damping conditions. Additionally, the microsystems designed in this chapter have two innovations; one is the distributive sensors on the microplate sensing surface and the other is the working-mode of the microsystem. The layout of distributive sensors potentially enables the application of more sophisticated algorithms to extract information of cells density and distribution from a few sensing points. As the PZT actuator and piezoresistive sensors in the microsystem can work independently, the microsystem can work either under static mode or under dynamic mode.

The work employing the microplate as a biosensing platform is presented in chapter 6. The analytical results (based on resonant frequency indices) from a large number of bio-experiments reveal that different types of microplates have different biosensing performances. Moreover different microplates within the same type (size, boundary conditions) also show variations in the application of biosensing. This is mainly due to the problem of fabrication precision of microplates, which is discussed in chapter 4. The neural network method was employed to perform a more accurate identification for the cell distribution. In the application of the neural network method, the variations of same type microplates were overcome

since the neural network ultilises the inherant nonlinear coupling of sensing points to identify cell properties.

In a summary, the most important contributions we achieved in this research are listed as follow:

1. In the two theoretical models, some difficulties of obtaining the analytical solutions of the fluid-loaded rectangular plates are first solved in this area. Those approaches would also benefit to the research of general fluid-structure interaction problems.

2. Although there are many published works on the dynamics of plate, few of them provided experimental results. Our work contributes lots of experimental data on the dynamics of microscale plate without or with fluid-loading. Those experimental results are very useful to the further research of the dynamics of plates.

3. Lastly we proposed a new methodology that using a neural-network based algorithm to perform the features identification of biological particles from a distributive sensory measurement. This brand new concept is never appear in biosensing field before.

7.2 Limitations

An interesting phenomenon that the vibration of a fluid-loaded plate possesses multiple resonance with a same or very close mode shape, is observed both from the experimental results of this research in chapter 4 (ie. the plots (b) in Figures 4.15, 4.18 and 4.21) and the theoretical predictions from other researchers[135]. Obviously this multiple resonance phenomenon is generated by the non-linear dynamics of fluid-plate interaction, which can not be analysed using the proposed theoretical models. Only linear dynamics of microplate and fluid are considered

in the derivations of the the two proposed theoretical models proposed in chapter 3.

For the experimental testing system, it mainly suffers the issues of limited band of excitation frequency, external disturbances, difficulty of calibration and the inherent system error. The excitation frequency band is 2MHz due to the limitation of actuator used in this experimental system. Due to the shortages of base-excitation apparatus, the dynamic testing process is very readily affected by external disturbances. Strong noises and feak resonant peaks in the original FRF measurements have been shown in Figure 4.15 $\sim$ 4.23. This adds the difficulties for the post-process of measured FRFs. The amplitudes of the excited vibration of microplates depend on not only the excitation force (applied voltage) from actuator, but also the mass of the base. As the amount of water in the petri dish (base) varies in every experiment, the amplitudes of the measured FRFs are very difficult to calibrate.

The fabrication is challenging for the microsystem designed in chapter 5, especially on the process of PZT thin film deposition. Due to the complication of fabrication processes as illustrated in Figure 5.9, the cost of making such microsystems inevitably becomes high. Therefore it will limit the applications of this proposed microsystem.

Although a large number of batches of bio-experiments have been implemented in this work, the samples on each type of microplate are insufficient, especially for the application of neural network. The microplates are prone to be damaged in the cleaning process in the bio-experiment. The algorithms for cell identification from the sensory data of microplates were not adequately developed. Current methods (FDR, $AFDR$ and the BP neural network) can only estimate the vaules of cells density (population or mass). The prediction of shapes and positions (distribution) of cells will need further research.

7.3 Potential Applications

One of the most distinct achievement in this research is the designed and fabricated novel biosensing system. Although only two different type of biological cells are tested in the bio-experiments, this kind of biosensing platform is expected to have a wide range of applications (such as the protein and DNA detection) in the field of biosensing, as long as an appropriate identification method or algorithm is developed for the specific application.

In addition, the theoretical models built in this thesis are also very useful in the application of solving the general engineering problems of fluid-structure interactions. These theoretical models can help to form the added mass matrix and related damping matrix in the process of finite element analysis for complicated structures.

The dynamic testing system designed for the microplates can also be applied to test other types of microstructures. If the excitation frequency band can be raised, its applications can be then expanded into much a microstructures or even nanostructures.

7.4 Suggested Further Work

Both the dynamics testing and bio-experiments based on the microplates have been implemented in this thesis. This is only an important preliminary work on this research. In order to create a device (sensor) using the microplate as the transducer and apply it in practical biosensing tasks, the following work needs to be finished.

1. Many more bio-experiments on the selected types of microplates need to be completed to create a sufficient large database for the development the cell identification approach.

2. For specific biological applications, suitable, robust, reliable and accurate algorithms (neural networks) must be developed.

3. A lab-on-chip integrated system needs to be created, in which the biological cells can be cultured and detected and the corresponding information can be measured, recorded and analysed without the need for external measurement equipment.

Appendix A

Quasi-Monte Carlo Integration

Monte Carlo algorithms, also called computational random simulating method, is widely used to solve physical and mathematical problems(Wikipedia). It also provides a fast convergence way to integrate multi-dimensional function with a relative precise. Consider a n-dimensional Integrand function f which is defined in the domain V, randomly peaking N points $\{\xi_1, \xi_2, \cdots, \xi_N\}$ in this domain, then Monte Carlo integration method can be expressed in the following way[136],

$$\int_V f dV \approx V \cdot \frac{1}{N} \sum_{i=1}^{N} f(\xi_i) \tag{A.1}$$

Quasi-Monte Carlo(QMC) method employs deterministic sequence rather than random points in the evaluation procedures, in this way we can obtain a faster convergence rate of numerical integration and lower the corresponding expected errors. The most important characteristic of these deterministic sequences is that they are uniformly distributed in the integration domain V, called low discrepancy sequences[137]. There exists many ways to construct low discrepancy sequences, such as Faure, Halton, Hammersley, Sobol, Niederreiter and van der

Corput etc(Wikipedia). Here in this report, Halson sequences were used. The following MATLAB codes exhibit the algorithms of generating Halson sequences.

```
function HaltonSeq = HaltonS(N, base)
HaltonSeq = zeros(N,1);
for i=1:1:N
  HaltonSeq(i) = GenOneEleForHaltonSeq(i,base);
end

function outside = GenOneEleForHaltonSeq(index, base)
    localIndex = index;
    remainder = 0;
    outside = 0;
    fraction  = 1 / base;
    while localIndex > 0
        remainder = mod(localIndex,base);
        outside = outside + fraction*remainder;
        localIndex = fix(localIndex/base);
        fraction  = fraction/base;
    end
end
```

Appendix B

Closed-Form Solutions on the Integrations

The functions of $FX(u,m,q)$ or $FY(v,n,r)$ in chapter 3 can be expanded into the following form by substituting the mode shape functions. The case of only clamped boundary conditions is demonstrated, the other boundary conditions are similar.

$$FX(u,m,q) = I_1 + I_2 + I_3 + \cdots + I_{14} + I_{15} + I_{16} \tag{B.1}$$

where

$$I_1 = \int_u^1 \cosh(\epsilon_m x)\cosh(\epsilon_q(x-u))dx + \int_0^{1-u} \cosh(\epsilon_m x)\cosh(\epsilon_q(x+u))dx$$

$$I_2 = \int_u^1 \cos(\epsilon_m x)\cosh(\epsilon_q(x-u))dx + \int_0^{1-u} \cos(\epsilon_m x)\cosh(\epsilon_q(x+u))dx$$

$$I_3 = -\alpha_m \left[\int_u^1 \sinh(\epsilon_m x) \cosh(\epsilon_q (x-u)) dx + \int_0^{1-u} \sinh(\epsilon_m x) \cosh(\epsilon_q (x+u)) dx \right]$$

$$I_4 = \alpha_m \left[\int_u^1 \sin(\epsilon_m x) \cosh(\epsilon_q (x-u)) dx + \int_0^{1-u} \sin(\epsilon_m x) \cosh(\epsilon_q (x+u)) dx \right]$$

$$I_5 = \int_u^1 \cosh(\epsilon_m x) \cos(\epsilon_q (x-u)) dx + \int_0^{1-u} \cosh(\epsilon_m x) \cos(\epsilon_q (x+u)) dx$$

$$I_6 = \int_u^1 \cos(\epsilon_m x) \cos(\epsilon_q (x-u)) dx + \int_0^{1-u} \cos(\epsilon_m x) \cos(\epsilon_q (x+u)) dx$$

$$I_7 = \alpha_m \left[\int_u^1 \sinh(\epsilon_m x) \cos(\epsilon_q (x-u)) dx + \int_0^{1-u} \sinh(\epsilon_m x) \cos(\epsilon_q (x+u)) dx \right]$$

$$I_8 = -\alpha_m \left[\int_u^1 \sin(\epsilon_m x) \cos(\epsilon_q (x-u)) dx + \int_0^{1-u} \sin(\epsilon_m x) \cos(\epsilon_q (x+u)) dx \right]$$

$$I_9 = -\alpha_q \left[\int_u^1 \cosh(\epsilon_m x) \sinh(\epsilon_q (x-u)) dx + \int_0^{1-u} \cosh(\epsilon_m x) \sinh(\epsilon_q (x+u)) dx \right]$$

$$I_{10} = \alpha_q \left[\int_u^1 \cos(\epsilon_m x) \sinh(\epsilon_q (x-u)) dx + \int_0^{1-u} \cos(\epsilon_m x) \sinh(\epsilon_q (x+u)) dx \right]$$

$$I_{11} = \alpha_m \alpha_q \left[\int_u^1 \sinh(\epsilon_m x) \sinh(\epsilon_q (x-u)) dx + \int_0^{1-u} \sinh(\epsilon_m x) \sinh(\epsilon_q (x+u)) dx \right]$$

$$I_{12} = -\alpha_m \alpha_q \left[\int_u^1 \sin(\epsilon_m x) \sinh(\epsilon_q (x-u)) dx + \int_0^{1-u} \sin(\epsilon_m x) \sinh(\epsilon_q (x+u)) dx \right]$$

$$I_{13} = \alpha_q \left[\int_u^1 \cosh(\epsilon_m x) \sin(\epsilon_q (x-u)) dx + \int_0^{1-u} \cosh(\epsilon_m x) \sin(\epsilon_q (x+u)) dx \right]$$

$$I_{14} = -\alpha_q \left[\int_u^1 \cos(\epsilon_m x) \sin(\epsilon_q (x-u)) dx + \int_0^{1-u} \cos(\epsilon_m x) \sin(\epsilon_q (x+u)) dx \right]$$

$$I_{15} = -\alpha_m \alpha_q \left[\int_u^1 \sinh(\epsilon_m x) \sin(\epsilon_q (x-u)) dx + \int_0^{1-u} \sinh(\epsilon_m x) \sin(\epsilon_q (x+u)) dx \right]$$

$$I_{16} = \alpha_m \alpha_q \left[\int_u^1 \sin(\epsilon_m x) \sin(\epsilon_q (x-u)) dx + \int_0^{1-u} \sin(\epsilon_m x) \sin(\epsilon_q (x+u)) dx \right]$$

All of these above separated integrations can be solved as in the following closed forms.

$$I_1 = \frac{1}{2} \left[\frac{1}{2\epsilon_m} (e^{2\epsilon_m - \epsilon_m u} - e^{-2\epsilon_m + \epsilon_m u} - e^{\epsilon_m u} + e^{-\epsilon_m u}) + (e^{-\epsilon_m u} + e^{\epsilon_m u})(1-u) \right] \ (m = q)$$

$$I_1 = \frac{1}{4} \left(\frac{e^{\epsilon_m + \epsilon_q - \epsilon_q u}}{\epsilon_m + \epsilon_q} - \frac{e^{-\epsilon_m - \epsilon_q + \epsilon_q u}}{\epsilon_m + \epsilon_q} + \frac{e^{\epsilon_m - \epsilon_q + \epsilon_q u}}{\epsilon_m - \epsilon_q} - \frac{-e^{\epsilon_m + \epsilon_q - \epsilon_q u}}{\epsilon_m - \epsilon_q} - \right.$$
$$\frac{e^{\epsilon_m u}}{\epsilon_m + \epsilon_q} - \frac{-e^{\epsilon_m u}}{\epsilon_m + \epsilon_q} + \frac{e^{\epsilon_m u}}{\epsilon_m - \epsilon_q} - \frac{-e^{\epsilon_m u}}{\epsilon_m - \epsilon_q} +$$
$$\frac{e^{\epsilon_m + \epsilon_q - \epsilon_m u}}{\epsilon_m + \epsilon_q} - \frac{e^{-\epsilon_m - \epsilon_q + \epsilon_m u}}{\epsilon_m + \epsilon_q} + \frac{e^{\epsilon_m - \epsilon_q + \epsilon_m u}}{\epsilon_m - \epsilon_q} - \frac{-e^{\epsilon_m + \epsilon_q - \epsilon_m u}}{\epsilon_m - \epsilon_q} -$$
$$\left. \frac{e^{\epsilon_q u}}{\epsilon_m + \epsilon_q} - \frac{-e^{\epsilon_q u}}{\epsilon_m + \epsilon_q} + \frac{e^{\epsilon_q u}}{\epsilon_m - \epsilon_q} - \frac{-e^{\epsilon_q u}}{\epsilon_m - \epsilon_q} \right) (m \neq q)$$

$$I_2 = -\frac{1}{2(\epsilon_m^2+\epsilon_q^2)}\Big[e^{\epsilon_q-\epsilon_q u}(\epsilon_m\sin(\epsilon_m)+\epsilon_q\cos(\epsilon_m))-(\epsilon_m\sin(\epsilon_m u)+\epsilon_q\cos(\epsilon_m u))+$$
$$e^{-\epsilon_q+\epsilon_q u}(\epsilon_m\sin(\epsilon_m)-\epsilon_q\cos(\epsilon_m))-(\epsilon_m\sin(\epsilon_m u)-\epsilon_q\cos(\epsilon_m u))+$$
$$e^{\epsilon_q}(\epsilon_m\sin(\epsilon_m(1-u))+\epsilon_q\cos(\epsilon_m(1-u)))-e^{\epsilon_q u}\epsilon_q+$$
$$e^{-\epsilon_q}(\epsilon_m\sin(\epsilon_m(1-u))-\epsilon_q\cos(\epsilon_m(1-u)))-e^{-\epsilon_q u}(-\epsilon_q)\Big]$$

$$I_3 = -\frac{\alpha_m}{4\epsilon_m}(e^{2\epsilon_m-\epsilon_m u}+e^{-2\epsilon_m+\epsilon_m u}-e^{\epsilon_m u}) \quad (m=q)$$

$$I_3 = -\frac{1}{4}\alpha_m\Big[\frac{1}{\epsilon_m+\epsilon_q}(e^{\epsilon_m+\epsilon_q-\epsilon_q u}+e^{-\epsilon_m-\epsilon_q+\epsilon_q u}-e^{\epsilon_m u}+e^{-\epsilon_m u}+$$
$$e^{\epsilon_m+\epsilon_q-\epsilon_m u}+e^{-\epsilon_m-\epsilon_q+\epsilon_m u}-e^{\epsilon_q u}+e^{-\epsilon_q u})$$
$$+\frac{1}{\epsilon_m-\epsilon_q}(e^{\epsilon_m-\epsilon_q+\epsilon_q u}+e^{-\epsilon_m+\epsilon_q-\epsilon_q u}+e^{\epsilon_m u}+e^{-\epsilon_m u}+$$
$$e^{\epsilon_m-\epsilon_q+\epsilon_m u}+e^{-\epsilon_m+\epsilon_q-\epsilon_m u}+e^{\epsilon u}+e^{-\epsilon_q u})\Big] \quad (m\neq q)$$

$$I_4 = -\frac{\alpha_m}{2(\epsilon_m^2+\epsilon_q^2)}\Big[$$
$$e^{\epsilon_q-\epsilon_q u}(\epsilon_m\cos(\epsilon_m)-\epsilon_q\sin(\epsilon_m))-(\epsilon_m\cos(\epsilon_m u)-\epsilon_q\sin(\epsilon_m u))+$$
$$e^{-\epsilon_q+\epsilon_q u}(\epsilon_m\cos(\epsilon_m)+\epsilon_q\sin(\epsilon_m))-(\epsilon_m\cos(\epsilon_m u)+\epsilon_q\sin(\epsilon_m u))+$$
$$e^{\epsilon_q}(\epsilon_m\cos(\epsilon_m(1-u))-\epsilon_q\sin(\epsilon_m(1-u)))-e^{\epsilon_q u}\epsilon_m+$$
$$e^{-\epsilon_q}(\epsilon_m\cos(\epsilon_m(1-u))-\epsilon_q\sin(\epsilon_m(1-u)))-e^{-\epsilon_q u}\epsilon_m\Big]$$

$$I_5 = -\frac{1}{2(\epsilon_m^2+\epsilon_q^2)}\Big[$$
$$e^{\epsilon_m}(\epsilon_q \sin(\epsilon_q(1-u)) + \epsilon_m \cos(\epsilon_q(1-u))) - e^{\epsilon_m u}\epsilon_m +$$
$$e^{-\epsilon_m}(\epsilon_q \sin(\epsilon_q(1-u)) - \epsilon_m \cos(\epsilon_q(1-u))) + e^{-\epsilon_m u}\epsilon_m +$$
$$e^{\epsilon_m(1-u)}(\epsilon_q \sin(\epsilon_q) + \epsilon_m \cos(\epsilon_q)) - (\epsilon_q \sin(\epsilon_q u) + \epsilon_m \cos(\epsilon_q u)) +$$
$$e^{-\epsilon_m(1-u)}(\epsilon_q \sin(\epsilon_q) - \epsilon_m \cos(\epsilon_q)) - (\epsilon_q \sin(\epsilon_q u) - \epsilon_m \cos(\epsilon_q u))\Big]$$

$$I_6 = \sin(2\epsilon_m - \epsilon_m u)/(2\epsilon_m) + \cos(\epsilon_m u) - \sin(\epsilon_m u)/(2\epsilon_m) - \cos(\epsilon_m u)u \quad (m = q)$$

$$I_6 = \frac{1}{2}\Big[\frac{1}{\epsilon_m+\epsilon_q}(\sin(\epsilon_m+\epsilon_q-\epsilon_q u) - \sin(\epsilon_m u) + \sin(\epsilon_m+\epsilon_q-\epsilon_m u) - \sin(\epsilon_q u)) +$$
$$\frac{1}{\epsilon_m-\epsilon_q}(\sin(\epsilon_m-\epsilon_q+\epsilon_q u) - \sin(\epsilon_m u) + \sin(\epsilon_m-\epsilon_q-\epsilon_m u) + \sin(\epsilon_q u))\Big] \quad (m \neq q)$$

$$I_7 = \frac{\alpha_m}{2(\epsilon_m^2+\epsilon_q^2)}\Big[$$
$$e^{\epsilon_m}(\epsilon_q \sin(\epsilon_q(1-u)) + \epsilon_m \cos(\epsilon_q(1-u))) - e^{\epsilon_m u}\epsilon_m -$$
$$e^{-\epsilon_m}(\epsilon_q \sin(\epsilon_q(1-u)) - \epsilon_m \cos(\epsilon_q(1-u))) + e^{-\epsilon_m u}\epsilon_m +$$
$$e^{\epsilon_m(1-u)}(\epsilon_q \sin(\epsilon_q) + \epsilon_m \cos(\epsilon_q)) - (\epsilon_q \sin(\epsilon_q u) + \epsilon_m \cos(\epsilon_q u)) -$$
$$e^{-\epsilon_m(1-u)}(\epsilon_q \sin(\epsilon_q) - \epsilon_m \cos(\epsilon_q)) - (\epsilon_q \sin(\epsilon_q u) - \epsilon_m \cos(\epsilon_q u))\Big]$$

$$I_8 = \frac{\alpha_m}{2\epsilon_m}(\cos(2\epsilon_m - \epsilon_m u) - \cos(\epsilon_m u)) \quad (m = q)$$

$$I_8 = \frac{1}{2}\Bigg[\frac{1}{\epsilon_m+\epsilon_q}(\cos(\epsilon_m+\epsilon_q-\epsilon_q u)-\cos(\epsilon_m u)+\cos(\epsilon_m+\epsilon_q-\epsilon_m u)-\cos(\epsilon_q u))+$$
$$\frac{1}{\epsilon_m-\epsilon_q}(\cos(\epsilon_m-\epsilon_q+\epsilon_q u)-\cos(\epsilon_m u)+\cos(\epsilon_m-\epsilon_q-\epsilon_m u)-\cos(\epsilon_q u))\Bigg] \quad (m \neq q)$$

$$I_9 = -\frac{\alpha_q}{4}\Bigg[\frac{1}{\epsilon_m}(e^{2\epsilon_m-\epsilon_m u}+e^{-2\epsilon_m+\epsilon_m u}-$$
$$e^{\epsilon_m u}-e^{-\epsilon_m u})+(1-u)(1+e^{-1})(e^{-\epsilon_m u}-e^{\epsilon_m u})\Bigg] \quad (m=q)$$

$$I_9 = -\frac{\alpha_q}{4}\Bigg[\frac{1}{\epsilon_m+\epsilon_q}(e^{\epsilon_m+\epsilon_q-\epsilon_q u}+e^{-\epsilon_m-\epsilon_q+\epsilon_q u}-e^{\epsilon_m u}+e^{-\epsilon_m u}+$$
$$e^{\epsilon_m+\epsilon_q-\epsilon_m u}+e^{-\epsilon_m-\epsilon_q+\epsilon_m u}-e^{\epsilon_q u}+e^{-\epsilon_q u})-$$
$$\frac{1}{\epsilon_m-\epsilon_q}(e^{\epsilon_m-\epsilon_q+\epsilon_q u}+e^{-\epsilon_m+\epsilon_q-\epsilon_q u}+e^{\epsilon_m u}+e^{-\epsilon_m u}+$$
$$e^{\epsilon_m-\epsilon_q-\epsilon_m u}+e^{-\epsilon_m+\epsilon_q+\epsilon_m u}+e^{\epsilon_q u}+e^{-\epsilon_q u})\Bigg] \quad (m \neq q)$$

$$I_{10} = \frac{\alpha_q}{2(\epsilon_m^2+\epsilon_q^2)}\Bigg[$$
$$(e^{\epsilon_q-\epsilon_q u}-1)(\epsilon_m\sin(\epsilon_m)+\epsilon_q\cos(\epsilon_m))-(e^{-\epsilon_q+\epsilon_q u}-1)(\epsilon_m\sin(\epsilon_m)-\epsilon_q\cos(\epsilon_m))+$$
$$e^{\epsilon_q}(\epsilon_m\sin(\epsilon_m(1-u))+\epsilon_q\cos(\epsilon_m(1-u)))-e^{\epsilon_q u}\epsilon_q-$$
$$e^{-\epsilon_q}(\epsilon_m\sin(\epsilon_m(1-u))-\epsilon_q\cos(\epsilon_m(1-u)))-e^{-\epsilon_q u}\epsilon_q\Bigg]$$

$$I_{11} = \frac{\alpha_m\alpha_q}{2}\left[\frac{1}{2\epsilon_m}(e^{2\epsilon_m-\epsilon_m u}-e^{-2\epsilon_m+\epsilon_m u}-e^{\epsilon_m u}+e^{-\epsilon_m u})-(e^{-\epsilon_m u}+e^{\epsilon_m u})(1-u)\right] \quad (m=q)$$

$$I_{11} = \frac{\alpha_m \alpha_q}{4}\Bigg[\frac{1}{\epsilon_m + \epsilon_q}(e^{\epsilon_m+\epsilon_q-\epsilon_q u} - e^{-\epsilon_m-\epsilon_q+\epsilon_q u} - e^{\epsilon_m u} + e^{-\epsilon_m u} +$$
$$e^{\epsilon_m+\epsilon_q-\epsilon_m u} - e^{-\epsilon_m-\epsilon_q+\epsilon_m u} - e^{\epsilon_q u} + e^{-\epsilon_q u}) +$$
$$\frac{1}{\epsilon_m - \epsilon_q}(-e^{\epsilon_m-\epsilon_q+\epsilon_q u} + e^{-\epsilon_m+\epsilon_q-\epsilon_q u} + e^{\epsilon_m u} - e^{-\epsilon_m u} -$$
$$e^{\epsilon_m-\epsilon_q-\epsilon_m u} + e^{-\epsilon_m+\epsilon_q+\epsilon_m u} + e^{-\epsilon_q u} - e^{\epsilon_q u})\Bigg] \quad (m \neq q)$$

$$I_{12} = -\frac{\alpha_m \alpha_q}{2(\epsilon_m^2 + \epsilon_q^2)}\Bigg[e^{\epsilon_q-\epsilon_q u}(\epsilon_m \cos(\epsilon_m) - \epsilon_q \sin(\epsilon_m)) - (\epsilon_m \cos(\epsilon_m u) - \epsilon_q \sin(\epsilon_m u)) -$$
$$e^{-\epsilon_q+\epsilon_q u}(\epsilon_m \cos(\epsilon_m) + \epsilon_q \sin(\epsilon_m)) - (\epsilon_m \cos(\epsilon_m u) + \epsilon_q \sin(\epsilon_m u)) -$$
$$e^{\epsilon_q}(\epsilon_m \cos(\epsilon_m(1-u)) - \epsilon_q \sin(\epsilon_m(1-u))) - e^{\epsilon_q u}\epsilon_m -$$
$$e^{\epsilon_- q}(\epsilon_m \cos(\epsilon_m(1-u)) + \epsilon_q \sin(\epsilon_m(1-u))) - e^{-\epsilon_q u}\epsilon_m\Bigg]$$

$$I_{13} = -\frac{\alpha_q}{2(\epsilon_m^2 + \epsilon_q^2)}\Bigg[e^{\epsilon_m}(\epsilon_q \cos(\epsilon_q(1-u)) - \epsilon_m \sin(\epsilon_q(1-u))) - e^{\epsilon_m u}\epsilon_q +$$
$$e^{-\epsilon_m}(\epsilon_q \cos(\epsilon_q(1-u)) + \epsilon_m \sin(\epsilon_q(1-u))) - e^{-\epsilon_m u}\epsilon_q +$$
$$e^{\epsilon_m(1-u)}(\epsilon_q \cos(\epsilon_q) - \epsilon_m \sin(\epsilon_q)) - (\epsilon_q \cos(\epsilon_q u) - \epsilon_m \sin(\epsilon_q u)) +$$
$$e^{-\epsilon_m(1-u)}(\epsilon_q \cos(\epsilon_q) - \epsilon_m \sin(\epsilon_q)) - (\epsilon_q \cos(\epsilon_q u) - \epsilon_m \sin(\epsilon_q u))\Bigg]$$

$$I_{14} = \frac{\alpha_q}{2\epsilon_m}(\cos(2\epsilon_m - \epsilon_m u) - \cos(\epsilon_m u)) \quad (m = q)$$

$$I_{14} = \frac{\alpha_q}{2}\Bigg[\frac{1}{\epsilon_m + \epsilon_q}(\cos(\epsilon_m + \epsilon_q - \epsilon_q u) - \cos(\epsilon_m u) + \cos(\epsilon_m + \epsilon_q - \epsilon_m u) - \cos(\epsilon_q u)) +$$
$$\frac{1}{\epsilon_m - \epsilon_q}(-\cos(\epsilon_m - \epsilon_q + \epsilon_q u) + \cos(\epsilon_m u) - \cos(\epsilon_m - \epsilon_q - \epsilon_m u) + \cos(\epsilon_q u))\Bigg] \quad (m \neq q)$$

$$I_{15} = \frac{\alpha_m \alpha_q}{2(\epsilon_m^2 + \epsilon_q^2)} \Big[e^{\epsilon_m} (\epsilon_q \cos(\epsilon_q(1-u)) - \epsilon_m \sin(\epsilon_q(1-u))) - e^{\epsilon_m u} \epsilon_q -$$
$$e^{-\epsilon_m} (\epsilon_q \cos(\epsilon_q(1-u)) + \epsilon_m \sin(\epsilon_q(1-u))) + e^{-\epsilon_m u} \epsilon_q +$$
$$e^{\epsilon_m (1-u)} (\epsilon_q \cos(\epsilon_q) - \epsilon_m \sin(\epsilon_q)) - (\epsilon_q \cos(\epsilon_q u) - \epsilon_m \sin(\epsilon_q) u) -$$
$$e^{-\epsilon_m (1-u)} (\epsilon_q \cos(\epsilon_q) + \epsilon_m \sin(\epsilon_q)) + (\epsilon_q \cos(\epsilon_q u) + \epsilon_m \sin(\epsilon_q u)) \Big]$$

$$I_{16} = -\alpha_m \alpha_q \left[\frac{1}{2\epsilon_m} (\sin(2\epsilon_m - \epsilon_m u) - sin(\epsilon_m u)) - (1-u)\cos(\epsilon_m u) \right] \quad (m = q)$$

$$I_{16} = -\frac{\alpha_m \alpha_q}{2} \Big[\frac{1}{\epsilon_m + \epsilon_q} (\sin(\epsilon_m + \epsilon_q - \epsilon_q u) - \sin(\epsilon_m u) + \sin(\epsilon_m + \epsilon_q - \epsilon_m u) - \sin(\epsilon_q u) +$$
$$\frac{1}{\epsilon_m - \epsilon_q} (-\sin(\epsilon_m - \epsilon_q + \epsilon_q u) + \sin(\epsilon_m u) - \sin(\epsilon_m - \epsilon_q - \epsilon_m u) - \sin(\epsilon_q u)) \Big] \quad (m \neq q)$$

Appendix C

FEM Simulation Model for Designed Microsystems(Ansys APDL Codes)

```
!---------------------------------
! PZT actuated Microsystem Simulation, Zhangming Wu 2008 @ ASTON
! Reference: 1. VM231 (ANSYS Tutorial)
!            2. Francois Pigache, 2007,
!               Tutorial for ANSYS piezoelectric simulation
!---------------------------------

!*****************************************
! Initilize Ansys
!*****************************************
Finish
/clear                                          ! Clear previous work
/CWD, C:\PZTSimulation\Microsystem_2 ! Set work directory
```

```
/FILNAME, pzt_mems2_analysis, 1                ! Set job name

/prep7
!emunit,mks          !define units
csys,0              !define coordinate system

!*********************************************
! Geometrical Parameters of Microsystem
!*********************************************
uMKSV system, um, uN, uC
len_plate   = 200
width_plate = 200
th_plate    = 5
len_pzt     = 60
width_pzt   = 60
th_pzt      = 1
len_hinge   = 18
width_hinge = 12
y_offset1 = 0!(-width_plate + width_hinge)/2
y_offset2 = y_offset1
y_offset3 = 0!(width_plate - width_hinge)/2
y_offset4 = y_offset3

!*********************************************
! Design Microsytem Structures
!*********************************************
!silicon plate with pzt base
!A1
K, 1, len_plate/2,  width_plate/2
K, 2, -len_plate/2, width_plate/2
K, 3, -len_plate/2, -width_plate/2
K, 4, len_plate/2, -width_plate/2
A,4,3,2,1
```

```
!A2
K, 5, len_plate/2+len_hinge,  width_hinge/2+y_offset1
K, 6, len_plate/2,            width_hinge/2+y_offset1
K, 7, len_plate/2,            -width_hinge/2+y_offset1
K, 8, len_plate/2+len_hinge,  -width_hinge/2+y_offset1
A,8,7,6,5
!A3
K, 9,  len_plate/2+len_hinge+len_pzt,  width_pzt/2+y_offset2
K, 10, len_plate/2+len_hinge,          width_pzt/2+y_offset2
K, 11, len_plate/2+len_hinge,          -width_pzt/2+y_offset2
K, 12, len_plate/2+len_hinge+len_pzt,  -width_pzt/2+y_offset2
A,12,11,10,9
!A4
K, 13, -len_plate/2,              width_hinge/2+y_offset3
K, 14, -(len_plate/2+len_hinge), width_hinge/2+y_offset3
K, 15, -(len_plate/2+len_hinge), -width_hinge/2+y_offset3
K, 16, -len_plate/2,              -width_hinge/2+y_offset3
A,16,15,14,13
!A5
K, 17, -(len_plate/2+len_hinge),          width_pzt/2+y_offset4
K, 18, -(len_plate/2+len_hinge+len_pzt), width_pzt/2+y_offset4
K, 19, -(len_plate/2+len_hinge+len_pzt), -width_pzt/2+y_offset4
K, 20, -(len_plate/2+len_hinge),          -width_pzt/2+y_offset4
A,20,19,18,17
VOFFST, 1, th_plate  ! left hand, nagetive normal
VOFFST, 2, th_plate
VOFFST, 3, th_plate
VOFFST, 4, th_plate
VOFFST, 5, th_plate
!pzt actuators
BLC4, len_plate/2+len_hinge,
      (-width_pzt/2+y_offset2), len_pzt, width_pzt, th_pzt
BLC4, -(len_plate/2+len_hinge+len_pzt),
```

```
      (-width_pzt/2+y_offset4), len_pzt, width_pzt, th_pzt
!glue together
VSEL, ALL
VGLUE, ALL

!*****************
! Element Types
!*****************
ET, 1, solid98, 0    ! for pzt actuator
KEYOPT, 1, 3, 1
ET, 2, solid92       ! for silicon plate
ALLSEL

!*********************************************
! Materials Properties of PZT
!*********************************************
/com PZT4 Z-polarized
/com Stiffness Matrix
TB, ANEL, 1                              ! DEFINE STRUCTURAL TABLE
TBDATA, 1,  13.2E4, 7.1E4, 7.3E4         ! INPUT [C] MATRIX
TBDATA, 7,  13.2E4, 7.3E4
TBDATA, 12, 11.5E4
TBDATA, 16, 3.0E4
TBDATA, 19, 2.6E4
TBDATA, 21, 2.6E4
/com Piezo Matrix
TB,PIEZ,1                              ! DEFINE PIEZ. TABLE
TBDATA, 16, 10.5                       ! E61 PIEZOELECTRIC CONSTANT
TBDATA, 14, 10.5                       ! E52 PIEZOELECTRIC CONSTANT
TBDATA, 3,  -4.1                       ! E13 PIEZOELECTRIC CONSTANT
TBDATA, 6,  -4.1                       ! E23 PIEZOELECTRIC CONSTANT
TBDATA, 9,  14.1                       ! E33 PIEZOELECTRIC CONSTANT
/com Dielectric Matrix
```

```
MP, PERX, 1, 804.6                    ! PERMITTIVITY (X DIRECTION)
MP, PERY, 1, 804.6                    ! PERMITTIVITY (Y DIRECTION)
MP, PERZ, 1, 659.7                    ! PERMITTIVITY (Z DIRECTION)
/com Density
MP, DENS, 1 , 7500e-18

!*********************************************
! Materials Properties of Silicon
!*********************************************
density_si = 2330e-18
young_si   = 1.5e5
poisson_si = 0.17

MP, DENS, 2, density_si
MP, EX,   2, young_si
MP, NUXY, 2, poisson_si

!*******************************************
! ET & Material Affiliation
!*******************************************
VSEL, ALL
VSEL, S, LOC, Z, 0, th_pzt  !pzt actuators
VATT, 1, , 1                !pzt ET & Material 1
VSEL, ALL
VSEL, S, LOC, Z, -th_plate, 0      !silicon plate
VATT, 2, , 1                       !silicon ET & Material 2

ALLSEL

!*******************************************
! MESHING
!*******************************************
ESIZE, 10
```

```
VMESH, ALL
ALLSEL
FINISH

!*****************************************
! Apply Loads on Electrodes
!*****************************************
/PREP7
NSEL, S, LOC, Z, 0
NSEL, R, LOC, X,
len_plate/2+len_hinge, len_plate/2+len_hinge+len_pzt
NSEL, R, LOC, Y,
      -width_pzt/2+y_offset2, width_pzt/2+y_offset2
CP, 1, VOLT, ALL
*GET, n_ground1, NODE, 0, NUM, MIN
ALLSEL

NSEL, S, LOC, Z, 0
NSEL, R, LOC, X,
      -(len_plate/2+len_hinge+len_pzt), -(len_plate/2+len_hinge)
NSEL, R, LOC, Y,
      -width_pzt/2+y_offset4, width_pzt/2+y_offset4
CP, 1, VOLT, ALL
*GET, n_ground2, NODE, 0, NUM, MIN
ALLSEL
NSEL, S, LOC, Z, th_pzt
NSEL, R, LOC, X,
      len_plate/2+len_hinge, len_plate/2+len_hinge+len_pzt
NSEL, R, LOC, Y,
      -width_pzt/2+y_offset2, width_pzt/2+y_offset2
CP, 3, VOLT, ALL
*GET, n_supply1, NODE, 0, NUM, MIN
ALLSEL
```

```
NSEL, S, LOC, Z, th_pzt
NSEL, R, LOC, X,
      -(len_plate/2+len_hinge+len_pzt), -(len_plate/2+len_hinge)
NSEL, R, LOC, Y,
      -width_pzt/2+y_offset4, width_pzt/2+y_offset4
CP, 3, VOLT, ALL
*GET, n_supply2, NODE, 0, NUM, MIN
ALLSEL

D, n_ground1, VOLT, 0 ! Apply 0 voltage to the ground electrode
D, n_ground2, VOLT, 0
D, n_supply1, VOLT, 5 ! Apply 5 voltage to top electrode
D, n_supply2, VOLT, 5
ALLSEL

!*****************************************
! Boundary Conditions
!*****************************************
NSEL, S, LOC, Y, width_plate/2
NSEL, R, LOC, X, -len_plate/2, len_plate/2
D,ALL,UX,,,,,UY,UZ

NSEL, S, LOC, Y, -width_plate/2
NSEL, R, LOC, X, -len_plate/2, len_plate/2
D,ALL,UX,,,,,UY,UZ

NSEL, S, LOC, X, len_plate/2+len_hinge+len_pzt
!NSEL, R, LOC, Y, -width_pzt/2, width_pzt/2
D,ALL,UX,,,,,UY,UZ

NSEL, S, LOC, X, -(len_plate/2+len_hinge+len_pzt)
!NSEL, R, LOC, Y, -width_pzt/2, width_pzt/2
D,ALL,UX,,,,,UY,UZ
```

```
ALLSEL
FINISH

!*****************************************
! Static Analysis
!*****************************************
/SOLU
ANTYPE, STATIC
SOLVE
FINISH

!*****************************************
! Modal Analysis
!*****************************************
!/SOLU
!ANTYPE, MODAL
!MODOPT,LANB,3,10000,20000000, ,ON
!solve
!finish
!/POST1
!SET,LIST
!FINISH

!*****************************************
! Harmonic Analysis
!*****************************************
!/SOLU
!ANTYPE, HARMIC
!HARFRQ,500,30000,
!NSUBST,200
!SOLVE
!FINISH
```

Appendix D

Simulation Source Codes

All the simulation routines developed and all original and analytic resutls in this thesis are provided in a Disk. The following table lists the catalogues and gives a short description on the contents.

Table D.1: Simulation Source Codes Lists

MicroClamped	This folder contains the m files (MATLAB) developed on Rayleigh-Ritz theoretical model that can generate simulation results on natural frequencies and mode shapes of C-C-C-C microplates. Outputs of functions in U_mnqr.m, Tp_mnqr.m and Tf_mnqr.m files are three key coefficients of Rayleigh-Ritz model.

MicroCantilever	For C-F-F-F microplates on Rayleigh-Ritz model.
Micro2C2F	For C-F-C-F microplates on Rayleigh-Ritz model.
DampingClamped	This folder contains the routines (MATLAB) that can generate the FRFs for C-C-C-C microplates under different damping conditions. Functions in Imnqr.m, Imnqr01.m and Imnqr00.m files are the fluid-loading impedances of microplate for the cases of assuming fluid to be viscous compressible, inviscous compressible and inviscous incompressible, respectively.
DampingCantilever	For damping analysis of C-F-F-F microplates.
Damping2C2F	For damping analysis of C-F-C-F microplates.
DynamicExp	The programme provided in this folder are used to process the experimental data of microplates. MPE.m is the function designed to estimate modal parameters from the original data. This folder also contains all the dynamic experimental results for different types and sizes of microplates.
Bioplates	The routines in this folder are used to analyse the bio-experimental results. Both the original data and processed results from the bio-experiments were also copied into this folder.
NNplates	This folder contains the source codes of a BP neural network used in this thesis, as well as the data process mehods (normalization and PCA).

References

[1] O.B. Ozdoganlar, B.D. Hansche, and T.G. Carne. Experimental modal analysis for microelectromechanical systems. *Experimental Mechanics*, 45 (6):498–506, 2005. 1, 20, 21, 88, 89, 90

[2] M. Elliot. *A smart sensing platform for the discrimination of human movement.* PhD thesis, Department of Engineering Systems and Managemen, Aston University, 2007. 3

[3] H.S. Tzou and C.I. Tseng. Distributed piezoelectric sensor/actuator design for dynamic measurement/control of distributed parameter systems: a piezoelectric finite element approach. *Journal of Sound and Vibration*, 138 (1):17–34, 1990. 3

[4] F. Mustapha, G. Manson, and K. Worden. Damage location in an isotropic plate using a vector of novelty indices. *Mechanical Systems and Signal Processing*, 21(4):1885–906, 2007. 3

[5] J. B. Ihn and F. K. Chang. Damage location in an isotropic plate using a vector of novelty indices. *Mechanical Systems and Signal Processing*, 13(3): 609–20, 2004. 3

[6] Liviu Nicu and C. Ayela. Micromachined piezoelectric membranes with high nominal quality factors in newtonian liquid media: A lamb's model validation at the microscale. *Sensors and Actuators B (Chemical)*, 123(2): 860–868, 2007. 4, 30, 37, 72, 73

[7] E. T. Carlen, M. S. Weinberg, C. E. Dub, A. M. Zapata, and J. T. Borenstein. Micromachined silicon plates for sensing molecular interactions. *Applied Physics Letters*, 89(17):173123–173124, 2006. 4, 27, 28

[8] A.W. Leissa. The free vibration of rectangular plates. *Proceedings A of the Royal Society*, 31(3):257–293, 1973. 11

[9] W. Leissa. *Vibration of Plates.* Scientific and Technical Information Division, National Aeronautics and Space Administration, US, 1969. 11, 34

[10] R. D. Blevins. *Formulas for natural frequency and mode shape.* Robert E. Krieger Publishing Company, 1979. 11, 83

[11] G.B. Warburton. The vibration of rectangular plates. *Proceedings A of the Institution of Mechanical Engineers*, 168:371–384, 1954. 11

[12] S.F. Bassily and S.M. Dickinson. On the use of beam functions for problems of plates involving free edge. *Transactions of the ASME. Series E, Journal of Applied Mechanics*, 42(4):858–864, 1975. 11

[13] D.J. Gorman. *Vibration Analysis of Plates by the Superposition Method.* World Scientific Publishing Co Pte Ltd, 1999. 11

[14] D.J. Gorman. Free vibration analysis of cantilever plates by the method of superpositionn. *Journal of Sound and Vibration*, 49(4):453–467, 1976. 11

[15] C.G. Boay. Free vibration of rectangular isotropic plates with and without a concentrated mass. *Computers and Structures*, 48(3):529–533, 1993. 11, 41

[16] C. Rajalingham, R.B. Bhat, and G.D. Xistris. Vibration of rectangular plates using plate characteristic functions as shape functions in the Rayleigh-Ritz method. *Journal of Sound and Vibration*, 193(2):497–509, 1996. 11

[17] R.S. Groves and R.L. Clark. Comments on the natural frequencies of rectangular plates derived from the Rayleigh-Ritz method. *Journal of Sound and Vibration*, 217(3):579–584, 1998. 11

[18] H. Lamb. On the vibrations of an elastic plate in contact with water. *Proceedings of the Royal Society of London*, 98(A):205–216, 1921. 12

[19] M.K. Kwak. Vibration of circular plates in contact with water. *Journal of Applied Mechanics*, 58(2):480–483, 1991. 12, 37, 38, 81

[20] M.K. Kwak. Vibration of circular membranes in contact with water. *Journal of Sound and Vibration*, 178(5):688–690, 1994. 12

[21] M.K. Kwak. Hydroelastic vibration of rectangular plates. *Journal of Applied Mechanics*, 63(1):110–115, 1996. 12, 47

[22] C. Liang, C. Liao, Y. Tai, and W. Lai. The free vibration analysis of submerged cantilever plates. *Ocean Engineering*, 28(9):1225–1245, 2001. 12

[23] H.G. Davies. Low frequency random excitation of water-loaded rectangular plates. *Journal of Sound and Vibration*, 15(1):107–126, 1971. 12, 13

[24] M. Lax. The effect of radiation on the vibrations of a circular diaphragm. *Journal of the Acoustical Society of America*, 16:5–13, 1944. 12, 36

[25] M. C. Junger and D. Feit. *Sound, Structures and Their Interaction.* The MIT Press, Cambridge, Massachusetts, 1972. 12, 13, 33, 36, 37, 53, 58, 72

[26] A.D. Pierce, R.O. Cleveland, and M. Zampolli. Radiation impedance matrices for rectangular interfaces within rigid baffles: Calculation methodology and applications. *Journal of the Acoustical Society of America*, 111(2): 672–684, 2002. 13, 14, 37, 41, 42

[27] J.W.S. Rayleigh. *Theory of Sound, Vol. 2.* WDover Publications; 2nd edition, 1976. 13

[28] C.E. Wallace. Radiation resistance of a rectangular panel. *Journal of the Acoustical Society of America*, 51(3):946–52, 1972. 13

[29] L.D. Pope and R.C. Leibowitz. Intermodal coupling coefficients for a fluid-loaded rectangular plate. *Journal of the Acoustical Society of America*, 56 (2):408–415, 1974. 13

[30] Y.M. Chang and P. Leehey. Acoustic impedance of rectangular panels. *Journal of Sound and Vibration*, 64(2):243–256, 1996. 13, 14, 58

[31] W.L. Li. An analytical solution for the self- and mutual radiation resistances of a rectangular plate. *Journal of Sound and Vibration*, 245(1):1–16, 2001. 13

[32] W.R. Graham. High-frequency vibration and acoustic radiation of fluid-loaded plates. *Philosophical Transactions of the Royal Society, Series A*, 352(1698):1–43, 1995. 13, 58, 63

[33] W.R. Graham. Analytical approximations for the modal acoustic impedances of simply supported, rectangular plates. *Journal of the Acoustical Society of America*, 12(2):719–730, 2007. 13, 37

[34] B.E. Sandman. Fluid loaded vibration of an elastic plate carrying a concentrated mass. *Journal of the Acoustical Society of America*, 61(6):1503–1510, 1977. 14, 17

[35] P. C. Chowdhury. Fluid finite elements for added-mass calculations. *International Shipbuilding Progress*, 19(217):302–309, 1972. 14

[36] Marcus and S. Melvyn. Finite-element method applied to the vibration of submerged plates. *Journal of Ship Research*, 22(2):94–99, 1978. 14

[37] J.A. Deruntz and T.L. Geers. Added mass computation by the boundary integral method. *International Journal for Numerical Methods in Engineering*, 12(3):531–550, 1978. 14

[38] H. Huang and Y.F. Wang. Asymptotic fluid-structure interaction theories for acoustic radiation prediction. *Journal of the Acoustical Society of America*, 77(4):1389–1394, 1985. 14

[39] B. S. Massey. *Mechanics of Fluids.* Van NOstrand Reinhold Company, Letchworth, Hertfordshire, 1970. 14, 51

[40] C. Atkinson and M. Manrique de Lara. The frequency response of a rectangular cantilever plate vibrating in a viscous fluid. *Journal of Sound and Vibration*, 300(1):352–367, 2007. 14, 16, 37

[41] J. E. Sader. Frequency response of cantilever beams immersed in viscous fluids with applications to the atomic force microscope. *Journal of applied physics*, 84(1):64–76, 1998. 15, 31, 71

[42] G.Y. Chen, R.J. Warmack, T. Thundat, D.P. Allison, and A. Huang. Resonance response of scanning force microscopy cantilevers. *Review of Scientific Instruments*, 65(8):2532–2537, 1994. 15

[43] W.Y. Shih, X. Li, H. Gu, W. H. Shih, and I.A Aksay. Simultaneous liquid viscosity and density determination with piezoelectric unimorph cantilevers. *Journal of Applied Physics*, 89(2):1497–1505, 2001. 15

[44] J.W.M. Chon, P. Mulvaney, and J.E. Sader. Experimental validation of theoretical models for the frequency response of atomic force microscope cantilever beams immersed in fluids. *Journal of Applied Physics*, 87(8): 3978–3988, 2000. 15

[45] Y.H. Chen and W.H. Huang. Resonant response of rectangular afm cantilever in liquid. *Chinese Physics Letters*, 24(2):363–365, 2007. 15

[46] P. Decuzzi, A. Granaldi, and G. Pascazio. Dynamic response of microcantilever-based sensors in a fluidic chamber. *Journal of Applied Physics*, 101(2):024303–1–6, 2007. 15

[47] S. Basak and A. Raman. Hydrodynamic loading of microcantilevers vibrating in viscous fluids. *Journal of applied physics*, 99(11):114906–1–14906–10, 2006. 15, 71

[48] J.L. Dohner. The contribution of radiation and viscous loss in a fluid loaded flexural plate wave sensor. *Journal of Sound and Vibration*, 217(1):113–126, 1998. 16

[49] S.V. Sorokin and A.V. Chubinskij. On the role of fluid viscosity in wave propagation in elastic plates under heavy fluid loading. *Journal of Sound and Vibration*, 311(3-5):1020–1038, 2008. 16

[50] A. N. GUZ. Problems of hydroelasticity for compressible viscous fluids. *International Applied Mechanics*, 27(1):1–12, 1991. 16, 51

[51] A. N. GUZ. Compressible, viscous fluid dynamics. part i. *International Applied Mechanics*, 36(1):14–39, 2000. 16, 51

[52] A. N. GUZ. Dynamics of rigid bodies in an incompressible viscous fluid (quiescent liquid). *International Applied Mechanics*, 17(3):207–223, 1981. 16

[53] O. Kopmaz and S. Telli. Free vibrations of a rectangular plate carrying a distributed mass. *Journal of Sound and Vibration*, 251(1):323–40, 2002. 17

[54] W.O. Wong. The effects of distributed mass loading on plate vibration behavior. *Journal of Sound and Vibration*, 253(3):577–83, 2002. 17, 33

[55] R.M. Lin and W.J. Wang. Structural dynamics of microsystemscurrent state of research and future directions. *Mechanical Systems and Signal Processing*, 20(5):1015–43, 2006. 17, 18, 20

[56] D.S. Epp, O.B. Ozdoganlar, P.M. Hansche, and T.G. Carne. A base excitation test facility for dynamic testing of microsystems. *Proc. 22nd Int. Modal Analysis Conf. (IMAC) (Dearborn, MI, 2629 January 2004)*, page 2629, 2004. 17, 19, 92, 94

[57] D.J. IJntema and H.A.C. Tilmans. Non-destructive resonant frequency measurement on mems actuators. *Sensors and Actuators A*, A35(2):121–128, 1992. 18

[58] D.J. Burns and H.F. Helbig. Non-destructive resonant frequency measurement on mems actuators. *Journal of Microelectromechanical Systems*, 8(4): 473–482, 1999. 18

[59] N.F. Smith, D.M. Tanner, S.E. Swanson, and S.L. Miller. Non-destructive resonant frequency measurement on mems actuators. *Proceedings of International Reliability Physics Symposium*, pages 99–105, 2001. 18

[60] H.A.C. Tilmans, D.J. IJntema, and J.H.J. Fluitman. Single element excitation and detection of (micro-)mechanical resonators. *International Conference on Solid-State Sensors and Actuators*, 8(4):533–537, 1991. 18

[61] S.M. Swei, P. Gao, and R. Lin. A dynamic analysis for the suspension structure in hard disk drives using piezofilm actuators. *Smart Materials and Structures*, 10(2):409–413, 2001. 18

[62] M. Khoo and C. Liu. Micro magnetic silicone elastomer membrane actuator. *Sensors and Actuators A*, 89(3):259–266, 2001. 18

[63] C.J. Wilson and D.B. Bogy. An experimental modal analysis technique for miniature structures. *Journal of Vibration and Acoustics*, 118(1):1–9, 1996. 18

[64] B. Charlot, S. Mir, F. Parrain, and B. Courtois. Electrically induced stimuli for mems self-test. *Proceedings 19th IEEE VLSI Test Symposium*, pages 210–215, 2001. 18

[65] N. Dumas, F. Azais, L. Latorre, and P. Nouet. Electro-thermal stimuli for mems testing in fsbm technology. *Journal of Electronic Testing: Theory and Applications*, 22(2):189–198, 2006. 18

[66] Y.M. Amraoui and N.A.J. Lieven. Noncontacting excitation and measurement of light structures. *Journal of Vibration and Acoustics*, 125(1):114–119, 2003. 18

[67] J.G. Beliveau, F.R. Vigneron, Y. Soucy, and S. Draisey. Modal parameter estimation from base excitation. *Journal of Sound and Vibration*, 107(3): 435–49, 1986. 19, 21, 88, 91, 98

[68] Yuan-Fang Chou and Li-Chung Wang. On the modal testing of microstructures: its theoretical approach and experimental setup. *Journal of Vibration and Acoustics*, 123(1):104–109, 2001. 19, 88

[69] Wen-Pin Lai and Weileun Fang. Novel bulk acoustic wave hammer to determinate the dynamic response of microstructures using pulsed broad bandwidth ultrasonic transducers. *Sensors and Actuators A*, 96:43–52, 2002. 19

[70] M. Hu, J. Xie, S. Ling, H. Du, and Y. Fu. Dynamic testing of micro devices using pzt base excitation. *Proceedings of the SPIE - The International Society for Optical Engineering*, 5852(1):633–638, 2005. 19

[71] Clarence W. De Silva. *Vibration and Shock Handbook.* CRC Press, 2005. 19, 40, 98

[72] P. Avitabile. Modal space: back to basics [modal analysis]. *Experimental Techniques*, 29(2):15–16, 2005. 20

[73] M.J. Lowrey. Use of correlation techniques in vibration studies of plate systems. *Experimental Mechanics*, 29(2):476–481, 1975. 20, 95

[74] L. Rufer, S. Mir, E. Simeu, and C. Domingues. On-chip pseudorandom mems testing. *Journal of Electronic Testing: Theory and Applications*, 21 (3):233–241, 2005. 20

[75] M. H. Richardson and D. L. Formenti. Parameter estimation from frequency response measurements using rational fraction polynomials. *Proceedings of the International Modal Analysis Conference*, pages 167–181, 1982. 21, 102, 103

[76] Jyh-Chiang Lee and Yuan-Fang Chou. Driven-base modal parameter estimation for continuous structure. *Journal of Vibration and Acoustics*, 1: 711–718, 1991. 21, 88

[77] Kyung Wook Wee, Ghi Yuun Kang, Jaebum Park, Ji Yoon Kang, Dae Sung Yoon, Jung Ho Park, and Tae Song Kim. Novel electrical detection of label-free disease marker proteins using piezoresistive self-sensing microcantilevers. *Biosensors and Bioelectronics*, 20(10):1932–1938, 2005. 21, 23, 26

[78] Dazhong Jin, Xinxin Li, Jian Liu, Guomin Zuo, Yuelin Wang, Min Liu, and Haitao Yu. High-mode resonant piezoresistive cantilever sensors for tens-femtogram resoluble mass sensing in air. *Journal of Micromechanics and Microengineering*, 16(5):1017–23, 2006. 21, 23

[79] J. Lu, T. Ikehara, Y. Zhang, T. Mihara, T. Itoh, and R. Maeda. High quality factor silicon cantilever driven by pzt actuator for resonant based mass detection. *2008 Symposium on Design, Test, Integration and Packaging of MEMS/MOEMS*, pages 60–5, 2008. 22, 124

[80] Il-Han Hwang and Jong-Hyun Lee. Self-actuating biosensor using a piezoelectric cantilever and its optimization. *Journal of Physics: Conference Series*, 34(1):362–7, 2006. 22

[81] Wonkyu Moon, Yeolho Lee, and G. Lim. A self-excited micro cantilever biosensor actuated by pzt using the mass micro balancing technique. *Sensors and Actuators A (Physical)*, 130-131:105–10, 2006. 22

[82] Hyung Joon Kim, Yong Bum Kim, Jaebum Park, and Tae Song Kim. Biological element detection sensor application of micromachined pzt thick film cantilever. *Proceedings of IEEE Sensors 2003 (IEEE Cat. No.03CH37498)*, 2:1054–8, 2003. 22

[83] J. Lu, T. Ikehara, Y. Zhang, R. Maeda, and T. Mihara. Energy dissipation mechanisms in lead zirconate titanate thin film transduced micro cantilevers. *Japanese Journal of Applied Physics, Part 1*, 45(11):8795–800, 2006. 22, 23

[84] Jian Lu, Tsuyoshi Ikehara, Yi Zhang, Takashi Mihara, Toshihiro Itoh, and Ryutaro Maeda. Characterization and improvement on quality factor of microcantilevers with self-actuation and self-sensing capability. *Microelectronic Engineering*, 86(4-6):1208–1211, 2009. 22

[85] Marc J. Madou. *Fundamentals of Microfabrication: The Science of Miniaturization, Second Edition.* CRC, 2002. 23, 125

[86] J. Cho, M. Anderson, R. Richards, D. Bahr, and C. Richards. Optimization of electromechanical coupling for a thin-film pzt membrane: I. modeling. *Journal of Micromechanics and Microengineering*, 15(10):1797–1803, 2005. ISSN 09601317. 23

[87] J. Cho, M. Anderson, R. Richards, D. Bahr, and C. Richards. Optimization of electromechanical coupling for a thin-film pzt membrane: Ii. experiment. *Journal of Micromechanics and Microengineering*, 15(10):1804–1809, 2005. ISSN 09601317. 23

[88] J.E.A. Southin and R.W. Whatmore. Finite element modelling of nanostructured piezoelectric resonators (napiers). *IEEE Transactions on Ultrasonics, Ferroelectrics and Frequency Control*, 51(6):654–62, 2004. ISSN 0885-3010. 23, 126, 128

[89] Jian Lu, Tsuyoshi Ikehara, Takeshi Kobayashi, Ryutaro Maeda, and Takashi Mihara. Quality factor of micro cantilevers transduced by piezoelectric lead zirconate titanate film. *Microsystem Technologies*, 13(11-12): 1517–1522, 2007. ISSN 09467076. 23

[90] Jae Hong Park, Tae Yun Kwon, Dae Sung Yoon, Hwan Kim, and Tae Song Kim. Fabrication of microcantilever sensors actuated by piezoelectric pb(zr0.52ti0.48)o3 thick films and determination of their electromechanical characteristics. *Advanced Functional Materials*, 15(12):2021–8, 2005. ISSN 1616-301X. 23

[91] F.F.C. Duval, S.A. Wilson, G. Ensell, N.M.P. Evanno, M.G. Cain, and R.W. Whatmore. Characterisation of pzt thin film micro-actuators using a silicon micro-force sensor. *Sensors and Actuators A (Physical)*, 133(1): 35–44, 2007. ISSN 0924-4247. 23, 24

[92] S. Kon, K. Oldham, and R. Horowitz. Piezoresistive and piezoelectric mems strain sensors for vibration detection. *Proceedings of the SPIE - The International Society for Optical Engineering*, 6529:65292V–11, 2007. 23

[93] Xianghong Ma and P.N. Brett. The performance of a 1-d distributive tactile sensing system for detecting the position, weight, and width of a contacting load. *IEEE Transactions on Instrumentation and Measurement*, 51(2):331–6, 2002. 24

[94] Barbara M. Cowie, David J. Webb, Betty Tam, Paul Slack, and Peter N. Brett. Distributive tactile sensing using fibre bragg grating sensors for biomedical applications. *Proceedings of the First IEEE/RAS-EMBS International Conference on Biomedical Robotics and Biomechatronics, 2006, BioRob 2006*, 2006:312–317, 2006. 24

[95] M.T. Elliott, X. Ma, and P.N. Brett. Tracking the position of an unknown moving load along a plate using the distributive sensing method. *Sensors and Actuators: A. Physical*, 138(1):28–36, 2007. 24

[96] S.P. Mohanty and E. Kougianos. Biosensors: a tutorial review. *IEEE Potentials*, 25(2):35–40, 2006. 25

[97] H. Eltoukhy, K. Salama, and A.E. Gamal. Biosensors: a tutorial review. *IEEE Journal of Solid-State Circuits*, 41(3):651–62, 2006. 25

[98] K. Lnge, B. E. Rapp, and M. Rapp. Surface acoustic wave biosensors: A review. *Analytical and Bioanalytical Chemistry*, 391(5):1509–1519, 2008. 25, 26

[99] L. Nicu etc. Resonating piezoelectric membranes for microelectromechanically based bioassay: detection of streptavidin-gold nanoparticles interaction with biotinylated dna. *Sensors and Actuators B*, 110(1):125–36, 2005. 26, 28, 29, 135

[100] R. Raiteri, M. Grattarola, H.-J. Butt, and P. Skladal. Micromechanical cantilever-based biosensors. *Sensors and Actuators B*, 79(2-3):115–126, 2001. 26

[101] N.V. Lavrik, M.J. Sepaniak, and P.G. Datskos. Cantilever transducers as a platform for chemical and biological sensors. *Review of Scientific Instruments*, 75(7):2229–2253, 2004. 26

[102] G. Wu, R.H. Datar, K.M. Hansen, T. Thundat, R.J. Cote, and A. Majumdar. Bioassay of prostate-specific antigen (psa) using microcantilevers. *Nature Biotechnology*, 19(9):856–860, 2001. 26

[103] Hai-Feng Ji and T. Thundat. In situ detection of calcium ions with chemically modified microcantilevers. *Biosens. Bioelectron. (UK)*, 17(4):337–43, 2002. 26

[104] A. Subramanian, P.I. Oden, S.J. Kennel, K.B. Jacobson, R.J. Warmack, T. Thundat, and M.J. Doktycz. Glucose biosensing using an enzyme-coated microcantilever. *Applied Physics Letters*, 81(2):385–7, 2002. 26

[105] A. Gupta, D. Akin, and R. Bashir. Single virus particle mass detection using microresonators with nanoscale thickness. *Applied Physics Letters*, 84(11):1976–1978, 2004. 26, 153

[106] K.L. Ekinci, Y.T. Yang, and M.L. Roukes. Ultimate limits to inertial mass sensing based upon nanoelectromechanical systems. *Journal of Applied Physics*, 95(5):2682–9, 2004. 26

[107] W. Zhang and K.L. Turner. Application of parametric resonance amplification in a single-crystal silicon micro-oscillator based mass sensor. *Sensors and Actuators A (Physical)*, 122(1):23–30, 2005. 26

[108] T. Braun, V. Barwich, M.K. Ghatkesar, A.H. Bredekamp, C. Gerber, M. Hegner, and H.P. Lang. Micromechanical mass sensors for biomolecular detection in a physiological environment. *Physical Review E (Statistical, Nonlinear, and Soft Matter Physics)*, 72(3):31907–1, 2005. 26

[109] Kyo Seon Hwang, K. Eom, Jeong Hoon Lee, Dong Won Chun, Byung Hak Cha, Dae Sung Yoon, Tae Song Kim, and Jung Ho Park. Dominant surface stress driven by biomolecular interactions in the dynamical response of nanomechanical microcantilevers. *Applied Physics Letters*, 89(17):173905–1, 2006. 26

[110] B. Ilic, D. Czaplewski, H.G. Craighead, P. Neuzil, C. Campagnolo, and C. Batt. Mechanical resonant immunospecific biological detector. *Applied Physics Letters*, 77(3):450–2, 2000. 26

[111] B. Ilic, Y. Yang, and H.G. Craighead. Virus detection using nanoelectromechanical devices. *Applied Physics Letters*, 85(13):2604–2606, 2004. 26, 153

[112] S.M. Yang, C. Chang, T.I. Yin, and P.L. Kuo. Dna hybridization measurement by self-sensing piezoresistive microcantilevers in cmos biosensor. *Sensors and Actuators, B: Chemical*, 130(2):674–681, 2008. 26

[113] A. Mehta, S. Cherian, D. Hedden, and T. Thundat. Manipulation and controlled amplification of brownian motion of microcantilever sensors. *Applied Physics Letters*, 78(11):1637–9, 2001. 27

[114] A. Vidic, D. Then, and C. Ziegler. A new cantilever system for gas and liquid sensing. *Ultramicroscopy*, 97(1-4):407–16, 2003. 27

[115] Suiqiong Li, Liling Fu, J.M. Barbaree, and Z.-Y. Cheng. Resonance behavior of magnetostrictive micro/milli-cantilever and its application as a biosensor. *Sensors and Actuators, B: Chemical*, 137(2):692–699, 2009. 27

[116] Sui-Qiong Li, Zhi-Min Li, Bryan.B. Chin, and Z.-Y. Cheng. Development of biosensor based on micro-diaphragm. *Proceedings of SPIE - The International Society for Optical Engineering*, 5389:306–313, 2004. 27, 28

[117] T. Xu, Z. Wang, J. Miao, L. Yu, and C. Li. Micro-machined piezoelectric membrane-based immunosensor array. *Biosensors and Bioelectronics*, 24 (4):638–432, 2008. 28, 29, 30, 135

[118] N. Liviu etc. Resonating piezoelectric membranes for microelectromechanically based bioassay: detection of streptavidin-gold nanoparticles interaction with biotinylated dna. *Sensors and Actuators B*, 110(1):125–36, 2005. 30

[119] Z. Wu, X. Ma, P. Brett, and J. Xu. Vibration analysis of submerged micro rectangular plates with distributed mass loading. *Proceedings A of the Royal Society*, 465(A):205–216, 2009. 31

[120] A.H. Nayfeh and M. I. Younis. A new approach to the modeling and simulation of flexible microstructures under the effect of squeeze-film damping. *Journal of Micromechanics and Microengineering*, 14(2):170–181, 2004. 31

[121] M.K. Andrews and P.D. Harris. Damping and gas viscosity measurements using a microstructure. *Sensors and Actuators, A: Physical*, 49(1-2):103–108, 1995. 31

[122] R. Szilard. *Theory and analysis of plates, classical and numerical methods.* Prentice-Hall, New Jersey, 1974. 34

[123] F. Zhu. Rayleigh quotients for coupled free vibrations. *Journal of Sound and Vibration*, 171(5):641–649, 1994. 38

[124] U.S. Lindholm, D.D. Kana, W.H. Chu, and H.N. Abramson. Elastic vibration characteristics of cantilever plates in water. *Journal of Ship Research*, 9:11–22, 1965. 47

[125] Herrmann Schlichting. *Boundary-Layer Theory.* McGraw-Hill, Inc, 1979. 53, 54

[126] L. Cremer and M. Heckl. *Structure-Borne Sound.* Springer, 1973. 54

[127] W. A. Strawderman and R. A. Christman. Turbulence-induced plate vibrations: some effects of fluid loading on finite and infinite plates. *Journal of the Acoustical Society of America*, 52(5):1537–1552, 1972. 58, 72

[128] M.H. Meylan. The forced vibration of a thin plate floating on an infinite liquid. *Journal of Sound and Vibration*, 205(5):581–91, 1997. ISSN 0022-460X. 62

[129] A.W. Roberts and W.H. Charlton. Determination of natural responses of mechanical systems using correlation techniques. *Experimental Mechanics*, 15(1):17–22, 1975. 95

[130] M. H. Richardson and D. L. Formenti. Global curve fitting of frequency response measurements using the rational fraction polynomial method. *Proceedings of the International Modal Analysis Conference*, 1:390–397, 1985. 98

[131] Michael Lee and Mark Richardson. Determining the accuracy of modal parameter estimation methods. *Proceedings of the International Modal Analysis Conference*, 1:159–166, 1992. 102

[132] Steve P. Beeby, Graham Ensel, and Michael Kraft. *MEMS Mechanical Sensors.* Artech House Publishers, 2004. 131

[133] Yanqing Lu, V. Chivukula, Ming Wang, and Hai-Feng Ji. Simulation and fabrication of sio2-based piezoresistive microbridges for chem/biosensors. *Journal of Micromechanics and Microengineering*, 16(4):692–8, 2006. ISSN 0960-1317. 132

[134] Xianghong Ma, A.F. Vakakis, and L.A. Bergman. Karhunen-Loeve analysis and order reduction of the transient dynamics of linear coupled oscillators with strongly nonlinear end attachments. *Journal of Sound and Vibration*, 309(3-5):569–87, 2008. 168

[135] P.-O. Mattei. Multiple resonances in fluid-loaded vibrating structures. *Acta Acustica united with Acustica*, 95(2):314–324, 2009. 178

[136] W.H. Press, B.P. Flannery, S.A. Teukolsky, and W.T. Vetterling. *"Simple Monte Carlo Integration" and "Adaptive and Recursive Monte Carlo Methods." 7.6 and 7.8 in Numerical Recipes in FORTRAN: The Art of Scientific Computing, 2nd ed.* Cambridge University Press, Cambridge, England, 1992. 182

[137] A. Papageorgiou. Fast convergence of quasi-monte carlo for a class of isotropic integrals. *Mathematics of Computation*, 70(233):297–306, 2001. 182